Substrate Integrated Waveguide Technology for Rx/Tx Integrated Array Antennas

Vom Promotionsausschuss der
Technischen Universität Hamburg
zur Erlangung des akademischen Grades
Doktor-Ingenieur (Dr.-Ing.)
genehmigte Dissertation

von

Thomas Jaschke 

aus

Hamburg

2021

1. Examiner:	Prof. Dr.-Ing. Arne F. Jacob
2. Examiner:	Prof. Dr.-Ing. Christian Waldschmidt
3. Examiner:	Prof. Dr.-Ing. habil. Alexander Kölpin
4. Examiner:	Prof. Dr.-Ing. Gerhard Bauch

Date of Thesis Defense: November 05, 2020

DOI: https://doi.org/10.15480/882.3648.2

This work is licensed under a Creative Commons "Attribution-NonCommercial 4.0 International" license.

Acknowledgment

The support of many people has been invaluable for the development of this manuscript. First of all, I would like to thank my supervisor Prof. Dr.-Ing. Arne F. Jacob for giving me the opportunity to work at his institute. From him, I received the right combination of freedom, support, and trust for my research activities. I also thank Prof. Dr.-Ing. Christian Waldschmidt and Prof. Dr.-Ing. habil. Alexander Kölpin for the preparation of their expertises and Prof. Dr.-Ing. Gerhard Bauch for chairing the examination committee.

The research project *SAMOA* funded by the *German Aerospace Center* (DLR) served as foundation for this thesis. Here, I would like to thank the whole *SAMOA* team and especially Dr. Siegfried Voigt for their outstanding support.

I would like to thank my colleges, students, and friends of the institute of *High Frequency Technology*, who created an atmosphere, where I enjoyed working every day. I appreciate the great support and expertise of Carmen Hajunga, Anja-Maria Doobe-Jöstingmeier, Werner Thun, and Jürgen Winkelmann regarding the preparation of numerous laboratory demonstrators. Also, I would like to acknowledge Dr. Martin Jenett and Claudia Bredehöft for their administrative and organizational help. I would like to extend my gratitude to all my former students. Particularly, Hans Mitto and Lars Grundhöfer for the continuous collaboration. Special thanks to my close collages Christan Rave, Benjamin Rohrdantz, Frauke Gellersen, Djamschid Safi, and Anton Sieganschin for the uncountable fruitful discussions, convivial evenings, and not least proofreading of this manuscript.

Finally, I would like to thank my family and Katja Kelm for the continuous encouragement to finish this project.

Hamburg, November 05, 2020 Thomas Jaschke

Contents

Notation, Symbols, and Acronyms

The used notations, symbols, and acronyms are listed in the following. To keep the symbol list short, locally used variables like dimensions of components are not included. Ambiguities are avoided, as far as possible. However, remaining ambiguities must be dissolved based on the context.

Notation and Functions

$|x|$ ..... absolute value

$\min(a,b), \max(a,b)$ ..... minimum and maximum value

$\operatorname{atan2}(x,y)$ ..... four-quadrant inverse tangent

$\operatorname{erfc}(z)$ ..... complementary error function

$\mathrm{J}_\chi(z)$ ..... Bessel function

$\mathrm{H}_\chi^{(2)}(z)$ ..... Hankel function of second kind

$\mathrm{T}_\chi(z)$ ..... Chebyshev polynomial

$\lfloor x \rfloor, \lceil x \rceil$ ..... floor and ceiling function

$\delta_m = \begin{cases} 1, & m = 0 \\ 0, & m \neq 0 \end{cases}$ ..... Kronecker delta

$\varepsilon_m = 2 - \delta_m$ ..... Neumann's number

$\mathrm{j} = \sqrt{-1}$ ..... imaginary unit

$\operatorname{Re}(z), \operatorname{Im}(z)$ ..... real and imaginary part

$\arg(z)$ ..... argument of complex number

$(a + \mathrm{j}\,b)^* = a - \mathrm{j}\,b$ ..... conjugate-complex

$\vec{x}$ ..... vector

$\vec{x}^T$ ..... transposed vector

$\vec{a} \times \vec{b}$, $\vec{a} \bullet \vec{b}$ ..... cross and scalar product

$[S]$ ..... matrix

$[S]^{-1}$ ..... inverse matrix

$[I]$ ..... unit matrix

$\det([S])$ ..... determinant

$[A] \circ [B]$ ..... element-wise matrix product (Hadamard product)

Differential Operators

$\frac{d\omega}{dk}$ ..... total derivative
$\frac{\partial \vec{E}(x,y,z)}{\partial x}$ ..... partial derivative
$\nabla \Psi(x,y,z)$ ..... gradient of scalar field
$\nabla^2 \Psi(x,y,z)$ ..... Laplacian operator of scalar field
$\nabla^2_{xy} \Psi(x,y,z)$ ..... two-dimensional Laplacian operator
$\nabla \bullet \vec{E}(x,y,z)$ ..... divergence of vector field
$\nabla \times \vec{E}(x,y,z)$ ..... curl of vector field
$\nabla^2 \vec{E}(x,y,z)$ ..... Laplacian operator of vector field

Physical Constants and Quantities

$c_0 = 2.998 \cdot 10^8 \, \frac{\mathrm{m}}{\mathrm{s}}$ ..... speed of light in vacuum
$\epsilon_0 = 8.854 \cdot 10^{-12} \, \frac{\mathrm{A\,s}}{\mathrm{V\,m}}$ ..... vacuum permittivity
$\mu_0 = 4\pi \cdot 10^{-7} \, \frac{\mathrm{V\,s}}{\mathrm{A\,m}}$ ..... vacuum permeability
$\epsilon = \epsilon_0 \, \epsilon_r \, (1 - \mathrm{j} \tan(\delta_d))$ ..... permittivity in medium
$\mu = \mu_0 \, \mu_r$ ..... permeability in medium
$k = 1.381 \cdot 10^{-23} \, \frac{\mathrm{W}}{\mathrm{K\,Hz}}$ ..... Boltzmann constant
$\tan(\delta_d)$ ..... loss tangent
σ_0 ..... conductivity
t ..... time
f, $\omega = 2\,\pi\,f$ ..... frequency and angular frequency
$k_0 = \frac{\omega}{c}$ ..... wave number in medium
$\lambda_0 = \frac{c}{f}$ ..... wavelength in medium
$Z_0 = \sqrt{\frac{\mu}{\epsilon}}$, $Y_0 = \frac{1}{Z_0}$ ..... wave impedance and admittance in medium

Antenna and Terminal Parameters

$\vec{g}$	far-field pattern
G_R, G, D	realized gain, gain, and directivity
P_{stim}, P_{acc}, P_{rad}	stimulating, accepted, and radiated power
η_{rad}, η_{tot}, η_A	radiation, total, and aperture efficiency
A, D	aperture area and diameter
SLL	side-lobe level
T_e	equivalent system noise temperature
G/T	gain-to-system-noise-temperature
$EIRP$	equivalent isotropically radiated power

Array and Element Parameters

(θ_0, ϕ_0)	pointing direction
θ_{max}	maximum scan angle
$\bar{n}$	Taylor taper design parameter
$\vec{r}_n$, d	element position and spacing
s, U	row distance and unit cell surface area
L_{ant}	antenna element loss
D_{ele}, P_{ele}, $EIRP_{ele}$	directivity, power, and EIRP of the element

Receiver and Noise Parameters

B	bandwidth
C/N	carrier-to-noise ratio
L_{atm}	atmospheric loss
L_M	system margin
G_r	receiver gain
T_0, $T_{e,r}$	reference and equivalent receiver noise temperature
$T_{e,sky}$	equivalent noise temperature of the sky
$T_{e,atm}$, T_{atm}	equivalent noise and physical temperature of the atmosphere
$T_{e,ant}$, T_{ant}	equivalent noise and physical temperature of the antenna
$T_{e,surf}$, T_{surf}	equivalent noise and physical temperature of the surface
α_{atm}	fraction of radiation pattern that receives noise from the atmosphere

Coordinate Systems and Unit Vectors

$\vec{E}(x,y,z)$, $\vec{u}_x, \vec{u}_y, \vec{u}_z$ ..... global Cartesian coordinates and unit vectors
$\vec{E}(u,v,w)$, $\vec{u}_u, \vec{u}_v, \vec{u}_w$ ..... local Cartesian coordinates and unit vectors
$\vec{E}(r,\theta,\phi)$, $\vec{u}_r, \vec{u}_\theta, \vec{u}_\phi$ ..... spherical coordinates and unit vectors
$\vec{E}(r,\phi)$, $\vec{u}_r, \vec{u}_\phi$ ..... polar coordinates and unit vectors
$\vec{u}_n$ ..... normal vector of transverse plane
$\vec{u}_B$ ..... normal vector of boundary B
$\vec{u}_S$ ..... normal vector of surface S

Electromagnetic Quantities

All frequency domain quantities are assumed to be root-mean-square value phasors with a harmonic time dependency of $\mathrm{e}^{\mathrm{j}\omega t}$.

$\vec{E}(x,y,z), \vec{H}(x,y,z)$ ..... electric and magnetic field
$\vec{J}(x,y,z)$ ..... electric current density
$\vec{F}(x,y,z), \vec{A}(x,y,z)$ ..... electric and magnetic vector potential
$\vec{E}_{xy}(x,y,z)$ ..... x- and y-components of vector field
$\vec{J}_s(x,y,z)$ ..... electric surface current density
$\Psi(x,y,z) = \Psi_x(x)\,\Psi_y(y)\,\Psi_z(z)$ scalar potential
$\Psi_x(x), \Psi_y(y), \Psi_z(z)$ ..... factors of scalar potential
$\Psi_{xy}(x,y) = \Psi_x(x)\,\Psi_y(y)$ ..... combinations of factors

Indices

$n, \bar{n}$ ..... waveguide component
$\boldsymbol{p}, \bar{\boldsymbol{p}}$ ..... waveguide port
$m, \bar{m}$ ..... waveguide mode order
$\nu, \bar{\nu}, \hat{\nu}$ ..... parallel-plate, cylinder, or Floquet component
$\boldsymbol{\rho}, \bar{\boldsymbol{\rho}}$ ..... parallel-plate, cylinder, or Floquet port
$\mu, \bar{\mu}$ ..... parallel-plate mode order
$\chi, \bar{\chi}$ ..... cylinder mode order
$\xi, \bar{\xi}$ ..... Floquet mode order
$s_{\boldsymbol{A}}, s_{\boldsymbol{B}}$ ..... set of ports
$(n, \boldsymbol{p}[m]), (n, \boldsymbol{p}), n[m], \boldsymbol{p}[m]$ ... notation for index combinations

Scattering Parameters

$a_{\boldsymbol{p}[m]}, b_{\boldsymbol{p}[m]}, \vec{a}, \vec{b}$ ..... incident and reflected wave amplitude and vector
$S_{\boldsymbol{p}[m],\bar{\boldsymbol{p}}[\bar{m}]}, [S]$ ..... scattering parameter and matrix
$C_{\boldsymbol{p}[m],\bar{\boldsymbol{p}}[\bar{m}]}, [C]$ ..... coupling coefficient and matrix
$\Gamma, [\Gamma]$ ..... reflection coefficient and matrix
$[T]$ ..... transmission matrix

Waveguide Parameters

S ..... waveguide cross-section
B ..... waveguide boundaries
$Z, Y = 1/Z$ ..... modal wave impedance and admittance
$A^{\pm}$ ..... wave amplitude with propagation in $\pm w$-direction
a, b ..... width and height of rectangular waveguide
$\gamma = \alpha + \mathrm{j}\,\beta$ ..... propagation constant
α, β ..... attenuation and phase constant
k_c, f_c ..... cutoff wave number and frequency
$k_{xz}^2 = k_x^2 + k_z^2$ ..... two-dimensional wave number
$\vec{e}^{\pm}(x,y), \vec{h}^{\pm}(x,y)$ ..... modal electric and magnetic field
$V(w), I(w)$ ..... modal voltage and current
P ..... real power
K ..... normalization coefficient
$S_{\mathbf{1}} \cap S_{\mathbf{2}}$ ..... intersection of cross-sections $S_{\mathbf{1}}$ and $S_{\mathbf{2}}$

Floquet and SIW Parameters

h ..... parallel-plate height
p ..... via pitch
d ..... via diameter
$w, \Delta w = (w-a)/2$ ..... via row distance and offset
θ ..... propagation angle
Φ_z ..... phase difference

Rough Surfaces and Waveguide Losses

R_z, R_q ..... surface roughness (peak-to-valley, root-mean-square)
δ_s ..... skin depth of smooth surface
δ_c, δ_m ..... skin depth of effective current density and magnetic field
z_S ..... normalized surface impedance

Acronyms

C/N	carrier-to-noise ratio
CPW	coplanar waveguide
EIRP	equivalent isotropically radiated power
ETSI	European Telecommunications Standards Institute
FEM	finite element method
FSS	fixed-satellite service
G/T	gain-to-system-noise-temperature
GEO	geostationary orbit
GSM	generalized scattering matrix
GTRM	generalized transverse resonance method
HTS	high-throughput satellite
LEO	low Earth orbit
LHCP	left-handed circular polarization
LNA	low-noise amplifier
MEO	medium Earth orbit
MODCOD	modulation and coding
MSIW	multilayer substrate integrated waveguide
NURBS	non-uniform rational basis splines
PA	power amplifier
PCB	printed circuit board
PEC	perfect electric conductor
PMC	perfect magnetic conductor
PTFE	polytetrafluoroethylene (*Teflon*)
RHCP	right-handed circular polarization
Rx	receive
SIW	substrate integrated waveguide
SLL	side-lobe level
SMD	surface-mounted device
TE	transverse electric
TM	transverse magnetic
TRL	thru-reflect-line
TRM	transverse resonance method
Tx	transmit

1 Introduction

The aim of this work is to develop a concept for very compact antennas for satellite communications. To achieve this, the receive (Rx) and transmit (Tx) functionality is integrated into a single antenna aperture. The enabling technology is based on substrate integrated waveguides (SIWs), which are analyzed in depth. Beginning with the fundamental SIW properties, modeling and design techniques for components are developed. Finally, resulting components are combined to an Rx/Tx integrated antenna.

Mobile Satellite Communications

Nowadays, wireless communications play an important role in our everyday life. Using the Internet with mobile computers and smartphones is desired everywhere we work and live. In recent years, especially the mobile-broadband traffic drastically increased [1]. In densely populated areas, terrestrial networks of the fourth or fifth generation provide high-speed connections allowing to cope with the increased traffic. However, in rural and remote areas, setting up these networks is often too costly or even impossible. Here, satellite communications are a feasible alternative. Users are connected to the Internet via satellites and gateways on the ground, as depicted in Fig. 1.1. Thus, a local terrestrial or wired infrastructure is not necessary. A user terminal itself can act as an access point for a number of mobile devices. These access points build local networks, for example from the rooftop of a remote school building or inside an airplane during a transatlantic flight.

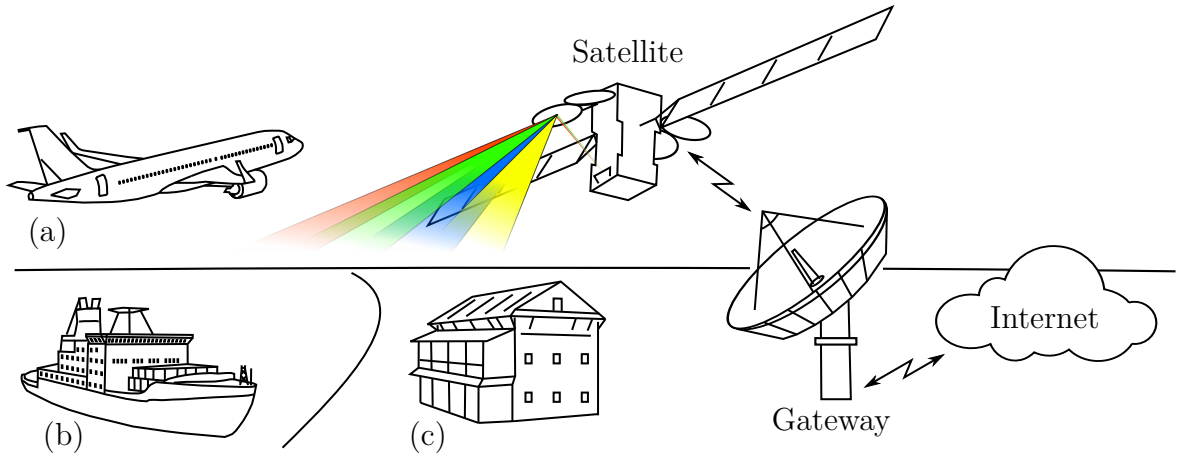

Figure 1.1: Satellite communications with (a) aeronautic, (b) maritime, and (c) fixed user.

The satellites are typically placed in geocentric orbits that are classified in three altitude regions, the low Earth orbit (LEO), the medium Earth orbit (MEO), and the geostationary orbit (GEO). A LEO satellite orbits the Earth at an altitude of less than 2000 km in a few hours. A GEO satellite rotates synchronously to the Earth at an altitude of 36 000 km above the equator and, thus, is fixed in relation to the Earth's surface. The MEO lies between these two orbits. Today, high-throughput satellites (HTSs) operating in the GEO provide broadband connections to most parts of the Earth's surface. These satellite systems cover a service region using multiple narrow spot beams. The available frequency bandwidth is reused in different spot beams by means of the four-color scheme [2]. The colors represent two frequency and two polarization states. Services such as *Epic*^{NG} from *Intelsat* and *Exede* from *Viasat* operate in the GEO and are ready to use. To increase the capacity, satellite constellations are implemented in the LEO and MEO. Since 2014, the *O3b* consortium offers broadband communications for the equatorial region with 20 satellites (status 2019) in the MEO. Upcoming mega-constellations such as *Starlink* from *SpaceX* and *OneWeb* will use several hundred to several thousand satellites in the LEO [3].

For broadband satellite communications, typically, the Ku- and K/Ka-band are used. In the K/Ka-band, a bandwidth of 3.5 GHz is allocated for both downlink (17.7 GHz to 21.2 GHz) and uplink (27.5 GHz to 31 GHz) [4]. Compared to well established Ku-band systems, this is an advantage and, thus, the K/Ka-band is considered in the following. The upper GHz of both bands is allocated to governmental applications, as depicted in Fig. 1.2. 500 MHz of both bands are globally available and supported by most of the K/Ka-band satellites. In addition, some satellites support other bands, as shown in Fig. 1.2. For the antenna design in this work, the typical (Rx: 18.7 GHz to 21.2 GHz, Tx: 27.5 GHz

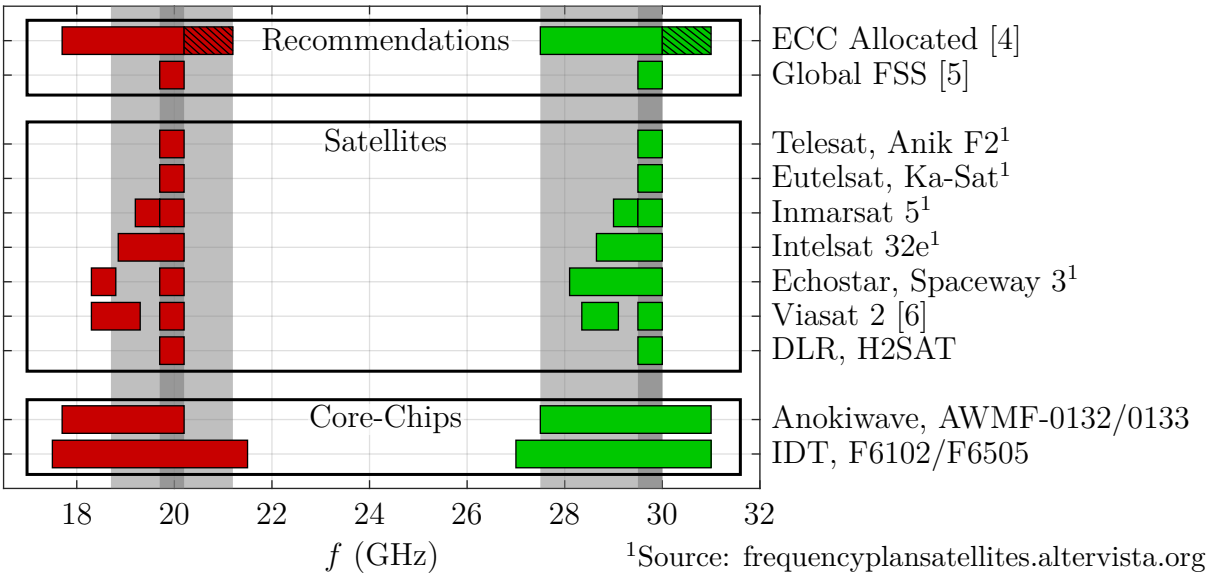

Figure 1.2: Overview of frequency bands for satellite communications (■ Rx / ■ Tx frequency bands, ▨ governmental, ■ typical / ■ reference bands).

to 30 GHz) and reference frequency bands (Rx: 19.7 GHz to 20.2 GHz, Tx: 29.5 GHz to 30 GHz) are defined with a bandwidth of 2.5 GHz and 0.5 GHz, respectively. In the following figures, these bands are marked in gray. The typical frequency bands include most of the bands supported by the listed satellites.

Originally, HTSs are constructed for fixed-satellite service (FSS), where the terminals are installed at fixed positions. However, mobile Internet access for so-called earth stations on mobile platform is a key driver for satellite communications nowadays. In this work, terminals on aircrafts, ships, and trains are considered. Due to the vehicular movement, the antenna beam must be continuously readjusted towards the satellite. For this, classical reflector antennas are combined with mechanical positioning systems. Such terminals are available for example from *Epak* and *Orbit*. However, these systems are mechanically complex and bulky. An alternative are electrically steered phased array antennas. For this, hundreds to thousands of antenna elements are used simultaneously. The resulting solutions are flat and no mechanical positioning systems are necessary. However, the number of electronic components increases considerably. Recent developments have significantly reduced the cost of these components, such that phased array antennas become more affordable for commercial use. On the semiconductor market, so-called core-chips combine the functionality for multiple antenna elements in a single chip with amplifiers, phase shifters, and combining networks [7–9]. *Anokiwave* and *Integrated Device Technology (IDT)* provide commercial chips for the intended application at the desired frequency bands, as depicted in Fig. 1.2. Antenna solutions for Rx and Tx based on these chips are presented in [10–12].

In this work, the aperture size is reduced by combining the Rx and Tx functionality in a single array antenna. The wide frequency spread between Rx and Tx requires novel solutions. The research project *FLEXWIN* funded by the European Union has addressed this problem. Here, a core-chip [9], antenna elements [13], and an active transmit array [14] were developed. However, the presented solutions only support a single polarization and operate in a half-duplex mode. Thus, the usability is limited in combination with the four-color scheme. In this work, a concept for the Rx/Tx integrated array antenna with two circular polarizations is developed and verified by a passive demonstrator. The results were obtained within the research projects *SAMOA* [15] and *SANTANA-AERO* funded by the German Aerospace Center (DLR) on behalf of the German Federal Ministry of Economics and Technology (BMWi).

Substrate Integrated Waveguide Technology

Classical array antennas are often based on waveguide technology, which provides very low losses and complete shielding. However, this leads to bulky, heavy, and costly components. For the design of a compact array antenna, this work employs the SIW technology. It is basically an implementation of waveguide technology in planar printed circuit boards (PCBs). The top and bottom metalizations of the waveguide are realized by the metal layers of the PCB. The sidewalls are implemented in a discrete form as via rows, as depicted in Fig. 1.3. Thus, SIWs combine advantages from waveguides and PCB technology.

The SIW was first mentioned in a Japanese patent in 1994 [16]. Since then, this technology has attracted a lot of research interest. Most waveguide designs can be transformed to SIW technology in a straightforward fashion. Nowadays, various SIW components, such as transitions [17–19], filters [20–22], and antennas [23–25], are available.

A major advantage of SIW components is their good shielding, provided the via pitch is properly chosen. Additionally, the integration of semiconductor devices is possible within standard PCB assembly processes. Modern low-loss packaging technologies allow for the integration of semiconductor devices as surface-mounted devices (SMDs) up to the micro- and millimeter-wave region. Thus, for the active array antenna, the passive, analog, and digital components can be implemented and assembled on the same PCB. Compared to empty waveguides, the dielectric inside the SIW reduces the size and allows for a tight element spacing. A drawback of this filling is the increased loss, which is comparable to that of planar transmission lines.

The proposed antenna concept is based on an end-fire solution with square SIWs, as presented in [24] and [26]. However, the cited solution is rather narrowband and only supports Tx operation. In the course of this work, the solution is substantially extended to an Rx/Tx integrated array antenna. This requires a careful design of broadband SIW components. For the antenna elements, this is achieved by matching the square SIWs with a dielectric lens.

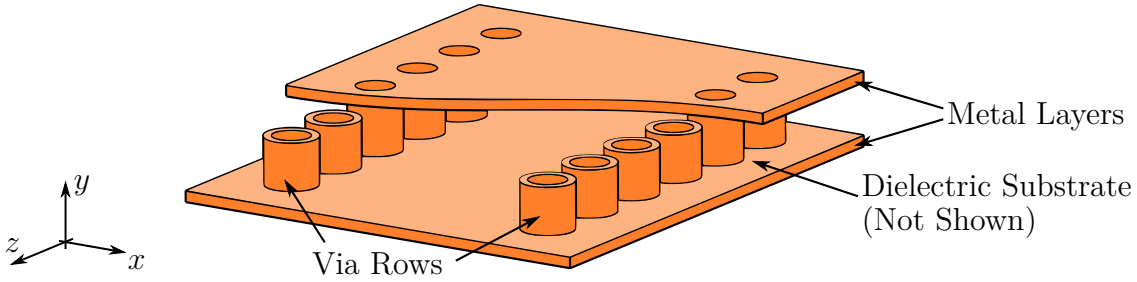

Figure 1.3: Model of an SIW with two via rows.

Structure of this Work

This work is structured in four content chapters. First, a concept for Rx/Tx integrated array antennas is developed. Then, the theory of SIWs is discussed and a modeling method for SIW components is presented. Based on this method, components are designed and, finally, the Rx/Tx integrated array antenna is built by combining these components with a dielectric lens.

Chapter 2 starts with a link budget of a reference scenario with GEO satellites. The data rate is determined as a function of the terminal parameters. Next, the arrangement of the antenna elements is discussed. Here, the wide frequency spread of Rx and Tx allows for interleaved array grids with combined Rx/Tx and Tx-only elements. Then, requirements for the array antenna are determined from satellite communication regulations. Depending on the array size, a maximum transmit power is determined and a possible frontend architecture is outlined. Terminal parameters for an Rx/Tx integrated array antenna are determined and compared to separate Rx and Tx antenna arrays with equivalent characteristics. The possible size reduction is quantified. Subsequently, antenna architectures are discussed and a lens antenna concept is proposed.

This concept utilizes the SIW technology, as detailed in Chapter 3. It starts with a review of the guided-wave theory and discusses waveguides with rough conductor surfaces. The equivalence of SIWs and rectangular waveguides is outlined. This concept is extended to the class of multilayer substrate integrated waveguides (MSIWs). The modal characteristics are determined using the transverse resonance method (TRM) and the mode matching method. Based on this, a method for modeling MSIW components is derived.

Chapter 4 utilizes the presented theory to model MSIW components. Design and synthesis procedures for transitions between SIWs with different cross-sections are introduced. The resulting components are realized and the functionality is verified by measurements. Next, polarizers for the antenna elements are designed and a technique to compensate the cross-polarization is presented.

In Chapter 5, the lens antenna concept is implemented. First, a single antenna element with a dielectric lens is analyzed and ultra-broadband characteristics are achieved. Finally, the SIW components and a dielectric lens are combined to a demonstrator for the Rx/Tx integrated array antenna. This work concludes with a summary and an outlook.

2 Array Antennas with Rx/Tx Integration

An array antenna consists of an ensemble of antenna elements that are usually arranged in a periodic grid. These elements are excited coherently and operate together as a single large antenna. The concept of an Rx/Tx integrated array antenna is analyzed in the following. This chapter starts with a link budget analysis for a satellite communication scenario. Then, the basic operation principle of array antennas is reviewed and array parameters are determined for circular apertures. Different array grids for integrated Rx/Tx array antennas are discussed and a concept for active frontends with a beam forming network is outlined. Furthermore, the system noise temperature is analyzed and the achievable data rate of exemplary terminal antennas is determined. To quantify the advantage of an Rx/Tx integrated array, the size of such a terminal is compared to that of separate terminals. Finally, possible array and feed architectures are discussed and a modular lens antenna concept is presented.

2.1 Link Budget

A GEO satellite communication scenario is analyzed in the following. For this purpose, the terminal antenna is represented by the equivalent isotropically radiated power (EIRP) and the gain-to-system-noise-temperature (G/T). The EIRP characterizes the Tx antenna performance and is given by the product of the input power and the antenna gain. The G/T characterizes the Rx performance and is defined as the ratio of the antenna gain to the equivalent system noise temperature. The data rate is determined by a generic link budget analysis as a function of these parameters. Parameters and results are given in Tab. 2.1. For the satellite, an EIRP of 55 dBW and a G/T of 12 dB/K are assumed. These values are determined from a comparison of typical commercial satellite systems but can vary depending on the specific system. The large distance between the terminal and satellite of about 38 000 km results in a free space loss of 210 dB and 214 dB in the downlink at 20 GHz and uplink at 30 GHz, respectively. Additionally, atmospheric losses result from the attenuation due to gases, clouds, fog, rain, or even sand storms. The attenuation due to atmospheric gases depends on the temperature, pressure, and water-vapor profile of the atmosphere and strongly on the signal frequency [27]. For a standard atmosphere with a

Table 2.1: Link budget for a typical GEO satellite.

Description	**Downlink**	**Uplink**
Transmitter	Satellite	Terminal
Receiver	Terminal	Satellite
Frequency (GHz)	20	30
Distance (km)	38 000	38 000
Free Space Loss (dB)	210	214
Atmospheric Loss (dB)	L_{atm}	L_{atm}
Path Loss (dB)	$210 + L_{atm}$	$214 + L_{atm}$
EIRP (dBW)	55	$EIRP$
G/T (dBi/K)	G/T	12
System Margin (dB)	L_M	L_M
k (dB(W/K/MHz))[1]	-169	-169
Bandwidth (dBMHz)	B	B
C/N (dB)	$14\,\mathrm{dB(K\,MHz)} + G/T$ $-L_{atm} - L_M - B$	$-33\,\mathrm{dB(MHz/W)} + EIRP$ $-L_{atm} - L_M - B$

[1] Boltzmann constant.

clear sky [28], the atmospheric loss is typically below 1 dB for the intended frequency bands. When heavy clouds (2 kg/m^2 columnar liquid water content) cover the propagation path, the loss is increased by about 1.5 dB and 3 dB in the down- and uplink, respectively [29]. Very heavy rain (35 mm/h, Hamburg, Germany) has a huge influence and increases the atmospheric loss by about 17 dB and 33 dB for the down- and uplink, respectively [30]. In addition, the noise emission of the relatively warm atmosphere rises similarly to the losses of the atmosphere. Thus, for the Rx case, the equivalent antenna noise temperature of the terminal increases with the atmospheric losses. The carrier-to-noise ratio (C/N) can now be determined in terms of the terminal antenna parameters, the atmospheric loss L_{atm}, a system margin L_M, and the bandwidth B, as given in the last row of Tab. 2.1. The system margin includes variations in the link budget parameters and neglected effects such as the link of a base station to the satellite.

The DVB-S standards (*Digital Video Broadcasting - Satellite*) define several channel modulation and coding (MODCOD) schemes for digital data transmission. The DVB-S2 [31] and DVB-S2X [32] standards are state-of-the-art and widely used in satellite communications. For each MODCOD, a minimum C/N is required for quasi error-free data transmission. With a higher C/N, a MODCOD with higher spectral efficiency, i.e., information bit per symbol, can be used [33]. The maximum possible data rate versus the terminal antenna parameters for different bandwidths is depicted in Fig. 2.1. Here, the MODCODs of the DVB-S2 standard, a roll-off factor of 0.2 for the matched filter, and a packet error rate of 10^{-7} are presumed. The data rate increases stepwise with G/T and $EIRP$ of the terminal for the down- and uplink, respectively. Each step corresponds to

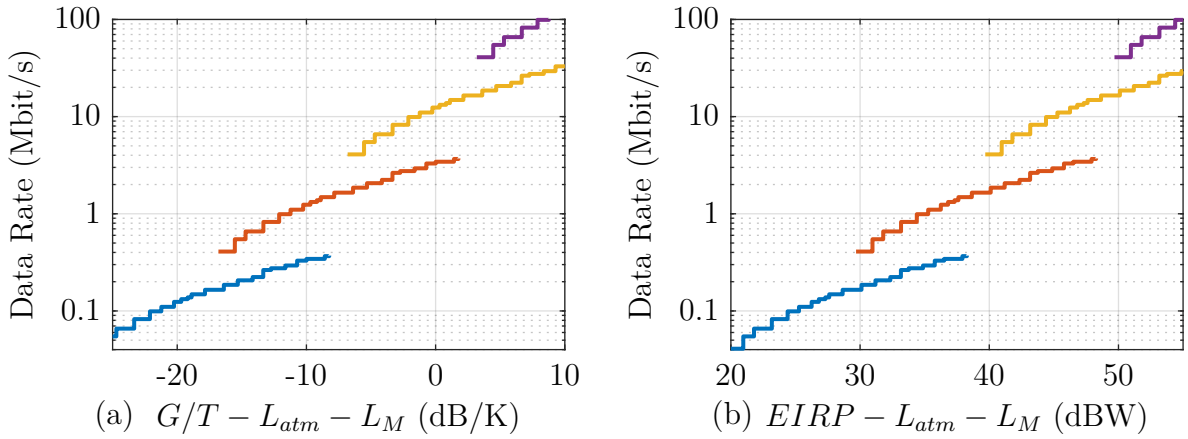

Figure 2.1: Data rate versus (a) G/T and (b) $EIRP$ (— $B = 100\,\text{kHz}$, — $B = 1\,\text{MHz}$, — $B = 10\,\text{MHz}$, — $B = 100\,\text{MHz}$).

a specific MODCOD. For example, a data rate of 1 MBit/s can be achieved with a bandwidth of 1 MHz and the terminal antenna parameters of $G/T = -11\,\text{dB/K} + L_{atm} + L_M$ and $EIRP = 35\,\text{dBW} + L_{atm} + L_M$.

It should be pointed out that the described link budget only takes the most important effects into account and a real application needs a considerable system margin. This margin can include additional signal attenuation that could occur due to pointing errors, polarization impurity, and at the edges of the spot beam. In a multiuser scenario, interferences from other users can also degrade the C/N. Furthermore, the parameters of the terminal antenna are not fixed and vary with the scan angle, the mounting position, and the installation environment. However, the given link budget analyzes a generic reference scenario and can be easily adapted for a specific application.

2.2 Array Grids

For the Rx/Tx integrated array antenna, different array grids are interleaved and then compared to each other [34]. To prevent grating lobes in the far-field, the element distances d_{Rx} and d_{Tx} in the Rx and Tx band must be lower than $0.5\,\alpha\,\lambda$ in case of a rectangular grid and below $0.577\,\alpha\,\lambda$ for a triangular one. The constant

$$\alpha = \frac{2}{1 + \sin\theta_{max}} \tag{2.1}$$

depends on the maximum scan angle θ_{max} and ranges from $\alpha = 1$ for coverage of the complete hemisphere to $\alpha = 2$ for a fixed beam in broadside direction.

Fig. 2.2 depicts four array grids that combine Rx and Tx. First, the rectangular and the triangular grid completely filled with combined Rx/Tx elements are investigated, as depicted in Fig. 2.2a and Fig. 2.2b. The maximum distance between elements is determined by the highest frequency involved, which is given by the Tx band. This leads to spatial oversampling of the Rx grids and, thus, to a higher than necessary number of Rx elements.

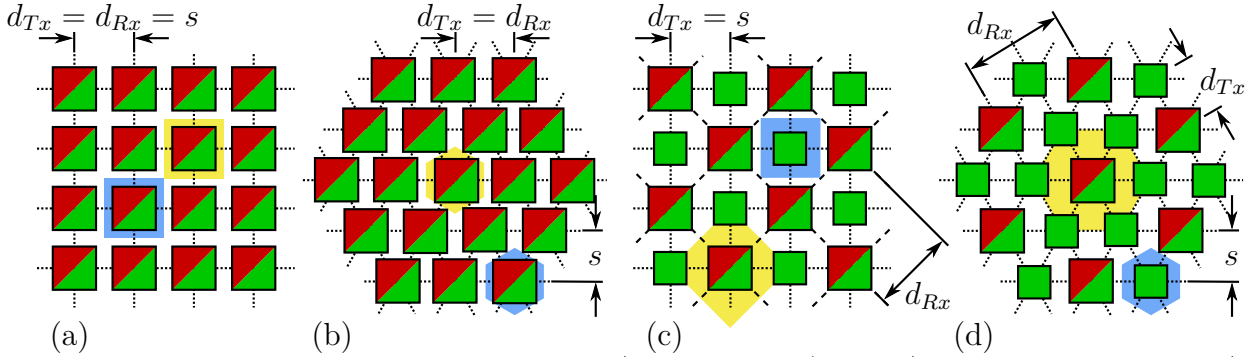

Figure 2.2: Array grids for a combined Rx/Tx aperture (■ Rx / ■ Tx element, ■ Rx / ■ Tx unit cell surface area, ···· grid lines).

In addition, the distance s between the element rows is depicted. The relative distances are listed in Tab. 2.2. Important figures of merit are the Rx and Tx unit cell surface areas U_{Rx} and U_{Tx}. For a specific aperture area, the respective number of elements is inversely proportional to the unit cell surface area. In the case of the triangular grid, the unit area is 15 % higher than for the rectangular one. As the Tx and Rx elements are co-located, the normalized unit cell surface area of the Tx elements is considerably larger than that of the Rx elements. The array complexity depends on the total number of channels. Each Rx/Tx element requires two Rx and two Tx channels if dual polarization is assumed. This yields a number of Rx as well as Tx channels per area of $8\,\alpha^{-2}\mathrm{cm}^{-2}$ for a rectangular grid and $6.9\,\alpha^{-2}\mathrm{cm}^{-2}$ for the triangular one.

Interleaved grids, such as the rectangular [35] and the triangular one shown in Fig. 2.2c and Fig. 2.2d, allow to reduce the number of Rx elements. Here, the array is built from the superposition of a Tx grid and a rotated Rx grid. This requires both combined Rx/Tx and Tx-only elements. In both configurations, the maximum allowable element distance depends on the involved frequencies. Here, the maximum of each reference frequency band (see Chapter 1) is assumed. In the rectangular grid, the spacing is dictated by the Tx frequency, which leads to a (slight) oversampling of the Rx grid, whereas the opposite applies in the triangular case. The number of Tx and Rx channels per unit cell surface area is $8\,\alpha^{-2}\mathrm{cm}^{-2}$ and $4\,\alpha^{-2}\mathrm{cm}^{-2}$ for the rectangular grid and $9.5\,\alpha^{-2}\mathrm{cm}^{-2}$ and $3.1\,\alpha^{-2}\mathrm{cm}^{-2}$ for the triangular one, respectively. It can be observed that the interleaved grids significantly reduce the number of Rx channels and, thus, also the integration density and complexity.

Table 2.2: Parameters of the array grids.

Grid	Fig.	Oversampling	d_{Rx}/λ_{Rx}	d_{Tx}/λ_{Tx}	U_{Rx}/λ_{Rx}^2	U_{Tx}/λ_{Tx}^2	s/λ_{Tx}
Rectangular	2.2a	Rx Band	0.337α	0.500α	$0.114\alpha^2$	$0.250\alpha^2$	$\mathbf{0.500\alpha}$
Triangular	2.2b	Rx Band	0.389α	$\mathbf{0.577\alpha}$	$0.131\alpha^2$	$\mathbf{0.289\alpha^2}$	$\mathbf{0.500\alpha}$
Rectangular[1]	2.2c	Rx Band	0.476α	0.500α	$0.227\alpha^2$	$0.250\alpha^2$	$\mathbf{0.500\alpha}$
Triangular[1]	2.2d	Tx Band	$\mathbf{0.577\alpha}$	0.495α	$\mathbf{0.289\alpha^2}$	$0.212\alpha^2$	0.429α

[1] Interleaved grid.

In particular in the brick architecture, as discussed in Sec. 2.6, the distance s between element rows is crucial, because it determines the available space for a modular approach. For the interleaved triangular grid this distance is 14 % smaller than for the other grids. However, the integration density along the grid lines is reduced, because a combined Rx/Tx element alternates with two Tx-only elements, compared to one in the rectangular case.

For the array design in this work, an interleaved rectangular grid is chosen. The total number of channels is minimum for this grid and s is larger than for the interleaved triangular grid. Furthermore, the arrangement of modules is simpler for a rectangular than for a triangular grid. Here, $\alpha = 1$ is assumed such that the scanning range is not limited by grating lobes. The maximum Tx frequency of 30 GHz results in an element distance of $d_{Tx} = 5\,\text{mm}$. For the Rx elements, this yields a distance of $d_{Rx} = 7.1\,\text{mm}$ and a maximum operation frequency of 21.2 GHz.

2.3 Array Antennas

Fig. 2.3 shows an array antenna consisting of several antenna elements. To begin with, the properties of a single element n are reviewed. This element is located at the position $\vec{r}_n$ and is excited by the wave amplitude a_n with a stimulating power of

$$P_{stim,n} = |a_n|^2 \,. \tag{2.2a}$$

It radiates the power

$$P_{rad,n} = Y_0\, r^2 \oiint \left|\vec{E}_n(r,\theta,\phi)\right|^2 \, d\Omega, \tag{2.2b}$$

where $Y_0 = 1/Z_0$, $Z_0 = \sqrt{\mu_0/\epsilon_0}$, $\vec{E}_n(r,\theta,\phi)$, and Ω are the wave admittance, the wave impedance, the electric field of the element, and the solid angle, respectively. In the far-field region, the electric field

$$\vec{E}_n(r,\theta,\phi) = a_n \sqrt{\frac{Z_0}{4\,\pi}}\, \frac{\mathrm{e}^{-\mathrm{j}\,k_0\,r}}{r}\, \vec{g}_n(\theta,\phi) \tag{2.3a}$$

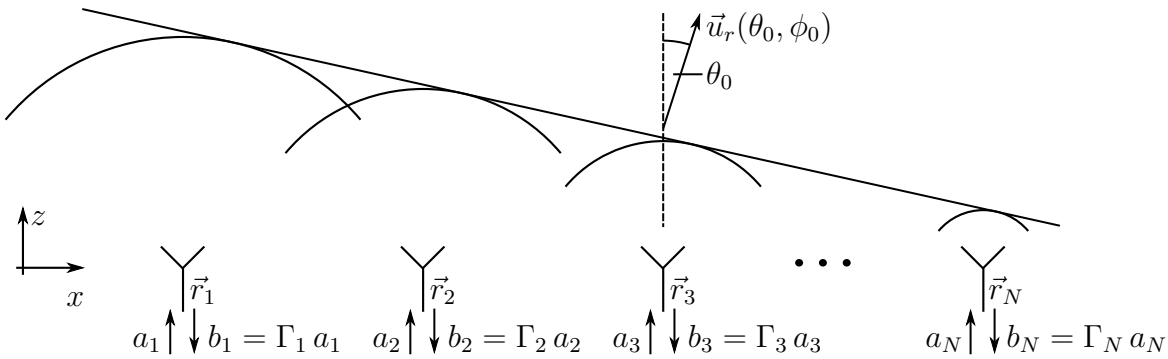

Figure 2.3: The operation principle of an array antenna.

and the magnetic field

$$\vec{H}_n(r,\theta,\phi) = a_n \sqrt{\frac{Y_0}{4\,\pi}}\,\frac{\mathrm{e}^{-\mathrm{j}\,k_0\,r}}{r}\;(\vec{u}_r(\theta,\phi)\times\vec{g}_n(\theta,\phi)) \tag{2.3b}$$

can be expressed by the so-called far-field pattern $\vec{g}_n(\theta,\phi)$ [36, p. 49], which is independent of the radius r and only depends on the spherical angles (θ,ϕ). Here, $k_0 = \omega\,\sqrt{\mu_0\,\epsilon_0}$ is the wave number and $\omega = 2\,\pi\,f$ the angular frequency. The radiated power propagates in the direction of the radial unit vector

$$\vec{u}_r(\theta,\phi) = \Big[\sin(\theta)\,\cos(\phi)\quad \sin(\theta)\,\sin(\phi)\quad \cos(\theta)\Big]^T, \tag{2.4}$$

which is orthogonal to the electric and magnetic field. The far-field pattern $\vec{g}_n(\theta,\phi)$ can be normalized to that of an isotropic radiator by

$$\frac{1}{4\,\pi}\oiint |\vec{g}_n(\theta,\phi)|^2\;d\Omega = \eta_{tot}, \tag{2.5}$$

where the total efficiency is defined by the power ratio

$$\eta_{tot} = \frac{P_{rad,n}}{P_{stim,n}}. \tag{2.6}$$

With this normalization, the realized gain

$$G_{R,n}(\theta,\phi) = |\vec{g}_n(\theta,\phi)|^2 \tag{2.7a}$$

is given by the squared magnitude of the far-field pattern. The directivity

$$D_n(\theta,\phi) = \frac{1}{\eta_{tot}}\;|\vec{g}_n(\theta,\phi)|^2 \tag{2.7b}$$

and gain

$$G_n(\theta,\phi) = \frac{\eta_{rad}}{\eta_{tot}}\;|\vec{g}_n(\theta,\phi)|^2 \tag{2.7c}$$

are scaled versions of the realized gain, where the radiated efficiency

$$\eta_{rad} = \frac{P_{rad,n}}{P_{acc,n}} \tag{2.8}$$

is given by the ratio of $P_{rad,n}$ and the accepted power

$$P_{acc,n} = P_{stim,n}\,(1-|\Gamma_n|^2). \tag{2.9}$$

Here, $\Gamma_n = b_n/a_n$ is the reflection coefficient of the antenna element with the reflected wave amplitude b_n. In an array environment, the wave amplitude b_n is altered by the excitations of all elements due to mutual coupling. In this context, Γ_n is called scan or active reflection coefficient [37, Sec. 7.2.2].

The far-field pattern of the array is given by a superposition of weighted element patterns

$$\vec{g}(\theta,\phi) = \frac{1}{\sqrt{P_{stim}}}\sum_{n=1}^{N} a_n\,\vec{g}_n(\theta,\phi), \tag{2.10a}$$

where $P_{stim} = \sum_n |a_n|^2$ is the stimulating power of the array. For equal element patterns $\vec{g}_0(\theta,\phi)$ this equation can be simplified to

$$\vec{g}(\theta,\phi) = A(\theta,\phi)\,\vec{g}_0(\theta,\phi) \tag{2.10b}$$

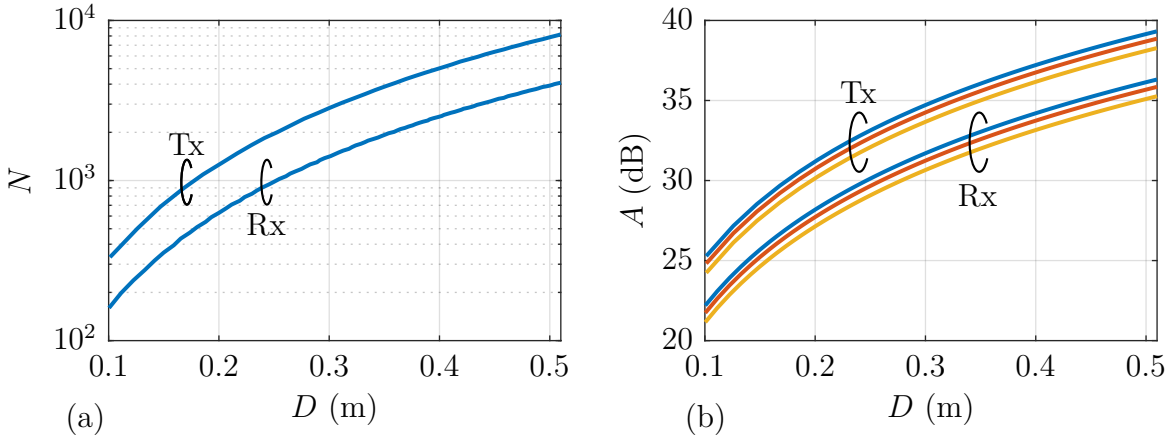

Figure 2.4: (a) Number of antenna elements and (b) maximum of the array factor of a circular aperture versus diameter D (— Uniform, — Taylor taper ($\bar{n} = 2$), — Taylor taper ($\bar{n} = 3$)).

with the array factor

$$A(\theta, \phi) = \frac{1}{\sqrt{P_{stim}}} \sum_{n=1}^{N} a_n \, \mathrm{e}^{\mathrm{j}\, k_0 \, \vec{r}_n \bullet \vec{u}_r(\theta,\phi)}, \tag{2.10c}$$

which depends on the wave amplitudes, the relative position of the elements, and the spherical angles (θ, ϕ). In a phased array antenna, the wave amplitudes a_n can be individually controlled in magnitude and phase. To steer the main array beam in the pointing direction (θ_0, ϕ_0), the phases of the wave amplitudes are tuned to

$$\arg(a_n) = -k_0 \, \vec{r}_n \bullet \vec{u}_r(\theta_0, \phi_0). \tag{2.11}$$

In this case, the fields of the individual elements interfere constructively in the pointing direction, as indicated in Fig. 2.3. The maximum directivity[1] is achieved for a uniform amplitude taper with equal wave amplitudes $|a_n| = a_0$. The side-lobe level (SLL) can be reduced for non-uniform amplitude tapers, where the excitations decrease to the edge of the array. However, this results in an increased beamwidth and a decreased array factor of the main beam.

In the following, a circular aperture with a diameter D is analyzed for the system design. The aperture is filled with antenna elements on the interleaved rectangular grid (see Sec. 2.2). The number of elements is depicted in Fig. 2.4a. For a diameter of $D = 0.1\,\mathrm{m}$ to $0.5\,\mathrm{m}$ several hundred to nearly ten thousand elements are necessary. Caused by the smaller element spacing due to the smaller wavelength of the Tx signal, more Tx than Rx elements are necessary for the same aperture size. Fig. 2.4b shows the array factor of the main beam for a uniform and two Taylor tapers [38]. The latter provides two independent parameters to control the side lobes. These parameters are related to the

[1] Higher directivity is theoretically achieved by the so-called superdirectivity. However, this requires a close element spacing below half a wavelength, rapid phase variation, and very high precision of the wave amplitudes [37]. For large arrays, this concept is thus of limited relevance.

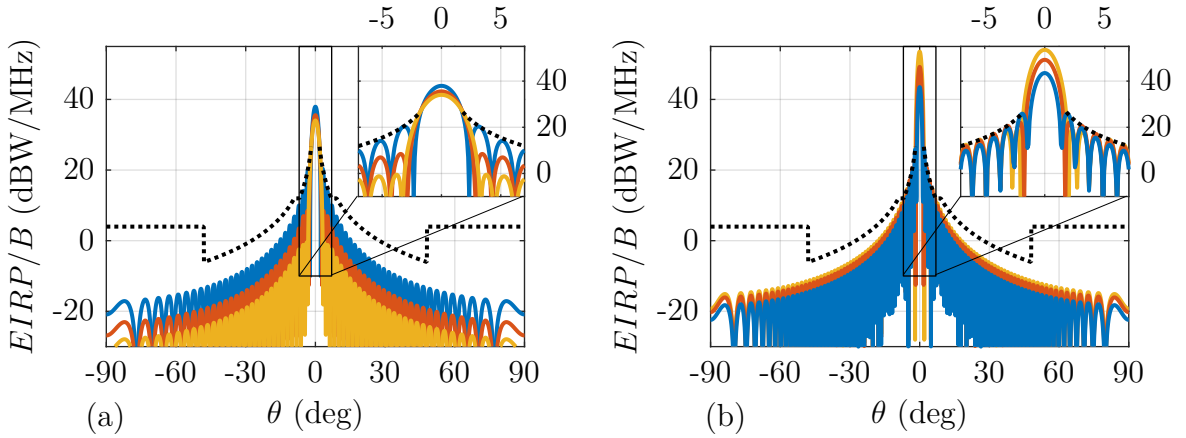

Figure 2.5: Maximum $EIRP/B$ in broadside direction of circular apertures with (a) $D = 0.3\,\mathrm{m}$ and (b) $D = 0.5\,\mathrm{m}$ versus θ (···· ETSI mask, — Uniform, — Taylor taper ($\bar{n} = 2$), — Taylor taper ($\bar{n} = 3$)).

number $\bar{n}$ of modified nulls and to the intended SLL. The SLL is reduced by using an amplitude distribution that shifts the nulls of the array factor close to the main beam. For the first Taylor taper, the closest nulls are modified ($\bar{n} = 2$) and an SLL of 26 dB is chosen. The second Taylor taper modifies the first two nulls ($\bar{n} = 3$) with a selected SLL of 34 dB. The decrease of the array factors for the Taylor tapers in comparison to the uniform taper is measured by the so-called taper efficiency η_T [37, p. 23]. For the selected tapers, η_T is 90 % ($\bar{n} = 2$) and 79 % ($\bar{n} = 3$). The resulting amplitudes $|a_n|$ are not constant over the aperture, but rather decrease towards its edges. The maximum (minimum) amplitude value is 4.8 dB (−4 dB) and 5.8 dB (−7.9 dB) above (below) the mean value for the Taylor tapers for $\bar{n} = 2$ and $\bar{n} = 3$, respectively.

For the Tx case, the EIRP per bandwidth B is limited in the K/Ka-band by the European Telecommunications Standards Institute (ETSI). The standard [39] ensures that the interference with neighboring GEO satellites is acceptable. Fig. 2.5 shows the ETSI mask of the maximum allowed $EIRP/B$. In bad weather conditions, additional atmospheric losses can be compensated and this limit may be exceeded by up to 20 dB. To determine the maximum allowed EIRP in the main beam, the far-field pattern of the array is scaled by a maximum factor such that it stays below the ETSI mask. The shape of the far-field pattern is approximated by the array factor. The radiation patterns of apertures with $D = 0.3\,\mathrm{m}$ with 2828 elements and $D = 0.5\,\mathrm{m}$ with 7860 elements are depicted for a beam steered in broadside direction. The reduced SLL with the Taylor tapers can be clearly seen in the insets. As a drawback, the beamwidth increases and, thus, the maximum EIRP decreases for the smaller aperture. For the larger aperture, the maximum EIRP is increased with the Taylor tapers, because the first side lobes are reduced. This is different for the uniform taper, where the first side lobes limits the EIRP.

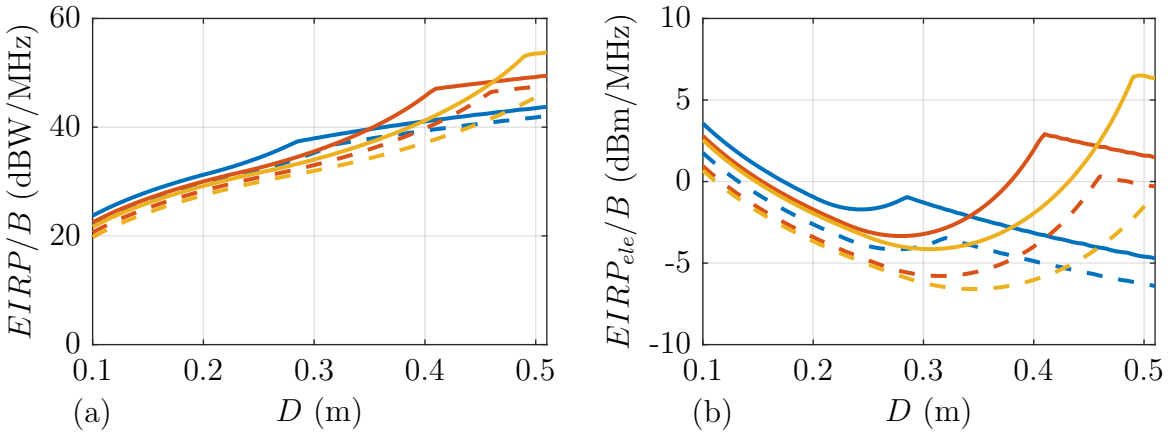

Figure 2.6: Maximum allowed $EIRP/B$ of (a) circular aperture and (b) respective elements versus diameter D for — $\theta_0 = 0°$ and - - - $\theta_0 = 30°$ (— Uniform, — Taylor taper ($\bar{n} = 2$), — Taylor taper ($\bar{n} = 3$)).

Fig. 2.6a shows the maximum allowed $EIRP/B$ versus aperture diameter for the three tapers. The $EIRP/B$ monotonously increases up to a diameter, where the slope significantly decreases. For diameters below and above this value, the $EIRP/B$ is limited by the main beam and the side lobes, respectively. If the beam points in broadside direction, the uniform taper allows for the highest $EIRP/B$ for small apertures with $D < 0.35\,\text{m}$. The second Taylor taper allows for the highest $EIRP/B$ for large aperture with $D > 0.45\,\text{m}$. For a beam steered to $\theta_0 > 0$, the beamwidth is increased and, thus, the maximum allowed $EIRP/B$ is decreased, as depicted for $\theta_0 = 30°$. Fig. 2.6b shows the mean $EIRP_{ele}/B$ per bandwidth and element, which varies from $-6.6\,\text{dBm/MHz}$ to $6.5\,\text{dBm/MHz}$ for the analyzed apertures. Knowing the element gain, this graph can be used to determine the maximum allowed output power per element. Note that for the Taylor tapers, the output power of the central elements must be considerably higher than the mean value.

The discussion of the maximum EIRP assumes ideal wave amplitudes and a precise knowledge of the necessary pointing direction. Small random variations in the wave amplitudes caused by quantization, calibration inaccuracies, or time variations mainly lead to an increased SLL and a broadened beamwidth. However, in a real system, they cannot be avoided and have to be considered in the system design. A quantitative discussion of the influence of such errors is found in [37, Cha. 7].

2.4 Rx/Tx Frontend

For the interleaved array grids, two different antenna elements are used. The Tx-only element has two ports, as depicted in Fig. 2.7a. Each port is fed by a Tx frontend that excites one polarization. The combined Rx/Tx element also has two ports and additionally supports dual-band operation. These ports are connected to diplexers which separate the Rx and Tx signals, as depicted in Fig. 2.7b. The diplexer has to provide isolation between

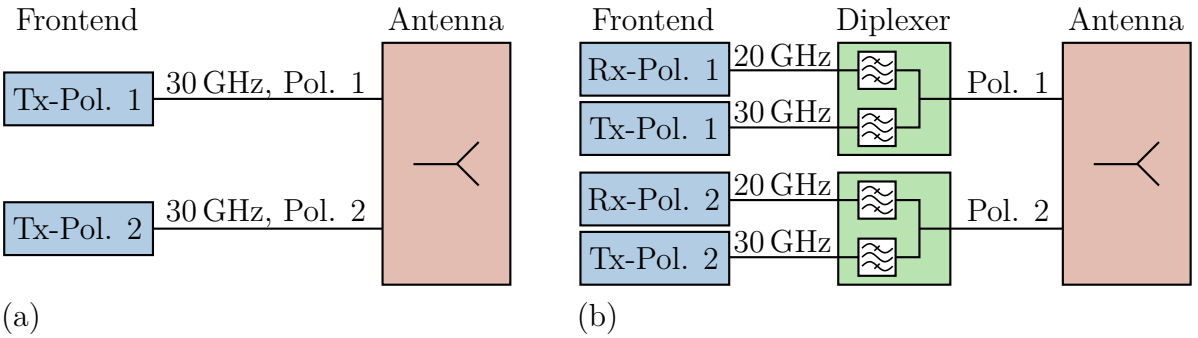

Figure 2.7: Schematic of (a) a Tx-only antenna element and (b) a combined Tx/Rx antenna element with dual polarization.

the Tx and Rx channels to prevent the relatively strong transmitter signal from saturating the receiver, while the Rx insertion loss must be minimized [40–44].

Fig. 2.8a and Fig. 2.8b show schematics of the Rx and Tx frontend with several channels. In the Rx frontend, the very low power received signal is at first amplified by a low-noise amplifier (LNA). This arrangement ensures a low receiver noise figure F_r, which is mainly dominated by the LNA, assuming its gain is sufficiently high. The output power P_{ele} of the Tx frontend is limited by the power amplifier (PA). The wave amplitudes of the antenna elements are adjusted by a beamforming network. Here, each channel can be controlled by a phase shifter and an amplitude tuner. The combining network sums-up the channels to a single output or splits a single input to the channels for the Rx or Tx frontend, respectively. The available core-chip solutions combine several beamforming channels in a small SMD package. An antenna with analog beamforming networks is known as (analog) phased array antenna. Alternatively, digital beamforming is possible, where the phase shifters, amplitude tuners, and combining networks are realized in the digital domain [45]. This concept requires a digital-to-analog or analog-to-digital converter for each channel and immense computational resources, which results in expensive systems with a huge power consumption [37]. However, digital beamforming systems are very flexible and provide advanced signal processing features like multibeam capabilities or advanced calibration algorithms [46].

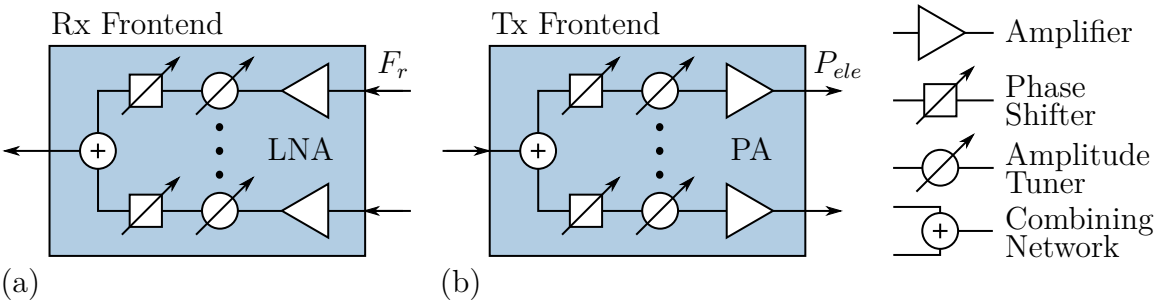

Figure 2.8: Schematic of (a) the Rx and (b) the Tx frontend with a beamforming network.

2.5 Rx/Tx Terminal

In this section, the G/T and EIRP of exemplary terminal antennas are determined for Rx and Tx, respectively. For this analysis, it is assumed that all components are non-reflective. At first, the Rx case is analyzed and for this the gain G and the equivalent system noise temperature T_e are determined. As reference plane, the input of the receiver in front of the LNA is chosen. If mutual coupling is neglected, the gain G can be directly calculated from the array factor, the element directivity, and the antenna loss $L_{ant} = 1/\eta_{rad}$ of the terminal (see Sec. 2.3). The system noise temperature T_e does not only depend on the terminal antenna itself, but also involves the environment and the terminal alignment. All major sources of thermal noise have to be considered. The sky, the atmosphere, and the Earth's surface emit thermal noise that is received by the antenna. The lossy antenna itself and the receiver generate additional noise. An equivalent circuit with these sources is depicted in Fig. 2.9a. The equivalent system noise temperature

$$T_e = T_{e,r} + T_{e,ant} \tag{2.12a}$$

combines all sources to a single value at the input of the now noiseless receiver, as depicted in Fig. 2.9b. Here, $T_{e,r} = T_0\,(F_r - 1)$ is the equivalent input receiver noise temperature, F_r the receiver noise figure, and T_0 the reference temperature. The equivalent antenna noise temperature

$$T_{e,ant} = \frac{T_{ant}\,(L_{ant} - 1) + T_{e,atm} + T_{e,surf}}{L_{ant}} \tag{2.12b}$$

is composed of the noise generated by the lossy antenna with a physical temperature T_{ant} and the noise received by the antenna. The latter is determined from a simple model, where the radiation pattern is split into an atmospheric and a surface part with a constant noise temperature. A fraction α_{atm} and $1 - \alpha_{atm}$ of the radiation pattern receives noise from the atmosphere and the Earth's surface, respectively. The equivalent atmospheric noise temperature

$$T_{e,atm} = \alpha_{atm}\,\frac{T_{e,sky} + T_{atm}\,(L_{atm} - 1)}{L_{atm}} \tag{2.12c}$$

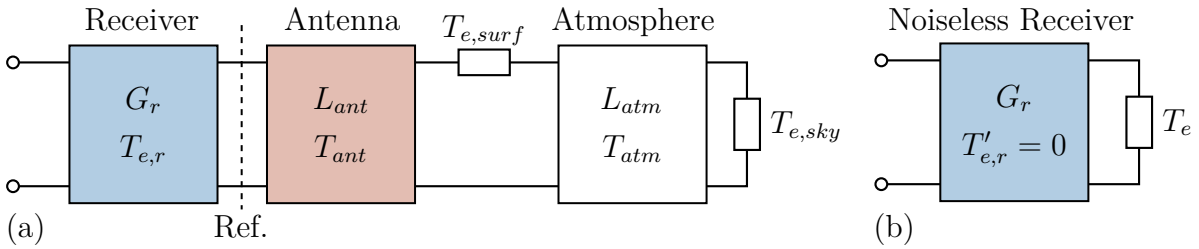

Figure 2.9: (a) Equivalent circuit of terminal antenna receiver system and (b) a simplified equivalent circuit with a noiseless receiver.

Table 2.3: Noise temperatures and related values of a reference environment and receiver.

T_0	$T_{e,sky}$	T_{atm}	T_{surf}	T_{ant}	α_{atm}	F_r	$T_{e,surf}$	$T_{e,r}$
290 K	2.7 K	275 K	290 K	320 K	0.9	1.5 dB	29 K	120 K

represents the noise of the sky with an equivalent noise temperature $T_{e,sky}$ and additional noise of the lossy atmosphere with a physical temperature of T_{atm}. The noise of the Earth's surface with a physical temperature of T_{surf} is represented by the equivalent noise temperature

$$T_{e,surf} = (1 - \alpha_{atm})\, T_{surf}. \tag{2.12d}$$

In a rigorous calculation, the noise temperature varies as a function of the solid angle and the equivalent noise temperature must be calculated by an overlap integral of the noise temperature and the radiation pattern [47]. However, the given simple model is a reasonable approximation and shows the general characteristics. A similar model for T_e is given in [48].

Tab. 2.3 lists the noise temperatures of a selected reference environment, where it is assumed that $\alpha_{atm} = 90\,\%$ of the radiation pattern receives noise from the atmosphere. This is of course only a rough estimation. With the given values, $T_{e,ant}$ can be analyzed versus L_{atm} and L_{ant}, as depicted in Fig. 2.10a. For a lossless antenna and atmosphere, the noise temperature $T_{e,ant} = 31\,\mathrm{K}$ is very low and mainly generated by the Earth surface. However, it rapidly increases with L_{atm} and L_{ant}. For a reference antenna with $L_{ant} = 3\,\mathrm{dB}$, the equivalent antenna noise temperature is $T_{e,ant} = 201\,\mathrm{K}$ for clear sky with $L_{atm} = 1\,\mathrm{dB}$, and $T_{e,ant} = 279\,\mathrm{K}$ for the same antenna at heavy rain (10 mm/h, Hamburg, Germany) with $L_{atm} = 8\,\mathrm{dB}$ [30]. For the receiver, a noise figure of $F_r = 1.5\,\mathrm{dB}$ is assumed, which corresponds to $T_{e,r} = 120\,\mathrm{K}$. The low noise figure can be achieved with state-of-the-art LNAs that are available as SMD components[2].

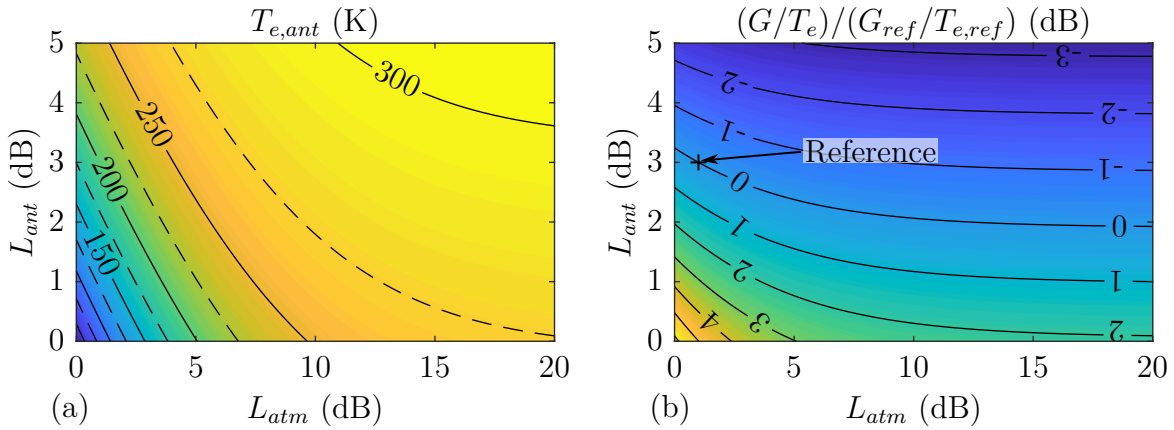

Figure 2.10: (a) Equivalent antenna noise temperature and (b) G/T variation with respect to a reference scenario ($L_{atm} = 1\,\mathrm{dB}$, $L_{ant} = 3\,\mathrm{dB}$) versus atmospheric and antenna loss.

[2] See, for example, the LNA *QPA2626* from *Qorvo*.

Table 2.4: G/T and Rx data rate for two terminals in different weather scenarios.

Description	**Terminal 1 (D =0.3 m)**		**Terminal 2 (D =0.5 m)**	
	Clear Sky	**Heavy Rain**	**Clear Sky**	**Heavy Rain**
Atmospheric Loss (dB)	1.0	8.0	1.0	8.0
System Margin (dB)	3.0	3.0	3.0	3.0
Element Loss (dB)	3.0	3.0	3.0	3.0
Element Directivity (dBi)	5.0	5.0	5.0	5.0
Frequency (GHz)	20.0	20.0	20.0	20.0
Bandwidth (MHz)	10.0	10.0	10.0	10.0
Antenna Noise Temp. (K)[1]	200.6	278.7	200.6	278.7
Receiver Noise Temp. (K)[2]	119.6	119.6	119.6	119.6
System Noise Temp. (K)	320.3	398.4	320.3	398.4
Diameter (m)	0.3	0.3	0.5	0.5
Element Distance (mm)	7.1	7.1	7.1	7.1
Number of Elements[3]	1396	1396	3908	3908
Array Taper	Uniform	Uniform	Uniform	Uniform
Array Factor (dB)[4]	31.7	31.7	36.1	36.1
Terminal Directivity (dBi)	36.7	36.7	41.1	41.1
Terminal Gain (dBi)	33.7	33.7	38.1	38.1
G/T (dBi/K)	8.6	7.7	13.1	12.1
C/N (dB)[5]	8.2	0.2	12.6	4.7
MODCOD	8PSK 3/4	QPSK 1/2	16APSK 8/9	8PSK 3/5
Roll-Off Factor	0.2	0.2	0.2	0.2
Data Rate (MBit/s)[6]	18.6	8.2	29.4	14.8

[1] See Fig. 2.10a. [2] See Tab. 2.3. [3] See Fig. 2.4a.
[4] See Fig. 2.4b. [5] See Tab. 2.1. [6] See Fig. 2.1a.

The variation of G/T is depicted in Fig. 2.10b. Here, the clear sky scenario and the antenna with $L_{ant} = 3\,\text{dB}$ are used as reference. The G/T is decreased when L_{ant} and L_{atm} are increased. The degradation due to the atmospheric loss is limited because the maximum equivalent noise temperature of the atmosphere is its physical temperature. G/T can be significantly improved if L_{ant} is reduced. Low losses are normally achieved by feeds of classical reflector antennas. However, for active array antennas based on PCB technology, low losses are a huge challenge. An interesting fact is that very low-loss antennas are more sensitive to atmospheric losses, which can be seen by inspecting the contour line density in Fig. 2.10b.

Tab. 2.4 shows a calculation of G/T for two terminal antennas with a diameter of 0.3 m and 0.5 m for clear sky and heavy rain. For the array elements, an antenna loss of $L_{ant} = 3\,\text{dB}$ and a maximum directivity of $D_{ele} = 5\,\text{dBi}$ are assumed to be realistic values. The elements are arranged in an interleaved rectangular grid and the beamforming network applies a uniform array taper. This yields a gain of $G = 33.7\,\text{dBi}$ and 38.1 dBi for

Table 2.5: EIRP and Tx data rate for two terminals in different weather scenarios.

Description	**Terminal 1 (D =0.3 m)**		**Terminal 2 (D =0.5 m)**	
	Clear Sky	**Heavy Rain**	**Clear Sky**	**Heavy Rain**
Atmospheric Loss (dB)	1.0	16.0	1.0	16.0
System Margin (dB)	3.0	3.0	3.0	3.0
Frequency (GHz)	30.0	30.0	30.0	30.0
Bandwidth (MHz)	10.0	1.0	10.0	10.0
Element Loss (dB)	3.0	3.0	3.0	3.0
Element Directivity (dBi)	5.0	5.0	5.0	5.0
Element Power (dBm)[1]	6.7	10.0	3.4	10.0
Diameter (m)	0.3	0.3	0.5	0.5
Element Distance (mm)	5.0	5.0	5.0	5.0
Number of Elements[2]	2828	2828	7860	7860
Array Taper	Uniform	Uniform	Uniform	Uniform
Array Factor (dB)[3]	34.7	34.7	39.2	39.2
Terminal Directivity (dBi)	39.7	39.7	44.2	44.2
Terminal Gain (dBi)	36.7	36.7	41.2	41.2
EIRP (dBW)	47.9	51.2	53.5	60.1
$EIRP/B/\Delta L_{atm}$ (dBW/MHz)	37.9	36.2	43.5	35.1
$EIRP/B$ Limit (dBW/MHz)[4]	37.9	37.9	43.5	43.5
C/N (dB)[5]	1.0	−0.8	6.5	−1.9
MODCOD	QPSK 1/2	QPSK 2/5	8PSK 2/3	QPSK 1/3
Roll-Off Factor	0.2	0.2	0.2	0.2
Data Rate (MBit/s)[6]	8.2	0.7	16.5	5.5

[1] See Fig. 2.6b with $\theta_0 = 0°$. [2] See Fig. 2.4a. [3] See Fig. 2.4b.
[4] See Fig. 2.6a with $\theta_0 = 0°$. [5] See Tab. 2.1. [6] See Fig. 2.1b.

the two terminals. With the mentioned assumptions the system noise temperature only depends on the weather scenario. The possible data rate can be determined with the link budget from Tab. 2.1 and Fig. 2.1a. Here, a system margin of 3 dB is assumed. For the clear sky scenario and a bandwidth of 10 MHz, this results in a data rate of 18.6 MBit/s and 29.4 MBit/s for the two terminals, respectively. For heavy rain, the data rate drops considerably and only 8.2 MBit/s and 14.8 MBit/s can be achieved.

For the analysis of the Tx case, the EIRP of the terminals is determined in Tab. 2.5. Here, the same clear sky and heavy rain scenarios are considered, which at 30 GHz gives an attenuation of about $L_{atm} = 1\,\text{dB}$ and $L_{atm} = 16\,\text{dB}$ [30], respectively. The gain is calculated in the same manner as in the Rx case. With an element directivity of $D_{ele} = 5\,\text{dBi}$ and an element loss of $L_{ant} = 3\,\text{dB}$, the gain is $G = 36.7\,\text{dBi}$ and 41.2 dBi for the two terminals. The $EIRP/B$ is limited to 37.9 dBW/MHz and 43.5 dBW/MHz for these terminals, assuming broadside radiation and a uniform amplitude taper (see. Fig. 2.6a). This gives a maximum element $EIRP_{ele}/B/\Delta L_{atm}$ of −1.3 dBm/MHz and −4.6 dBm/MHz

(see. Fig. 2.6b), respectively. The factor $\Delta L_{atm} = L_{atm}/L_{atm,0}$ accounts for the increased EIRP limit, when atmospheric losses L_{atm} are increased in comparison to the losses $L_{atm,0}$ for clear sky. For a bandwidth of 10 MHz and clear sky, this results in EIRPs of 47.9 dBW and 53.5 dBW. With a system margin of 3 dB, this corresponds to data rates of 8.2 MBit/s and 16.5 MBit/s, respectively. In the heavy rain scenario, the element power could be increased by the additional atmospheric loss $\Delta L_{atm} = 15\,\text{dB}$. However, the available element power of real frontends is limited. For example, the mentioned core-chips have normally a maximum output power of about $P_{ele} = 10\,\text{dBm}$, which in the following is used as the maximum available power. To obtain an acceptable C/N, the bandwidth is reduced to 1 MHz for the smaller terminal. Thus, for heavy rain, only data rates of 0.7 MBit/s and 5.5 MBit/s can be achieved. The degradation due to rain is thus more crucial for Tx than for Rx.

In the discussed scenarios, where the terminal surface is completely filled with interleaved Rx and Tx elements, the Rx data rate is higher than the Tx data rate. In some cases, this is intended. In other cases, however, the bandwidth and element power can be adapted. Even terminals that are only partially filled with Rx or Tx elements are possible.

In the following, the surface area A of the Rx/Tx integrated array antenna is compared with that of two separate array antennas for Rx and Tx, as depicted in Fig. 2.11a. The latter do not need diplexers and shorter transmission lines can be used, which reduces the antenna loss. This, in turn, allows for smaller separate arrays with the same performance. This total surface area can then be compared with that of the integrated antenna. In this analysis, the unprimed quantities of the integrated array are proportional to the primed ones of the separate arrays. The surface areas scale as

$$A'_{Rx} = \Delta A_{Rx}\, A \qquad \text{and} \qquad A'_{Tx} = \Delta A_{Tx}\, A. \tag{2.13a}$$

In the same manner, the losses and gains are related by

$$L'_{ant,Rx} = \Delta L_{ant,Rx}\, L_{ant,Rx} \qquad \text{and} \qquad L'_{ant,Tx} = \Delta L_{ant,Tx}\, L_{ant,Tx}, \tag{2.13b}$$

and

$$G'_{Rx} = \Delta G_{Rx}\, G_{Rx} \qquad \text{and} \qquad G'_{Tx} = \Delta G_{Tx}\, G_{Tx}. \tag{2.13c}$$

The gain of an array is proportional to the aperture area and inversely proportional to the antenna losses. Thus, the gain factors are given by

$$\Delta G_{Rx} = \frac{\Delta A_{Rx}}{\Delta L_{ant,Rx}} \qquad \text{and} \qquad \Delta G_{Tx} = \frac{\Delta A_{Tx}}{\Delta L_{ant,Tx}}. \tag{2.14}$$

For the Rx case, the G/T is set to be equal for the Rx-only and the integrated array. The system noise temperatures T_e and $T'_e = \Delta T_e\, T_e$ of the respective arrays depend on the antenna losses according to (2.12). As a result, the variation in the G/T is given by

$$\Delta G/T = \frac{\Delta G_{Rx}}{\Delta T_e} = \frac{\Delta A_{Rx}}{\Delta L_{ant,Rx}\, \Delta T_e} \tag{2.15a}$$

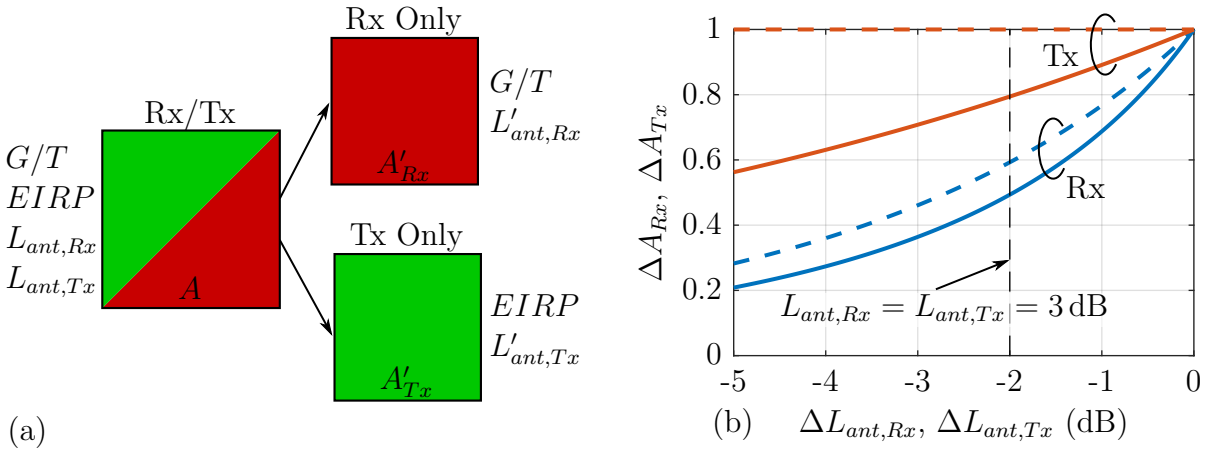

Figure 2.11: (a) Schematic diagram of integrated and separate array antennas. (b) Area factors of separate array antennas versus $\Delta L_{ant,Rx}$ or $\Delta L_{ant,Tx}$ (— ΔA_{Rx} for $L_{atm} = 1\,\mathrm{dB}$, - - - ΔA_{Rx} for $L_{atm} = 8\,\mathrm{dB}$, — ΔA_{Tx} for $\Delta P_{ele} = 1$, - - - ΔA_{Tx} for $\Delta P_{ele} = \Delta L_{ant,Tx}$).

and for an area factor of

$$\Delta A_{Rx} = \Delta L_{ant,Rx}\,\Delta T_e, \tag{2.15b}$$

the G/T is unchanged and the same performance is achieved for both arrays.

For the Tx case, the EIRP should be the same for the Tx-only and the integrated array. The total stimulating powers P and $P' = \Delta P\,P$ of both arrays are proportional to the mean element powers P_{ele} and $P'_{ele} = \Delta P_{ele}\,P_{ele}$, respectively. In addition, the stimulating powers are proportional to the element numbers and, thus, to the aperture areas. Therefore, the variation of the stimulating power is given by

$$\Delta P = \Delta A_{Tx}\,\Delta P_{ele}. \tag{2.16}$$

As a result, the variation of the EIRP is given by

$$\Delta EIRP = \Delta P\,\Delta G_{Tx} = \Delta A_{Tx}^2\,\frac{\Delta P_{ele}}{\Delta L_{ant,Tx}} \tag{2.17a}$$

and for an area factor of

$$\Delta A_{Tx} = \sqrt{\frac{\Delta L_{ant,Tx}}{\Delta P_{ele}}}, \tag{2.17b}$$

the EIRP of both arrays is equal. The element power P_{ele} is limited either by the maximum available frontend power or by EIRP regulations (see. Sec. 2.3).

Fig. 2.11b shows the area factors versus the scaling factors of the antenna loss. It is assumed that the Rx- and Tx-only arrays have a loss of $L'_{ant,Rx} = L'_{ant,Tx} = 1\,\mathrm{dB}$. For the calculation of the Rx case, the system noise temperatures are determined with the values of Tab. 2.3 and an atmospheric loss of $L_{atm} = 1\,\mathrm{dB}$ and $8\,\mathrm{dB}$. For the example from Tab. 2.4, the antenna loss of $L_{ant,Rx} = 3\,\mathrm{dB}$ means a reduction of $\Delta L_{ant,Rx} = -2\,\mathrm{dB}$ in comparison to the Rx-only array. For the two weather scenarios, this results in a surface area reduction of $\Delta A_{Rx} = 0.49$ and 0.59 for the Rx-only array. The reduction is smaller

for the lossier atmosphere because the system noise temperature is already high due to the atmospheric noise. For the Tx case, no surface area reduction $\Delta A_{Tx} = 1$ is feasible, if the EIRP is limited by the ETSI mask. Here, the element power of the Tx-only array has to be reduced by $\Delta P_{ele} = \Delta L_{ant,Tx}$. If the EIRP is limited by the available element power and not by the ETSI mask, then $\Delta P_{ele} = 1$ and a surface area reduction is possible, as depicted in Fig. 2.11b. For the example of Tab. 2.5, the antenna loss of $L_{ant,Tx} = 3\,\text{dB}$ means $\Delta L_{ant,Tx} = -2\,\text{dB}$, which results in a possible reduction of $\Delta A_{Tx} = 0.79$ for the Tx-only array. For the heavy rain scenarios, a size reduction can be achieved because the EIRP is not limited by the ETSI mask. However, for clear sky, the EIRP is limited by the ETSI mask and, thus, no surface area reduction is possible. The Rx antenna losses are thus more crucial than the Tx losses, as visible in the graphs of Fig. 2.11b.

The factor $\Delta A = \Delta A_{Rx} + \Delta A_{Tx}$ is a quantitative measure to compare the total surface area of the integrated array with that of the separate arrays. Fig. 2.12 shows this factor versus $\Delta L_{ant,Rx}$ and $\Delta L_{ant,Tx}$ for the two weather scenarios. Here, it is assumed that the EIRP is not limited by the ETSI mask. If no additional losses occur in the integrated array, the total surface area is increased by the factor $\Delta A = 2$. For higher losses, the total surface area of the separate arrays decreases. $\Delta A = 1$ is a limit, where the total surface area is the same as that of the integrated antenna and no surface area reduction is achieved by the integrated antenna. For the example from Tab. 2.4 and Tab. 2.5, the surface area of the separate arrays is increased by $\Delta A = 1.29$ and 1.39 for the two weather scenarios.

In conclusion, the antenna losses are crucial for the possible surface area reduction. For clear sky and an integrated antenna with $L_{ant,Rx} = L_{ant,Tx} = 3\,\text{dB}$, the surface area of the separate arrays must be increased by about 50 % or 30 %, when the EIRP is limited or is not limited by the ETSI mask, respectively.

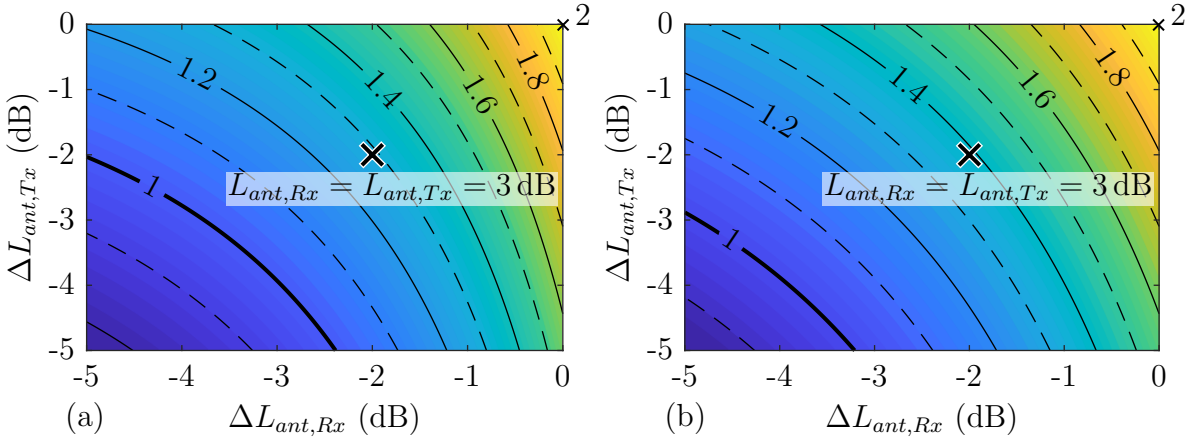

Figure 2.12: Contour plot of the total surface area factor ΔA versus $\Delta L_{ant,Rx}$ and $\Delta L_{ant,Tx}$ for (a) $L_{atm} = 1\,\text{dB}$ and (b) $L_{atm} = 8\,\text{dB}$.

2.6 Antenna Architecture

The architecture of an array antenna is a fundamental design choice. It substantially influences the possible antenna element types, the available real estate for components, the beamforming network, and the thermal management. Furthermore, this choice dictates how the elements are grouped and fed. Generally one distinguishes between the brick and the tile architecture [49, 50], as depicted in Fig. 2.13a and Fig. 2.13c, respectively.

The brick architecture inherits its name from a building brick. The circuitry is aligned perpendicularly to the aperture plane. Often, the circuitry is implemented using PCB technology, where the components are directly implemented in or soldered on the PCBs. The array elements are commonly grouped in rows and share a common PCB, as depicted in Fig. 2.13b. These groups are so-called (sub-)modules and in the limiting case, a module can contain only a single element. The tile architecture arrangement is similar to that of bathroom tiles. Here, the circuitry is aligned in parallel to the aperture plane and the elements are commonly grouped in square modules, as illustrated in Fig. 2.13d. The available real estate for components is limited by the element distance and, thus, depends on the operation frequency. Further real estate can only be gained by using multiple layers that are vertically interconnected. Especially, board-to-board interconnects can be quite challenging when size, losses, reliability, and costs are considered. However, antennas with

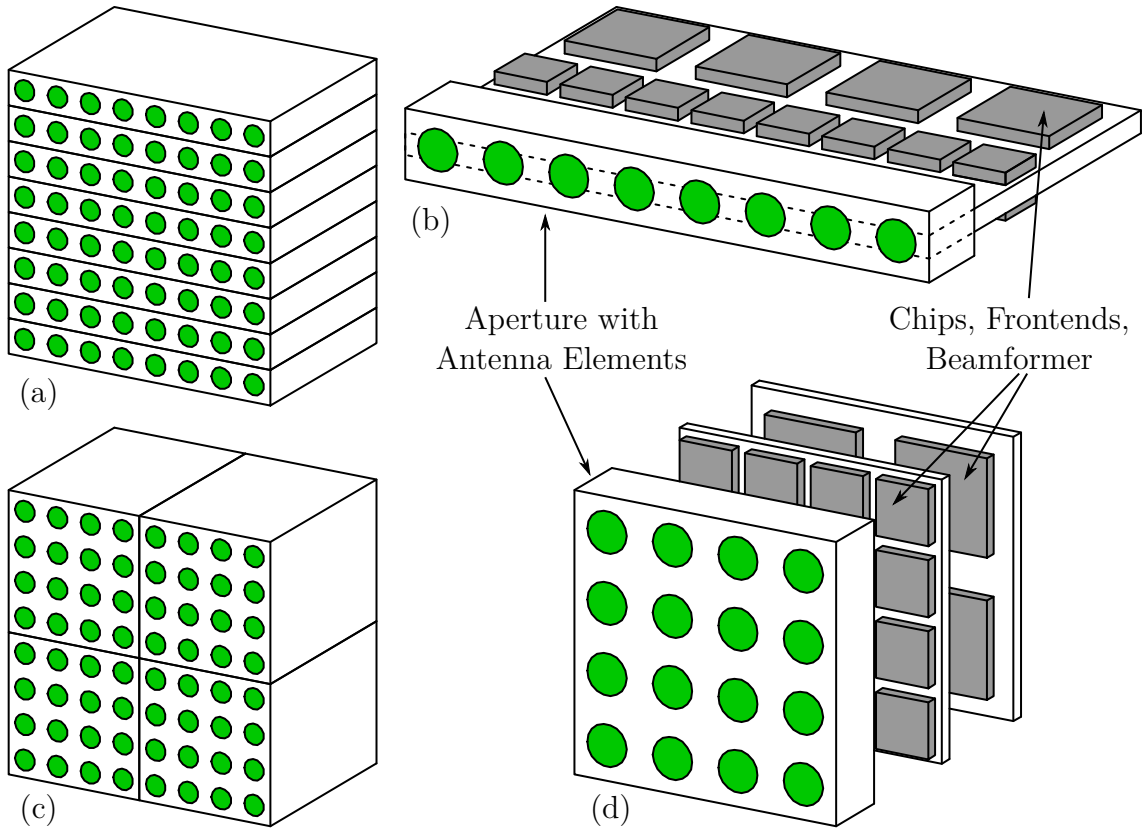

Figure 2.13: (a) Brick and (c) tile array architecture. (b) Brick and (d) tile module with frontends and beamformer.

this architecture are often very flat. In the brick architecture, the available real estate can be adjusted by changing the length of the modules without the need for complex interconnects. This allows for the design of antennas with very high functionality using many components.

To distribute a single input signal to the array elements, different feed architectures are available. One differentiates between space-fed antennas and antennas with constrained feeds. The space-fed antennas utilize the free space to distribute the signal to the elements. Transmit arrays are illuminated by a single antenna on the back side of the aperture. Each element receives the signal, adjusts its amplitude and phase, and re-emits the signals at the front side of the aperture. These antennas are also called space-fed active lens antennas. An other space-fed architecture is the reflect array, where the front side of the aperture is illuminated by a single antenna. Each element receives the signal, adjusts its amplitude and phase, and re-emits the signals on the same side. Typically, two orthogonal polarizations are used for receiving and re-emission. The operation principles of the space-fed antennas in the Rx case is dual to the discussed Tx case. Implementations of the transmit and reflect array for K/Ka-band satellite communications are reported in [14] and [51], respectively. Antennas with constrained feeds distribute the signals using networks with power dividers and transmission lines. The power dividers are cascaded in a tree-like structure and distribute the signal from a single input to each element. They can be implemented in PCB technology using, for example, Wilkinson dividers [52]. This architecture suffers from the losses of the PCB technology. However, in active arrays, losses can be compensated by amplifiers. In general, antennas with constrained feeds are flatter than space-fed antennas. For this reason, planar constrained distribution networks are often used. In a different architecture, the array antenna itself is used as a feed for a reflector. In a multi-beam antenna, the array is placed in the focal plane of the reflector. Here, each array element generates a unique pencil beam and beam steering is achieved by selecting an element. An implementation of this architecture can be found in [53, 54].

The array architecture is closely related to the type of antenna element. For the tile architecture, planar elements like microstrip patch antennas [13, 55–58] are common. The brick architecture often utilizes dipole [59–61] or Vivaldi antennas [62, 63]. In the last century [64], a variety of antenna elements and arrays have been developed for all kinds of applications. The major challenge in this thesis is to develop an antenna element with two polarizations and a dual-band characteristic for the interleaved Rx/Tx array grid. For the tile architecture, planar antennas featuring either dual polarization or dual-band operation are presented in [13] and [56]. Simulation results of a combined solution that is based on two nested annular slot elements, one into the other, is presented in [65]. Another combined solution is shown in [57] and [58]. It is based on stacked microstrip patches fed by two crossed aperture coupled feed lines. However, these solutions are

rather narrowband. An alternative are wideband array antennas that can handle multiple bands in a single aperture. For the tile architecture, tightly coupled dipole antennas show an ultra-wideband characteristic [59, 60]. A drawback of this antenna concept is that the element spacing is less than half a wavelength of the maximum operation frequency. Thus, more elements per area are required, which increases the overall element number and the integration density. Anyhow, the Rx/Tx integrated dual-polarized array requires a very high number of components. In the tile architecture, even with state-of-the-art frontend components, this represents a tremendous packaging challenge.

This challenge can be overcome in brick architecture. [63] and [66] show implementations of tightly coupled dipole and Vivaldi antennas in this architecture. However, they utilize crossed PCBs to realize dual polarization, which results in mechanically complicated setups. Classical solutions are often based on waveguide technology [67–69]. These antennas have many advantages, such as large bandwidth, dual-polarization capability, low losses, and good element isolation. However, waveguide technology is in general bulky and expensive.

The SIW technology combines the waveguide technology with planar fabrication techniques and, thus, reduces the manufacturing costs while maintaining most of the advantages of waveguides. An end-fire solution that is based on square SIWs is presented in [24] and [26]. Here, the square SIW is excited by planar transmission lines and the waveguide is matched by means of a choke. This choke is a concentric square coaxial waveguide that can be represented by a stub line. This matching concept is relatively narrowband and does not support the dual-band characteristic. In this thesis, the SIW is terminated by a dielectric lens to achieve a wideband matching [70–72]. Lenses have been shown to be a powerful means of input matching as well as of shaping an antenna's radiation pattern [73–76]. A related single radiator intended for another application is presented in [77]. Here, an SIW H-plane horn antenna with an arc lens in the same substrate is presented. However, it only supports a single polarization, is rather narrowband, and it is too large for the array grid.

2.7 Lens Antenna Concept

Fig. 2.14 shows the basic concept of the proposed SIW lens antenna element. The square waveguide, depicted in Fig. 2.14a, supports two fundamental degenerated modes with the same phase constant. A superposition of these modes can generate any polarization, in particular, right-handed (RHCP) and left-handed circular polarization (LHCP), as commonly used in mobile satellite communications. The square SIW consists of a standard PCB sandwiched between two superstrates and a surrounding copper layer. The dielectric properties of the sub- and superstrate are assumed to be the same and, thus, the square SIW is a homogeneous, dielectric-filled waveguide. This waveguide is matched by a dielectric lens, as illustrated in Fig. 2.14b. The circularly-polarized modes can be excited using a septum polarizer [78–80], which transforms two linearly-polarized modes in two stacked waveguides to either RHCP or LHCP. The stacked waveguides thus require full-height, which is defined as a 2 : 1 ratio of waveguide width to height. These waveguides themselves are excited by transitions from planar transmission lines, which are located on the top and bottom layer of the standard PCB. These planar transmission lines allow for simple integration of the diplexer, frontend components, and further circuitry. The reduced height of the standard PCB is a further advantage of this concept in comparison with a thick multilayer [24, 26]. It allows for thicker SMD components and provides more space for thermal management. Multiple SIW antenna elements can be placed next to each other on the PCB to form one brick module. Several of these brick modules are then stacked to a square module. The aperture of a larger array is then composed of such square modules. The size and, thus, the performance of the antenna can simply be adjusted by the number of modules. The passive components for this antenna concept are developed and combined in the course of this thesis.

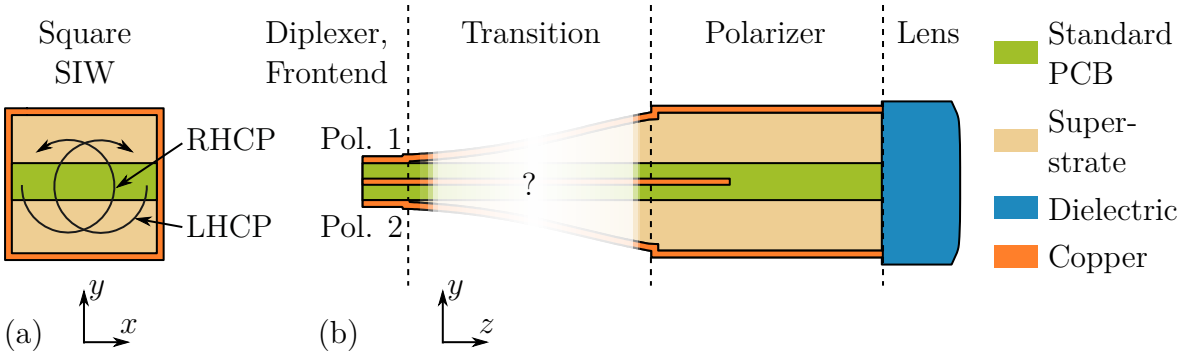

Figure 2.14: Schematic of the lens antenna concept. (a) Cross and (b) longitudinal section.

Theory for Substrate Integrated Waveguide Components

3

This chapter is intended to provide the necessary theory for modeling SIW components. The components are described as generalized equivalent circuits consisting of transmission lines and discontinuities. The first section reviews the theory of guided waves and introduces the used symbols and notations. A cylindrical waveguide is studied and the modes of parallel-plate waveguides and periodic structures are determined. Next, the effect of rough conductor surfaces is studied and their impact on cylindrical waveguide structures is analyzed. The modes are used to model a via row of the SIW and calculate the parameters of an equivalent rectangular waveguide. The resulting model describes an SIW with rough conductor surfaces. Then, the class of waveguide structures is extended to the MSIW. The modal characteristics are determined by the TRM from an equivalent circuit of the cross-section. For this circuit, a parallel-plate furcation is analyzed with the mode matching method. Finally, a generic MSIW discontinuity is analyzed, which is a major building block for the component model.

3.1 Guided-Wave Theory

This section is devoted to the wave propagation in guided-wave structures. A homogeneous medium without sources and a harmonic time dependence of $\exp(\mathrm{j}\omega t)$ is assumed. In this case Maxwell's equations are given in the differential form by

$$\nabla \times \vec{E} = -\mathrm{j}\omega\mu\vec{H}, \tag{3.1a}$$

$$\nabla \times \vec{H} = \mathrm{j}\omega\epsilon\vec{E}, \tag{3.1b}$$

$$\nabla \bullet \vec{E} = 0, \tag{3.1c}$$

and

$$\nabla \bullet \vec{H} = 0. \tag{3.1d}$$

They are a system of coupled partial differential equations and relate the electric field $\vec{E}$ and the magnetic field $\vec{H}$ to each other. The material properties are described by the permeability $\mu = \mu_0\,\mu_r$ and the permittivity ϵ. The relative permeability is $\mu_r = 1$ for non-magnetic materials. Dielectric materials are usually characterized by the relative

permittivity ϵ_r (dielectric constant) and the loss tangent $\tan(\delta_d)$. Here, losses due to a finite conductivity σ are included in the permittivity $\epsilon = \epsilon_0\epsilon_r(1 - \mathrm{j}\tan(\delta_d)) = \epsilon_d - \mathrm{j}\frac{\sigma}{\omega}$, where ϵ_d is the complex dielectric permittivity. In general, the material parameters depend on the field orientation. However, if not explicitly stated otherwise, isotropic properties are assumed. The fields $\vec{E}$ and $\vec{H}$ are divergence-free and can thus be expressed by

$$\vec{E}_F = -\nabla \times \vec{F} \qquad \text{and} \qquad \vec{H}_A = \nabla \times \vec{A} \tag{3.2}$$

using the curl of the electric vector potential $\vec{F}$ and the magnetic vector potential $\vec{A}$, respectively. With Maxwell's equations and the Lorenz gauge these equations can be transformed [81, Sec. 3-12] to the Helmholtz equations

$$\nabla^2\vec{A} + k_0^2\vec{A} = 0 \qquad \text{and} \qquad \nabla^2\vec{F} + k_0^2\vec{F} = 0, \tag{3.3}$$

where $k_0 = \omega\sqrt{\mu\,\epsilon}$ is the wave number in the medium. The associated fields are calculated from the vector potentials by

$$\vec{E} = \vec{E}_F + \vec{E}_A = -\nabla \times \vec{F} - \mathrm{j}\frac{Z_0}{k_0}\nabla \times \nabla \times \vec{A} \tag{3.4a}$$

and

$$\vec{H} = \vec{H}_A + \vec{H}_F = \nabla \times \vec{A} - \mathrm{j}\frac{Y_0}{k_0}\nabla \times \nabla \times \vec{F}. \tag{3.4b}$$

The wave impedance $Z_0 = \sqrt{\mu/\epsilon}$ and wave admittance $Y_0 = 1/Z_0$ are given by the material parameters of the medium. Solutions of the Helmholtz equation for several coordinate systems are reported in [82, Cha. 6].

In addition to the Helmholtz equation, boundary conditions must be satisfied to determine a solution for guided-wave structures. In general, this is very involved and calls for numerical methods. However, the structures can often be split into smaller components, where simpler boundary conditions result in a set of modes. For boundaries with a perfect electric conductor (PEC) or perfect magnetic conductor (PMC) the tangential electric or magnetic field components must vanish as given by

$$\vec{E} \times \vec{u}_B\Big|_{B_{\mathrm{PEC}}} = 0 \qquad \text{or} \qquad \vec{H} \times \vec{u}_B\Big|_{B_{\mathrm{PMC}}} = 0. \tag{3.5}$$

B_{PEC} and B_{PMC} are the corresponding boundaries with the normal vector $\vec{u}_B$. Good conductors can be approximated by PEC, which results in a quite accurate field distribution outside the conductor. For symmetric structures, it is useful to replace the symmetry plane by PEC or PMC to halve the model size, according to image theory [82, Sec. 7.4].

The different components of the guided-wave structure are then reassembled considering the boundary conditions. For this purpose, the tangential field components must be equal

$$\vec{E}_1 \times \vec{u}_S\Big|_S = \vec{E}_2 \times \vec{u}_S\Big|_S \qquad \text{and} \qquad \vec{H}_1 \times \vec{u}_S\Big|_S = \vec{H}_2 \times \vec{u}_S\Big|_S \tag{3.6}$$

at a common surface S with the normal vector $\vec{u}_S$. The indices 1 and 2 refer to the two sides. Using this boundary condition and a modal field representation results in the mode matching method, as explained in Sec. 3.4.

3.1.1 Cylindrical Waveguides

Fig. 3.1 shows a cylindrical waveguide with PEC walls and a homogeneous filling in a local (u, v, w)-coordinate system. In this context, a cylindrical structure has an arbitrary cross-section S in the uv-plane that remains constant along the w-direction. In the following, the waveguide is assumed to be lossless. This structure supports wave propagation in the $\pm w$-direction. The solutions of the boundary value problem are transverse electric (TE) and transverse magnetic (TM) modes. The transverse plane is defined by a normal vector $\vec{u}_n$. With a scalar potential $\Psi^{\pm}(u, v, w)$ the TE^n-modes are given by the vector potentials

$$\vec{F}^{\pm} = A^{\pm}\sqrt{Z}\,\Psi^{\pm}(u, v, w)\,\vec{u}_n \qquad \text{and} \qquad \vec{A}^{\pm} = 0, \tag{3.7}$$

and the TM^n-modes are given by

$$\vec{F}^{\pm} = 0 \qquad \text{and} \qquad \vec{A}^{\pm} = \pm A^{\pm}\sqrt{Y}\,\Psi^{\pm}(u, v, w)\,\vec{u}_n. \tag{3.8}$$

The values $A^{\pm}$, Z, and $Y = 1/Z$ are the wave amplitude, modal wave impedance, and modal wave admittance, respectively. Notice that $\vec{A}^{\pm}$ and $A^{\pm}$ have a different meaning. The potential $\Psi^{\pm}(u, v, w)$ must fulfill the scalar wave equation

$$\nabla^2\Psi^{\pm}(u, v, w) + k_0^2\Psi^{\pm}(u, v, w) = 0. \tag{3.9}$$

For the further analysis, $\Psi^{\pm}(u, v, w)$ is separated into a transverse $\Psi_{uv}(u, v)$ and a longitudinal factor $\Psi_w^{\pm}(w)$, such that

$$\Psi^{\pm}(u, v, w) = \Psi_{uv}(u, v)\,\Psi_w^{\pm}(w) = \Psi_{uv}(u, v)\,\mathrm{e}^{\mp \mathrm{j}\,\beta\,w}. \tag{3.10}$$

The longitudinal factor describes a mode that propagates in the $\pm w$-direction with a phase constant β. The wave equation (3.9) is now simplified to two dimensions

$$\nabla_{uv}^2\Psi_{uv}(u, v) + \underbrace{(k_0^2 - \beta^2)}_{k_c^2}\Psi_{uv}(u, v) = 0, \tag{3.11}$$

where the two-dimensional Laplace operator is defined by $\nabla_{uv}^2 = \frac{\partial^2}{\partial u^2} + \frac{\partial^2}{\partial v^2}$ and the subscript indicates the involved spatial dimensions. The cutoff wave number k_c results from the analysis of the two-dimensional problem and is a characteristic value of a specific mode.

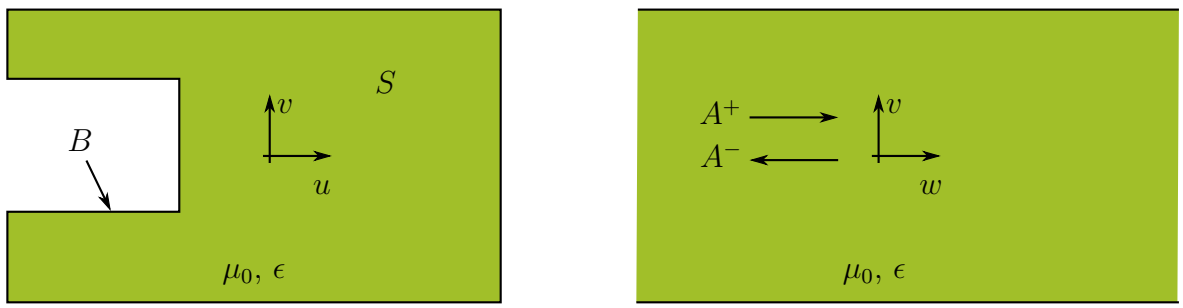

(a) (b)

Figure 3.1: (a) Cross- and (b) longitudinal section of a cylindrical waveguide.

The propagation constant is thus given by

$$\beta = -\mathrm{j}\sqrt{k_c^2 - k_0^2}. \tag{3.12}$$

Depending on the operating frequency, one differentiates between propagating ($k_c \leq k_0$) and evanescent ($k_c \geq k_0$) modes, where the latter fall off exponentially in the propagation direction. The term of (3.12) accounts for the correct sign in both cases if as usual the principal value of the complex square root is taken.

For the numerical analysis, it is helpful to introduce the modal fields $\vec{e}^{\pm}(u,v)$ and $\vec{h}^{\pm}(u,v)$ according to

$$\vec{E}^{\pm}(u,v,w) = A^{\pm}\sqrt{Z}\,\vec{e}^{\pm}(u,v)\,\mathrm{e}^{\mp\mathrm{j}\,\beta\,w} \tag{3.13a}$$

and

$$\vec{H}^{\pm}(u,v,w) = \pm A^{\pm}\sqrt{Y}\,\vec{h}^{\pm}(u,v)\,\mathrm{e}^{\mp\mathrm{j}\,\beta\,w}, \tag{3.13b}$$

where the modal impedance is given by

$$Z = \frac{1}{Y} = \begin{cases} Z_w^{TE} = Z_0\,\frac{k_0}{\beta}, & \mathrm{TE}^n\text{-modes}, \\ Z_w^{TM} = Z_0\,\frac{\beta}{k_0}, & \mathrm{TM}^n\text{-modes}. \end{cases} \tag{3.14}$$

The field equations (3.4) can then by rearranged to

$$\vec{e}^{\pm}(u,v) = -\mathrm{e}^{\pm\mathrm{j}\,\beta\,w} \begin{cases} \nabla \times (\Psi^{\pm}(u,v,w)\,\vec{u}_n), & \mathrm{TE}^n\text{-modes}, \\ \frac{1}{\mp\mathrm{j}\beta}\,\nabla \times \nabla \times (\Psi^{\pm}(u,v,w)\,\vec{u}_n), & \mathrm{TM}^n\text{-modes} \end{cases} \tag{3.15a}$$

and

$$\vec{h}^{\pm}(u,v) = \mathrm{e}^{\pm\mathrm{j}\,\beta\,w} \begin{cases} \frac{-1}{\mp\mathrm{j}\beta}\,\nabla \times \nabla \times (\Psi^{\pm}(u,v,w)\,\vec{u}_n), & \mathrm{TE}^n\text{-modes}, \\ \nabla \times (\Psi^{\pm}(u,v,w)\,\vec{u}_n). & \mathrm{TM}^n\text{-modes}. \end{cases} \tag{3.15b}$$

These equations can be further simplified, if the propagation direction $\vec{u}_w$ is equivalent to the normal direction $\vec{u}_n$ of the transverse mode. The transverse fields are given by

$$\vec{e}_{uv}(u,v) = \begin{cases} -\nabla_{uv}\Psi_{uv}(u,v) \times \vec{u}_w, & \mathrm{TE}^w\text{-modes}, \\ -\nabla_{uv}\Psi_{uv}(u,v), & \mathrm{TM}^w\text{-modes} \end{cases} \tag{3.16a}$$

and

$$\vec{h}_{uv}(u,v) = \vec{u}_w \times \vec{e}_{uv}(u,v) = \begin{cases} -\nabla_{uv}\Psi_{uv}(u,v), & \mathrm{TE}^w\text{-modes}, \\ \nabla_{uv}\Psi_{uv}(u,v) \times \vec{u}_w, & \mathrm{TM}^w\text{-modes} \end{cases} \tag{3.16b}$$

and the longitudinal fields are given by

$$e_w^{\pm}(u,v) = \begin{cases} 0, & \mathrm{TE}^w\text{-modes}, \\ -\frac{k_c^2}{\mp\mathrm{j}\beta}\,\Psi_{uv}(u,v), & \mathrm{TM}^w\text{-modes} \end{cases} \tag{3.17a}$$

and

$$h_w^{\pm}(u,v) = \begin{cases} -\frac{k_c^2}{\mp\mathrm{j}\beta}\,\Psi_{uv}(u,v), & \mathrm{TE}^w\text{-modes}, \\ 0, & \mathrm{TM}^w\text{-modes}. \end{cases} \tag{3.17b}$$

Here, $\nabla_{uv} = \frac{\partial}{\partial u}\,\vec{u}_u + \frac{\partial}{\partial v}\,\vec{u}_v$ is the two-dimensional gradient. In transmission line theory, modal voltages

$$V(w) = \sqrt{Z}(A^+\,\mathrm{e}^{-\mathrm{j}\beta w} + A^-\,\mathrm{e}^{\mathrm{j}\beta w}) \tag{3.18a}$$

and currents

$$I(w) = \sqrt{Y}(A^+\,\mathrm{e}^{-\mathrm{j}\beta w} - A^-\,\mathrm{e}^{\mathrm{j}\beta w}) \tag{3.18b}$$

are also commonly used. For components with waveguide ports, the wave amplitudes $A^\pm$ are also labeled by a and b for the incident and reflected wave amplitudes, respectively. To distinguish between different modes, the mode quantities are marked with an index m in the following. The eigenfunctions are commonly normalized to be orthonormal, such that the relation

$$\iint_S \left(\vec{e}_m^{\pm}(u,v) \times \vec{h}_{\bar{m}}^{\pm}(u,v)\right) \bullet \vec{u}_w\,dS = \delta_{m-\bar{m}} \tag{3.19}$$

between mode m and $\bar{m}$ is valid. Here, $\delta_{m-\bar{m}}$ is the Kronecker delta function and the mode index with an overbar stands for a second index. The normalization relation is simplified to

$$\iint_S \vec{e}_{uv,m(u,v)} \bullet \vec{e}_{uv,\bar{m}}(u,v)\,dS = \iint_S \vec{h}_{uv,m(u,v)} \bullet \vec{h}_{uv,\bar{m}}(u,v)\,dS = \delta_{m-\bar{m}} \tag{3.20}$$

for modes with $\vec{u}_n = \vec{u}_w$. The real power of a mode propagating in $\pm w$-direction is then simply given by $P = |A^\pm|^2$.

TEM^w-modes can be viewed as a special case of the discussed mode types, where the cutoff wave number $k_c = 0$ and all longitudinal components given by (3.17) vanish. A waveguide with N conductors supports $(N-1)$ TEM^w-modes and an infinite number of TE^w- and TM^w-modes. An arbitrary transverse field distribution can be represented by a superposition of the waveguide modes

$$\vec{E}_{uv}(u,v,w) = \sum_m V_m(w)\,\vec{e}_{uv,m}(u,v) \tag{3.21a}$$

and

$$\vec{H}_{uv}(u,v,w) = \sum_m I_m(w)\,\vec{h}_{uv,m}(u,v), \tag{3.21b}$$

where the individual mode order is m. The infinite series are truncated in practice, as they converge quite rapidly. Further details on cylindrical waveguides can be found in [83] and [84].

3.1.2 Parallel-Plate Modes

In PCB technology the dielectric core of the substrate is laminated from both sides with metal foils. This can be interpreted as a parallel-plate waveguide, where the top and bottom metalizations are represented by two parallel conducting planes. In this section, the wave propagation in lossless parallel-plate waveguides is studied.

Fig. 3.2 depicts a parallel-plate waveguide, consisting of a dielectric core of thickness h and two PEC planes. It supports TE$^{\pm\theta}$- and TM$^{\pm\theta}$-modes, where the normal vector is given by

$$\vec{u}_n^{\pm} = \begin{bmatrix} \cos(\theta) & 0 & \pm\sin(\theta) \end{bmatrix}^T \tag{3.22}$$

and the propagation angle θ is defined by $\cos(\theta) = k_x/k_{xz}$. In the following analysis, the waveguide direction w is aligned with the x-direction. The scalar potential can be separated in an in-plane factor $\Psi_{xz}(x,z)$ and an factor out-of-plane $\Psi_y(y)$, such that

$$\Psi^{\pm}(x,y,z) = \Psi_y(y)\,\Psi_{xz}^{\pm}(x,z). \tag{3.23}$$

With the potential

$$\Psi_y(y) = \begin{cases} \frac{1}{k_y}\,\Psi_c(y) \text{ with } \Psi_c(y) = \sqrt{\frac{\varepsilon_\mu}{h}}\cos\left(k_y\,(y-y_0)\right), & \text{TE}^{\pm\theta}\text{-modes}, \\ \frac{1}{k_y}\,\Psi_s(y) \text{ with } \Psi_s(y) = \sqrt{\frac{\varepsilon_\mu}{h}}\sin\left(k_y\,(y-y_0)\right), & \text{TM}^{\pm\theta}\text{-modes}, \end{cases} \tag{3.24}$$

the wave equation (3.9) is simplified to a two-dimensional problem

$$\nabla_{xz}^2\Psi_{xz}^{\pm}(x,z) + k_{xz}^2\Psi_{xz}^{\pm}(x,z) = 0 \qquad \text{with} \qquad k_{xz} = -\mathrm{j}\sqrt{k_y^2 - k_0^2}. \tag{3.25}$$

The potential $\Psi_y(y)$ describes a standing wave in y-direction with the wave number $k_y = \mu\pi/h$ and the parallel-plate mode index μ. This index is added as a subscript to parallel-plate quantities if required. Depending on the mode type (TE/TM), one of these solutions satisfies the boundary conditions at $y = y_0$ and $y = y_0 + h$. With the chosen normalization and the Neumann number $\varepsilon_\mu = 2 - \delta_\mu$, the orthonormal relation

$$\int_0^h \frac{\partial\Psi_{y,\mu}(y)}{\partial y}\frac{\partial\Psi_{y,\bar{\mu}}(y)}{\partial y}dy = \delta_{\mu-\bar{\mu}} \tag{3.26}$$

is satisfied between mode μ and $\bar{\mu}$. For the zeroth order ($\mu = 0$), $\Psi_{y,0}(y)$ is undefined for TE$^{\pm\theta}$-modes and given by $(y-y_0)/\sqrt{h}$ for TM$^{\pm\theta}$-modes.

In Cartesian coordinates, (3.25) is fulfilled by traveling waves that are given by

$$\Psi_{xz}^{\pm}(x,z) = \mathrm{e}^{-\mathrm{j}(\pm k_x x + k_z z)}. \tag{3.27}$$

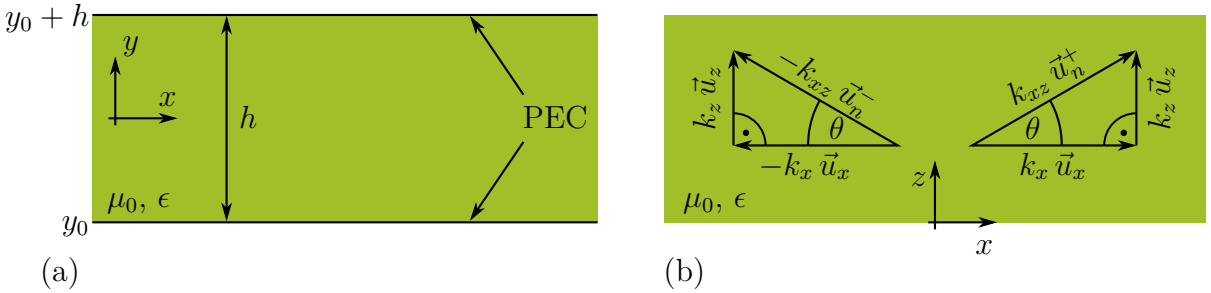

Figure 3.2: (a) Cross-section and (b) top view of a parallel-plate waveguide.

According to (3.15), the modal fields result in

$$\vec{e}^{\pm}(y,z) = \mathrm{e}^{-\mathrm{j}\,k_z\,z} \begin{cases} \left[\pm\frac{k_z}{k_{xz}}\Psi_s \quad 0 \quad -\frac{k_x}{k_{xz}}\Psi_s\right]^T, & \mathrm{TE}^{\pm\theta}\text{-modes}, \\ \left[\mp\mathrm{j}\frac{k_y}{k_{xz}}\Psi_s \quad -\frac{k_{xz}}{k_x}\Psi_c \quad -\mathrm{j}\frac{k_y k_z}{k_{xz} k_x}\Psi_s\right]^T, & \mathrm{TM}^{\pm\theta}\text{-modes} \end{cases} \tag{3.28a}$$

and

$$\vec{h}^{\pm}(y,z) = \mathrm{e}^{-\mathrm{j}\,k_z\,z} \begin{cases} \left[\mp\mathrm{j}\frac{k_y}{k_{xz}}\Psi_c \quad +\frac{k_{xz}}{k_x}\Psi_s \quad -\mathrm{j}\frac{k_y k_z}{k_{xz} k_x}\Psi_c\right]^T, & \mathrm{TE}^{\pm\theta}\text{-modes}, \\ \left[\pm\frac{k_z}{k_{xz}}\Psi_c \quad 0 \quad -\frac{k_x}{k_{xz}}\Psi_c\right]^T, & \mathrm{TM}^{\pm\theta}\text{-modes}. \end{cases} \tag{3.28b}$$

These modes can also be called TE^y- and TM^y-modes because of the vanishing field components in y-direction. The zeroth order $TM_0^{\pm\theta}$-mode is a $\mathrm{TEM}^{\pm\theta}$-mode. The defined modes build a complete normalized set and can be used for the analysis of parallel-plate waveguide components.

3.1.3 Floquet Modes

The SIW is, in a strict sense, a periodic structure and can be analyzed with the Floquet theory [85, Sec. 8.8]. In this section, the wave propagation in a parallel-plate waveguide with periodic boundary conditions in z-direction is studied. The results are later used for the SIW analysis. The periodic structure has a pitch p and the so-called Floquet modes are eigenmodes of the three-dimensional unit cell. The field distribution repeats in each unit cell except for a propagation factor $\mathrm{e}^{-\mathrm{j}\Phi_z}$. If losses are existent, the phase difference Φ_z is complex. For the parallel-plate waveguide, this is equivalent to the Floquet theorem

$$\Psi_{xz}^{\pm}(x, z+p) = \mathrm{e}^{-\mathrm{j}\Phi_z}\Psi_{xz}^{\pm}(x,z). \tag{3.29}$$

The two-dimensional potential is identical to (3.27). This theorem can be viewed as a periodic boundary condition in z-direction and is fulfilled for the wave numbers

$$k_z = \frac{\Phi_z + 2\,\pi\,\xi}{p} \qquad \text{and} \qquad k_x = -\mathrm{j}\sqrt{k_z^2 - k_{xz}^2}, \tag{3.30}$$

with ξ the Floquet mode order (positive or negative integer). The phase difference is given by $\Phi_z = k_{xz}\,p\,\sin(\theta)$. For $\xi = 0$, the Floquet mode is identical to the parallel-plate mode. The Floquet modes are also called spatial harmonics and a superposition can be viewed as Fourier series. With this series further boundary conditions of the unit cell can be satisfied.

Fig. 3.3 shows Floquet mode potentials for $\theta = 30°$ and $\Phi_z = 90°$. The pitch of the unit cell is marked by horizontal solid lines. Fig. 3.3a shows the fundamental parallel-plate mode ($\xi = 0$) traveling in θ-direction. Fig. 3.3b represents a higher-order Floquet mode ($\xi = -1$). In this case, it is evanescent in x-direction and can be viewed as a surface wave of a periodic structure that is located in $x < 0$ (e.g., a via row). In general all higher-order Floquet modes ($\xi \neq 0$) are evanescent in the x-direction, if $k_{xz} \leq \frac{2\pi}{p}\frac{1}{1+\sin(|\theta|)}$. At higher

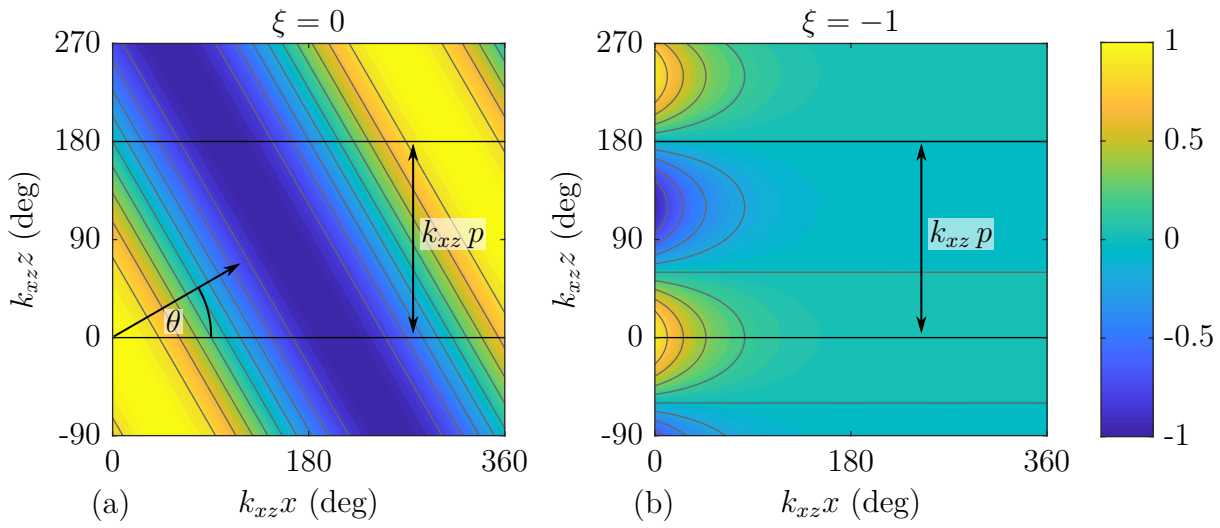

Figure 3.3: Real part of Floquet mode potential $\mathrm{Re}\,(\Psi^{+}_{xz}(x,z))$ ($\theta = 30°$, $\Phi_z = 90°$).

frequencies they can propagate and form passband-stopband characteristics, as it is typical for periodic structures. One further important property of the Floquet modes is that the group velocity

$$v_g = \frac{d\omega}{dk_z} = p\,\frac{d\omega}{d\Phi_z} \tag{3.31}$$

is not a function of ξ. Thus, the power of all Floquet modes is transported with the same velocity. More information on periodic structures is given in [85, Cha. 8].

3.2 Cylindrical Waveguides with Rough Surfaces

The losses and the dispersion of waveguides with rough surfaces are studied in the following. For this, the skin effect in conductors with rough surfaces is first analyzed in a general way. Then, based on these results, a model for lossy waveguides with rough surfaces is developed.

3.2.1 Skin Effect in Rough Surfaces

The skin effect describes the tendency of an alternating electric current density to concentrate near the surface of a good conductor. This effect is illustrated for a plane wave with normal incidence on a conductor in the vw-plane, as depicted in Fig. 3.4a. For a smooth surface, the transmitted fields in the conductor and hence the current density decay exponentially with e^{-u/δ_s}. Here,

$$\delta_s = \sqrt{\frac{2}{\omega\,\mu_0\,\sigma_0}} \tag{3.32}$$

is the skin depth. For copper with $\sigma_0 = \sigma_{0,Cu} \approx 5.8 \cdot 10^7\,\mathrm{S/m}$, it is below 1 µm at K-band frequencies. Fig. 3.4b shows the detail of a typical high-frequency substrate with a copper foil. On the left-hand side of the foil, a rough surface profile is visible. The maximum

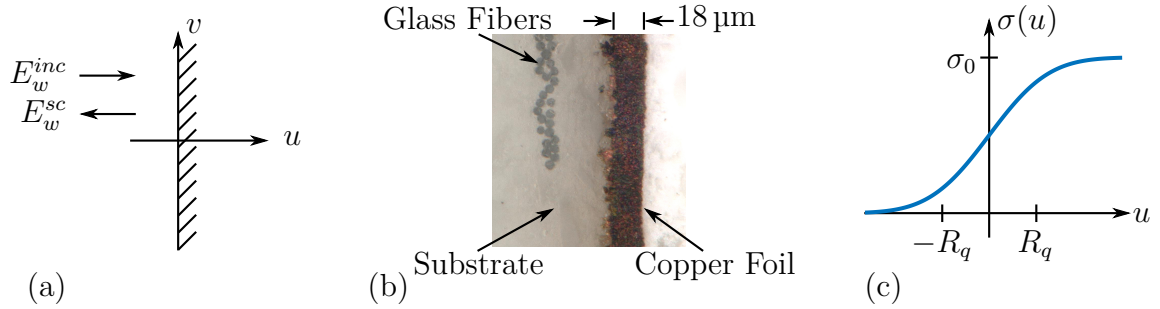

Figure 3.4: (a) Conducting plane with an incident plane wave, (b) RO4003 substrate with copper foil, and (c) conductivity profile of a rough surface.

peak-to-valley profile height is in the range of $R_z \approx 10\,\mu\text{m}$ and is thus greater than the skin depth. In this case, the assumption of a smooth surface is not correct anymore. Various models are available to take rough surfaces into account. They can be categorized in phenomenological, topological, and statistical models. The phenomenological models [86, 87] are described by empirical equations that are based on microwave measurement results. In topological models, mostly periodic surface structures like grooves [88, 89] or stacked spheres [90] are assumed. Recently, a statistical model called gradient model has been developed [91–93]. It is based on the statistics of the surface profile and, in contrast to the phenomenological models, does not need microwave measurement data. Also, the calculation is much simpler than for the more complicated topological models. In the following, this model is presented and then simplified by empirical equations.

The microscopic structure of rough surfaces is typically in the micrometer range and, thus, much smaller than the wavelength up to millimeter waves. This allows to describe its structure by statistical means. In the gradient model, the rough surface in the vw-plane is modeled by a one-dimensional macroscopic conductivity profile

$$\sigma(u) = \sigma_0\,\sigma_r(u) \qquad \text{with} \qquad \sigma_r(u) = \frac{1}{2}\,\text{erfc}\left(-\frac{u}{\sqrt{2}\,R_q}\right) \tag{3.33}$$

in u-direction (see Fig. 3.4c). The conductivity profile is a smooth function from the dielectric with $\sigma = 0$ to the conductor with $\sigma = \sigma_0$. In this case, $\sigma_r(u)$ is a cumulative distribution function of a normally distributed roughness profile with a root-mean-square roughness R_q [94]. This value can be directly determined from measurements with optical systems like confocal laser scanning microscopes.

With Maxwell's equations and the conductivity profile, the plane wave incidence on the rough surface is now studied. For a good conductor ($\sigma/\omega \gg \epsilon_0$), the displacement current $\vec{J}_D = \mathrm{j}\,\omega\,\epsilon_d\,\vec{E}$ is much smaller than the electric current $\vec{J} = \sigma\,\vec{E}$ and can thus be neglected. Ampère's law of (3.1b) is then given by

$$\nabla \times \vec{H} = \sigma\,\vec{E} = \vec{J}. \tag{3.34a}$$

This quasi-stationary approximation is even reasonable for a conductivity of $10^{-6}\,\sigma_{0,Cu}$ and frequencies up to 100 GHz [93]. Taking the curl of (3.34a) and inserting Faraday's

law (3.1a) yields

$$\nabla \times \vec{J} = \nabla \times \left(\sigma \vec{E}\right) = \sigma \nabla \times \vec{E} + \nabla\sigma \times \vec{E} = -\mathrm{j}\,\frac{2}{\delta_s^2}\,\sigma_r\,\vec{H} + \frac{\nabla\sigma_r}{\sigma_r} \times \vec{J}. \tag{3.34b}$$

The system of partial differential equations (3.34) is reduced to the system of ordinary differential equations

$$\frac{\partial}{\partial u}\begin{bmatrix} H_v \\ J_w \end{bmatrix} = \begin{bmatrix} 0 & 1 \\ \mathrm{j}\,\frac{2}{\delta_s^2}\,\sigma_r & -\frac{1}{\sigma_r}\,\frac{\partial\sigma_r}{\partial u} \end{bmatrix} \begin{bmatrix} H_v \\ J_w \end{bmatrix}, \tag{3.35}$$

for plane wave incidence in u-direction, $\vec{H} = H_v\,\vec{u}_v$, and $\vec{J} = J_w\,\vec{u}_w$. The resulting boundary value problem has in general no analytical solution and is solved numerically for the following analysis [95].

Fig. 3.5 shows the conductivity profiles and the distribution of the magnetic field H_v and the current density J_w for a smooth and a rough surface. The values are normalized such that the maxima are unity for the smooth surface. The conductivity step results in the well known exponential decay of H_v and J_w. The distribution changes abruptly and shows a sharp peak for J_w at $u = 0$. The rough surface yields a continuous distribution and the current density is spread over a thicker layer. The magnetic field also changes remarkably and is no longer constant for $u < 0$. This leads to higher losses and alters the dispersion characteristics [96].

For the following analysis, the rough conductor material is replaced by an effective material with a smooth surface. The losses are modeled by a frequency dependent effective relative conductivity $\sigma_{r,eff}$ that is determined from the current density by comparing the power losses of both models. The magnetic field is related to the stored magnetic energy of the conductor. The stored magnetic energies of the smooth and the rough surfaces are matched by means of an effective relative permeability $\mu_{r,eff}$. The relations and a detailed derivation are reported in [93]. These two parameters characterize the effective material, which can be used in transmission line models. Fig. 3.6 shows these effective

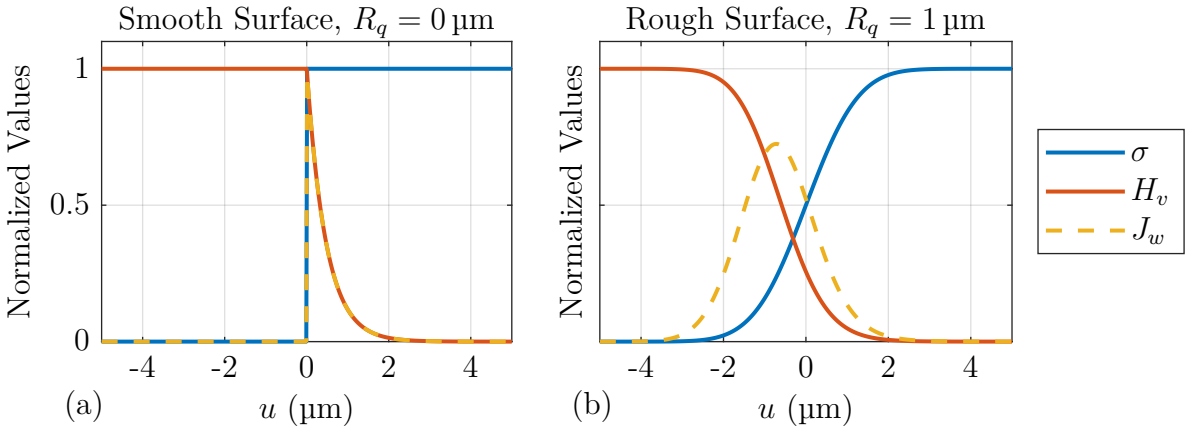

Figure 3.5: Normalized magnetic field H_v and current density J_w for a smooth and a rough conductivity profile $\sigma(u)$ ($\sigma_0 = 5.8 \cdot 10^7\,\mathrm{S/m}$, $f = 20\,\mathrm{GHz}$).

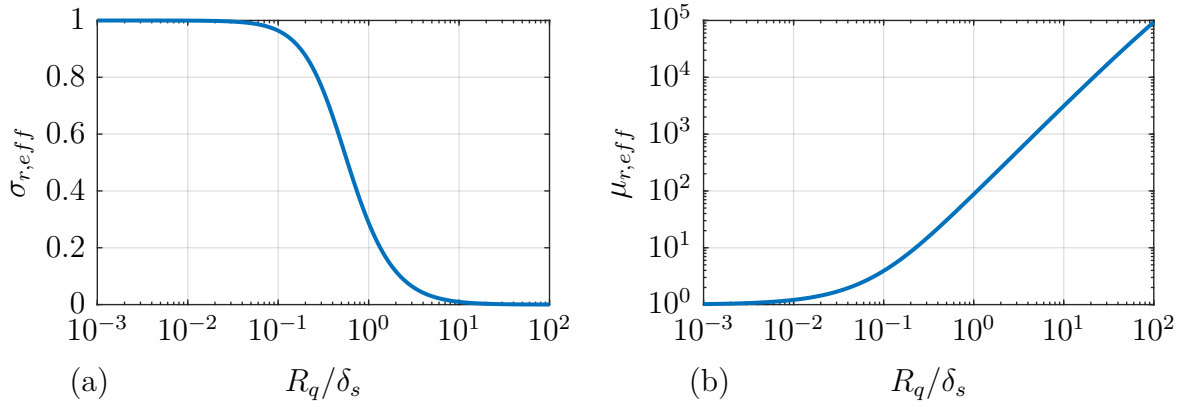

Figure 3.6: (a) Effective relative conductivity $\sigma_{r,eff}$ and (b) effective relative permeability $\mu_{r,eff}$ versus R_q/δ_s.

parameters versus R_q/δ_s. Starting from a smooth surface ($\sigma_{r,eff} = \mu_{r,eff} = 1$), $\sigma_{r,eff}$ decreases and $\mu_{r,eff}$ increases for rougher surfaces. For $R_q = \delta_s$, $\sigma_{r,eff}$ drops to 29 % and $\mu_{r,eff}$ is increased by a factor of 87. The effective material parameters only depend on the ratio R_q/δ_s. This can be understood from the similitude theorem [97, Sec. 9.3], which is also known as frequency-scaling for the lossless case. The quasi-stationary boundary value problem (3.35) yields similar results[1], if all physical dimensions (u, R_q) are scaled by a factor q and the frequency f as well as the conductivity σ_0 are scaled by a factor $1/q$. Hence, the skin depth δ_s is also scaled by q. For a fixed ratio R_q/δ_s, the boundary value problem gives thus a similar result, which yields the same effective material parameters.

The numerical solution of the boundary value problem is inconvenient in practice. However, the empirical equations

$$\sigma_{r,eff} = \left(1 + \frac{53}{10}\left(\frac{R_q}{\delta_s}\right)^2 + \frac{11}{6}\left(\frac{R_q}{\delta_s}\right)^3\right)^{-46/77} \tag{3.36a}$$

and

$$\mu_{r,eff} = \exp\left(-\frac{R_q}{405\,\delta_s}\right)\left(\frac{17\,R_q}{\delta_s} + \frac{2\,\delta_s}{2\,\delta_s + 9\,R_q}\right)^{267/170} \tag{3.36b}$$

approximate the effective material parameter with a maximum relative error of 1 % for $R_q/\delta_s \leq 100$. The equations are determined from the simulation data of Fig. 3.6 using the software tool *Eureqa* [98], which automatically searches for an analytical model.

Often, it is more convenient to use the frequency dependent complex surface impedance

$$Z_S = R_S + \mathrm{j}\,\omega\,L_S = \frac{1}{\sigma_0\,\sigma_{r,eff}\,\delta_c} + \mathrm{j}\,\frac{1}{\sigma_0\,\delta_m}, \tag{3.37a}$$

which can be decomposed in a surface resistance R_S and a surface inductance L_S, as used later in this work [92]. The effective skin depths of the current density and the magnetic

[1] In this context, similar results are defined in a strict sense and refer to results that are scaled versions from each other.

field are given by

$$\delta_c = \sqrt{\frac{2}{\omega\,\mu_0\,\sigma_0\,\sigma_{r,eff}}} \qquad \text{and} \qquad \delta_m = \sqrt{\frac{2}{\omega\,\mu_0\,\mu_{r,eff}\,\sigma_0}}, \tag{3.37b}$$

respectively. This model is available in *CST Microwave Studio 2017* and later versions. In a strict sense, the presented model is only valid for the conducting half-space. However, the model is also very accurate for other structures, if the conductor thickness and the curvature radius of the structure are larger than several skin depths. Note that the same assumptions are implied for the surface impedance of a smooth conductor.

3.2.2 Loss and Dispersion Mechanisms

The loss and dispersion mechanisms in case of rough conductor surfaces are now studied for the dielectric-filled cylindrical waveguide, as depicted in Fig. 3.7a. At first, the equivalent circuit of a waveguide with an infinitesimal length dz is considered. For lossless TEM-modes the well known equivalent circuit [99, Sec. 2.1] features a shunt capacitor and a series inductor for the transverse electric and magnetic field, respectively. For TE- and TM-modes this circuit must be extended by a shunt inductor and a series capacitor to account for the longitudinal magnetic and electric field, respectively. The associated losses are represented by resistors or conductors, as depicted in Fig. 3.7b and Fig. 3.7c. To calculate the circuit elements, the field distribution for a lossless smooth waveguide is assumed within the dielectric. The resulting parameters of the equivalent circuit elements are listed in Tab. 3.1. For smooth and lossless walls, the parameters are well known [100, Sec. 10.1] and the surface impedance is $Z_S = R_S = L_S = 0$. The transverse field in the dielectric is represented by the capacitance $C'\,dz$, the conductance $G'\,dz$, and the outer inductance $L'_o\,dz$. Likewise, the longitudinal field in the dielectric is represented by the capacitance C''/dz and the conductance G''/dz or the outer inductance L''_o/dz for TE- or TM-modes, respectively. The conductances are proportional to the capacitances and the dielectric loss tangent $\tan(\delta_d)$. The rough and lossy walls are considered through the classical perturbation approach [83]. This yields $R'\,dz$ and R''/dz, which account for the conductor losses. The inner inductances $L'_i\,dz$ and L''_i/dz result from the magnetic field

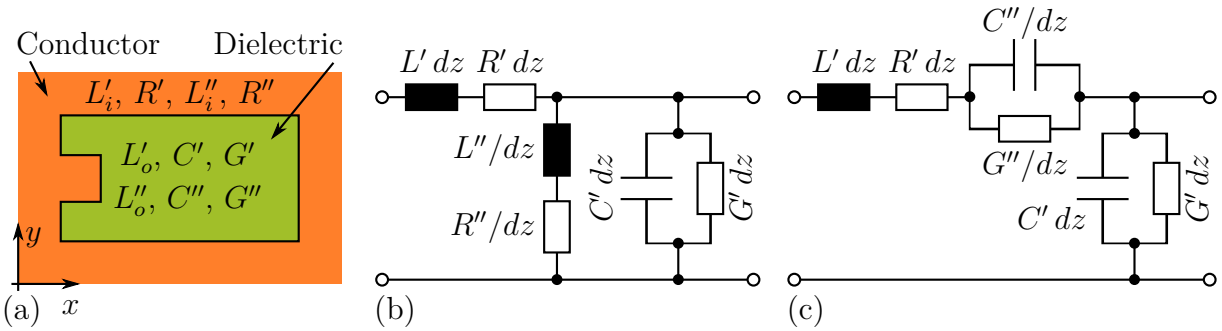

Figure 3.7: (a) Dielectric-filled cylindrical waveguide and equivalent circuit models of an infinitesimal length dz for lossy (b) TE^z- and (c) TM^z-modes.

Table 3.1: Equivalent circuit elements for lossy waveguides with rough surfaces.

Field	Reactive Element	Resistive Element
$\vec{E}_{xy}$	$C' = \epsilon_0\,\epsilon_r$	$G' = \omega\,C'\tan(\delta_d)$
E_z	$C'' = \frac{\epsilon_0\,\epsilon_r}{k_c^2}$	$G'' = \omega\,C''\tan(\delta_d)$
$\vec{H}_{xy}$, $J_{s,z}$	$L' = L'_o + L'_i$, $L'_o = \mu_0$, $L'_i = L_S\,I'$	$R' = R_S\,I'$
H_z, $J_{s,t}$	$L'' = L''_o + L''_i$, $L''_o = \frac{\mu_0}{k_c^2}$, $L''_i = L_S\,I''$	$R'' = R_S\,I''$

inside the conductor [101]. They are not considered in the classical model, which is a reasonably good approximation for smooth waveguides well above the cutoff frequency. However, for rough surfaces the inner inductance noticeably decreases the phase constant. The equivalent circuit elements related to the rough conductors are determined by comparing the stored magnetic energy, the dissipated power of the fields, and the equivalent circuit parameters. A derivation is given in Sec. A.1. The equivalent circuit parameters can be calculated from the current distribution integrals

$$I' = \oint_C |h_t(x,y)|^2\,dC, \tag{3.38a}$$

$$I'' = \oint_C |\Psi_{xy}(x,y)|^2\,dC, \tag{3.38b}$$

and the surface impedance $Z_S = R_S + \mathrm{j}\,\omega\,L_S$. Here, C is the conductor contour of the waveguide cross-section and $h_t(x,y)$ is the transverse magnetic field component tangential to the conductor surface. Furthermore, a normalization of the modal fields according to (3.20) is assumed. The integral I'' is only necessary for TE-modes.

Using the equivalent circuit, the propagation constant is given by

$$\gamma = \alpha + \mathrm{j}\beta = \sqrt{Z'\,Y'}, \tag{3.39}$$

where α is the attenuation and β the phase constant. For TE^z-modes, the series impedance and shunt admittance are related to the circuit elements by

$$Z' = R' + \mathrm{j}\,\omega\,L' \qquad \text{and} \qquad Y' = G' + \mathrm{j}\,\omega\,C' + \frac{1}{R'' + \mathrm{j}\,\omega\,L''} \tag{3.40a}$$

and for TM^z-modes by

$$Z' = R' + \mathrm{j}\,\omega\,L' + \frac{1}{G'' + \mathrm{j}\,\omega\,C''} \quad \text{and} \qquad Y' = G' + \mathrm{j}\,\omega\,C'. \tag{3.40b}$$

For rough surfaces, the phase constant reduction can also be modeled by a larger effective dielectric constant, which, in turn, increases the cutoff frequency. In the context of microstrip lines, this parameter is also called design dielectric constant [102]. The phase constants of a waveguide with a rough and of one with a smooth PEC surface can be matched by using the analytical expressions

$$\frac{\epsilon_{r,eff}}{\epsilon_r} = 1 + \frac{L'_i}{L'_o} + \left(\frac{f_c}{f}\right)^2 \frac{L''_i/L''_o - L'_i/L'_o}{1 + L''_i/L''_o} \tag{3.41a}$$

and

$$\frac{\epsilon_{r,eff}}{\epsilon_r} = 1 + \frac{L'_i}{L'_o} \tag{3.41b}$$

for TE^z-modes and TM^z-modes, respectively. Here, lossless waveguides ($R' = R'' = G' = 0 = G'' = 0$) are assumed and the inner inductances ($L'_i = L''_i = 0$) of the smooth waveguide are neglected. In general, $\epsilon_{r,eff}$ is frequency dependent but can be approximated by a fixed value above cutoff. This effective dielectric constant is useful for the design of components. In particular for resonant structures with a large group delay, as for example filters, the frequency response can be severely shifted by rough conductors.

3.3 Substrate Integrated Waveguides

The SIW is a periodic guided-wave structure as depicted in Fig. 1.3. A widespread model for the SIW is the equivalent rectangular waveguide with a proper width. It is a simple model which allows to use the guided-wave theory of cylindrical waveguides. The main goal is to determine the width of the equivalent waveguide for an SIW arrangement. The available analysis techniques can be classified in three main groups [103, Sec. 9.2.2]:

1. full-wave simulation with multimode excitation [104–106],
2. unit cell eigenmode analysis [107], and
3. techniques that utilize the surface impedance concept [108].

In full-wave simulation the SIW structure is excited with an adequate number of auxiliary waveguide modes. In this case, either commercial or specialized tools can be used [104]. The properties of the SIW modes are calculated from a superposition of the auxiliary modes. A typical method is called multimode calibration technique [105]. In the second approach, a unit cell composed of two vias is analyzed with an eigenmode solver, which straightforwardly gives the propagation coefficient. In the third case, the via rows are modeled by equivalent surfaces with a surface impedance. For this, the reflection properties of a single via row are analyzed. Based on the presented techniques, different empirical equations for the width of an equivalent waveguide have been proposed [106, 109, 110].

This section shows the relationship between the SIW and the equivalent rectangular waveguide using the surface impedance concept. Furthermore, different loss mechanisms of the SIW are discussed and the influence of surface roughness is shown.

3.3.1 Equivalent Rectangular Waveguide

At first, the basic properties of rectangular waveguides are reformulated in terms of Floquet modes. The waveguide has width a, height h, and is orientated in z-direction. The field distributions of a TE$^z_{m_x m_y}$- and TM$^z_{m_x m_y}$-waveguide mode of orders m_x and m_y can be represented by a superposition of fundamental Floquet modes ($\xi = 0$). For this, the

auxiliary TE^y- and TM^y-modes are defined by

$$[TE^y] = \sqrt{\frac{2}{a}}\,\frac{[TE^{-\theta}] - [TE^{+\theta}]}{2} \tag{3.42a}$$

and

$$[TM^y] = \sqrt{\frac{\varepsilon_{m_x}}{a}}\,\frac{[TM^{-\theta}] - [TM^{+\theta}]}{2\mathrm{j}}, \tag{3.42b}$$

respectively. These modes are standing waves in x-direction and a superposition of two traveling waves. The bracketed mode quantities can stand for vector potentials, fields, or wave amplitudes. With these modes the rectangular waveguide modes are given by

$$[TE^z] = \frac{\sqrt{Z_z^{TE}}}{k_{xz}\,k_c}\left(k_x^2\sqrt{Y_x^{TM}}\,[TM^y] - k_y\,k_z\sqrt{Y_x^{TE}}\,[TE^y]\right) \tag{3.43a}$$

and

$$[TM^z] = \frac{\sqrt{Y_z^{TM}}}{k_{xz}\,k_c}\left(k_x^2\sqrt{Z_x^{TE}}\,[TE^y] + k_y\,k_z\sqrt{Z_x^{TM}}\,[TM^y]\right), \tag{3.43b}$$

where $k_c = \sqrt{k_x^2 + k_y^2}$ is the cutoff wave number. The wave numbers in x- and z-direction are given by

$$k_x = \frac{m_x\,\pi}{a} \qquad \text{and} \qquad k_z = -\mathrm{j}\sqrt{k_x^2 - k_{xz}^2} \tag{3.44}$$

to match the boundary conditions at $x = 0$ and $x = a$. The waveguide mode order m_y is equivalent to the parallel-plate mode order μ, because the SIW geometry between the metal layers does not vary in y-direction. The pitch p can be arbitrarily chosen and no higher-order Floquet modes ($\xi \neq 0$) are present due to the cylindrical waveguide structure. Hence, the Floquet mode order is omitted in this section.

To keep this section short, it is focused on the $\mathrm{TE}^z_{m_x0}$-modes, which are most important for many applications. Here, $k_y = 0$ and the $\mathrm{TE}^z_{m_x0}$-modes are a simple superposition of $\mathrm{TM}_0^{+\theta}$- and $\mathrm{TM}_0^{-\theta}$-modes, as sketched in Fig. 3.8a. The propagation angle is then given

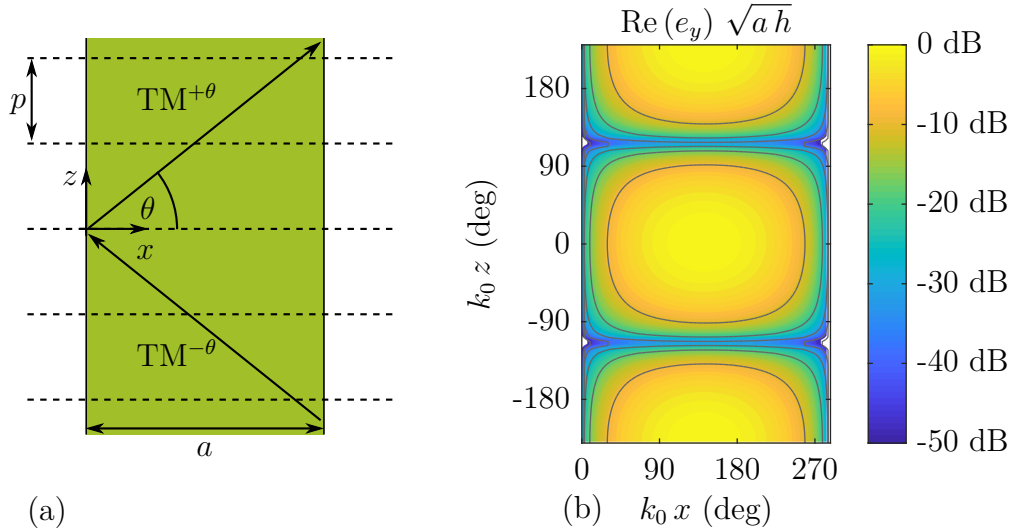

Figure 3.8: (a) Equivalent waveguide and (b) modal electric field $\mathrm{Re}\,(e_y(x,z))$ of the TE^z_{10}-mode in the xz-plane ($k_0/k_c = 1.6$).

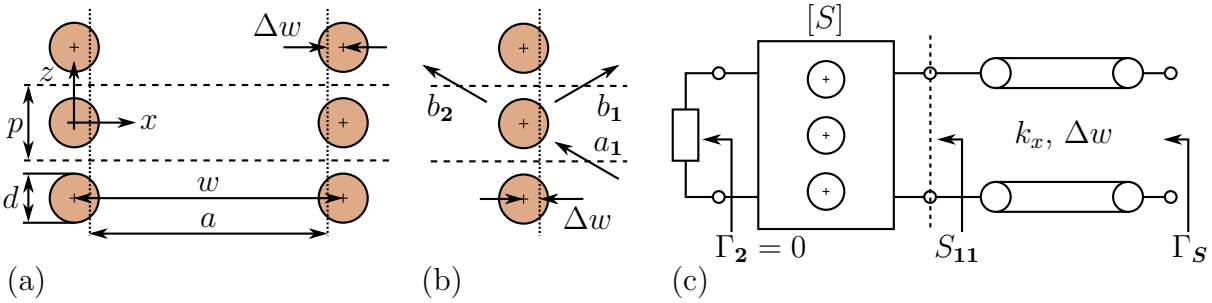

Figure 3.9: Cross-section of (a) the SIW and (b) a single via row in the xz-plane. (c) Equivalent circuit of the via row.

by $\cos(\theta) = k_c/k_0$ and at cutoff it is $\theta = 0$. As an example, the well known electric field distribution of a TE_{10}^{z}-mode at $k_0/k_c = 1.6$ is depicted in Fig. 3.8b.

In the following, an equivalent waveguide with similar properties than an SIW is determined. Fig. 3.9a shows the geometry of an SIW. The via rows are w apart. Each of them is composed of an array of circular cylinders with diameter d and pitch p. This periodic structure is analyzed with the Floquet theory from Sec. 3.1.3. The field in the source free space with $x < -d/2$, $d/2 < x < w - d/2$, or $w + d/2 < x$ can be expanded into Floquet modes.

In a first step, the left via row as depicted in Fig. 3.9b is analyzed. Like for the waveguide, a fundamental Floquet mode $a_\mathbf{1}$ is incident on the via row. This mode is scattered into a reflected wave $b_\mathbf{1}$ and a transmitted wave $b_\mathbf{2}$. The latter is also called leaky wave and induces radiation loss. In a rigorous analysis, also higher-order Floquet modes are excited at the via row. In practical structures, these modes are evanescent in x-direction and, thus, mainly contribute to the local field distribution in the vicinity of the via row. In Fig. 3.10 the field distributions for via rows with three different pitches are plotted. On the right-hand side of the via row the field distribution is similar to that in a rectangular

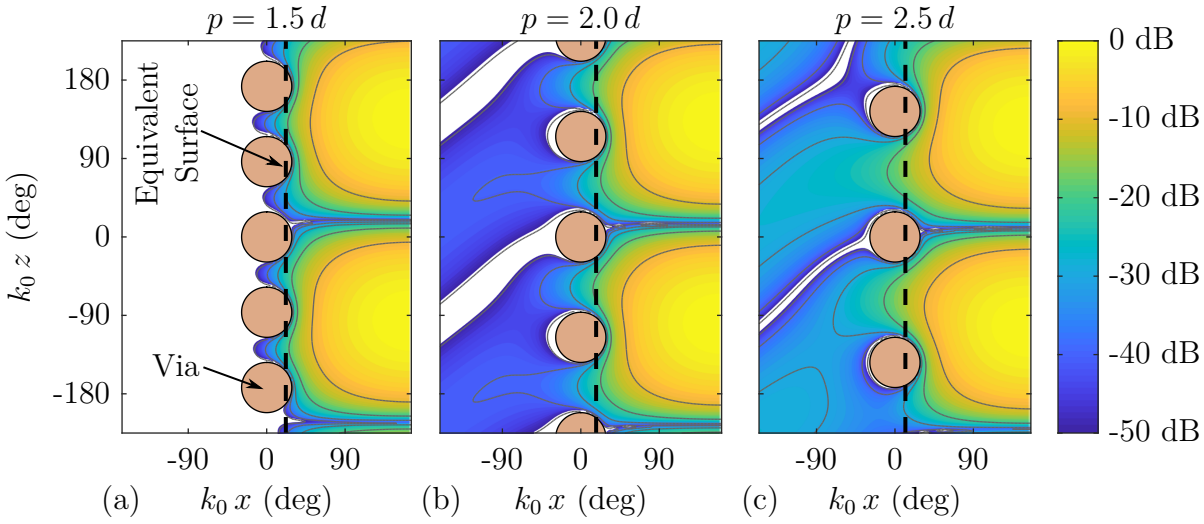

Figure 3.10: Normalized y-component of electric field $\mathrm{Re}\,(e_y(x,z))$ for via rows with different pitches p ($a/d = 5$, $k_0/k_c = 1.6$). Calculated with model from Sec. A.2.

waveguide (see Fig. 3.8b). In addition, the leaky wave with the propagation direction θ is clearly visible. The amplitude increases for larger pitches. The scattering matrix $[S]$ connects the wave amplitudes through

$$\begin{bmatrix} b_{\mathbf{1}} \\ b_{\mathbf{2}} \end{bmatrix} = [S] \begin{bmatrix} a_{\mathbf{1}} \\ a_{\mathbf{2}} \end{bmatrix}. \tag{3.45}$$

This scattering matrix can be calculated with a commercial full-wave solver from a unit cell with one via and periodic boundary conditions in z-direction. In this case, the particular structure allows for a very efficient semi-analytical calculation that is detailed in Sec. A.2.

In the next step, an equivalent surface is defined to describe the via row. The presented method is based on the surface impedance concept [108] and the radiation losses are treated like the ohmic losses of a good conductor. The surface impedance normalized to the wave impedance is then given by

$$z_S = r_S\,(1 + \mathrm{j}) \tag{3.46}$$

and the corresponding reflection coefficient is given by

$$\Gamma_{\boldsymbol{S}} = \frac{z_S - 1}{z_S + 1} = S_{\mathbf{11}}\,\mathrm{e}^{-\mathrm{j}\,2\,k_x\,\Delta w}. \tag{3.47}$$

The input reflection $S_{\mathbf{11}}$ of the via row is mapped to $\Gamma_{\boldsymbol{S}}$ by an offset Δw of the reference plane (see Fig. 3.9c). The condition $|\Gamma_{\boldsymbol{S}}|^2 = |S_{\mathbf{11}}|^2$ yields the quadratic equation

$$2\,r_{\boldsymbol{S}}^2\,(|S_{\mathbf{11}}|^2 - 1) + 2\,r_S\,(|S_{\mathbf{11}}|^2 + 1) + (|S_{\mathbf{11}}|^2 - 1) = 0 \tag{3.48}$$

from which the normalized surface resistance $r_{\boldsymbol{S}}$ can be calculated. The offset

$$\Delta w = \frac{1}{2\,k_x} \arg\left(\frac{S_{\mathbf{11}}}{\Gamma_{\boldsymbol{S}}}\right) \tag{3.49}$$

is found by equating the phases of (3.47). With $r_{\boldsymbol{S}}$ and Δw the equivalent surface is completely determined. In general, these parameters depend only slightly on the angle of incidence. However, this effect can be studied with the given equations.

In the following, two via rows are combined to form the SIW. According to the offset of both equivalent surfaces, the width a of the equivalent waveguide is given by

$$a = w - 2\,\Delta w. \tag{3.50}$$

To further analyze the radiation losses, an equivalent circuit is given in Fig. 3.11. Here, because of the symmetry at $x = w/2$ and image theory, it is sufficient to analyze only one

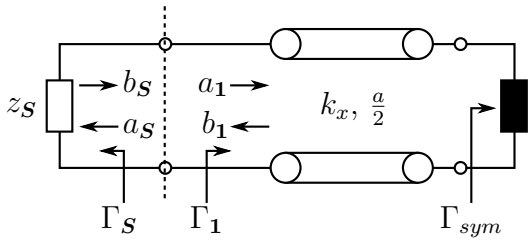

Figure 3.11: Transverse resonance equivalent circuit of the SIW arrangement.

half of the structure. The impedance z_S is connected to a transmission line of length $a/2$, which represents the inner side of the SIW and is terminated by a reflective load in the symmetry plane. The reflection coefficient of the latter is

$$\Gamma_{sym} = (-1)^{m_x - 1} = \begin{cases} 1, & \text{even mode,} \\ -1, & \text{odd mode.} \end{cases} \tag{3.51}$$

To find a solution, an eigenmode analysis of the equivalent circuit is carried out. This analysis is called TRM [111, 112]. For the analysis, the equivalent circuit is divided into two parts and the wave amplitudes are matched at the dashed interface. This yields the characteristic equation

$$1 - \Gamma_{\boldsymbol{S}}\,\Gamma_{\boldsymbol{1}} = 0 \qquad \text{with} \qquad \Gamma_{\boldsymbol{1}} = \Gamma_{sym}\,\mathrm{e}^{-\mathrm{j}\,2\,k_x\,a/2}. \tag{3.52}$$

To fulfill this equation, k_x becomes complex to account for the radiation losses and is given by

$$k_x = \frac{-\mathrm{j}}{a}\,\ln\left(\Gamma_{\boldsymbol{S}}\right) + \frac{m_x - 1}{a}\,\pi = \frac{2}{a}\,\mathrm{acot}\left(r_S\,(1 - \mathrm{j})\right) + \frac{m_x - 1}{a}\,\pi. \tag{3.53}$$

Finally, the attenuation constant α_r for the TE^z_{10}-mode can be determined from the wave number

$$k_z = -\mathrm{j}\gamma = \beta - \mathrm{j}\,\alpha_r = -\mathrm{j}\sqrt{k_x^2 - k_0^2}. \tag{3.54}$$

For calculating the via row offset Δw, previously a real wave number was assumed. For SIWs with small radiation losses, this is acceptable because the imaginary part of the wave number is very small. In a rigorous formulation, also the higher-order Floquet modes have to be considered. The multi-mode eigenvalue problem can be treated by the generalized transverse resonance method (GTRM) [113]. The influence of higher-order modes is more important for large pitches p and via diameters d, where the difference of the field patterns in the SIW and in the equivalent waveguide is more pronounced. However, as shown in [108], the results are sufficiently accurate for relevant SIWs. Nevertheless, the method could be expanded with the generalized scattering matrix (GSM) from Sec. A.2.

The properties of practically relevant SIW geometries are now further studied. Fig. 3.12a shows a contour diagram of the normalized offset $\Delta w/d$ versus the ratios p/d and w/p. For increasing ordinate values, the number of vias per length increases and, for increasing abscissa values, the gap between vias increases. The normalized offset depends mainly on p/d and only slightly on w/p. For $p/d = 1$, the vias touch each other and for $p/d \approx 3.7$ the offset is zero $\Delta w = 0$ ($a = w$). The offset ranges from $-0.2\,d$ to $0.4\,d$ for the studied parameters and the effective width ranges from $1.05\,w$ to $0.8\,w$. Fig. 3.12b depicts the normalized radiation losses α_r/k_0 for $k_0/k_c = 1.2$. They decrease for smaller p/d and larger w/p, since the gap between the vias decreases and, thus, the coupling between the guided modes and the leakage wave is reduced. For $\alpha_r/k_0 > 10^{-3}$, the radiated power is

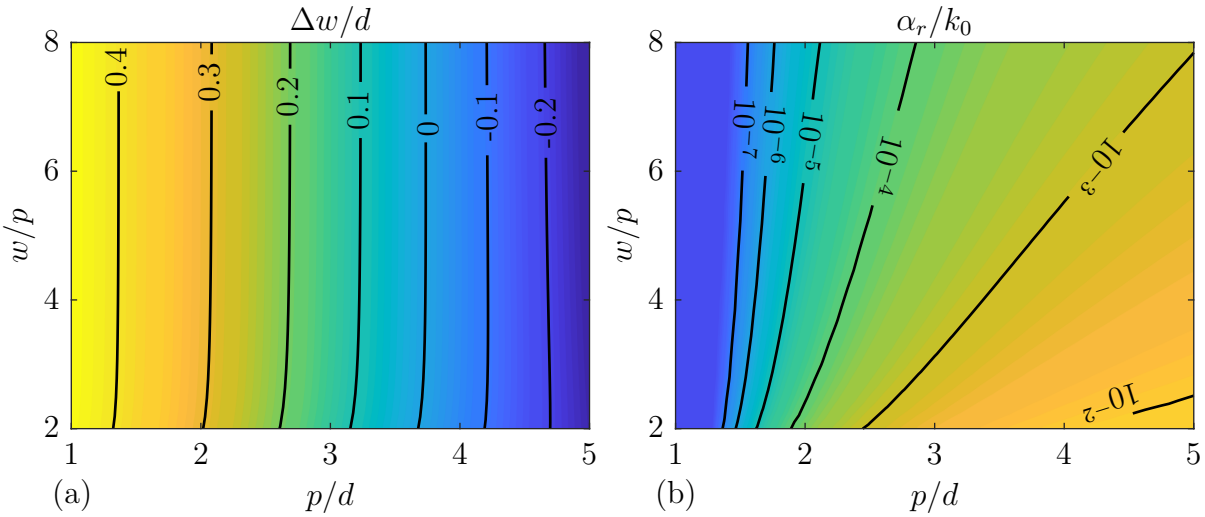

Figure 3.12: Contour diagram of (a) normalized offset $\Delta w/d$ and (b) radiation loss α_r/k_0 versus p/d and w/p ($k_0/k_c = 1.2$).

large enough for the design of leaky wave antennas [25]. When $\alpha_r/k_0 < 10^{-4}$, the radiation losses are smaller than the dielectric and the conductor losses for typical low-loss materials.

In general, the derived parameters depend on frequency, as depicted in Fig. 3.13. This effect is more pronounced for large pitches. In a periodic structure the first bandgap appears at $k_z\, p = \pi$. Thus, for $a/p > \sqrt{3}$, no bandgap appears for the fundamental TE^z_{10}-mode if $k_c \leq k_0 \leq 2\, k_c$. Some dispersion is apparent below the bandgap, as can be seen in Fig. 3.13a and Fig. 3.13b. However, this effect can be neglected for large values of a/p. Fig. 3.13c depicts the attenuation constant. It is relatively large near cutoff and decreases at higher frequencies, as it is typical for waveguides.

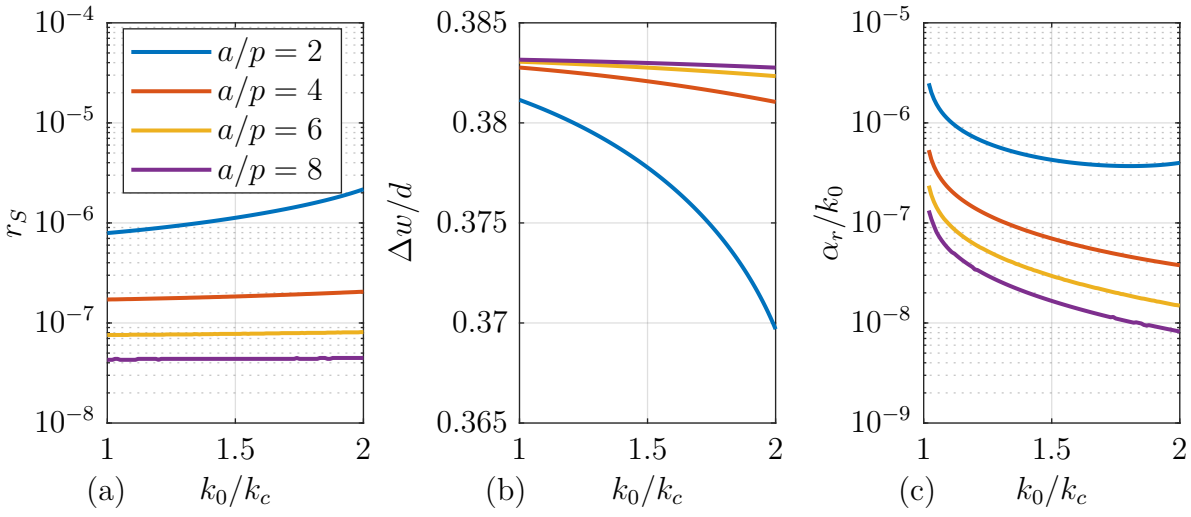

Figure 3.13: (a) Normalized surface resistance r_S, (b) normalized offset $\Delta w/d$, and (c) radiation loss α_r/k_0 versus k_0/k_x ($p/d = 1.5$).

The following constraints

$$p/d > 1, \tag{3.55a}$$

$$w/p > 2, \tag{3.55b}$$

$$\alpha_r/k_0 < 10^{-4}, \tag{3.55c}$$

and

$$w/p < 10 \tag{3.55d}$$

define the parameter range, where the SIW is almost equivalent to the conventional waveguide [108]. (3.55a) prohibits the vias from intersecting each other, (3.55b) precludes significant bandgap effects in the operating band, and (3.55c) constrains the maximum radiation loss. An additional constraint for the number of vias is given by (3.55d). It is not necessary from an electrical point of view, but limits the manufacturing effort. For the actual choice of SIW dimensions further aspects have to be considered. When designing adjacent components the isolation is often critical. It is ensured by a small via pitch and, thus, very low radiation losses. A slightly increased integration density can be achieved with small via diameters, because the total width $w + d$ is decreased.

Other higher-order TE^z- or TM^z-modes can also be studied with the presented method and suitable Floquet modes according to (3.43). In particular the TE^z_{01}-mode is interesting for this thesis. However, only a small part of the corresponding Floquet modes is reflected by the via rows and, thus, the wave is not properly guided. In contrast to the $\mathrm{TE}^z_{m_x0}$-modes, the surface current of the TE^z_{01}-mode in the equivalent surface has a longitudinal component, but in the via row only transverse currents can flow. This problem can be overcome in a multilayer PCB by using metal layers that connect the vias of each row in lateral direction.

3.3.2 Loss and Dispersion Mechanisms

The loss and dispersion of an SIW with rough surfaces are described by the complex propagation coefficient, as discussed in Sec. 3.2.2. For the fundamental TE_{10}-mode of the equivalent rectangular waveguide, the current integrals (3.38) can be calculated analytically and are given by

$$I' = \frac{2}{b}, \tag{3.56a}$$

and

$$I'' = \frac{2}{k_c^2}\left(\frac{2}{a} + \frac{1}{b}\right), \tag{3.56b}$$

which is consistent with [96, 101]. In this case, a constant surface impedance is assumed for all waveguide walls. In the following, it is calculated for the top and bottom metalization. For most practically relevant SIWs, the dielectric and conductor losses considerably

Table 3.2: Material parameters of typical high-frequency substrates (standard copper foils are printed in bold).

Substrate	ϵ_r	$\tan(\delta_d)$			Available Copper Foils
		10 GHz	20 GHz	30 GHz	
RO4835	3.48	0.0037	0.0041	–	**ED**, LoPro
RO4003C	3.38	0.0027	–	–	**ED**, LoPro
Megtron 6[1]	3.62	0.004	0.005	0.005	**RTF**, HVLP, HVLP2
Megtron 7[1]	3.60	0.003	0.0035	0.004	**RTF**, HVLP, HVLP2

[1] With 3313 electronic-grade glass fiber cloth.

exceed the radiation losses, which are thus neglected. In a rigorous analysis, the conductor loss of the via rows could be calculated from the actual current distribution, as outlined in Sec. A.2. It leads to a more complicated model and is beyond the scope of this work. Nevertheless, the model could be straightforwardly extended with different surface impedances for the walls.

In the following, the impact of rough surfaces is further studied considering typical high-frequency substrates. Tab. 3.2 lists some common substrates from *Rogers* (*RO4835*, *RO4003C*) and *Panasonic* (*Megtron 6*, *Megtron 7*). The dielectric core of these materials is composed of a woven glass fabric and a resin, yielding a similar dielectric constant of $\epsilon_r \approx 3.5$ for all listed materials. The *RO4003C* and *Megtron 7* materials have the lowest dielectric losses. For a standard substrate, the dielectric core is bonded to two copper foils. The substrates are available with different foils, the surface profiles of which depend on the manufacturing technology [114]. In general, the bonding strength for rougher foils is higher, but this yields higher losses for microwave applications. Tab. 3.3 lists the copper foils that are available for the considered materials. Commonly, the rougher side faces the dielectric. Here, the surface roughness ranges from 0.2 µm to 2.8 µm. The smooth outer side is roughened by various PCB manufacturing steps. For instance, an oxide treatment that is necessary for bonding multilayers increases the roughness of the outer side from $R_q \approx 0.3\,\mu\text{m}$ to about 0.6 µm [115].

As an example, a waveguide of width $a = 4.7\,\text{mm}$ and height $b = 0.5\,\text{mm}$ filled with *RO4003C* is considered. In Fig. 3.14a, the attenuation constant is plotted for different

Table 3.3: Surface roughness of typical high-frequency copper foils.

Copper Foil	Technology	Thickness	Surface Roughness R_q	
			Dielectric Side	Outer Side
ED	Electrodeposited	18 µm	∼2.8 µm	∼0.4 µm
LoPro	Low Profile Reverse Treated ED	18 µm	∼0.9 µm	∼0.8 µm
RTF	Reverse Treated ED	18 µm	∼0.5 µm	∼0.4 µm
HVLP	Hyper Very Low Profile	18 µm	∼0.3 µm	∼0.3 µm
HVLP2	Hyper Very Low Profile 2	18 µm	∼0.2 µm	∼0.3 µm

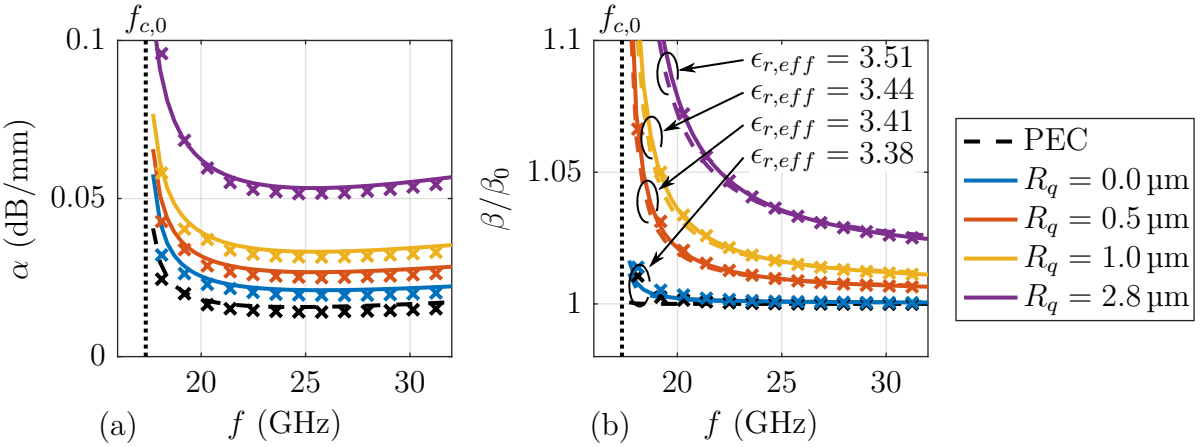

Figure 3.14: (a) Attenuation α and (b) normalized phase constant β/β_0 of the — equivalent circuit model, - - - effective permittivity model, and × full-wave simulation of an SIW with $w = 5.08\,\text{mm}$ ($a = 4.7\,\text{mm}$, $b = 0.5\,\text{mm}$, $\epsilon_r = 3.38$, $\tan(\delta_d) = 0.0027$, $\sigma_0 = 5.8 \cdot 10^7\,\text{S/m}$).

conductors. When the frequency decreases towards cutoff $f_{c,0}$, the group velocity decreases and, thus, the attenuation constant increases. For a waveguide with PEC walls, only dielectric loss is present and the attenuation constant is $\alpha \approx 0.016\,\text{dB/mm}$. For a smooth copper conductor, the losses increase to $\alpha \approx 0.022\,\text{dB/mm}$. In this case, the dielectric loss exceeds the conductor loss. For a rough surface, the attenuation constant increases to $\alpha \approx 0.027\,\text{dB/mm}$ and $\alpha \approx 0.055\,\text{dB/mm}$ for $R_q = 0.5\,\mu\text{m}$ and $R_q = 2.8\,\mu\text{m}$, respectively. Here, the conductor loss severely exceeds the dielectric loss. As a consequence, a low surface roughness can be more important than a low dielectric loss factor. At this point, it should be mentioned that $R_q = 2.8\,\mu\text{m}$ is the standard roughness of *RO4003C*, which is one of the commonly used substrates for microwave applications. Fig. 3.14b shows the influence of the different conductors on the phase constant. It is normalized to the phase constant of a waveguide with PEC walls. For the smooth copper conductor the phase constant differs only slightly, but the inner inductance increases with the surface roughness and, thus, the effect on the phase constant increases.

Furthermore, Fig. 3.14b shows the normalized phase constant of a waveguide with PEC walls, which is filled with a non-dispersive effective dielectric. Therefore, $\epsilon_{r,eff}$ is calculated from (3.41) at the frequency $1.5\,f_{c,0}$. This approximation is fairly good and can be used for a coarse component design. $\epsilon_{r,eff}$ increases for $R_q = 2.8\,\mu\text{m}$ by nearly 4 %. For comparison, Fig. 3.14 also shows full-wave simulation[2] results of a corresponding SIW. The agreement is good for both the attenuation and the phase constant.

In multilayer PCBs multiple substrates are bonded with prepreg[3] layers. The substrate and prepreg layers typically have a slightly different permittivity. Thus, the dielectric is

[2]Throughout this work, full-wave simulation is carried out in *CST Microwave Studio*, unless otherwise specified.

[3]Prepreg is a short form for pre-impregnated composite fibers.

not truly homogeneous. However, the static permittivity

$$\epsilon_r = \frac{h_1 + h_2}{h_1/\epsilon_{r,1} + h_2/\epsilon_{r,2}} \tag{3.57}$$

is a good approximation in this case [83, p. 392]. Here, h_1, h_2, $\epsilon_{r,1}$, and $\epsilon_{r,2}$ are the thicknesses and permittivities of these layers, respectively. It should be pointed out that the fundamental mode of an inhomogeneously filled rectangular waveguide is hybrid. However, as the dielectric contrast is typically relatively small, the effect is negligible.

Combining the concepts of an equivalent waveguide and the complex propagation constant of (3.39) gives a model for SIWs. This simple model is based on a rectangular waveguide with the effective width a and a complex propagation constant γ. In the following, it is used for the design of SIW components.

3.4 Mode Matching Method

Many microwave components can be efficiently described by an equivalent circuit using transmission lines and discontinuities. The transmission lines represent cylindrical waveguide sections and the discontinuities the connections to microwave circuits. The scattering parameters of these discontinuities can be calculated with the mode matching method. Early work on this approach goes back to 1941, where Hahn presented this approach for cavity resonators [116]. In 1944 Whinnery and Jamieson adapted this method for transmission line discontinuities [117]. Nowadays, the mode matching method is a standard tool for very efficient simulation of waveguide structures. Commercial implementations like *WASP-NET* from *Microwave Innovation Group* and *μWave Wizard* from *Mician* are available. A general overview can be found in [118].

Fig. 3.15 depicts a step discontinuity between two adjacent waveguides. The aim of the mode matching method is to satisfy the boundary conditions and to match the tangential field components in the common aperture $S_\mathbf{2}$. Here, it is assumed that the aperture $S_\mathbf{2}$ is part of $S_\mathbf{1}$. Using the modal expansion (3.21) of the two waveguides and the orthonormal

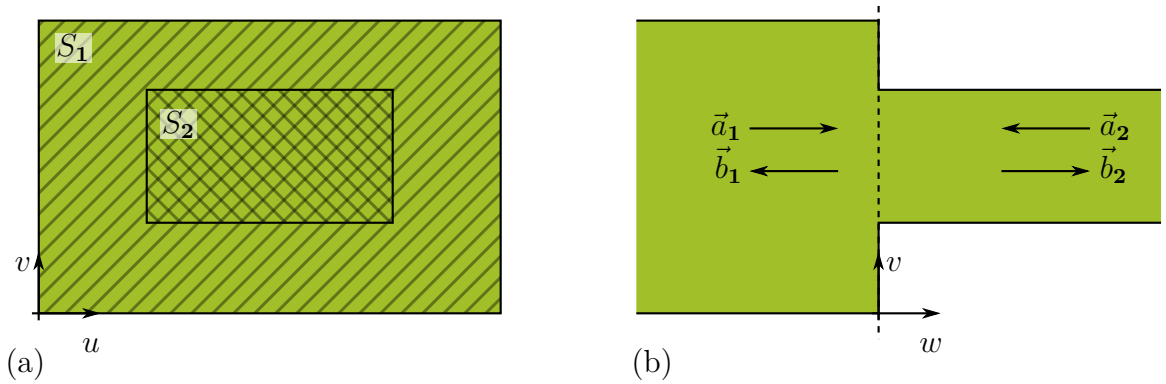

Figure 3.15: Cross-section of a step discontinuity in (a) the uv-plane and (b) the wv-plane.

relation (3.20), the mode matching equations are given by

$$\vec{V}_{\mathbf{1}}(0) = [C]\,\vec{V}_{\mathbf{2}}(0) \qquad \text{and} \qquad [C]^T\,\vec{I}_{\mathbf{1}}(0) = \vec{I}_{\mathbf{2}}(0) \tag{3.58}$$

in matrix notation. The modal voltages and currents are collected in the vectors $\vec{V}_{\boldsymbol{p}}$ and $\vec{I}_{\boldsymbol{p}}$, respectively. In the following, bold subscripts denote the corresponding waveguide port $\boldsymbol{p}$. The elements of the frequency independent coupling matrix are given by

$$C_{\mathbf{1}[m],\mathbf{2}[\bar{m}]} = \iint_{S_{\mathbf{2}}} \vec{e}_{uv,\mathbf{1}[m]}(u,v) \bullet \vec{e}_{uv,\mathbf{2}[\bar{m}]}(u,v)\, dS_{\mathbf{2}}. \tag{3.59}$$

With the incident wave amplitudes $\vec{a}_{\boldsymbol{p}}$ and the reflected wave amplitudes $\vec{b}_{\boldsymbol{p}}$, (3.58) can be written as

$$\left[\sqrt{Z_{\mathbf{1}}}\right](\vec{a}_{\mathbf{1}} + \vec{b}_{\mathbf{1}}) = [C]\left[\sqrt{Z_{\mathbf{2}}}\right](\vec{a}_{\mathbf{2}} + \vec{b}_{\mathbf{2}}) \tag{3.60a}$$

and

$$[C]^T\left[\sqrt{Y_{\mathbf{1}}}\right](\vec{a}_{\mathbf{1}} - \vec{b}_{\mathbf{1}}) = \left[\sqrt{Y_{\mathbf{2}}}\right](\vec{a}_{\mathbf{2}} - \vec{b}_{\mathbf{2}}) \tag{3.60b}$$

at the interface ($w_{\mathbf{1}} = w_{\mathbf{2}} = 0$) using (3.18). The impedance matrix $[Z_{\boldsymbol{p}}]$ and admittance matrix $[Y_{\boldsymbol{p}}]$ are diagonal with elements defined by (3.14). Rearranging (3.60) to the form of a GSM leads to

$$\vec{b} = [S]\,\vec{a} = \begin{bmatrix}\vec{b}_{\mathbf{1}}\\ \vec{b}_{\mathbf{2}}\end{bmatrix} = \begin{bmatrix}[S_{\mathbf{11}}] & [S_{\mathbf{12}}]\\ [S_{\mathbf{21}}] & [S_{\mathbf{22}}]\end{bmatrix}\begin{bmatrix}\vec{a}_{\mathbf{1}}\\ \vec{a}_{\mathbf{2}}\end{bmatrix}. \tag{3.61}$$

The submatrices are given by

$$[S_{\mathbf{11}}] = -[I] + [V]\,[S_{\mathbf{21}}], \tag{3.62a}$$

$$[S_{\mathbf{12}}] = [V]\,([I] + [S_{\mathbf{22}}]), \tag{3.62b}$$

$$[S_{\mathbf{21}}] = 2\,([I] + [V]^T[V])^{-1}[V]^T, \tag{3.62c}$$

and

$$[S_{\mathbf{22}}] = ([I] + [V]^T[V])^{-1}([I] - [V]^T[V]) \tag{3.62d}$$

with

$$[V] = \left[\sqrt{Y_{\mathbf{1}}}\right][C]\left[\sqrt{Z_{\mathbf{2}}}\right]. \tag{3.62e}$$

Here, $[I]$ is the unit matrix. The GSM is symmetric and self-inverting

$$[S] = [S]^T = [S]^{-1}, \tag{3.63}$$

which is advantageous for an efficient implementation. Further properties can be found in [119] and [120].

The number of modes on both sides of the discontinuity is important for the accuracy of the calculated scattering parameters. In particular, their ratio determines the convergence speed. The so-called relative convergence phenomenon is characteristic for the mode matching method. Fast convergence is achieved, when all higher-order modes up to

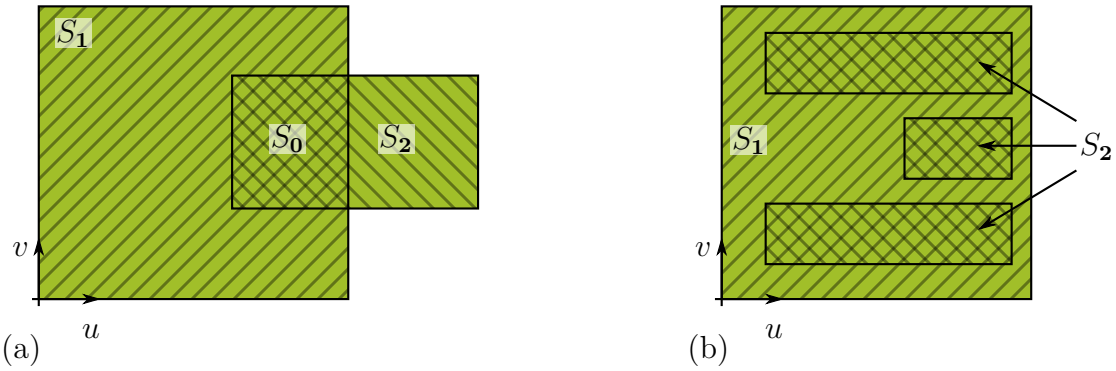

Figure 3.16: (a) Offset and (b) multi-port discontinuities.

a fixed cutoff frequency are included. For typical structures, accurate results are obtained for cutoff frequencies of 10 to 20 times the highest operating frequency [118, 119].

If the assumption that the aperture $S_\mathbf{2}$ is part of $S_\mathbf{1}$ is violated, (3.60) is in general linearly dependent [119] and the results are corrupted. In case the aperture $S_\mathbf{1}$ is part of $S_\mathbf{2}$, this limitation can be overcome by interchanging the waveguide ports. For the more general case of Fig. 3.16a, an intermediate cross-section $S_\mathbf{0} = S_\mathbf{1} \cap S_\mathbf{2}$ can be constructed and the single waveguide discontinuity is split into two discontinuities [121]. In this case $S_\mathbf{0}$ is part of $S_\mathbf{1}$ and $S_\mathbf{2}$. The resulting two scattering matrices $[S_A]$ and $[S_B]$ are cascaded using the general relation

$$[S_{\mathbf{11}}] = [S_{(A,\mathbf{11})}] + [S_{(A,\mathbf{12})}][S_{(B,\mathbf{11})}][Q][S_{(A,\mathbf{21})}], \tag{3.64a}$$

$$[S_{\mathbf{12}}] = [S_{(A,\mathbf{12})}]([I] + [S_{(B,\mathbf{11})}][Q][S_{(A,\mathbf{22})}])[S_{(B,\mathbf{12})}], \tag{3.64b}$$

$$[S_{\mathbf{21}}] = [S_{(B,\mathbf{21})}][Q][S_{(A,\mathbf{21})}], \tag{3.64c}$$

and

$$[S_{\mathbf{22}}] = [S_{(B,\mathbf{22})}] + [S_{(B,\mathbf{21})}][Q][S_{(A,\mathbf{22})}][S_{(B,\mathbf{12})}] \tag{3.64d}$$

with

$$[Q] = ([I] - [S_{(A,\mathbf{22})}][S_{(B,\mathbf{11})}])^{-1}. \tag{3.64e}$$

Furcations as depicted in Fig. 3.16b can be handled as generalized two-ports. In this case all the modes of the apertures in $S_\mathbf{2}$ are combined. Hence, the presented calculation scheme of the step discontinuity can also be used for multi-port discontinuities.

To add waveguide sections of length $w_\boldsymbol{p}$ to the GSM, the reference planes can be shifted using

$$[S'] = [T][S][T] \tag{3.65a}$$

with

$$[T] = \operatorname{diag}\left(\mathrm{e}^{-\mathrm{j}\beta_{\boldsymbol{p}[m]} w_\boldsymbol{p}}\right). \tag{3.65b}$$

By cascading discontinuities and waveguide sections, a huge class of waveguide and SIW components, as for example irises, transformers, filters, diplexers, and polarizers, can be

modeled [122]. In this process, one can differentiate between localized and accessible modes [123]. For higher-order modes below cutoff, the propagation coefficient β is imaginary and $\mathrm{e}^{-\mathrm{j}\beta w}$ can be very small. The accessible modes are above a threshold value of $\mathrm{e}^{-\mathrm{j}\beta w}$ and cause significant interaction with adjacent discontinuities. In contrast, localized modes remain confined to the neighborhood of the discontinuity and have no significant contribution at the ports. They can be considered as quasi lumped elements that store energy. The simulation time is reduced by considering only the accessible modes, when discontinuities are cascaded. The mentioned threshold value determines the accuracy of the model.

3.4.1 Parallel-Plate N-Furcation

The scattering parameters of a parallel-plate N-furcation are determined using the mode matching method. A common parallel-plate waveguide is split into multiple parallel-plate waveguides, as depicted in Fig. 3.17. The ports are labeled by an index $\boldsymbol{\rho}$ and have height $h_{\boldsymbol{\rho}}$ and the origin $y_{0,\boldsymbol{\rho}}$. TE^x- and TM^x-modes that propagate in $\pm x$-direction ($\theta = 0$) are assumed at the ports. The modes of the corresponding ports are labeled by $\boldsymbol{\rho}[\mu]$. According to (3.23) and (3.28) the scalar potential is given by

$$\Psi^{\pm}_{\boldsymbol{\rho}[\mu]}(x,y) = \frac{\mathrm{e}^{\mp\mathrm{j}\,k_{x,\boldsymbol{\rho}[\mu]}\,x}}{k_{y,\boldsymbol{\rho}[\mu]}} \begin{cases} \Psi_{c,\boldsymbol{\rho}[\mu]}(y), & \mathrm{TE}^x\text{-modes}, \\ \Psi_{s,\boldsymbol{\rho}[\mu]}(y), & \mathrm{TM}^x\text{-modes} \end{cases} \tag{3.66a}$$

and the modal electric fields are given by

$$\vec{e}_{yz,\boldsymbol{\rho}[\mu]}(y) = \begin{cases} -\Psi_{s,\boldsymbol{\rho}[\mu]}(y)\,\vec{u}_z, & \mathrm{TE}^x\text{-modes}, \\ -\Psi_{c,\boldsymbol{\rho}[\mu]}(y)\,\vec{u}_y, & \mathrm{TM}^x\text{-modes}. \end{cases} \tag{3.66b}$$

Based on these fields and (3.59), the elements of the coupling matrix are given by

$$C_{\mathbf{1}[\mu],\bar{\boldsymbol{\rho}}[\bar{\mu}]} = \int_{y_{0,\bar{\boldsymbol{\rho}}}}^{y_{0,\bar{\boldsymbol{\rho}}}+h_{\bar{\boldsymbol{\rho}}}} \vec{e}_{yz,\mathbf{1}[\mu]}(y) \bullet \vec{e}_{yz,\bar{\boldsymbol{\rho}}[\bar{\mu}]}(y)\,dy = \begin{cases} C^s_{\mathbf{1}[\mu],\bar{\boldsymbol{\rho}}[\bar{\mu}]}, & \mathrm{TE}^x\text{-modes}, \\ C^c_{\mathbf{1}[\mu],\bar{\boldsymbol{\rho}}[\bar{\mu}]}, & \mathrm{TM}^x\text{-modes}, \end{cases} \tag{3.67}$$

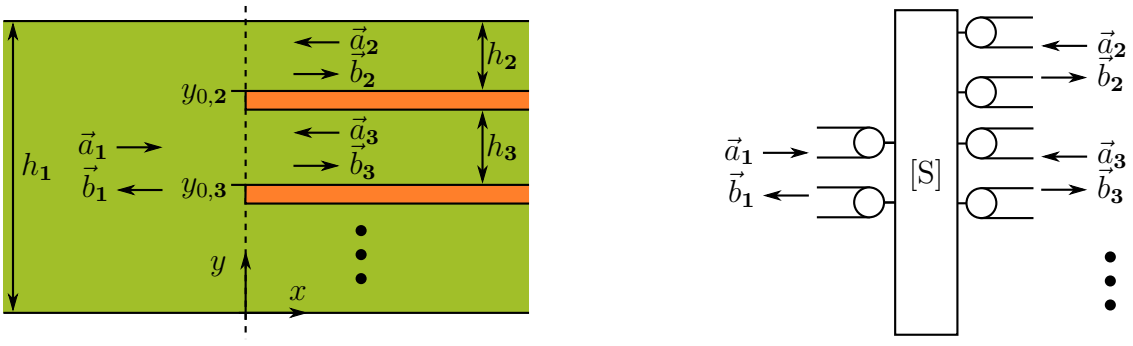

(a) (b)

Figure 3.17: (a) Cross-section and (b) equivalent circuit of parallel-plate N-furcation.

where the modes of the smaller waveguides are labeled $\bar{\boldsymbol{\rho}}[\bar{\mu}]$. The resulting analytical expressions are given in Sec. A.4.1. Finally, the scattering parameters are calculated from the coupling matrix $[C]$ using (3.62). Similar expressions are also reported in [124]. However, a different normalization and the conservation of complex power technique is used. Furthermore, the expressions of this work remove some singularities that need special attention in the implementation of [124].

3.5 Multilayer Substrate Integrated Waveguide

In an MSIW the metal layers are connected by via rows, as for the normal SIW. Fig. 3.18a shows an example with three metal layers and four via rows. The outer layers are continuous, whereas the middle layer has a gap. Fig. 3.18b depicts the cross-section of the MSIW. The equivalent waveguide is obtained by replacing the via rows by equivalent surfaces as previously discussed for the SIW. The offset Δw is determined in the same way as before (see Sec. 3.3.1). The field distribution is calculated from the equivalent waveguide with PEC walls, which is depicted in Fig. 3.18c.

Different MSIW structures have been proposed in the literature. Mostly they have counterparts in waveguide technology. Single- [125, 126] and double-ridged SIWs [127] are known for their large usable bandwidth and reduced size compared to normal SIWs. Folded SIWs [128] nearly halve the width of the arrangement, while retaining most of the SIW's properties. Even further size reduction is possible with folded half-mode SIWs [129]. Here, the symmetry plane is replaced by an open structure that approximates a magnetic wall. In [130], an SIW taper with a T-shaped cross-section, as depicted in Fig. 3.18b, is presented.

For the analysis of the equivalent waveguide, various numerical techniques are available. In this context, the finite element method (FEM) is one of the most popular techniques [131]. Here, the cross-section is typically discretized by means of small triangles. However, in this thesis a different semi-analytical technique is employed. Therefor, the cross-section is split into rectangular sections. The fields in each section can be charac-

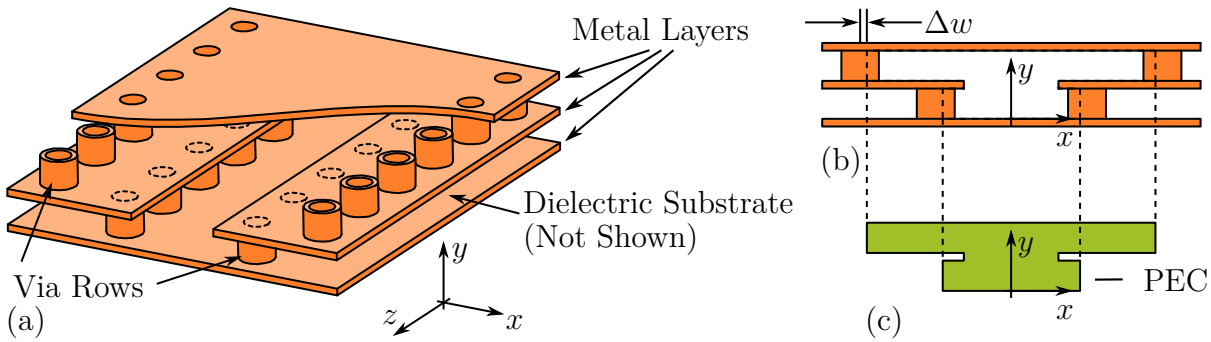

Figure 3.18: (a) Model and (b) cross-section of a MSIW. (c) Cross-section of the corresponding equivalent waveguide.

terized by only a few modes, which have to be matched at the interfaces between these sections. This approach has, for instance, been used for the analysis of ridged [132] and crossed rectangular waveguides [133]. In the following, the theory is modified and extended to the complete class of multilayer waveguides. It is based on an equivalent circuit representation for the cross-section and the modes are determined by the GTRM.

3.5.1 Equivalent Multilayer Waveguide

Each rectangular section ν has width w_ν and height h_ν, and can be interpreted as a parallel-plate waveguide with boundary conditions at $x_{(\nu,\boldsymbol{\rho})}$ ($\boldsymbol{\rho} = 1, 2$). Fig. 3.19a resumes the former example, with the symmetry plane being replaced by PMC for even and by PEC for odd modes. This structure is subdivided into three sections. Their ports are labeled by the tuple $(\nu, \boldsymbol{\rho})$. The scalar potential of the cross-section

$$\Psi_{PP,xy}(x,y) = K \sum_{\nu[\mu]} \frac{1}{k_{y,\nu[\mu]}} \begin{cases} I_{\nu[\mu]}(x)\, \Psi_{s,\nu[\mu]}(y), & \mathrm{TM}^x\text{-modes}, \\ V_{\nu[\mu]}(x)\, \Psi_{c,\nu[\mu]}(y), & \mathrm{TE}^x\text{-modes}, \end{cases} \tag{3.68a}$$

is expanded with respect to the TM^x- and TE^x-modes of the parallel-plate sections. The factor K is a constant to normalize the potential according to (3.20). The standing waves in y-direction are defined in Sec. 3.1.2 and the parallel-plate voltages and currents in x-direction are given by

$$V_{\nu[\mu]}(x) = \sqrt{Z_{x,\nu[\mu]}} \left(a_{(\nu,\mathbf{1}[\mu])}\, \mathrm{e}^{-\mathrm{j}\, k_{x,\nu[\mu]} \left(x - x_{(\nu,\mathbf{1})}\right)} + a_{(\nu,\mathbf{2}[\mu])}\, \mathrm{e}^{\mathrm{j}\, k_{x,\nu[\mu]} \left(x - x_{(\nu,\mathbf{2})}\right)} \right) \tag{3.68b}$$

and

$$I_{\nu[\mu]}(x) = \sqrt{Y_{x,\nu[\mu]}} \left(a_{(\nu,\mathbf{1}[\mu])}\, \mathrm{e}^{-\mathrm{j}\, k_{x,\nu[\mu]} \left(x - x_{(\nu,\mathbf{1})}\right)} - a_{(\nu,\mathbf{2}[\mu])}\, \mathrm{e}^{\mathrm{j}\, k_{x,\nu[\mu]} \left(x - x(\nu,\mathbf{2})\right)} \right). \tag{3.68c}$$

The incident wave amplitudes $a_{(\nu,\boldsymbol{\rho}[\mu])}$ are a set of constants that characterize the eigenmodes of the cross-section. They can be determined by adjusting the boundary conditions and a few are sufficient for a good approximation.

The scalar potential is a superposition of TM^x- or TE^x-modes that propagate in $\pm x$-direction. This can be represented by an equivalent circuit, as depicted in Fig. 3.19b

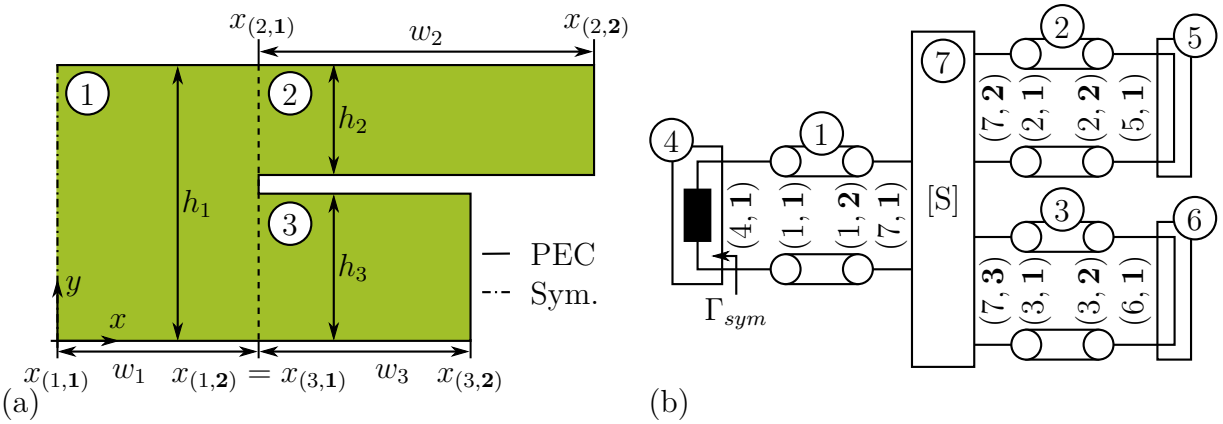

Figure 3.19: (a) Multilayer waveguide and (b) corresponding equivalent circuit.

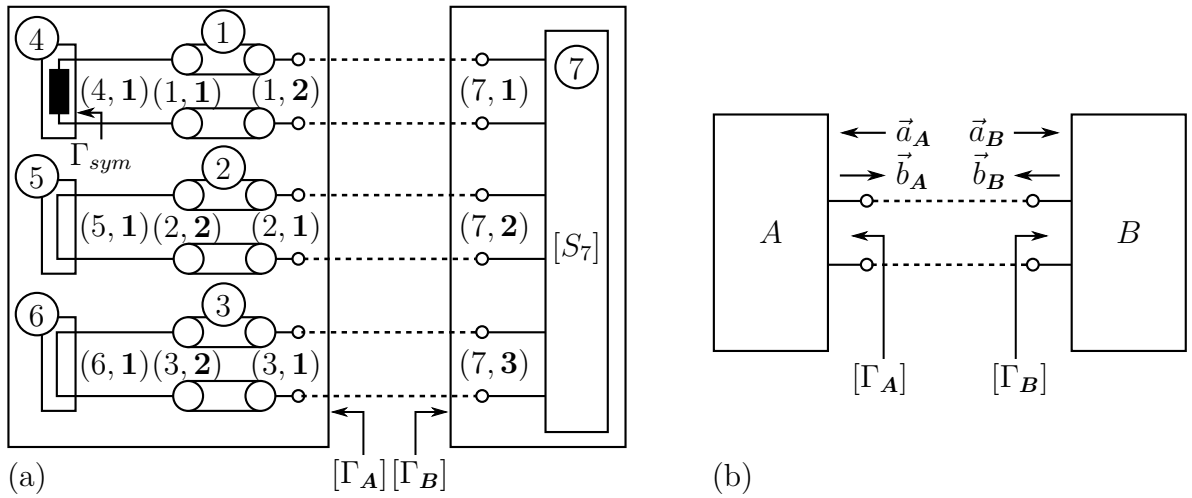

Figure 3.20: (a) Equivalent circuit and (b) generalized one-ports of a multilayer waveguide ($s_A = \{(1,2),(2,1),(3,1)\}$, $s_B = \{(7,1),(7,2),(7,3)\}$).

for the former example. Each section corresponds to a generalized transmission line that guides parallel-plate modes. The PEC and PMC boundary conditions correspond to short and open circuits, respectively. The furcation is described by scattering parameters, as discussed in Sec. 3.4.1. All components are numbered by a consecutive index ν, as depicted in Fig. 3.19b.

The wave amplitudes are determined from the equivalent circuit by an eigenmode analysis. For this, the circuit is split into two sub-circuits A and B. These are generalized one-ports, which combine the ports of the sets s_A and s_B, respectively. Fig. 3.20a shows a possible decomposition for the discussed example and Fig. 3.20b depicts the general case. A systematic calculation scheme to determine the reflection matrices $[\Gamma_A]$ and $[\Gamma_B]$ is detailed in Sec. A.3. The incident wave amplitudes $\vec{a}_A$ can be expressed using the reflection matrices by

$$\vec{a}_A = \vec{b}_B = [\Gamma_B]\,\vec{a}_B = [\Gamma_B]\,\vec{b}_A = [\Gamma_B]\,[\Gamma_A]\,\vec{a}_A, \tag{3.69}$$

which gives the eigenvalue equation

$$([I] - [\Gamma_B]\,[\Gamma_A])\,\vec{a}_A = [F(f)]\,\vec{a}_A = 0. \tag{3.70}$$

This class of equations is called nonlinear eigenvalue problems [134, 135]. A solution for the cutoff frequency f_c is found, when the matrix $[F(f)]$ is singular. This problem can be reduced to the scalar root finding problem given by

$$\det\left([F(f)]\right) = 0, \tag{3.71}$$

because the determinant must vanish for a singular matrix. This problem can be solved by standard algorithms, as, for example, the *Matlab* implementation of the trust-region dogleg method [136]. An initial value is required for the algorithm. The nullspace of $[F(f_c)]$ yields the unknown wave amplitudes $\vec{a}_A$. The wave amplitudes of the other components are calculated from circuit theory, as detailed in Sec. A.3. For the solution of nonlinear

eigenvalue problems, more involved algorithms have also been developed. A discussion of available numerical techniques can be found in [137]. The block Newton method [138], for example, is a robust way to calculate several eigenvalues and eigenvectors simultaneously. However, in the context of this thesis the simple algorithm based on (3.71) is sufficient.

The choice of ports $s_{\boldsymbol{A}}$ and $s_{\boldsymbol{B}}$ of the sub-circuits determines the stability of the problem. The radius of convergence is a measure for this stability. It is the largest difference between the initial value and the root. In general, good stability is achieved, when one port of each parallel-plate waveguide is selected, as in the discussed example. Instability can arise, for instance, when $s_{\boldsymbol{A}}$ contains only one port whose wave amplitudes are small. The matrix size of $[F(f)]$ increases with the number of selected ports. However, the calculation of the scattering parameters of the furcation dominates the computation time and, thus, the matrix size has only a minor influence on the total simulation time.

In the following, the scalar potential $\Psi_{PP,xy}(x,y)$ of the eigenmode analysis is used to determine the TE^z- and the TM^z-modes. The respective scalar potential is given by

$$\Psi^{\pm}(x,y,z) = \Psi_{xy}(x,y)\,\mathrm{e}^{\mp \mathrm{j}\,k_z\,z}. \tag{3.72a}$$

The exponential factor accounts for the propagation in z-direction, as discussed in Sec. 3.1. The modal potential

$$\begin{aligned}\Psi_{xy}(x,y) &= \frac{\mathrm{j}}{k_c}\,\frac{\partial \Psi_{PP,xy}(x,y)}{\partial y}\begin{cases}\left(-\sqrt{Z_0}\right), & \text{TE}^z\text{-mode/TM}^x\text{-modes},\\ \sqrt{Y_0}, & \text{TM}^z\text{-mode/TE}^x\text{-modes},\end{cases}\\ &= K\sum_{\nu[\mu]}\frac{\mathrm{j}}{k_c}\begin{cases}\left(-\sqrt{Z_0}\right)\,I_{\nu[\mu]}(x)\,\Psi_{c,\nu[\mu]}(y), & \text{TE}^z\text{-mode/TM}^x\text{-modes},\\ \left(-\sqrt{Y_0}\right)\,V_{\nu[\mu]}(x)\,\Psi_{s,\nu[\mu]}(y), & \text{TM}^z\text{-mode/TE}^x\text{-modes},\end{cases}\end{aligned} \tag{3.72b}$$

is proportional to the partial derivative of $\Psi_{PP,xy}(x,y)$ with respect to y. For the TE^z- or the TM^z-mode, the solution of the TM^x- or TE^x-problem must be used, respectively. With this definition, the modal electric field $\sqrt{Z_0}\,e_{xy}(x,y) = E_{PP}(x,y)$ of a TE^z-mode coincides with the electric field of the TM^x-modes and the modal magnetic field $\sqrt{Y_0}\,h_{xy}(x,y) = H_{PP}(x,y)$ of a TM^z-mode coincides with the magnetic field of the TE^x-modes. These relations are valid because the boundary conditions imposed by the geometry are satisfied in both cases.

The waveguide potential (3.72) completely specifies the modes. In the following, the corresponding modal fields and the normalization coefficient are calculated. The modal fields are determined from the potential (3.72) using (3.16). They can be written as

$$\vec{e}_{xy}(x,y) = \frac{K}{k_c}\sum_{\nu[\mu]}\vec{e}^{\,T}_{PP,\nu[\mu]}(y)\begin{cases}\begin{bmatrix}-\mathrm{j}\,k_{y,\nu[\mu]}\,\sqrt{Z_0}\,I_{\nu[\mu]}(x)\\ -k_c\,\sqrt{Y_0}\,V_{\nu[\mu]}(x)\end{bmatrix}, & \text{TE}^z\text{-mode},\\ \begin{bmatrix}k_c\,\sqrt{Z_0}\,I_{\nu[\mu]}(x)\\ \mathrm{j}\,k_{y,\nu[\mu]}\,\sqrt{Y_0}\,V_{\nu[\mu]}(x)\end{bmatrix}, & \text{TM}^z\text{-mode}\end{cases} \tag{3.73a}$$

and

$$\vec{h}_{xy}(x,y) = \vec{u}_z \times \vec{e}_{xy}(x,y) \tag{3.73b}$$

with the parallel-plate field

$$\vec{e}^{\,T}_{PP,\nu[\mu]}(y) = \left[\Psi_{s,\nu[\mu]}(y)\,\vec{u}_x \quad \Psi_{c,\nu[\mu]}(y)\,\vec{u}_y\right]. \tag{3.73c}$$

The modal electric field can be further rearranged to a condensed matrix notation

$$\vec{e}_{xy}(x,y) = K \sum_{\nu[\mu]} \vec{e}^{\,T}_{PP,\nu[\mu]}(y)\,[A_{\nu[\mu]}] \begin{bmatrix} \mathrm{e}^{-\mathrm{j}\,k_{x,\nu[\mu]}\,(x-x_{(\nu,\mathbf{1})})} \\ \mathrm{e}^{\mathrm{j}\,k_{x,\nu[\mu]}\,(x-x_{(\nu,\mathbf{2})})} \end{bmatrix} \tag{3.74a}$$

with the amplitude matrix

$$[A_{\nu[\mu]}] = \frac{1}{\sqrt{k_{x,\nu[\mu]}\,k_c}} \begin{cases} \begin{bmatrix} -\mathrm{j}\,k_{y,\nu[\mu]}\,a_{(\nu,\mathbf{1}[\mu])} & \mathrm{j}\,k_{y,\nu[\mu]}\,a_{(\nu,\mathbf{2}[\mu])} \\ -k_{x,\nu[\mu]}\,a_{(\nu,\mathbf{1}[\mu])} & -k_{x,\nu[\mu]}\,a_{(\nu,\mathbf{2}[\mu])} \end{bmatrix}, & \mathrm{TE}^z\text{-mode}, \\ \begin{bmatrix} k_{x,\nu[\mu]}\,a_{(\nu,\mathbf{1}[\mu])} & -k_{x,\nu[\mu]}\,a_{(\nu,\mathbf{2}[\mu])} \\ \mathrm{j}\,k_{y,\nu[\mu]}\,a_{(\nu,\mathbf{1}[\mu])} & \mathrm{j}\,k_{y,\nu[\mu]}\,a_{(\nu,\mathbf{2}[\mu])} \end{bmatrix}, & \mathrm{TM}^z\text{-mode}. \end{cases} \tag{3.74b}$$

This notation is very compact and simplifies the further calculation with the modal fields. The normalization coefficient K is calculated from (3.20) by an integration over the cross-section S

$$\begin{aligned} K^{-2} &= K^{-2} \underbrace{\iint_S \vec{e}_{xy}(x,y) \bullet \vec{e}_{xy}(x,y)\,dS}_{=1} \\ &= \sum_{\nu[\mu]} \begin{bmatrix} 1 & 1 \end{bmatrix} \left([C_{x,\nu[\mu],\nu[\mu]}] \circ \left([A_{\nu[\mu]}]^T\,[A_{\nu[\mu]}] \right) \right) \begin{bmatrix} 1 & 1 \end{bmatrix}^T. \end{aligned} \tag{3.75}$$

The operator $\circ$ stands for an element-wise matrix multiplication (Hadamard product). Due to the orthonormality of the $\vec{e}_{PP,\nu[\mu]}(y)$, the integration in y-direction results in a simple sum over all components and modes. The integration in x-direction is expressed by the coupling matrix

$$[C_{x,\nu[\mu],\nu[\mu]}] = \int_{x_{(\nu,\mathbf{1})}}^{x_{(\nu,\mathbf{2})}} \begin{bmatrix} \mathrm{e}^{-\mathrm{j}\,k_{x,\nu[\mu]}\,(x-x_{(\nu,\mathbf{1})})} \\ \mathrm{e}^{\mathrm{j}\,k_{x,\nu[\mu]}\,(x-x_{(\nu,\mathbf{2})})} \end{bmatrix} \begin{bmatrix} \mathrm{e}^{-\mathrm{j}\,k_{x,\nu[\mu]}\,(x-x_{(\nu,\mathbf{1})})} \\ \mathrm{e}^{\mathrm{j}\,k_{x,\nu[\mu]}\,(x-x_{(\nu,\mathbf{2})})} \end{bmatrix}^T dx. \tag{3.76}$$

Sec. A.4.2 provides analytical solutions of the coupling matrix $[C_{x,\nu[\mu],\nu[\mu]}]$ in a generalized form. For this case, $\bar{\nu} = \nu$ and $\bar{\mu} = \mu$ must be chosen.

The modal field solutions of the lossless waveguide can be used to approximate the complex propagation constant of a lossy waveguide with rough conductors, as discussed in Sec. 3.2.2. The solutions of the current distribution integrals are listed in Sec. A.4.3.

3.5.2 Synthesis of Multilayer Waveguides

One further major advantage of the presented method appears when synthesizing multilayer waveguides with a predefined cutoff frequency f_c. Suitable cross-sections are determined by adjusting the width $w_{\hat{\nu}}$ of the parallel-plate waveguide $\hat{\nu}$. For this purpose,

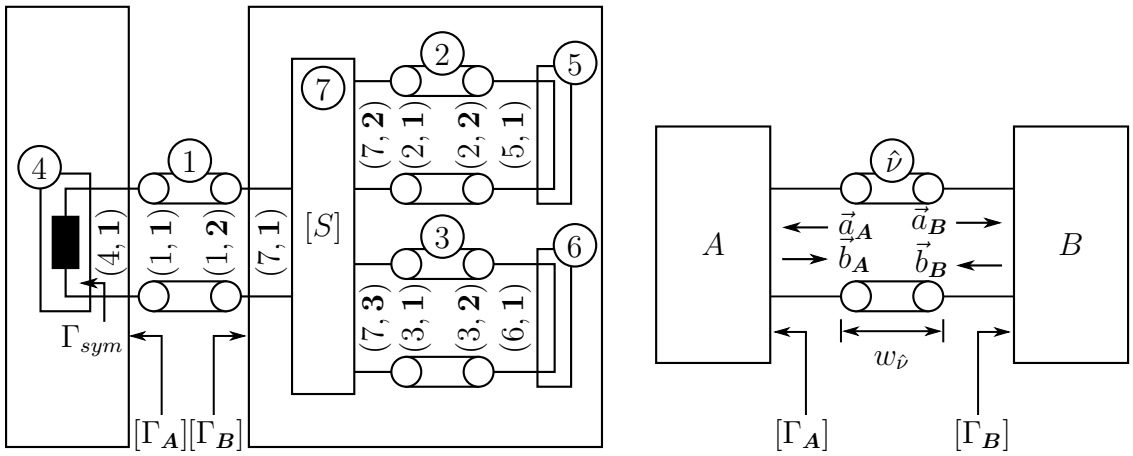

Figure 3.21: (a) Equivalent circuit and (b) generalized one-ports of a multilayer waveguide with isolated parallel-plate waveguide ($s_A = \{(1, \mathbf{1})\}$, $s_B = \{(1, \mathbf{2})\}$).

waveguide $\hat{\nu}$ is considered and its ports are terminated with the reflection matrices $[\Gamma_A]$ and $[\Gamma_B]$. Fig. 3.21a depicts the previously discussed example for $\hat{\nu} = 1$ and Fig. 3.21b shows the general case. The transmission from one port of the parallel-plate waveguide to the other is given by the matrix $[T]$, as defined in (3.65b). The reflected wave amplitudes $\vec{b}_A$ can be expressed with the reflection and transmission matrices as

$$\vec{b}_A = [\Gamma_A]\,\vec{a}_A = [\Gamma_A]\,[T]\,\vec{b}_B = [\Gamma_A]\,[T]\,[\Gamma_B]\,\vec{a}_B = [\Gamma_A]\,[T]\,[\Gamma_B]\,[T]\,\vec{b}_A, \tag{3.77}$$

which gives the nonlinear eigenvalue equation

$$([I] - [\Gamma_A]\,[T]\,[\Gamma_B]\,[T])\,\vec{b}_A = [F(w_{\hat{\nu}})]\,\vec{b}_A = 0. \tag{3.78}$$

The problem can be solved for the width $w_{\hat{\nu}}$ in the same way as the problem in (3.70). Furthermore, the reflection matrices must only be determined once, thus the synthesis is very efficient.

3.5.3 Multilayer Waveguide Discontinuity

Multilayer waveguides are generally cascaded to realize complex components. In the following, the properties of the associated discontinuities are determined using the mode matching method. Fig. 3.22 picks up the former example. The waveguides have the cross-sections S_1 and S_2 and it is assumed that S_2 is part of S_1. The coupling coefficients are calculated by integrating the modal fields over S_2. Here, it is distinguished between different parallel-plate and furcation regions. In a parallel-plate region ($\nu = 1, 2, 3$), the parallel plates are continuous in z-direction. In the furcation region ($\nu = 7$), a parallel-plate waveguide is split into multiple parallel-plate waveguides in z-direction. The waveguide modes $\mathbf{1}[m]$ and $\mathbf{2}[\bar{m}]$ are represented by a superposition of the parallel-plate modes with the indices $\boldsymbol{\rho}[\mu]$ and $\bar{\boldsymbol{\rho}}[\bar{\mu}]$, respectively. With this, the coupling coefficients result from the

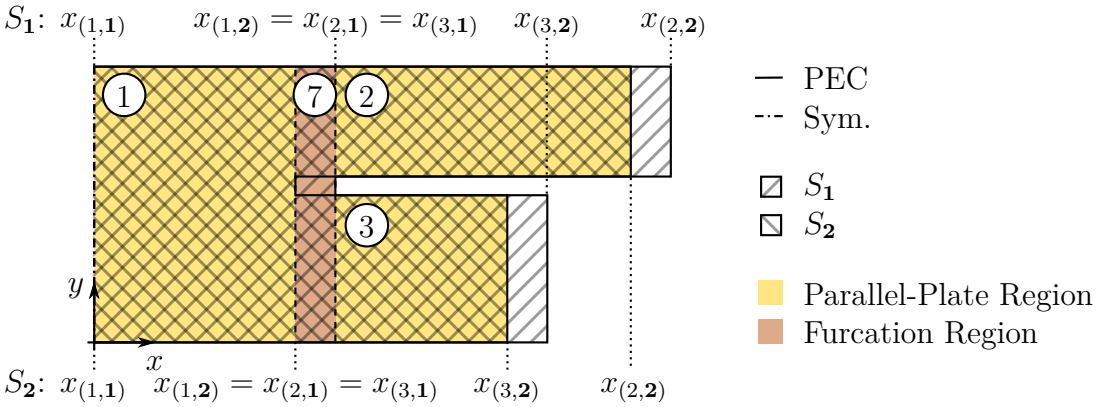

Figure 3.22: Cross-section of a multilayer waveguide discontinuity.

integral

$$
\begin{aligned}
C_{\mathbf{1}[m],\mathbf{2}[\bar{m}]} &= \iint_{S_\mathbf{2}} \vec{e}_{xy,\mathbf{1}[m]}(x,y) \bullet \vec{e}_{xy,\mathbf{2}[\bar{m}]}(x,y)\, dS_\mathbf{2} \qquad (3.79)\\
&= \sum_{\nu[\mu]} \begin{bmatrix} 1 & 1 \end{bmatrix} \left([C_{x,\nu[\mu],\bar{\nu}[\bar{\mu}]} \circ \left([A_{\nu[\mu]}]^T \, [A_{\bar{\nu}[\bar{\mu}]}] \right) \right) \begin{bmatrix} 1 & 1 \end{bmatrix}^T \\
&\quad + \sum_{\nu[\mu],\bar{\nu}[\bar{\mu}]} \begin{bmatrix} 1 & 1 \end{bmatrix} \left([C_{x,\nu[\mu],\bar{\nu}[\bar{\mu}]} \circ \left([A_{\nu[\mu]}]^T \, [C_{y,\nu[\mu],\bar{\nu}[\bar{\mu}]}] \, [A_{\bar{\nu}[\bar{\mu}]}] \right) \right) \begin{bmatrix} 1 & 1 \end{bmatrix}^T .
\end{aligned}
$$

The first sum accounts for the parallel-plate regions, where the parallel-plate modes are orthogonal and, thus, a simple sum over the sections and modes is sufficient. Here, the indices of $S_\mathbf{2}$ are given by $\bar{\nu} = \nu$ and $\bar{\mu} = \mu$. The furcation regions contribute through the second sum. The parallel-plate modes are coupled and a summation over all mode combinations is necessary. For convenience, the waveguide mode indices are omitted for parallel-plate values. The integration in x-direction is given in matrix notation by

$$
[C_{x,\nu[\mu],\bar{\nu}[\bar{\mu}]}] = \int_{x_\mathbf{1}}^{x_\mathbf{2}} \begin{bmatrix} \mathrm{e}^{-\mathrm{j}\, k_{x,\nu[\mu]}\, (x - x_{(\nu,\mathbf{1})})} \\ \mathrm{e}^{\mathrm{j}\, k_{x,\nu[\mu]}\, (x - x_{(\nu,\mathbf{2})})} \end{bmatrix} \begin{bmatrix} \mathrm{e}^{-\mathrm{j}\, k_{x,\bar{\nu}[\bar{\mu}]}\, (x - x_{(\bar{\nu},\mathbf{1})})} \\ \mathrm{e}^{\mathrm{j}\, k_{x,\bar{\nu}[\bar{\mu}]}\, (x - x_{(\bar{\nu},\mathbf{2})})} \end{bmatrix}^T dx \qquad (3.80)
$$

and analytical expressions are listed in Sec. A.4.2. For the furcation regions, the integration in y-direction is given by

$$
[C_{y,\nu[\mu],\bar{\nu}[\bar{\mu}]}] = \int_{y_{0,\bar{\nu}}}^{y_{0,\bar{\nu}}+h_{\bar{\nu}}} \vec{e}_{PP,\nu[\mu]}(y) \bullet \vec{e}_{PP,\bar{\nu}[\bar{\mu}]}(y)\, dy = \begin{bmatrix} C^s_{(\hat{\nu},\mathbf{1}[\mu],\hat{\boldsymbol{\rho}}[\bar{\mu}])} & 0 \\ 0 & C^c_{(\hat{\nu},\mathbf{1}[\mu],\hat{\boldsymbol{\rho}}[\bar{\mu}])} \end{bmatrix} . \qquad (3.81)
$$

This results in similar integrals as for the parallel-plate N-furcations that are reported in (A.30). The furcation has the index $\hat{\nu}$ and the large parallel-plate port $(\hat{\nu}, \mathbf{1})$ of the furcation is always the parallel-plate port $(\nu, \boldsymbol{\rho})$ of waveguide **1**. The small parallel-plate ports $(\hat{\nu}, \hat{\boldsymbol{\rho}})$ of the furcation must coincide with the parallel-plate ports $(\bar{\nu}, \bar{\boldsymbol{\rho}})$ of waveguide **2**. The scattering parameters can be directly calculated from the coupling coefficients using (3.62).

The assumption that $S_\mathbf{2}$ is part of $S_\mathbf{1}$ is of course not always satisfied. The general discontinuity can be solved by swapping the ports or by using an intermediate cross-section, as discussed in Sec. 3.4.

4 Design of Substrate Integrated Waveguide Components

This chapter discusses concepts, models, and design procedures for SIW components. First, SIW transitions are presented and compared to each other. Then, the septum polarizer is designed to excite circular polarization in the square SIWs. These components are the basic building blocks for the Rx/Tx integrated lens array antenna introduced in Sec. 2.7.

4.1 Transitions

Transitions connect different types of transmission lines. In PCB technology, microstrip lines and coplanar waveguides (CPWs) are typically used as planar transmission lines. They allow for an easy integration of SMD components. In this work, the substrate of the CPW is always backed by a metal plane. This arrangement is known as grounded or conductor-backed-coplanar waveguide. However, for simplicity, it is called CPW in the following. To feed an SIW, several transitions from planar transmission lines are known [17–19, 139–141]. CPWs are compatible with ground-signal-ground wafer probes, which allow for allows easy and accurate measurements. Thus, in this work, CPW-to-SIW transitions are used to feed SIW components. Here, a slightly modified version of the transition proposed in [17] is employed. Good matching over the full waveguide band is achieved. For completeness, the geometry of optimized transitions is given in Sec. B.4. A detailed description of the transition is omitted and can be found in [17].

This section deals with transitions that connect different SIW or MSIW cross-sections. The presented transitions change the height of SIWs. The first and the second transition are used to connect the SIWs of the standard PCB with the thicker SIWs of the antenna element (see. Sec. 2.7). Additionally, a third transition is introduced, which connects different SIWs in a multilayer PCB.

4.1.1 Stepped Transition

A stepped transition in SIW technology is presented in this section [142, 143]. It changes the height of an SIW using several steps, as depicted in Fig. 4.1. For the SIW antenna

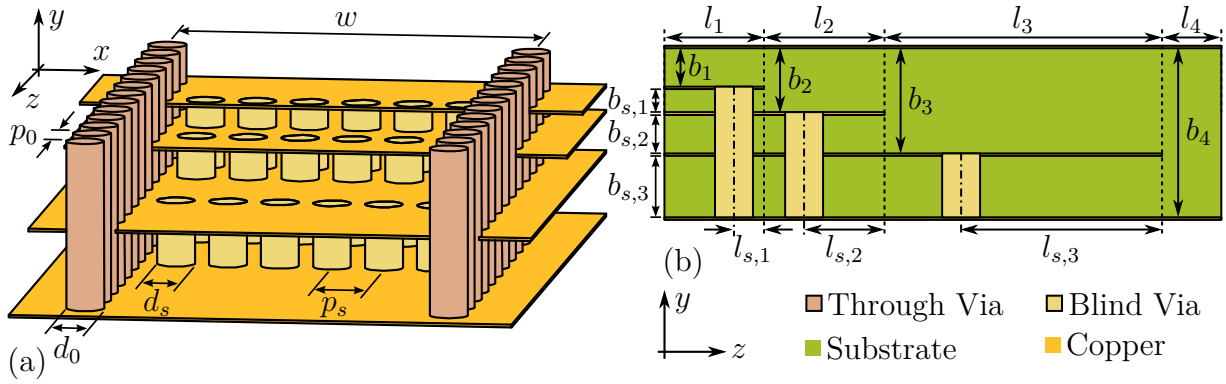

Figure 4.1: (a) Model and (b) cross-section of the stepped transition in SIW technology.

concept, it is used to increase the height from a standard to a full-height SIW. Two stacked full-height SIWs then feed the septum polarizer of the antenna element.

In general, the excitation of full-height SIWs is challenging. If it is directly excited by a microstrip transition, the high substrate thickness enables propagation of higher-order microstrip modes. If a CPW transition is used, a major part of the field is concentrated in the slots between the conductors on the substrate surface, making an excitation of a full-height SIW challenging. For small or moderate substrate thicknesses, CPW-to-SIW transitions as given in Sec. B.4 can be used. For full-height SIWs, narrowband transitions have been demonstrated in [26]. However, for the Rx/Tx antenna element, a broad- or dual-band solution is necessary. In the following, a dual-band solution is implemented as a stepped transition. The transition for the Tx-only element is relatively simple due to the single-band operation and is therefore not discussed.

Modeling the Transition

For an equivalent circuit model, a three-step transition is split into four SIW sections with increasing heights b_n. The steps consist of E-plane bifurcations, where one port is connected to an SIW section terminated by a transverse via row. The SIW sections are modeled by multimode transmission lines and the bifurcations by generalized three-port discontinuities, as depicted in Fig. 4.2. The steps are a combination of the bifurcations and the terminated SIW sections, which are modeled by short circuited stub lines. Thus, a step is a generalized two-port and can be tuned by varying the length $l_{s,n}$ of the shorted

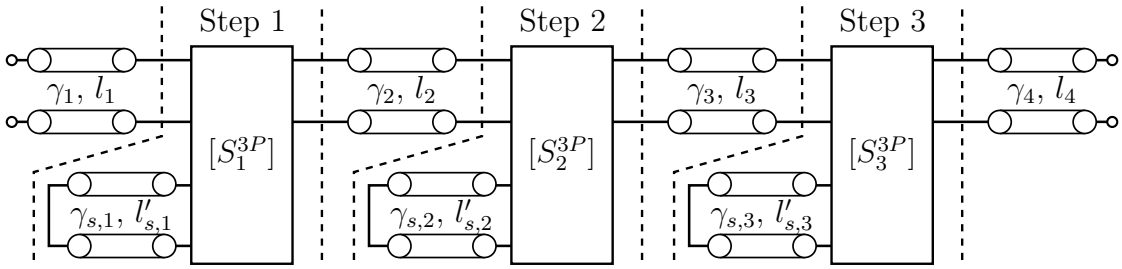

Figure 4.2: Equivalent circuit of the stepped transition.

stubs (see Fig. 4.1b). With a standard definition (e.g., power-voltage, power-current), the characteristic impedance of the fundamental mode is proportional to the SIW height [144, p. 227]. Thus, the impedances of the input, intermediate, and output SIW sections increase stepwise and the transition is a stepped-impedance transformer. In the following, the individual parts of the transition are analyzed.

The SIW sections are modeled by rectangular waveguides. The effective width a is calculated from the via row distance w, the via diameter d, and the via pitch p, as discussed in Sec. 3.3.1. The lengths l_n and $l_{s,n}$ of the sections are degrees of freedom to adjust the frequency response. The complex propagation constants γ_n and $\gamma_{s,n}$ of the SIW sections are obtained from (3.39) and depend on the effective width (a), the SIW heights (b_n, $b_{s,n}$), the dielectric properties of the substrate (ϵ_r, $\tan(\delta_d)$), and the properties of the copper foils (σ_0, R_q).

The stub lines are terminated by rows of vias with diameter d_s and pitch p_s, as depicted in Fig. 4.3a. They are modeled as a short circuit in a shifted equivalent plane. This offset is similar to that for an SIW via row, as discussed in Sec. 3.3.1. The only difference is that the angle of incidence is rotated by $\theta' = \theta + 90°$. Thus, the propagation angle changes from $\cos(\theta) = k_c/k_0$ to $\cos(\theta') = \beta/k_0$. However, for a high via density (e.g., $a/p_s \geq 5$), this effect can be neglected, as illustrated in Fig. 3.13, and a frequency independent offset Δl_s can be used for the equivalent circuit. The effective length of the stub is then given by

$$l'_{s,n} = l_{s,n} - \Delta l_s. \tag{4.1}$$

The accuracy of this model is verified by full-wave simulation of the via row in a lossless effective waveguide. The effective offset of a shorted SIW stub with six vias is plotted versus d_s/p_s in Fig. 4.3b. The full-wave simulation and the model differ by less than 1 % for $d_s/p_s > 0.4$. The offset increases for larger vias with same pitch. For comparison, the effective offset is calculated with an empirical equation from [106]. As this equation yields a significant difference for some cases, the via array model is used in the following.

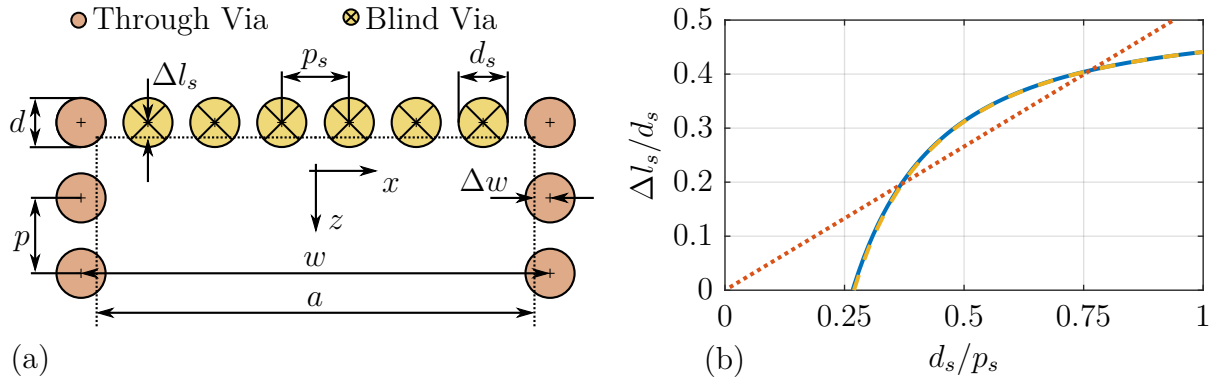

Figure 4.3: Effective offset of a via row (— via array model, - - - full-wave simulation, ···· empirical equation).

The GSM of the E-plane bifurcations $[S_n^{3P}]$ is calculated by the mode matching method, as discussed in Sec. 3.5.3. For this purpose, the two stacked SIWs on the left-hand side are combined to a single generalized port with the modes of both SIWs (see Fig. 3.16b). Due to the symmetry of the stepped transition, the fundamental TE_{10}-mode excites only TE_{1m}-modes at the discontinuities. In [142] and [143] the scattering parameters of the bifurcations are determined by full-wave simulation and only the fundamental modes are considered in the equivalent circuit. The attenuation $\exp(-\alpha_n l_n)$ and $\exp(-\alpha_{s,n} l_{s,n})$ of higher-order evanescent modes is relatively high and, thus, these modes can be considered as localized and the coupling across SIW sections can be neglected. However, the mode matching method provides the GSMs of the bifurcations and a treatment of the complete mode sets increases the accuracy. In addition, the full-wave simulation is time-consuming compared to the mode matching method.

Design and Realization

To implement the transition, the Rogers *RO4000* series of high-frequency laminates is chosen. The used multilayer stack is sketched in Fig. 4.4 and the used layer thicknesses h_n are listed in Tab. 4.1. The stack is manufactured using standard PCB processes. Here, three bond cycles with two, one, and again two prepreg sheets are used, respectively. The *RO4003C* substrate and the *RO4450* prepreg with thickness of 0.102 mm have a dielectric constant of $\epsilon_r = 3.38$ and $\epsilon_r = 3.52$, respectively. The laminates are bonded with copper foils and a surface roughness of $R_q = 2.8\,\mu\mathrm{m}$ is assumed for all copper surfaces. The effective dielectric constant of the SIW sections ranges from $\epsilon_{r,eff} = 3.47$ to 3.76 (see (3.41) and (3.57)). Here, also the inhomogeneous multilayer stack is taken into account. The simulation is carried out with and without losses. In the first case, the rough copper foils and the dielectric losses are considered. In the second case, the dielectric losses and the surface resistance R_S are set to zero. The SIW parameters are chosen to $d = 0.5\,\mathrm{mm}$, $p = 0.7\,\mathrm{mm}$, and $w = 4.85\,\mathrm{mm}$. This corresponds to an effective width of $a = 4.47\,\mathrm{mm}$ and a cutoff frequency of $f_c = 17.8\,\mathrm{GHz}$. The shorted stubs are terminated by rows of six vias with a diameter of $d_s = 0.5\,\mathrm{mm}$. This results in an offset of $\Delta l_s = 0.19\,\mathrm{mm}$. The total laminate thickness is chosen to be $b_4 \approx a/2$ to later obtain a full-height SIW.

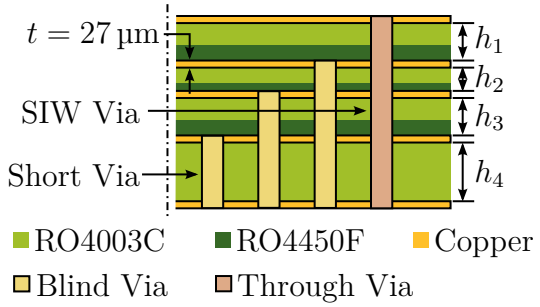

Figure 4.4: Stack of the transition.

Table 4.1: Parameters of the transition.

n	h_n (mm)	b_n (mm)	$b_{s,n}$ (mm)	l_n (mm)	$l_{s,n}$ (mm)
1	0.48	0.48	0.28	1.84	0.42[1]
2	0.28	0.78	0.48	1.59[1]	1.08[1]
3	0.48	1.29	0.81	3.67[1]	2.68[1]
4	0.81	2.13	-	4.79	-

[1] Optimized parameter.

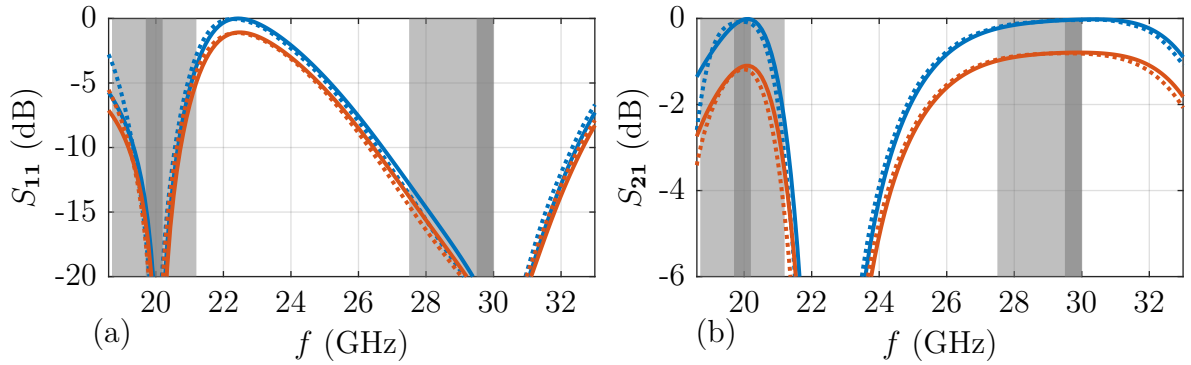

Figure 4.5: Scattering parameters of the three-step SIW transition (— mode matching, ···· full-wave simulation, — lossless, — lossy, ■ typical / ■ reference bands).

The equivalent circuit model is used for the optimization of the three-step transition. Tab. 4.1 summarizes the optimized lengths for a dual-band transition. The scattering parameters of the equivalent circuit model are compared to full-wave simulation of the actual SIW structure. As depicted in Fig. 4.5, the results agree well in both the lossless and the lossy case. They even fully agree if, in the lossless case, the equivalent waveguide structure is simulated instead of the SIW.

The lower and the upper passband exhibit an input reflection of less than −10 dB from 19.2 GHz to 20.6 GHz and from 26.3 GHz to 32.5 GHz, respectively. Thus, the transition is suitable for the reference Rx and Tx frequency bands. The typical and the reference bands, as defined in Chapter 1, are marked in light and dark gray, respectively. The insertion loss is about 1.1 dB in the lower and 0.8 dB in the upper frequency band. The total length of the transition is 11.9 mm including the first and the last SIW sections and 5.3 mm without them.

The transition is realized for validation purposes. It is fabricated in a back-to-back arrangement and CPW-to-SIW transitions are added for probing (see *CPW-SIW7* in Tab. B.5). The manufactured back-to-back transition is depicted in Fig. 4.6. It consists of the CPW line, the standard SIW, and the three-step transition. Fig. 4.7 reports the simulated and the measured scattering parameters. The measurements are performed with wafer probes and a network analyzer. A thru-reflect-line (TRL) calibration [145, 146] shifts the reference planes to the standard SIWs. Again, the results of the equivalent circuit model and of the full-wave simulation of the SIW transition agree well. Measurements and simulation yield similar results, but deviations are visible. For the input

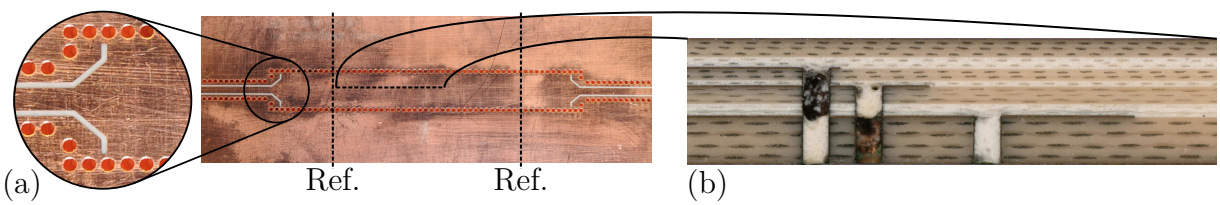

Figure 4.6: (a) Top and (b) cross-sectional view of the manufactured transition.

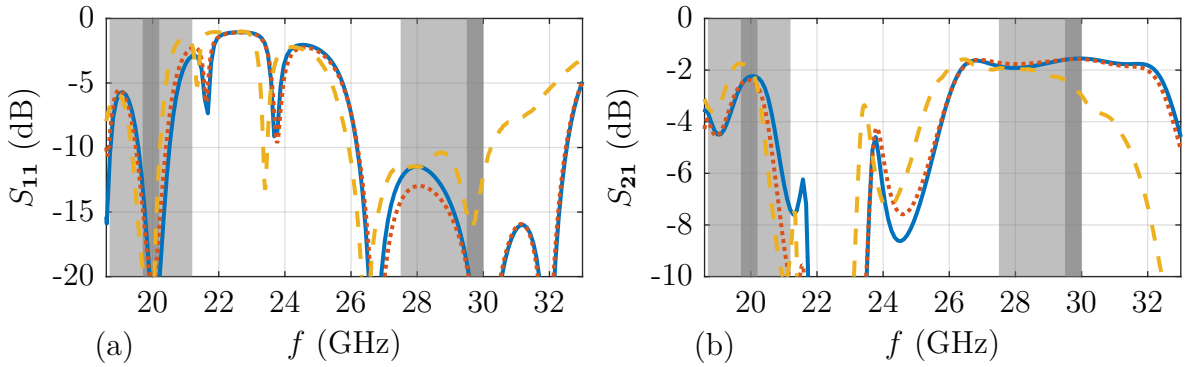

Figure 4.7: Simulation and measurement results of stepped SIW transition (— mode matching, - - full-wave simulation, ···· measurements, ■ typical / ■ reference bands).

reflection, the resonance frequency at 20 GHz is lowered by 100 MHz and that at 32 GHz is less pronounced such that the input reflection rises in the upper frequency band. A tolerance analysis shows that an offset of about 0.1 mm between the copper layers leads to such differences. The insertion loss in the lower (upper) passband is about 1.8 dB (1.9 dB) and 2.2 dB (1.6 dB) for the measurements and simulation, respectively. The losses in the simulation are thus overestimated in the lower and underestimated in the upper frequency band. Possible reasons are uncertainties in the dielectric material parameters, the different surface roughnesses of the dielectric and outer copper foil sides, and fabrication tolerances in general. The measurements nevertheless prove the feasibility of the stepped transition concept and validate the equivalent circuit model.

The stepped SIW transition can be used to excite the full-height SIW and is thus suitable for the SIW lens antenna concept. The upper passband can easily handle both the typical and the reference Tx frequency bands. The lower passband performance is only sufficient for the reference Rx frequency band. Also, the lower passband is rather narrowband and frequency shifts due to tolerances rapidly degrade the performance of the transition. In addition, the tolerances have a significant influence on the upper passband.

4.1.2 E-Plane Taper

In the following, the basic taper theory is briefly reviewed and a simple method to synthesize tapers is presented. Based on this method, an E-plane taper as alternative to the stepped-transition is synthesized, manufactured, and measured.

Taper Theory

A waveguide taper can be viewed as a nonuniform waveguide with varying transmission line parameters, as depicted in Fig. 4.8a. Ports **1** and **2** are located at $z = 0$ and $z = L$, respectively. The cross-section and, thus, the modal field patterns of the waveguide modes vary along z. Caused by that, the waveguide modes are coupled along z, similarly to the

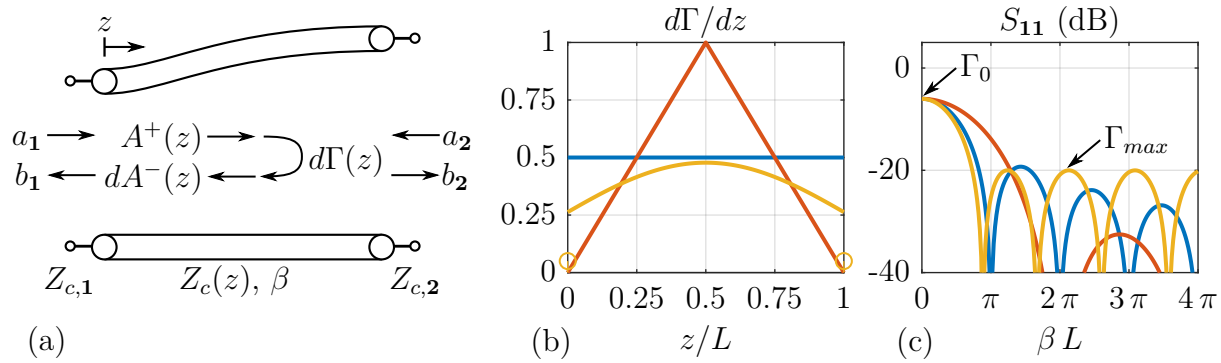

Figure 4.8: (a) Nonuniform waveguide, (b) taper profiles, and (c) input reflection ($\Gamma_0 = 1/2$, — uniform, — triangular, and — Klopfenstein taper for $\Gamma_{max} = -20\,\mathrm{dB}$).

coupling at step discontinuities. Uniform transmission lines are typically described by a system of differential equations known as the telegrapher's equations [99, Sec. 2.2]. To describe nonuniform transmission lines, the transmission line parameters are z-dependent and the mode coupling has to be considered in these equations. The general solution is studied extensively in [147] and [84]. Here, only an approximate model for small reflections is reviewed. This, on the other hand, allows for a simple scheme to synthesize tapers [82, Sec. 5.16].

A single mode is considered in this model and the effects of higher-order modes are neglected. The taper is excited by

$$a_{\mathbf{1}} = A_0 \quad \text{and} \quad a_{\mathbf{2}} = 0 \tag{4.2}$$

with the wave amplitude A_0 at port **1**. The theory of small reflections assumes that only the phase of the forward wave

$$A^+(z) \approx A_0\,\mathrm{e}^{-\mathrm{j}\,\beta\,z} \tag{4.3a}$$

changes along the transmission line. The attenuation due to reflections is neglected and, thus, the magnitude is constant. In addition, a phase constant β independent of z is assumed, which further simplifies the model. An extension with varying β is possible [148] but not necessary in this work. The forward wave is reflected by the incremental change of the cross-section. The associated reflection $d\Gamma(z)$ generates a backward wave $dA^-(z) = d\Gamma(z)\,A^+(z)$ at position z. At the input port this contributes

$$db_{\mathbf{1}}(z) = dA^-(z)\,\mathrm{e}^{-\mathrm{j}\,\beta\,z} = A_0\,d\Gamma(z)\,\mathrm{e}^{-\mathrm{j}\,2\,\beta\,z} \tag{4.3b}$$

to the reflected wave $b_{\mathbf{1}}$. The input reflection coefficient follows from

$$S_{\mathbf{11}} = \frac{b_{\mathbf{1}}}{a_{\mathbf{1}}} = \frac{1}{A_0}\int_0^L db_{\mathbf{1}}(z) = \int_0^L \frac{d\Gamma(z)}{dz}\,\mathrm{e}^{-\mathrm{j}\,2\,\beta\,z}\,dz, \tag{4.3c}$$

i.e., by integrating these increments along the nonuniform transmission line. This equation can be viewed as a Fourier transform over a finite interval, where the derivative of the reflection $d\Gamma(z)/dz$ and $S_{\mathbf{11}}$ are a Fourier transform pair. The derivative of the reflection

can be calculated from the change in the modal fields [84, 147], a finite step approximation of the taper [148], or the distribution of the characteristic impedance [82, Sec. 5.16]. With the latter approach, the derivative of the reflection can be approximated by

$$\frac{d\Gamma(z)}{dz} = \frac{1}{dz}\frac{Z_c + dZ_c - Z_c}{Z_c + dZ_c + Z_c} \approx \frac{1}{2\,Z_c}\frac{dZ_c}{dz} = \frac{1}{2}\frac{d\ln(Z_c)}{dz}. \tag{4.4}$$

Note that the definition of the characteristic impedance is not unique. It must be a good representation of the generated reflections and, thus, it depends on the specific taper.

The total reflection

$$\Gamma_0 = S_{\mathbf{11}}|_{\beta=0} = \int_0^L \frac{d\Gamma(z)}{dz}\,dz = \frac{1}{2}\ln\left(\frac{Z_{c,\mathbf{2}}}{Z_{c,\mathbf{1}}}\right) \tag{4.5}$$

is a characteristic measure for the reflection of the complete taper. It is approximately the reflection for zero phase constant $\beta = 0$ or the reflection of a step discontinuity connecting directly the input and the output cross-section. The distribution of $d\Gamma(z)/dz$ is called tapering function and determines the frequency response. This function is also called window or apodization function in the context of signal processing [149]. Typical tapering functions are the uniform, triangular, and Klopfenstein functions, as depicted in Fig. 4.8b. The uniform and triangular tapers are named after their tapering functions. A taper with uniform function is also called exponential taper because the corresponding characteristic impedance has an exponential profile. The normalized frequency responses are plotted in Fig. 4.8c for $\Gamma_0 = 1/2$. The highest reflection Γ_{max} of the secondary maxima is 13.3 dB and 26.5 dB below Γ_0 for the uniform and the triangular taper, respectively. If, in these cases, $\beta_1\,L = 0.82\,\pi$ and $\beta_1\,L = 1.62\,\pi$, the input reflection is below Γ_{max} for wave numbers exceeding β_1. Note, that β_1 is the corner wave number of the passband with the associated corner frequency f_1. Thus, the uniform taper is shorter but has a higher reflection than the triangular taper. The Klopfenstein taper has a user defined Γ_{max} and a Chebyshev frequency response [150, 151]. It has the smallest length $\beta_1\,L = \operatorname{acosh}(\Gamma_0/\Gamma_{max})$ for a given Γ_{max}. The tapering function has a unit impulse at the input and output, which corresponds to a step in the characteristic impedance profile and, accordingly, to a step discontinuity at these positions.

A taper is synthesized using the presented model by adjusting the reflection profile of the taper to a desired taper profile

$$\Gamma_T(z) = \int_0^z \frac{d\Gamma(z')}{dz'}\,dz'. \tag{4.6}$$

For this purpose, at first, a generic reflection profile

$$\Gamma_\xi(\xi) = \int_{\xi_1}^{\xi} \frac{d\Gamma(\xi')}{d\xi'}\,d\xi' = \frac{1}{2}\ln\left(\frac{Z_c(\xi)}{Z_c(\xi_1)}\right) \tag{4.7}$$

is defined, which is a function of a generic variable ξ. This variable can be a parameter of the waveguide cross-section as for example the waveguide height. The waveguide characteristics change along ξ from the input at ξ_1 to the output at ξ_2 and, thus, the principle

taper profile is predefined. To adjust the generic reflection profile with the taper profile, the equation

$$\Gamma_\xi(\xi) = \Gamma_T(z) \tag{4.8}$$

must be solved, which can be written as

$$\xi(z) = \Gamma_\xi^{-1}\left(\Gamma_T(z)\right) \tag{4.9}$$

with the inverse reflection profile $\Gamma_\xi^{-1}(\Gamma)$. Finally, the profile of the generic variable $\xi(z)$ defines the complete taper.

Design and Realization

Fig. 4.9 shows an E-plane taper of a rectangular waveguide. It is a classical component that is widely used [152]. Here, it is implemented using PCB technology. The input waveguide has width a and height b_1 and is fed by a standard SIW with the same effective width. In the taper section, the height $b(z)$ is continuously increased to obtain the desired frequency response and it reaches the full-height $b_2 \approx a/2$ at the output.

The E-plane taper is modeled by using a nonuniform transmission line with a varying characteristic impedance

$$Z_c = Z^{TE}\,\frac{2\,b}{a} = Z_0\,\frac{2\,b}{a}\,\frac{k_0}{\beta}. \tag{4.10}$$

A power-voltage definition is chosen, where the voltage is defined by integrating the electric field along the y-axis at the center of the waveguide [144, p. 227]. A constant permittivity is assumed and, thus, the propagation constant is independent of z. The waveguide height $\xi = b$ is chosen as the generic variable and, hence, the generic reflection profile (4.7) is given by

$$\Gamma_b(b) = \frac{1}{2}\,\ln\left(\frac{Z_c(b)}{Z_c(b_1)}\right) = \frac{1}{2}\,\ln\left(\frac{b}{b_1}\right). \tag{4.11}$$

This equation is rearranged for the desired taper profile $\Gamma_T(z)$ to obtain the height profile

$$b(z) = \Gamma_b^{-1}(\Gamma_T(z)) = b_1\,\exp\left(2\,\Gamma_T(z)\right). \tag{4.12}$$

Based on these results, a waveguide taper with a width of $a = 4.7\,\text{mm}$ and a permittivity of $\epsilon_{r,eff} = 3.55$ is synthesized. This corresponds to a cutoff frequency of $f_c = 16.9\,\text{GHz}$ for the fundamental TE_{10}^z-mode. The input and output heights are $b_1 = 0.61\,\text{mm}$ and

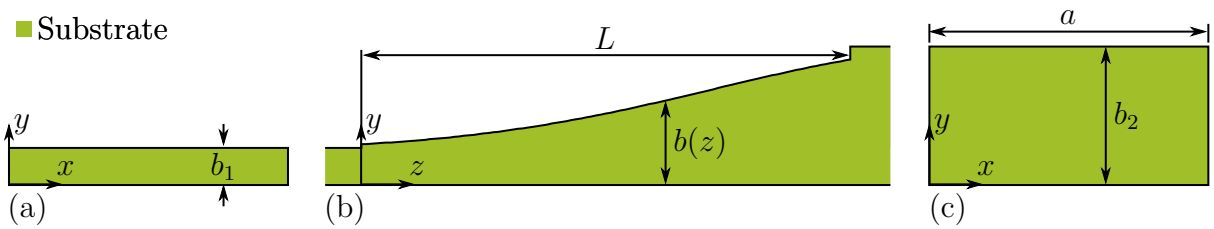

Figure 4.9: (b) Cross-section of E-plane waveguide taper with (a) input and (c) full-height output waveguides.

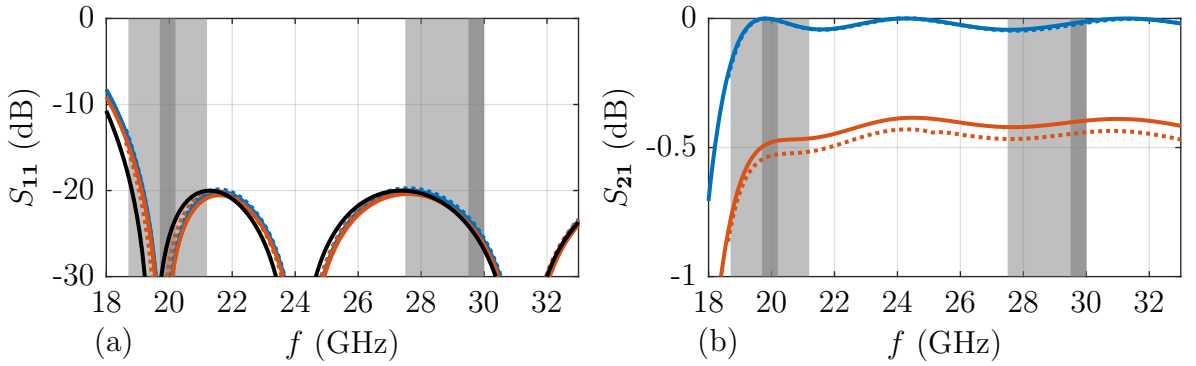

Figure 4.10: Scattering parameters of the E-plane taper (— ideal, —/— mode matching, ····/···· full-wave simulation, — lossless, — lossy, ■ typical / ■ reference bands).

$b_2 = 2.34\,\text{mm}$, respectively. This results in a total reflection of $\Gamma_0 = -3.4\,\text{dB}$. As tapering function, a Klopfenstein taper with $\Gamma_{max} = -20\,\text{dB}$ is chosen. With a taper length of $L = 8\,\text{mm}$ the corner frequency is $f_1 = 18.8\,\text{GHz}$. The synthesized taper profile and the ideal input reflection are depicted in Fig. 4.9b and Fig. 4.10a, respectively. Tab. B.6 lists the design specifications and this design is called *TAP1*.

The taper is realized in a multilayer PCB with laminates from the *Rogers RO4000* series and a superstrate based on *Preperm L335* from *Premix*. The multilayer has a thickness of b_1 and the superstrate is glued on the multilayer. The permittivities of the substrate and the superstrate have very similar nominal values of $\epsilon_{r,1} = 3.38$ and $\epsilon_{r,2} = 3.35$, respectively. The dielectric losses are listed in Tab. B.1 and, for the outer metalization, the conductivity of copper with $\sigma_0 = 5.8 \cdot 10^7\,\text{S/m}$ and a surface roughness of $R_q = 2.8\,\mu\text{m}$ are assumed. In addition, waveguides with a length of 2.4 mm and 4 mm are added at the input and output, respectively.

The scattering parameters of the taper are calculated by the mode matching method and full-wave simulation, as depicted in Fig. 4.10. For the mode matching, the taper is discretized in 101 short transmission line sections that are connected by step discontinuities. The surface roughness and the slightly inhomogeneous dielectric are taken into account. In general, the full-wave simulation agrees very well with the mode matching method. The simulated input reflections with and without losses are nearly the same and the ideal characteristic is very similar. The small frequency shift is related to the assumed effective dielectric constant in the synthesis. Along the taper, the actual effective dielectric constant $\epsilon_{r,eff}$ ranges from 3.44 to 3.56 depending on the taper cross-sections. Nevertheless, the Chebyshev characteristic is maintained over the complete frequency band and, thus, the assumed characteristic impedance is a good representation for the generated reflections. The taper has an insertion loss of about 0.5 dB, which is slightly underestimated by the mode matching method. A possible reason for this are the neglected losses

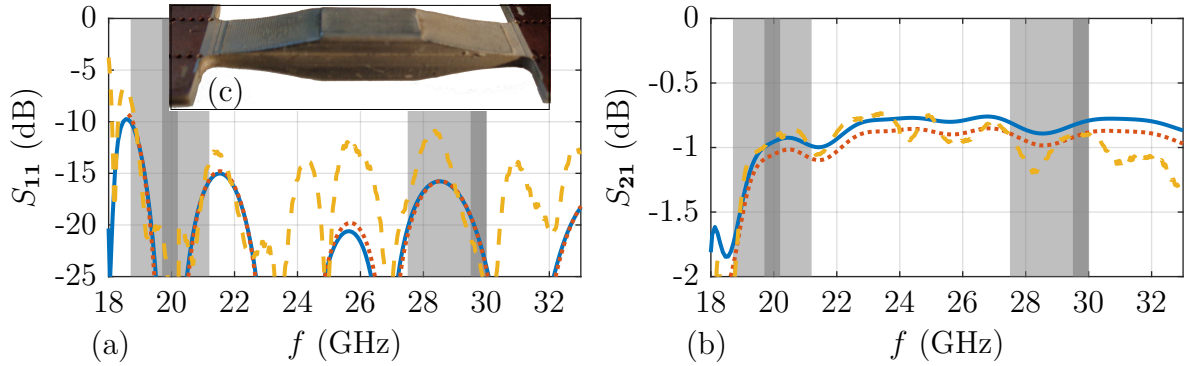

Figure 4.11: (a) Input reflection and (b) transmission coefficient of the E-plane taper in a back-to-back configuration (— mode matching, - - - full-wave simulation, ···· measurements, ■ typical / ■ reference bands). (c) Photograph of manufactured component.

in the transverse metal surfaces of the step discontinuities. However, in most cases, this difference is acceptable.

The simulation results are verified by measurements of a manufactured component. The setup is depicted in Fig. 4.11c. It consists of two stacked back-to-back transitions, which are completely decoupled by a metal layer. A detailed description of the manufacturing steps, including the outer metalization, can be found in Sec. 5.1.2. CPW-to-SIW transitions are added for the measurements (see *CPW-SIW4* in Tab. B.5). A TRL calibration is used to shift the reference planes to the taper inputs. The simulation agrees well with the measurements, as plotted in Fig. 4.11. The measured insertion loss is about 1 dB as estimated by simulation. At lower frequencies, the measured and the simulated insertion loss are almost the same, while differences are observed at higher frequencies. This deviation can be mostly reproduced in simulation, when the manufacturing tolerances of the taper profile are analyzed. Nevertheless, the simulated and the measured input reflections remain below −15 dB and −11 dB, respectively, for frequencies above 19 GHz.

Compared to the stepped transition of the last section, the presented E-plane taper exhibits better electrical performances. Its insertion loss is about 0.5 dB instead of 1 dB for the stepped transition. The taper and the stepped transition have lengths of 14.8 mm (8 mm) and 11.9 mm (5.3 mm) with (without) input and output waveguides, respectively. The higher losses of the stepped transition can be explained by a higher group delay due to the resonances and not by the transition length. In addition, the taper has an ultra-wide passband, covering both the Rx and the Tx frequency band. The taper performance degrades only at the lowest Rx frequencies. However, this issue can be overcome by reducing the cutoff frequency, as done in design *TAP3* (see Tab. B.6). For the stepped transition, especially the Rx frequency band is quite narrow and the level of the input reflection is higher. The manufacturing complexity of both transitions is comparable. While the stepped transition needs a complicated multilayer stack with multiple bond

cycles, the taper requires precise milling of the taper profile and a metalization of the milled surface. All in all, the taper is preferred and is used for the SIW lens antenna concept.

4.1.3 Multilayer Taper

In this section, yet another class of tapers is proposed for multilayer PCBs. Similarly to the previous transitions, the SIW thickness is changed. However, the output waveguide has a thickness of a typical PCB and not the full height. To provide such a transition between SIWs of different height, an MSIW taper was presented in [130]. The synthesis method proposed in this paper is combined with the mode matching method of Sec. 3.4 and Sec. 3.5.

Similar structures have been reported in the past for waveguide components. In [153, 154] a taper with a T-shaped waveguide cross-section is presented. Stepped transitions in SIW technology have been discussed in Sec. 4.1.1. However, the impedance step is matched using stub lines and is hence rather narrowband. Here, a smooth and, thus, very broadband transition is proposed.

The taper structure is depicted in Fig. 4.12. An input SIW of height h_2 is transformed into an output SIW of height h_1. For this purpose, the opening in the middle metal layer and the shape of the via rows through h_1, h_2, and h_3 have to be adjusted. For the following analysis, the SIW structure is transformed into an effective waveguide structure, where the via rows are replaced by continuous metal walls. The widths w_1, w_2, and w_3 vary along the propagation direction z to obtain the desired taper characteristic. All relevant dimensions and the coordinate system are defined in Fig. 4.12 and Fig. 4.13a. In the following, at first, the taper cross-sections and the waveguide characteristics are determined. Then, an exemplary taper is synthesized and realized in a multilayer PCB. Finally, simulation results are compared with measurements.

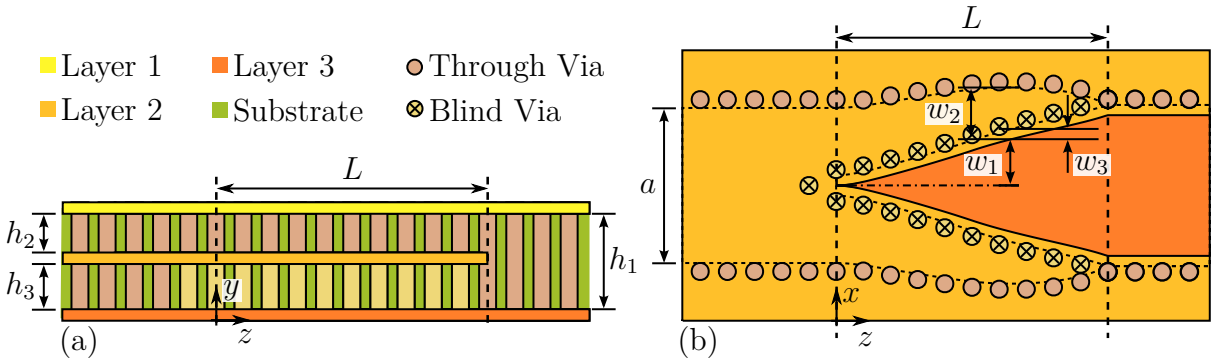

Figure 4.12: (a) Layer stack and (b) top view of the SIW multilayer taper.

Waveguide Characteristics

Fig. 4.13a shows a cross-section $S(z)$ of the effective waveguide structure. It is symmetric with respect to the yz-plane and the (half-)width w_1 increases from zero to a maximum value, while w_2 decreases from $a/2$ to a minimum value along the taper. To apply the single mode nonuniform waveguide theory presented in Sec. 4.1.2, the cutoff frequency f_c and the characteristic impedance Z_c of the fundamental TE^z-mode of each cross-section must be determined. Based on that, the taper profile is synthesized.

To achieve a broadband performance and limit the number of degrees of freedom, the cutoff frequency is chosen to be constant along the taper. The cross-sections are synthesized using the equivalent circuit of the MSIW, as depicted in Fig. 4.13b (see Sec. 3.5.1). For the waveguide mode an even symmetry is assumed and, thus, the symmetry plane is replaced by PMC, represented by an open circuit in the equivalent circuit. The parallel-plate sections are modeled as transmission lines connected by a bifurcation. The transmission lines 2 and 3 are short circuited. The scattering parameters of the bifurcation can be calculated using the mode matching presented in Sec. 3.4.1. Only the fundamental TEM^x-mode is considered for all parallel-plate sections. This considerably simplifies the synthesis procedure presented in Sec. 3.5.2. For this purpose, w_1 and w_3 are predefined and w_2 is adjusted. In this synthesis, the equivalent circuit is split into two disjunct parts, which are connected by the transmission line 2, as shown in Fig. 4.13b. The input reflection $\Gamma_{\boldsymbol{A}}$ of sub-circuit A can thus be determined for the cutoff frequency f_c and the input reflection $\Gamma_{\boldsymbol{B}} = -1$ of the sub-circuit B is given by the short circuit. The transverse resonance method yields the nonlinear eigenvalue problem

$$\det\left([F(w_2)]\right) = \det\left([I] - [\Gamma_{\boldsymbol{A}}]\,[T(w_2)]\,[\Gamma_{\boldsymbol{B}}]\,[T(w_2)]\right) = 0 \tag{4.13a}$$

from (3.78). For the single mode case, it simplifies to

$$1 - \Gamma_{\boldsymbol{A}}\,\Gamma_{\boldsymbol{B}}\,\mathrm{e}^{-2\,\mathrm{j}\,k_c\,w_2} = 0 \tag{4.13b}$$

and an analytical solution for the width is given by

$$w_2 = \frac{\arg\left(\Gamma_{\boldsymbol{A}}\right) + \pi}{2\,k_c}. \tag{4.13c}$$

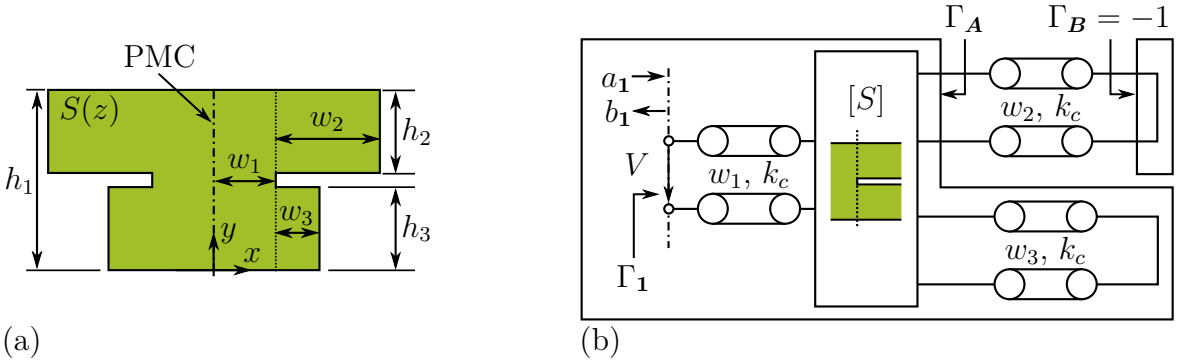

(a) (b)

Figure 4.13: (a) Cross-section $S(z)$ and (b) equivalent circuit of the half cross-section.

This completes the synthesis of cross-sections with a predefined cutoff frequency.

The next step is to determine the characteristic impedance of these cross-sections. Here, it follows from the voltage-power definition

$$Z_C = \frac{|V|^2}{P}. \tag{4.14}$$

The voltage is given by the line integral

$$V = -\int_l \vec{E}\,\vec{dl} \tag{4.15}$$

of the electric field $\vec{E}$ over an integration path l, whereas the power is determined from the Poynting theorem by

$$P = \iint_S \left(\vec{E} \times \vec{H}^*\right) \bullet \vec{dS} = \frac{1}{Z^{TE}} \iint_S \left|\vec{E}\right|^2 \, dS. \tag{4.16}$$

Using the average stored electric energy per unit length [82, Tab. 1-6]

$$W'_E = \frac{\epsilon_0\,\epsilon_r}{2} \iint_S \left|\vec{E}\right|^2 \, dS \tag{4.17}$$

the power can be reformulated as

$$P = \frac{2\,W'_E}{\epsilon_0\,\epsilon_r\,Z^{TE}}. \tag{4.18}$$

The remaining values V and W'_E are now determined from the equivalent circuit. Since the definition of the integration path for the voltage is not unique, it has to be defined for the particular waveguide. Reasonably good results are achieved for similar waveguide structures with a voltage path along the y-axis [153, 154]. With (3.13), (3.24), and (3.28) the line integral (4.15) results in

$$V = \sqrt{Z_0\,h_1}\,(a_{\mathbf{1}} + b_{\mathbf{1}}) = 2\sqrt{Z_0\,h_1}\,a_{\mathbf{1}}. \tag{4.19}$$

Here, the wave amplitudes $a_{\mathbf{1}}$ and $b_{\mathbf{1}}$ are defined in the symmetry plane (see Fig. 4.13b). For the full cross-section, the total average stored energy per unit length is given by

$$W' = 2\,\tau_g\,a_{\mathbf{1}}^2. \tag{4.20}$$

The group delay

$$\tau_g = -\left.\frac{d}{d\omega}\arg\left(\Gamma_{\mathbf{1}}\right)\right|_{\omega=2\pi f_c} \tag{4.21}$$

follows from the reflection coefficient $\Gamma_{\mathbf{1}}$ [155]. This result is used to determine the average stored electric energy per unit length

$$W'_E = W'_M = \frac{W'}{2}, \tag{4.22}$$

because the average stored electric energy W'_E and magnetic energy W'_M are equal at resonance. Finally, the characteristic impedance is given by

$$Z_C = 2\,Z^{TE}\,\frac{\sqrt{\epsilon_r}}{c_0}\,\frac{h_1}{\tau_g}, \tag{4.23}$$

where c_0 is the speed of light in vacuum. Alternatively, the characteristic impedance can be determined from the modal electric field (3.74) of the MSIW. This alternative definition includes multiple parallel-plate modes and is used as reference in the following.

Design and Realization

For the exemplary taper design, a standard multilayer stack based on the *Rogers 4000* series with heights $h_1 = 0.52\,\text{mm}$, $h_2 = 0.2\,\text{mm}$, and $h_3 = 0.3\,\text{mm}$ is used and an effective relative permittivity of $\epsilon_r = 3.55$ is assumed. The generic variable ξ is varied along the taper from 0 at the input to 1 at the output. A constant cutoff frequency $f_c = 16.9\,\text{GHz}$ is chosen, which gives a width of $w_2(0) = a/2 = 2.35\,\text{mm}$ for the input waveguide. The width $w_3 = 0.3\,\text{mm}$ is fixed for the complete taper and $w_2(1) = w_3$ is set for the output waveguide. This corresponds to a width of $w_1(1) = 2.06\,\text{mm}$ at the output. Along the generic taper, the width $w_1(\xi) = \xi\, w_1(1)$ increases linearly and the corresponding width $w_2(\xi)$ decreases monotonously, as depicted in Fig. 4.14a. For this synthesis, the scattering parameters of the parallel-plate bifurcation must only be determined once. Here, the presented mode matching method (see Sec. 3.4.1) or full-wave simulation can be used [130]. The generic taper is thus given by the widths $w_i(\xi)$. Furthermore, Fig. 4.14a depicts the deviation Δf_c of the intended f_c from the one of references. Here, full-wave simulation and the mode matching method with multiple parallel-plate modes serve as references. They agree very well and the deviation from the single mode model decreases from 3.5 % at $\xi = 0$ to zero at $\xi = 1$. The error for small w_1 is attributed to the neglected interaction of higher-order parallel-plate modes. Fig. 4.14b shows the impedance profile Z_c normalized to the input impedance $Z_c(0)$. The impedance varies by a factor 2.6 from the input to the output waveguide, which corresponds to $\Gamma_0 = -6.4\,\text{dB}$. In comparison to full-wave simulation and the mode matching method, the relative error is below 6 %. The error distribution is similar to that of Δf_c.

Based on the calculated generic impedance profile and the taper theory of Sec. 4.1.2, a triangular taper with a length of $L = 8\,\text{mm}$ is synthesized. The design is called *SIWTAP1*

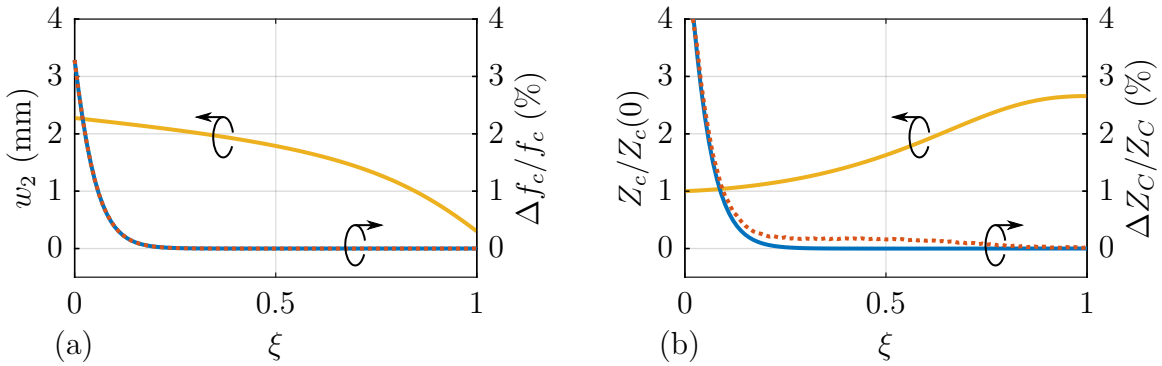

Figure 4.14: (a) Dimensions and (b) mode characteristics of the taper cross-sections (— mode matching, ···· full-wave simulation).

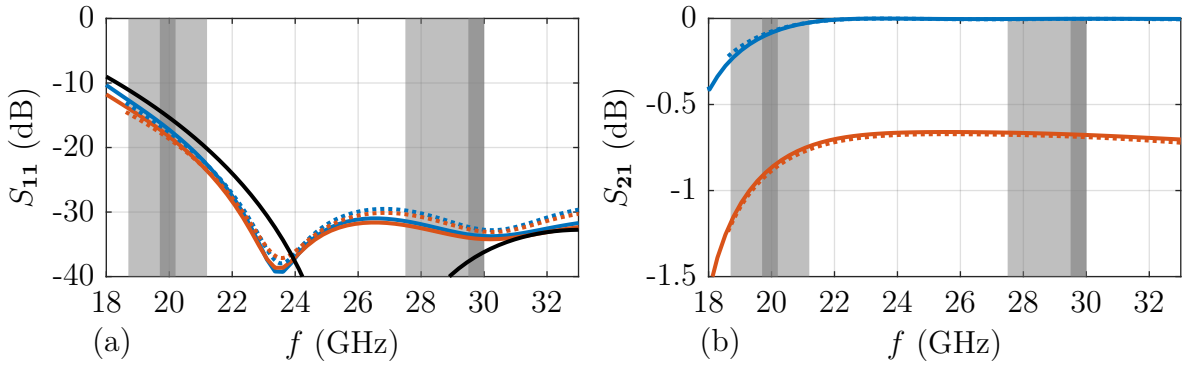

Figure 4.15: Scattering parameters of the SIW taper (— ideal, —/— mode matching, ····/···· full-wave simulation, — lossless, — lossy, ■ typical / ■ reference bands).

and the specifications are listed in Tab. B.7. Fig. 4.12b depicts the resulting taper profile with the widths $w_i(\xi(z))$. The effective waveguide structure is transformed to the SIW taper by a via row offset of $\Delta w = 0.18\,\text{mm}$ (see Sec. 3.3.1). Here, a via diameter of 0.5 mm and a pitch of 0.8 mm are taken for the via rows. Fig. 4.15a shows the input reflection. It compares the ideal characteristic of the triangular taper and simulation results of the effective waveguide and the actual SIW structure. For the ideal characteristic and the simulation, S_{11} decreases with frequency and stays below $-30\,\text{dB}$ above 23.1 GHz and 22.4 GHz, respectively. The results of the effective waveguide structure are simulated with the mode matching method. For this purpose, the taper is subdivided into 101 sections with varying cross-sections. For each section, the fundamental and five higher-order waveguide modes are considered. The actual SIW taper is analyzed by full-wave simulation. The substrate parameters are listed in Tab. B.1. The surface roughness of the metal layers is assumed to be 1 µm. The simulation results agree well to each other. The differences to the ideal characteristic stem mainly from the characteristic impedance model, which only considers the fundamental mode. Deviations in the waveguide characteristics (see Fig. 4.14) have only a minor influence. Furthermore, due to the surface roughness, the effective dielectric constant decreases along the taper from $\epsilon_{r,eff} = 3.54$ to 3.47 and is thus assumed to be slightly too high in the synthesis. Hence, the frequency shift is not based on this effect. For other taper profiles, these differences are even more pronounced. A uniform (exponential) taper is presented in [130]. However, these deviations can be accepted for a simple and very fast synthesis procedure. The insertion loss is about 0.7 dB for the taper with 3.2 mm and 2.4 mm long waveguides at the input and output, respectively. The attenuation coefficient of the fundamental mode decreases from 0.06 dB/mm to 0.04 dB/mm along the taper. This demonstrates that the losses can be significantly reduced with a thicker SIW.

To validate the concept, the taper is fabricated in a back-to-back configuration using a standard multilayer process (see Fig. 4.16c). CPW-to-SIW transitions (*CPW-SIW3* of

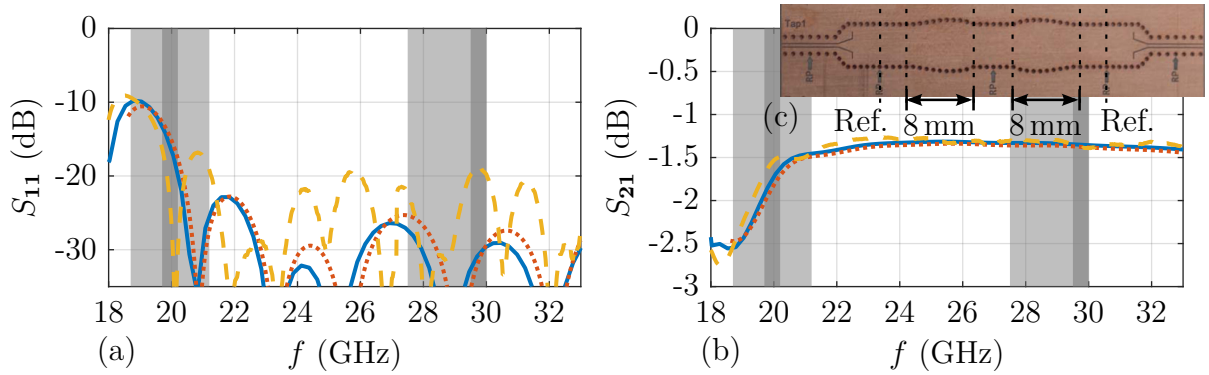

Figure 4.16: (a-b) Simulation and measurement results of the SIW taper in a back-to-back configuration (— mode matching, - - - full-wave simulation, ···· measurements, ■ typical / ■ reference bands). (c) Photograph of the manufactured SIW taper.

Tab. B.5) are added for the measurement setup. The reference planes are shifted to the SIWs using a TRL calibration. Fig. 4.16 shows the simulated and measured scattering parameters for the taper. Measurements and simulation show a good agreement. For frequencies above 19.7 GHz, the measured reflection coefficient stays below −17 dB. The insertion loss is about 1.4 dB in simulation and measurements. The simulation results of the equivalent waveguide and the SIW structure agree very well, which demonstrates the capabilities of the implemented mode matching method. Deviations in the measurements can result from manufacturing tolerances, like a misalignment of the metal layers. At the lower Rx frequencies the taper performance degrades. Like for the E-plane taper, this can be improved by lowering the cutoff frequency (see *SIWTAP2* of Tab. B.7).

In conclusion, a multilayer taper structure for SIWs with different heights is presented. It has several applications for multilayer PCBs. For example, the attenuation coefficient can be reduced by accessing thicker SIWs. The synthesis procedure requires only a single simulation of a parallel-plate bifurcation, which makes it extremely fast and simple.

4.2 Polarizer

Fig. 4.17 shows the cross-section of a polarizer in the yz- and xz-plane. It is a combination of a classic septum polarizer [78] and an E-plane taper. The taper changes the height of each of the two input SIWs from h_1 to $h_2 = a/2$ and the septum polarizer transforms

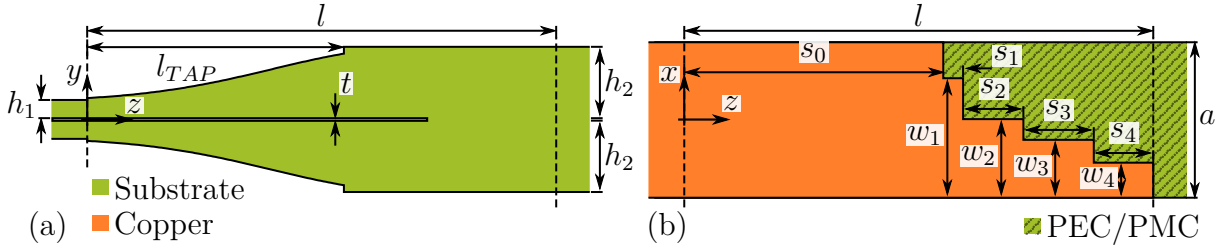

Figure 4.17: Cross-section of the polarizer in (a) the yz- and (b) the xz-plane.

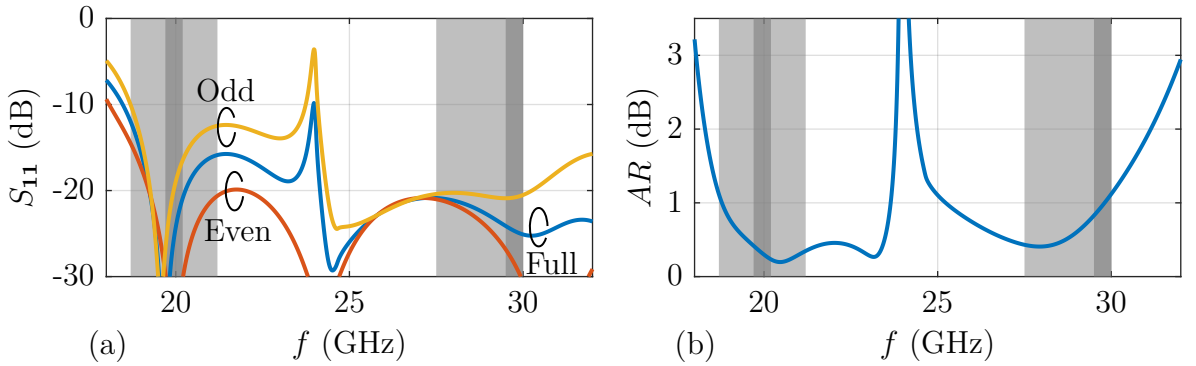

Figure 4.18: (a) Input reflection and (b) axial ratio of the polarizer (— full polarizer, — even-mode, — odd-mode, ■ typical / ■ reference bands).

the polarization from linear to circular. Polarizers are also called orthomode transducers as the input and output modes are orthogonal for an ideal component. In the square SIW, the TE_{10}- and TE_{01}-modes are degenerated and for circular polarization the wave amplitudes are in quadrature. In the following, an even- and odd-mode analysis is applied to design the polarizer.

For the even-mode, the xz-plane is treated as PEC and the resulting structure transforms the TE_{10}-mode of the input SIWs to that of the square SIW. The septum has almost no influence because it lies in the xz-plane and the finite thickness can be neglected. For the transition, the E-plane taper of Sec. 4.1.2, as well as the stepped transition of Sec. 4.1.1, can be used. Because of the higher bandwidth and the generally better performance, the E-plane taper is used for the polarizer. Full-wave simulation results of the input reflection are plotted in Fig. 4.18a.

For the odd-mode, the xz-plane is treated as PMC and the resulting structure transforms the TE_{10}-mode of the input SIWs to the TE_{01}-mode of the square SIW. Along the septum, the electric field pattern is rotated by 90° and the phase is shifted compared to the even-mode case. The scattering parameters of the full polarizer are computed from the even- and odd-mode results. During the optimization process, the even-mode case is simulated only once, in contrast to the odd-mode model which is used to determine the septum geometry. Here, the widths w_i, the lengths s_i, and the position s_0 are systematically varied. The input reflection and the axial ratio are optimized in the Rx and the Tx frequency band. The optimized parameters are listed in Tab. B.8 and the polarizer is called *POL1*. Fig. 4.18 shows the corresponding simulation results. Two bands are visible that are separated by a resonance at 24 GHz. This is a common effect due to higher-order modes, which is known to limit the usable bandwidth of septum polarizers [79]. However, in the considered satellite communication application, it is uncritical as it falls between the two bands. In the lower band, the input reflection of the full structure remains below −15 dB and the axial ratio is smaller than 0.8 dB from 19 GHz to 23.6 GHz. In the upper band, the input reflection is below −21 dB above 24.2 GHz and the axial ratio is lower

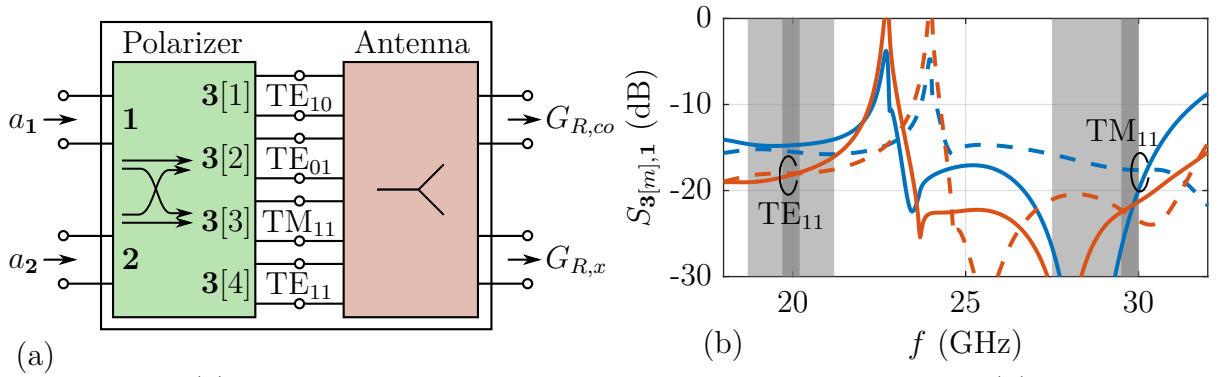

Figure 4.19: (a) Equivalent circuit of antenna and polarizer assembly. (b) Excitation of higher-order modes (— *POL2*, - - - *POL1*, ■ typical / ■ reference bands).

than 1 dB from 25.2 GHz to 29.8 GHz. Considering the typical frequency bands, the input reflection and the axial ratio degrade towards low Rx and high Tx frequencies, respectively. However, the performance is still acceptably good for the application considered here.

The polarizer is connected to an antenna element, as depicted in Fig. 4.19a. This raises several other issues. If an ideal polarizer is excited by a wave amplitude $a_\mathbf{1}$, the TE_{10}- and TE_{01}-modes are excited in quadrature and circular polarization in the center of the square waveguide is achieved. For symmetric antenna arrangements, this also leads to circular polarization in the far-field at boresight. In other directions, the wave is depolarized and cross-polarization rises. This effect can be minimized by an appropriate antenna design. However, this is very challenging for the wide frequency spread considered here and the depolarization cannot be completely avoided. For an array application, only the polarization in the pointing direction (θ_0, ϕ_0) is of interest and here the cross-polarization can be compensated by the second input $a_\mathbf{2}$. To illustrate this technique, the necessary excitation coefficients are determined. First, the far-field pattern in the pointing direction

$$\vec{g} = \frac{1}{\sqrt{P_{stim}}}\,[g] \begin{bmatrix} a_\mathbf{1} \\ a_\mathbf{2} \end{bmatrix} \quad \text{with} \quad [g] = \begin{bmatrix} \vec{g}_\mathbf{1}(\theta_0, \phi_0) & \vec{g}_\mathbf{2}(\theta_0, \phi_0) \end{bmatrix} \tag{4.24}$$

is given by a superposition of the two polarizations. The individual far-field patterns $\vec{g}_\boldsymbol{p}$ for an excitation at port $\boldsymbol{p}$ are collected in the gain matrix $[g]$. The stimulating power is given by $P_{stim} = |a_\mathbf{1}|^2 + |a_\mathbf{2}|^2$. For an intended polarization with the unit vector $\vec{e}_{pol}$, the far-field pattern can be written as

$$\vec{g} = |\vec{g}|\ \vec{e}_{pol}. \tag{4.25}$$

With (4.24) this leads to the excitation coefficients

$$\begin{bmatrix} a_\mathbf{1} \\ a_\mathbf{2} \end{bmatrix} = \sqrt{P_{stim}}\,[g]^{-1}\,\vec{g} = a_0\ |\vec{g}|\ [g]^{-1}\,\vec{e}_{pol}, \tag{4.26a}$$

where $\sqrt{P_{stim}}$ is replaced by a common wave amplitude a_0. From a comparison of the magnitudes of (4.26a), the magnitude of the far-field pattern is given by

$$|\vec{g}| = \left| [g]^{-1} \vec{e}_{pol} \right|^{-1} . \tag{4.26b}$$

The common wave amplitude a_0 can vary for each array element to form the radiation pattern (see Sec. 2.3). This compensation technique fails, when $[g]$ is singular and, thus, the patterns $\vec{g}_{\boldsymbol{p}}$ are linearly dependent. In general, the conditioning of the linear system [156, Sec. 50.5] is a measure for the necessary accuracy of the wave amplitudes $a_{\boldsymbol{p}}$ and the knowledge of the gain matrix $[g]$. Nearly orthogonal patterns $\vec{g}_{\boldsymbol{p}}$ give the best matrix condition. To implement the proposed compensation technique, the beamforming network must be able to control both wave amplitudes simultaneously. Additionally, in general, the excitation varies for different pointing directions, which have to be considered in the implementation of calibration routines. A further feature of this technique is that an arbitrary polarization, as for example linear polarization, can be generated.

Another issue can arise from multiple reflections in the square waveguide of the antenna and polarizer assembly. The fundamental TE_{10}- and TE_{01}-modes are typically well-matched at the polarizer output and antenna input and, thus, multiple reflections have almost no influence. This changes for higher-order waveguide modes in the square SIW section. Here, the TE_{11}- and TM_{11}-mode can propagate in the upper frequency band and they might experience a substantial reflection from the antenna input and polarizer output. If these modes are excited, resonances can occur due to multiple reflections. These resonances can notably decrease the gain and vary the phase of the far-field pattern. A detailed discussion of this effect is given in [72]. The transmission coefficients of the polarizer *POL1* from input **1** to higher-order modes in the square waveguide are given in Fig. 4.19b. In particular, the transmission to the TM_{11}-mode of about $-14\,\mathrm{dB}$ in the Tx frequency band can generate resonances. For the Rx frequency band, the higher-order modes are below cutoff and, thus, no resonances occur. In a redesign, called *POL2*, the transmission coefficients to higher-order modes are minimized and value of less than $-20\,\mathrm{dB}$ could be achieved for the Tx frequency bands.

For the redesign, the following specifications are also modified. The cutoff frequency of the fundamental modes is lowered from 17.5 GHz to 16.7 GHz by an electrically larger waveguide. This reduces the waveguide losses close to cutoff. In addition, the PCB stack is changed due to manufacturing issues. A further effect is that the employed substrate materials are anisotropic. The parallel and normal electric field components, with respect to the substrate, experience a different permittivity. This effect must be considered for the square waveguide because the TE_{10}- and TE_{01}-modes have normal and parallel electric field components, respectively. The permittivity in the parallel plane is determined by measurements with a split-cylinder resonator [157] and is listed in Tab. B.1. It is higher

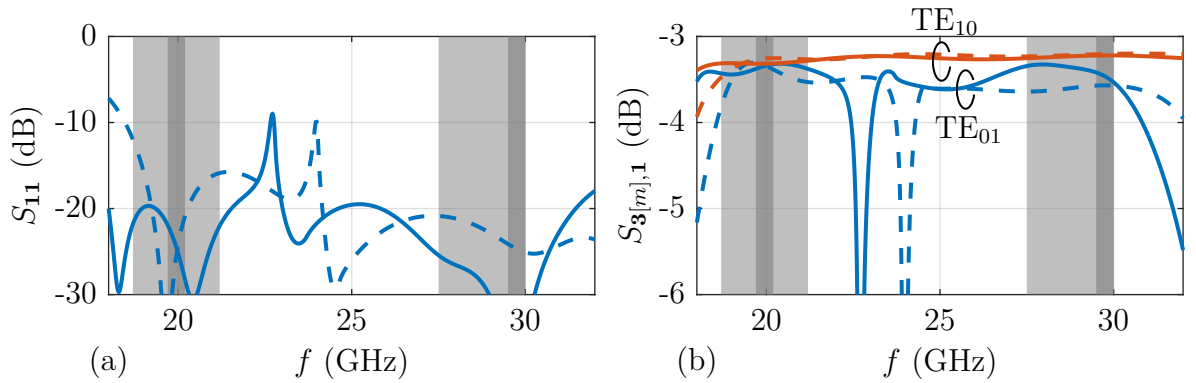

Figure 4.20: Scattering parameters of the designed polarizers (— *POL2*, - - · *POL1*, ■ typical / ■ reference bands).

than in the normal plane. Thus, for a square SIW, the phase constants of the modes differ. This effect is reduced by slightly decreasing the height of the square SIW. Despite its rectangular cross-section, the waveguide is still called square SIW in the following.

These modifications result in even more challenging requirements for the redesign. Especially, the wider frequency spread due to the lower cutoff frequency and the goal of a reduced excitation of higher-order modes are challenging. To obtain more degrees of freedom for the optimization, the phase relation of the fundamental modes for circular polarization is ignored. In general, this yields elliptically polarized waves in the square SIW and also in the far-field at boresight. However, this effect can be compensated with the proposed technique, if it is supported by the implementation of the beamforming network. The resulting dimensions of the optimized polarizer *POL2* are listed in Tab. B.8.

As discussed before, the excitation of higher-order modes is reduced in the redesign. Additionally, as shown by the scattering parameters of *POL1* and *POL2* in Fig. 4.20, the input reflection is improved in the redesign and does not exceed −20 dB in the marked frequency bands. Especially for the lower frequency band, a significant improvement is achieved. This is confirmed by the transmission coefficients, which exceed −3.5 dB from 18 GHz to 22 GHz and from 26.3 GHz to 30 GHz. The excitation of the TE$_{01}$-mode limits the usable bandwidth. The polarizer designs are verified in combination with an antenna element by far-field measurements in Chapter 5.

Rx/Tx Lens Antenna 5

Lens antennas are a combination of an antenna element or array with a single or several lenses. The lenses are often used to improve the radiation pattern. In lower frequency systems, they are seldom used because the resulting setups would be bulky and heavy. Nowadays, lens antennas attract much attention because, with increasing frequencies, the lens size becomes acceptable. A variety of lens antenna types for several applications have been developed [158]. For example, lenses are mounted at the end of waveguide horn antennas [159, 160], where they are used to change the amplitude or phase distribution to improve the radiation characteristics. More compact setups feature a dielectric lens directly on top of a PCB [75, 76, 161] or even on a semiconductor [73]. As feed elements, patches, dipoles, or slot antennas are used.

Depending on the antenna type and application, different numerical methods are utilized for the modeling. In case of electrical large lenses, variants of geometrical optics are very efficient and widely used [162]. Furthermore, methods to synthesize the lens surface for a predefined radiation pattern have been proposed in [163]. To analyze electrically small lenses, more rigorous methods are necessary. One efficient method is based on the spherical wave expansion [74–76] for the field of the feed element. However, for the proposed antenna concept, the space between an element and the dielectric interface or the neighboring elements is too small for this method[1]. As in this work the analyzed lens antennas are relatively small, full-wave methods yield acceptable simulation times and are, thus, employed for the lens modeling.

The lens antenna concept, as introduced in Sec. 2.7, is implemented with the designed components in the following. At first, a single antenna is designed for the Rx/Tx element. For this, the geometry of the dielectric lens is designed through a parameter study. The resulting design is verified experimentally with a lens fed by a square SIW. This lens antenna is then combined with a polarizer to demonstrate the dual-band and the dual-polarization functionality. Finally, a passive array is designed. For this purpose, Rx/Tx and Tx-only elements are arranged in the interleaved rectangular grid as discussed in

[1]The spherical wave expansion can only represent the field outside a minimal sphere that contains all sources. Therefore, the minimal spheres of the feed elements must not overlap each other or the dielectric interface. This limits the usability of the method.

Sec. 2.2. The lens surface is designed for this periodic arrangement. The concept of the Rx/Tx integrated lens array antenna is demonstrated by measurements.

5.1 Lens Antenna Element

The lens is simultaneously used as a matching element and for far-field optimization to enable broadband usage. For this purpose, an extended hemispherical dielectric lens is employed [70–73].

5.1.1 Lens Antenna

The hemispherical lens with the square SIW feed is depicted in Fig. 5.1a. In the following, the lens surface is designed and the performance is verified by measurements with a custom-designed test fixture [71]. The lens is made of a homogeneous dielectric and backed by a ground plane. The square SIW protrudes into a cavity on the backside of the lens. To validate the lens performance, the SIW is excited by the TE_{10}-mode in this section.

Lens Surface Design

The lens profile is determined by means of a full-wave parameter study. An infinite ground plane is assumed and simulation is carried out without losses. Fig. 5.1b depicts a parameterized model of the lens antenna. The square SIW is fabricated from a multilayer based on the *Rogers RO4003C* substrates and *RO4450F* prepregs. For the design, an effective permittivity of $\epsilon_{r,0} = 3.55$ is assumed and an SIW width of $a = 4.47\,\mathrm{mm}$ is selected, which corresponds to a cutoff frequency of $f_c = 17.8\,\mathrm{GHz}$. In the following study, the length l_0 of the SIW and the shape of the lens are varied. The lens geometry is parameterized by the radius r, the height z_0 of the cylinder, the cavity height $l_0 + l_1$, and the dielectric constant $\epsilon_{r,1}$. The square cavity is manufactured by milling and four holes with a radius of $r_D = 0.4\,\mathrm{mm}$ are drilled at the corners, as depicted in Fig. 5.1c. To assess the lens performance, two parameters are determined in the frequency range from 19.5 GHz to 32 GHz. These are the maximum input reflection Γ_{max} and the ratio of maximum to minimum di-

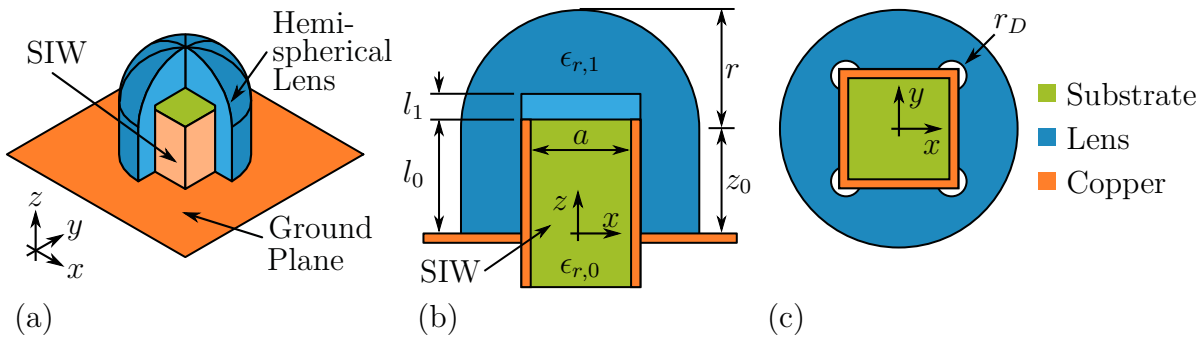

Figure 5.1: (a) Spherical lens antenna with SIW feed and cross-sections in the (b) xz- and (c) xy-plane.

rectivity $D_{rel} = D_{max}/D_{min}$ in boresight direction. For some lens arrangements and some frequency bands, the main beam splits into two distinct beams which leads to a minimum in boresight direction. To prevent this, the variation of the directivity and, thus, D_{rel} has to be minimized.

In the following, the remaining five parameters of the lens arrangement are systematically varied. In a first step, the gap between SIW and lens is set to $l_1 = 0$ and the lens radius is fixed to a small value of $r = 3.5\,\text{mm}$. The parameters l_0, $\epsilon_{r,1}$, and z_0 are varied. Fig. 5.2a and Fig. 5.2d show contour plots of Γ_{max} and D_{rel} versus l_0 and $\epsilon_{r,1}$ for $z_0 = 3.5\,\text{mm}$. For this particular value of z_0, one finds a parameter set (l_0, $\epsilon_{r,1}$), which yields good performance for both Γ_{max} and D_{rel}. It can be seen that Γ_{max} is minimum for $\epsilon_{r,1} \approx 2$ and $l_0 \approx 4.25\,\text{mm}$, whereas D_{rel} is minimum for $l_0 \approx 4\,\text{mm}$. In contrast to $\epsilon_{r,1}$ and z_0, l_0 strongly influences the directivity variation. The matching performance is affected by $\epsilon_{r,1}$ and l_0 has only a minor influence. The parameter set used in the following with $l_0 = 4\,\text{mm}$ and $\epsilon_{r,1} = 2.1$ is marked by crosses in Fig. 5.2a and Fig. 5.2d. It yields a D_{rel} value of only 0.5 dB and an acceptable matching of 14 dB. Slightly smaller values of $\epsilon_{r,1}$ would improve the matching. However, $\epsilon_{r,1}$ cannot be deliberately varied, as it depends on the available materials. Here, polytetrafluoroethylene (PTFE) is chosen because it has very low dielectric losses and is widely available.

Fig. 5.2b and Fig. 5.2e show Γ_{max} and D_{rel}, when z_0 and r are varied. The crosses correspond to those in Fig. 5.2a and Fig. 5.2d. Parameter combinations in the hatched

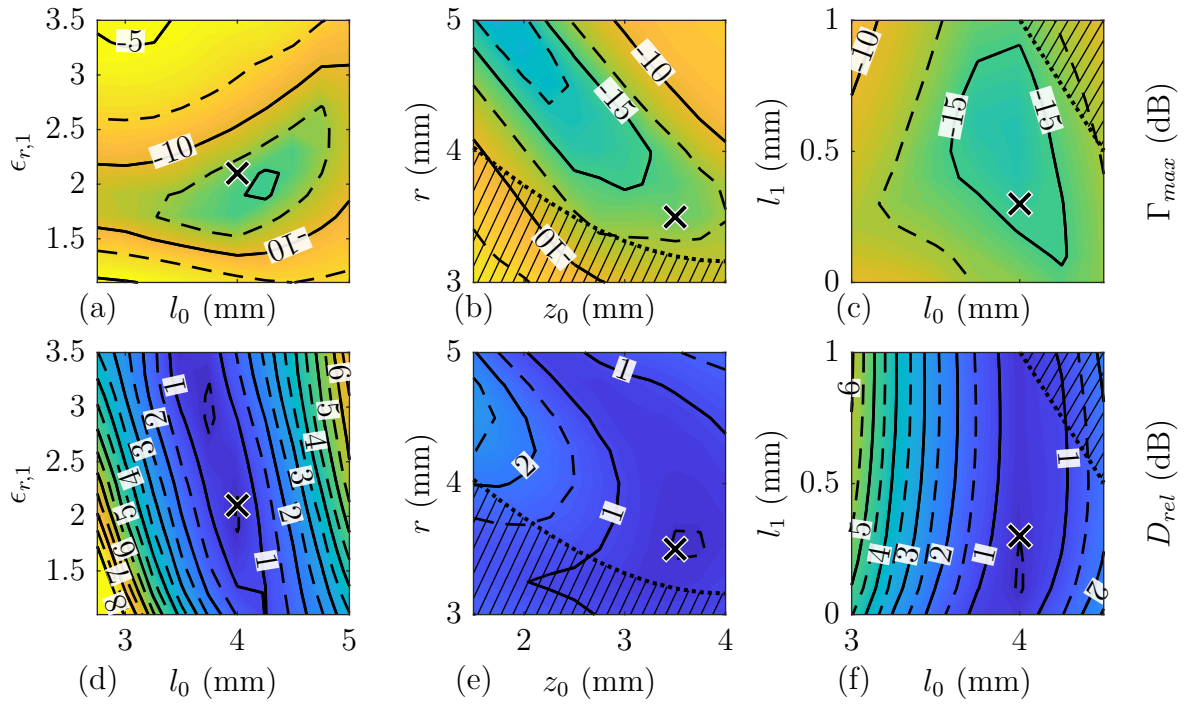

Figure 5.2: (a) Γ_{max} and (d) D_{rel} versus $\epsilon_{r,1}$ and l_0 ($z_0 = 3.5\,\text{mm}$, $r = 3.5\,\text{mm}$, $l_1 = 0$).
(b) Γ_{max} and (e) D_{rel} versus r and z_0 ($\epsilon_{r,1} = 2.1$, $l_0 = 4\,\text{mm}$, $l_1 = 0$).
(c) Γ_{max} and (f) D_{rel} versus l_0 and l_1 ($\epsilon_{r,1} = 2.1$, $z_0 = 3.5\,\text{mm}$, $r = 3.5\,\text{mm}$).

areas are technically not relevant. D_{rel} is relatively low over a large parameter range. A minimum Γ_{max} is observed, when $r + z_0 - l_0$ is in the order of a quarter wavelength.

Finally, Fig. 5.2c and Fig. 5.2f illustrate the effect of varying l_0 and l_1. The gap has a minor influence on D_{rel}. With the marked parameter set $l_0 = 4\,\text{mm}$ and $l_1 = 0.3\,\text{mm}$, Γ_{max} can be reduced to $-16\,\text{dB}$ while D_{rel} remains at 0.5 dB. The finial parameters of the lens antenna *LEN1* are summarized in Tab. B.9.

SIW Test Fixture

For a precise and reproducible characterization of the lens antenna, a test fixture is developed [71]. It essentially transforms the TE_{10}-mode of a WR42 waveguide into the TE_{10}-mode of the square SIW. The transition consists of nine symmetrical steps with lengths l_i, as depicted in Fig. 5.3b. At each step, the substrate width s_i is increased and the waveguide width w_i is decreased. The optimized parameters for a minimum input reflection are listed in Tab. B.10. The test fixture is machined as an aluminum split block and a photograph is shown in Fig. 5.3a. The square SIW is milled from the multilayer PCB and the sidewalls are metalized by electroplating. Precise alignment is provided by a pin in the aluminum block and a corresponding 0.5 mm deep hole in the substrate. To achieve a well-defined electric contact, highly conductive O-rings from *Soliani EMC* are inserted at the two ends of the square SIW section. This short-circuits small gaps between the block and the substrate resulting from manufacturing tolerances and, thus, prevents unpredictable reflections. All parts are assembled with screws and dowel pins. For frequencies from 19.4 GHz to 32 GHz, the input reflection remains below $-20\,\text{dB}$ and the insertion loss below 1 dB. This and further measurement results are reported in [71].

Realization and Measurements

A picture of the assembled lens antenna is given in Fig. 5.3c. The dielectric lens is placed on top of the square SIW, which is mounted in the test fixture. To minimize the effect of

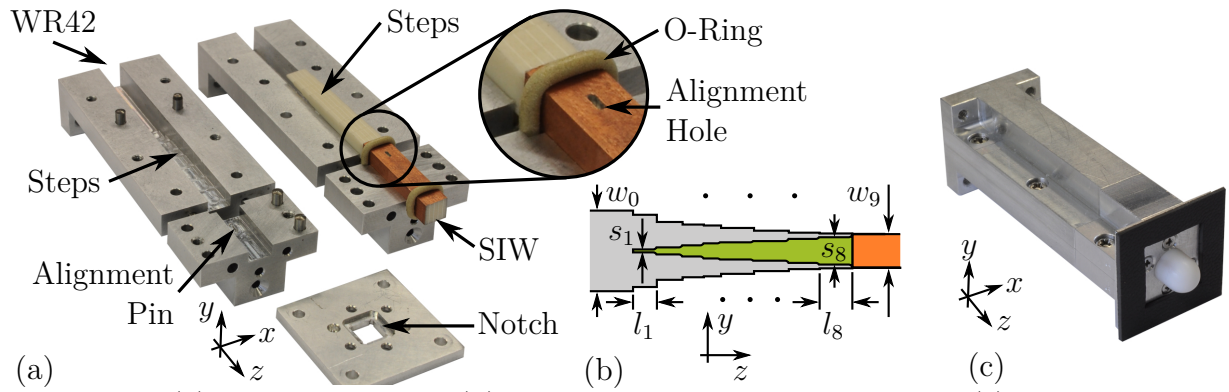

Figure 5.3: (a) Photograph and (b) cross-section of the test fixture. (c) Photograph of the assembled lens antenna.

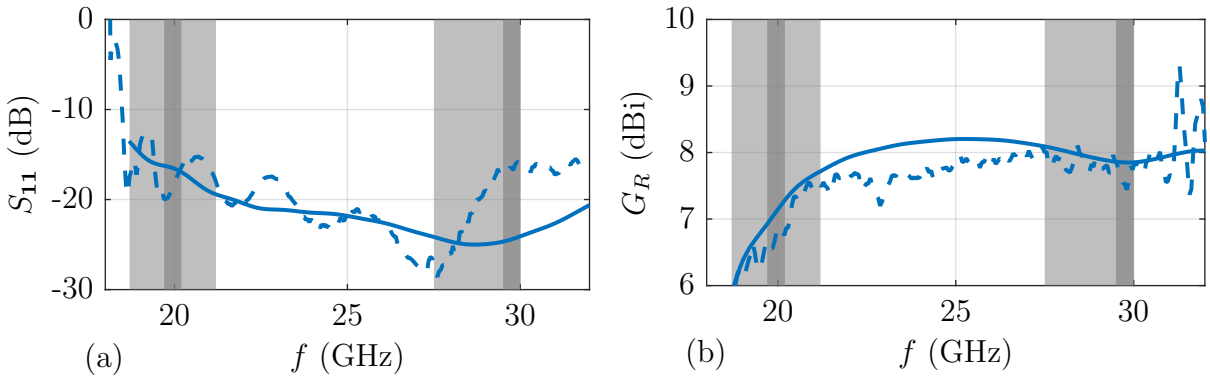

Figure 5.4: (a) Input reflection and (b) realized gain in the boresight direction of the SIW lens antenna (— simulation, - - - measurements, ■ typical / ■ reference bands).

the finite ground plane, an absorber (*Eccosorb BSR-U*) with a 14 mm square cutout and a thickness of 1 mm is placed around the lens.

Fig. 5.4a shows the input reflection. The reference plane is shifted to the square SIW using an offset short calibration. Simulated and measured results agree well and show a remarkable wideband matching. For frequencies above 19.5 GHz, the input reflection remains below −16 dB and −15 dB in simulation and measurements, respectively.

The realized gain in boresight direction is plotted in Fig. 5.4b. It reaches about 8 dBi and decreases at lower frequencies because the losses increase close to cutoff. The measurement results are relatively well predicted by simulation. The ripple measured at frequencies above 31 GHz stems from calibration issues due to the limited usable frequency range of the coaxial-to-waveguide transitions and the reference antennas. For frequencies above 19 GHz the simulated total antenna efficiency including a 4.4 mm long square SIW section ranges from 85 % to 95 %.

With the shown performance, the lens antenna can easily handle the typical Tx frequency band. However, the antenna losses notably increase at lower frequencies, which impairs Rx operation. To overcome this issue, the cutoff frequency of the square SIW can be decreased. This essentially shifts the frequency response to lower frequencies.

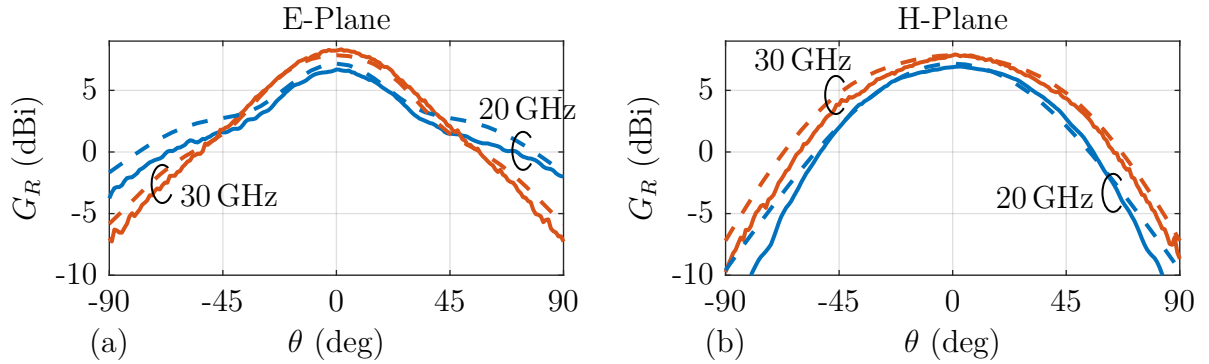

Figure 5.5: Simulated and measured realized gain in E- and H-plane (— simulation, - - - measurements).

Fig. 5.5 shows the realized gain in the E- and H-plane (xz- and yz-plane) versus the elevation angle at 20 GHz and 30 GHz. Simulation and measurement results are consistent. The 3 dB-beamwidth is 53° and 56° in the E-plane and 75° and 78° in the H-plane at 20 GHz and 30 GHz, respectively. Further measurement results are reported in [71].

The experiments validate the lens antenna concept. An ultra-wideband performance of more than 50 % is demonstrated with good matching and radiation properties. If a perfect symmetry of the lens antenna is assumed, the results of the linear excitation are transferable to a circular excitation.

5.1.2 Lens Antenna with Polarizer

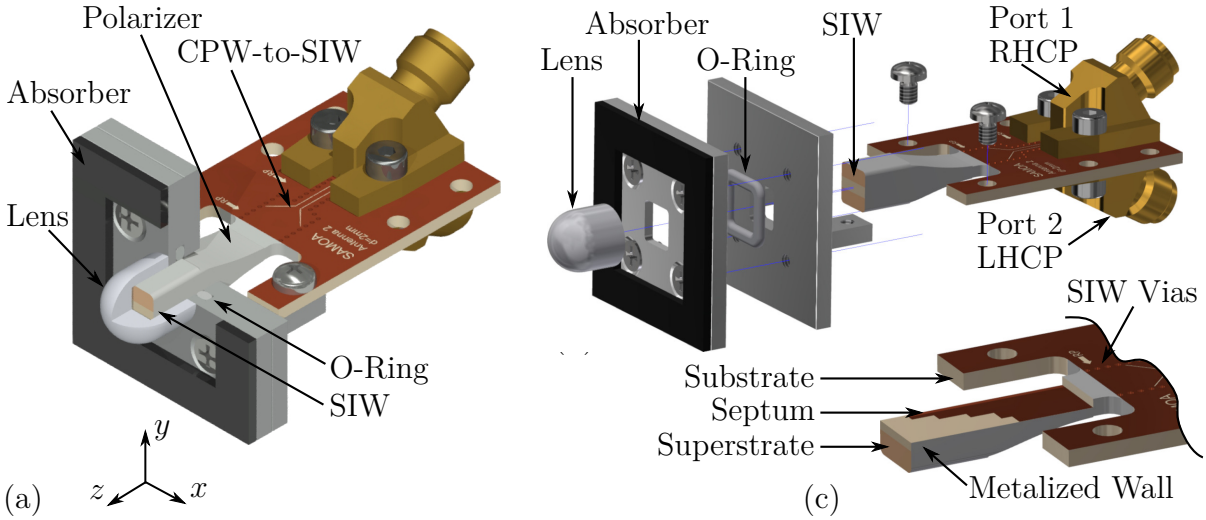

Figure 5.6: (a) Assembled and (b) exploded view of SIW lens antenna as well as (c) cut view of PCB.

Fig. 5.6a shows the lens antenna with a polarizer [70, 72]. The antenna feed is based on a multilayer PCB and tapered superstrates. The polarizer is embedded in this feed (see Fig. 5.6c) to allow for the excitation of two polarizations, as discussed in Sec. 4.2. The two polarizer inputs are connected to coaxial cables by a connector on each side of the PCB. The extended hemispherical lens is placed on top of the square SIW, as proposed in Sec. 5.1.1. An aluminum component attached to the PCB is used as ground plane for the lens antenna. The following reports the design of the lens antenna with the polarizer. The manufacturing and assembling steps are presented. Finally, simulation and measurement results are compared to verify the concept.

Lens Antenna Design

Fig. 5.7a depicts a cross-section (yz-plane) of the lens antenna with the polarizer. The latter includes E-plane tapers to match the height of the SIWs at the input to that of the square SIW on the antenna side. The superstrates consist of a material with dielectric

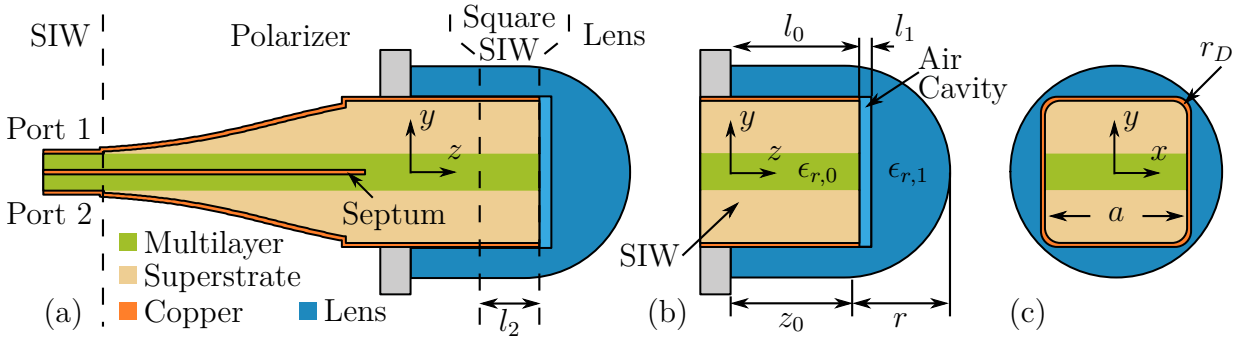

Figure 5.7: (a) Cross-section (xy-plane) of the SIW lens antenna and of the lens in (b) the xy-plane and (c) the yz-plane.

properties similar to those of the multilayer PCB. For the lens design, the square SIW is modeled by a homogeneous dielectric.

To reduce the antenna losses at lower frequencies, the cutoff frequency of the square SIW is reduced to 17.5 GHz by an increased width of $a = 4.7\,\text{mm}$. Furthermore, to ease the manufacturing of the cavity in the lens, the edges of the square SIW are rounded by a radius of $r_D = 0.5\,\text{mm}$, as illustrated in Fig. 5.7c. With the slightly modified square SIW, the design of the lens geometry is repeated as detailed in [72]. For this, the small lens radius of $r = 3.5\,\text{mm}$ and the lens material with $\epsilon_{r,1} = 2.1$ are unchanged. The remaining lens parameters are slightly increased and listed in Tab. B.9, where this lens antenna is called *LEN2*. For this design, the maximum input reflection is reduced to $\Gamma_{max} = -18\,\text{dB}$ and the directivity variation is slightly increased to $D_{rel} = 0.7\,\text{dB}$. Here, a frequency band from 18 GHz to 32 GHz is assessed. Thus, the fractional bandwidth of the lens antenna is increased to 58 %.

For the polarizer the design *POL1* from Sec. 4.2 is taken. It yields two circularly-polarized modes in the square SIW with a good axial ratio in the Rx and Tx frequency bands. However, the polarizer limits the usable bandwidth. Next, the polarizer is combined with the lens antenna. As discussed in Sec. 4.2, this is uncritical for the Rx frequency band because only the fundamental TE_{10}- and TE_{01}-modes can propagate in the square SIW and they are well-matched at the polarizer output and the antenna input. For the Tx frequency band, resonances due to multiple reflections of the TE_{11}- and the TM_{11}-modes can notably decrease the gain and vary the phase of the far-field components. The resonant frequencies depend on the length l_2 between the end of the polarizer septum and the end of the square SIW. As typical for a resonator, these frequencies are reduced for larger l_2. Here, $l_2 = 3\,\text{mm}$ is selected to place the first spurious resonance below the typical Tx frequency band at 27.2 GHz. A quantitative discussion of the resonance frequencies with an equivalent circuit model and antennas with three different lengths is given in [72].

Manufacturing

The employed multilayer is based on laminates from the *Rogers RO4000* series and glued superstrates. The layer stack is depicted in Fig. 5.8a and the manufacturing steps are detailed in the following:

1. A multilayer with three copper layers is manufactured in standard PCB processes, as depicted in Fig. 5.8b. The middle layer separates the two stacked SIWs and contains the septum from the polarizer. The outer layers include SIW-to-CPW transitions (see *CPW-SIW4* in Tab. B.5) and footprints for 2.92 mm-connectors (*Rosenberger 02K80A-40ML5*).
2. The superstrates are milled out of dielectric sheets (*Preperm L335* from *Premix*) and, then, glued on both sides of the multilayer with *Loctite 406*. They are shaped in such a way that enough material is available for the polarizer and to accommodate holes for the alignment pins, as depicted in Fig. 5.8c.
3. The taper of the polarizer and the sidewalls of the square SIW are milled. The resulting structure is shown in Fig. 5.8d.
4. To protect the outer copper layers, they are covered by a Kapton film (*P-221*) from *Nitto*.
5. The complete structure is metalized with silver. A process from *Jet Metal Technologies* is used that is based on an innovative spraying technique.
6. The Kapton film is removed and unplated holes are drilled. Finally, the antenna feed is milled out. Fig. 5.8e depicts the resulting structure. The walls of the polarizer and the square SIW are covered by metal, but of course not the antenna aperture.

An exploded view of the complete antenna assembly is shown in Fig. 5.6b. The lens is machined from PTFE and the ground plane is manufactured using two aluminum parts. A conductive O-ring from *Soliani EMC* between these parts ensures good galvanic contact

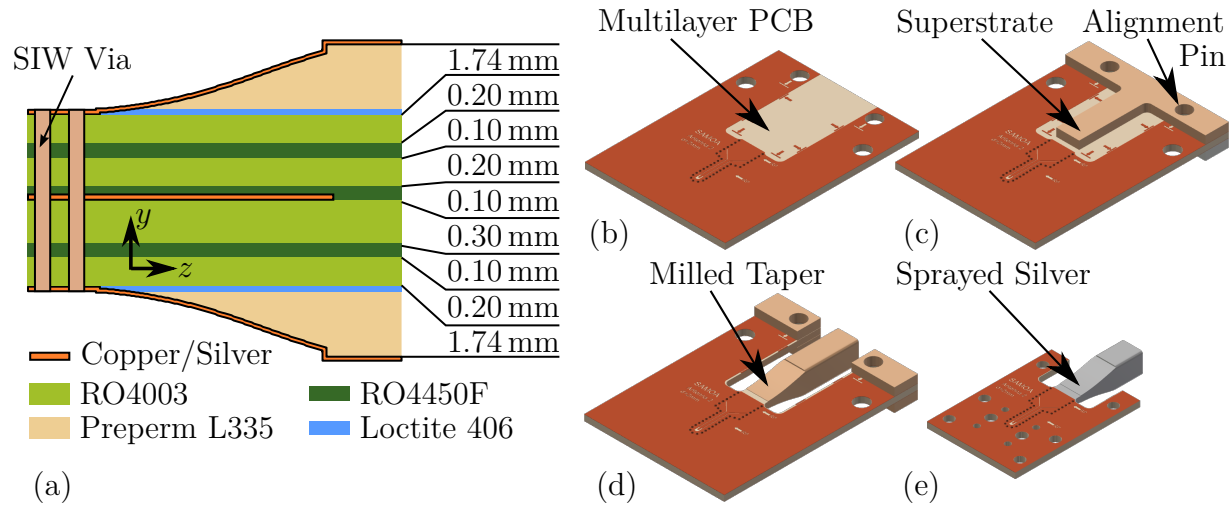

Figure 5.8: (a) Multilayer stack with superstrates. (b-e) Manufacturing steps of the SIW feed.

to the square SIW. An absorber is placed around the lens to mitigate the effects of the finite ground plane. Fig. 5.6c depicts the PCB with the square SIW cut open to show the septum.

Measurements

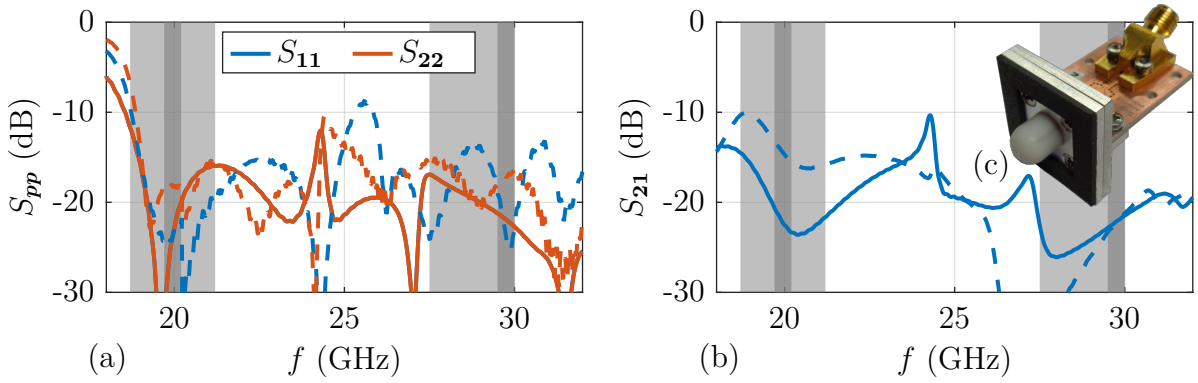

Figure 5.9: Scattering parameters of the lens antenna with polarizer (— simulation, - - - measurements, ■ typical / ■ reference bands).

Fig. 5.9c shows a photograph of the realized lens antenna. The scattering parameters of the two input ports are depicted in Fig. 5.9a and Fig. 5.9b. The reference planes are shifted to the multilayer SIW using a TRL calibration. The measured results agree acceptably well with the simulated ones. In the following, the performance is assessed in the frequency ranges from 19 GHz to 23 GHz and 27.5 GHz to 31 GHz. The measured input reflection remains below −13 dB and is higher than the simulated reflection of −16 dB. In the lower frequency band, the measured minimum port isolation is 10 dB and, thus, significantly smaller than the simulated 15 dB. In contrast, the measured minimum port isolation of 19 dB in the upper frequency band is slightly higher than the simulated value of 17 dB.

The far-field patterns of the antenna are measured in an anechoic chamber. The patterns are calibrated by the three-antenna method [164, Sec. 12.2.2] and the reference planes are shifted to the multilayer SIWs. Time gating with a window of 3.5 m is used to reduce the effect of multiple reflections in the measurement setup. In Fig. 5.10 the realized gain in

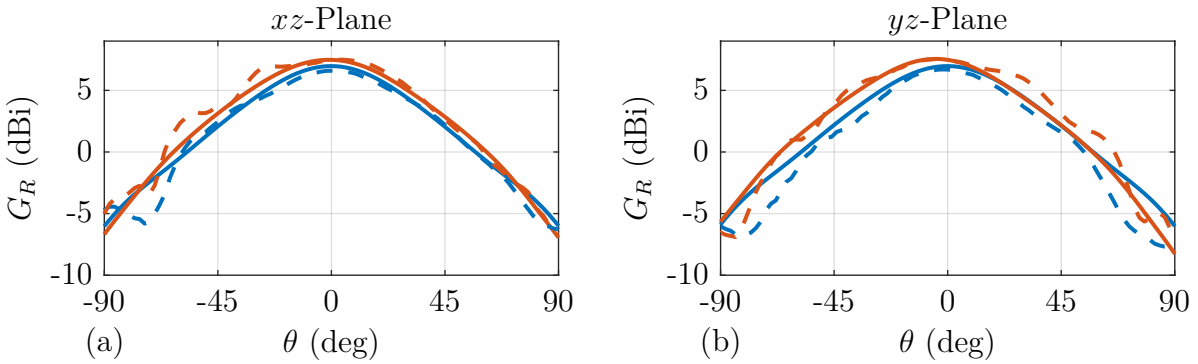

Figure 5.10: Realized gain in xz- and yz-plane for an excitation at port **2** (— simulation, - - - measurements, — 20 GHz, — 30 GHz).

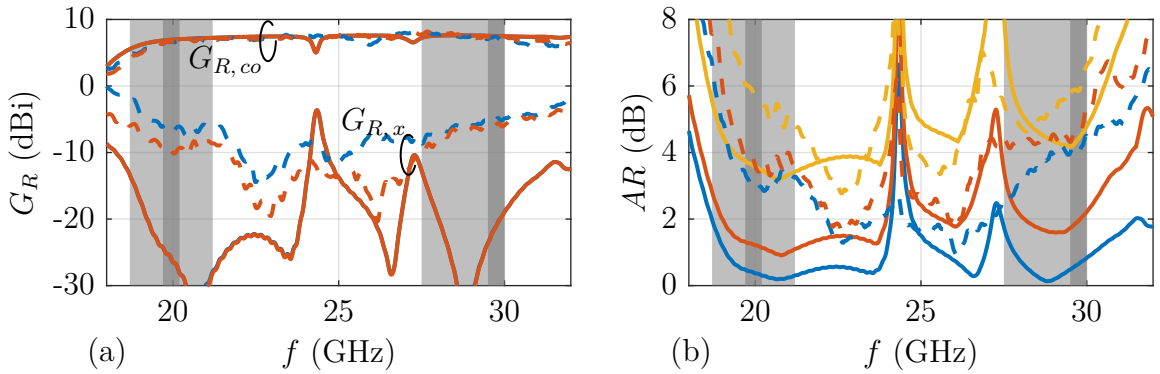

Figure 5.11: (a) Realized gain in boresight direction (— simulation, - - - measurements, — Port **1** / RHCP, — Port **2** / LHCP). (b) Maximum axial ratio in conical sectors (— $\theta = 0°$, — $\theta \leq 15°$, — $\theta \leq 30°$, ■ typical / ■ reference bands).

the xz- and yz-plane for an excitation at port **2** is plotted versus the elevation angle θ at 20 GHz and 30 GHz. The simulation and measurement results match reasonably well. The 3 dB-beamwidth is 66° and 72° at 20 GHz and 30 GHz, respectively.

Fig. 5.11a shows the realized gain in boresight direction for both RHCP (port **1**) and LHCP (port **2**). In the considered frequency ranges, the simulated co-polarized gain $G_{R,co}$ ranges between 6.2 dBi and 7.6 dBi. This is reasonably well confirmed by measurements, in contrast to the measured cross-polarized gain $G_{R,x}$, which is significantly higher than estimated by the simulation. Fig. 5.11b shows the resulting axial ratio AR in boresight direction. In the lower and upper band, the simulation yields values below 1.2 dB and 1.7 dB, respectively. However, the measured vales are considerably higher and reach up to 4.9 dB. In addition, Fig. 5.11b shows the maximum axial ratio in conical sectors of $\theta \leq 15°$ and of $\theta \leq 30°$. For the first sector, the simulated axial ratio rises to 2 dB and 3.5 dB in the lower and upper frequency band. The increase is even worse in the second sector. Here, the axial ratio rises to 4.5 dB and 8 dB in the two bands, respectively. In general, the axial ratio degrades for small and large frequencies as well as in the region of the resonances. The polarizer and the square SIW resonances are at 24.3 GHz and 27.3 GHz, respectively. This degradation might be acceptable in the boresight direction. However, for an array antenna, the axial ratio in the pointing direction is relevant. To overcome this issue, the axial ratio of the far-field pattern has be optimized. In view of the large bandwidth, this is quite challenging. An alternative is to apply the polarization compensation technique using a simultaneous excitation of both ports, as discussed in Sec. 4.2. However, the gain decreases at low frequencies and in the vicinity of the resonances due to higher losses. These losses can be reduced by a further reduction of the cutoff frequency and a careful polarizer design.

The notable increase in the measured axial ratio can be attributed to significant deviations of the material parameters. In particular, the dielectric constant of the superstrates is higher than assumed. This is confirmed by additional measurements in a split-cylinder

resonator [157] from which the dielectric constant is determined to be 3.6 rather than the nominal value of 3.35. This yields different propagation constants for the TE_{10}- and TE_{01}-modes in the square SIW. Thus, the circular polarization becomes elliptical, which increases the axial ratio along the square SIW. A more detailed discussion of these deviations is given in [72]. In conclusion, the presented lens antenna validates the concept and shows the dual-band and the dual-polarization functionality.

5.2 Lens Array Antenna

The design of the array antenna is based on the results from the single antenna element and on the components of Chapter 4. In addition to the presented Rx/Tx element, a Tx-only element is designed. Both element types are arranged in the interleaved rectangular array grid. The hemispherical lens surface is replaced by a periodic lens surface. Similar structures are known from classical waveguide arrays [67, 69]. Here, planar dielectric layers are placed inside the waveguides and on top of the aperture.

This section starts with the design of the lens surface. In a first step, the dielectric lens is excited by square SIWs. The resulting array structure is subsequently combined with polarizers. The manufacturing and assembly is discussed and, finally, the measured array performance is compared to simulation results.

5.2.1 Lens Surface Design

For the description of the lens surface, non-uniform rational basis splines (NURBS) are employed [165]. The same way splines can describe curves, NURBS can define surfaces. They are a standard tool used for many computer-aided designs. In this context, the NURBS are used as a flexible and simple description of the periodic lens surface. The Rx/Tx elements and the Tx-only elements are arranged in an alternating order with a distance d_{Tx}, as discussed in Sec. 2.2. The parameters of the respective elements are labeled by 1 and 2. The square SIWs have width a_n and height b_n and they protrude with length l_n into the backside of the lens, as depicted in Fig. 5.12a. The lens surface is

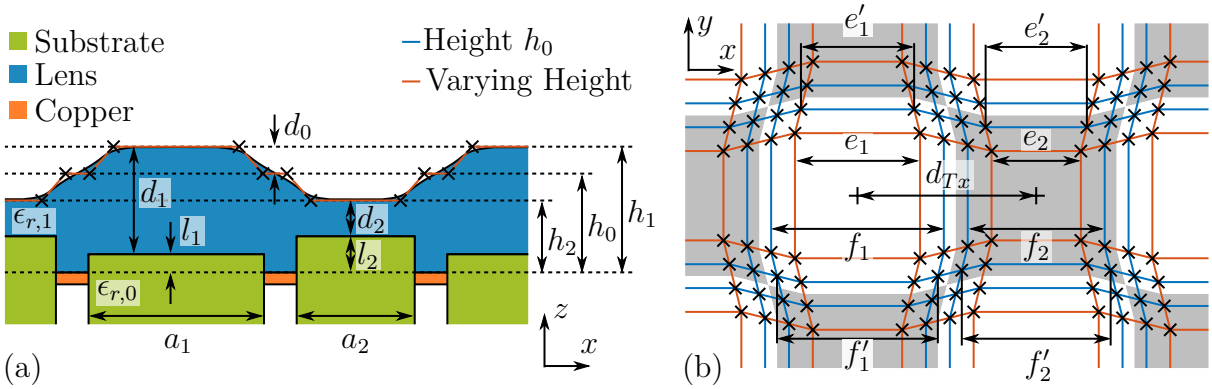

Figure 5.12: (a) Cross-section and (b) control point grid of parameterized lens surface.

defined by a grid of control points, as shown in Fig. 5.12b. For each element n, sixteen control points are specified in the white or gray area. The point arrangement imposes a rotational symmetry of order four and mirror symmetries in the xz- and yz-plane. Four of these points are placed in a square of width e_n around the element center at a height h_n. The remaining twelve intermediate points are placed concentrically around the element at height h_0. The polygon connecting these points is defined by the parameters

$$e'_n = e_n - \alpha \frac{e_1 + e_2}{2}, \tag{5.1a}$$

$$f_n = e_n + \alpha \left(d_{Tx} - \frac{a_1 + a_2}{2} \right), \tag{5.1b}$$

and

$$f'_n = f_n - \alpha \frac{f_1 + f_2}{2} \tag{5.1c}$$

as depicted in Fig. 5.12b. The factor α determines the relative position of the intermediate control points. For $\alpha = 0$, the intermediate points are placed at the edges of the square of width e_n. For $\alpha = 1$, the intermediate control points are placed in the middle between the two element types. The lens surface is generally smoother for larger α values. The heights $h_n = l_n + d_n$ and $h_0 = h_1 - d_0$ are parameterized by the distances d_n and d_0. Here, d_n is the distance between the end of the SIW and the lens surface, whereas d_0 is that between h_1 and h_0. The arrangement acts as an impedance transformer, e.g., a quarter-wave transformer, which matches the square SIW at the input. To obtain a smooth lens surface, an order of four is chosen for the NURBS. Thus, the piecewise rational basis functions has a degree of three. Further, each control point has a weighting factor. For larger factors, the surface is pulled closer to the control points. Each height h_n is associated with a weighting factor w_n. For the intermediate points, the weighting factors w_0 and w'_0 are assigned to the eight points separated by f_n and to the four points separated by f'_n, respectively. For this parameterization, the coordinates and weighting factors of the control points of an element are given in (B.2).

In the following, the parameterized lens surface is used to optimize the array performance by means of a parameter study. As a result from the selected materials and prior investigations, some parameters are fixed. The square SIWs and the lens consists of *Megtron 6* substrate from *Panasonic* and *Duroid 5880* substrate from *Rogers*, respectively. The lens material has a dielectric constant of 2.2 and is thus similar to the previously used lens material. Tab. B.1 summarizes the dielectric properties of the selected materials. For the square SIWs, widths of $a_1 = 4.8\,\text{mm}$ and $a_2 = 3.2\,\text{mm}$ and heights of $b_1 = 4.6\,\text{mm}$ and $b_2 = 3.1\,\text{mm}$ are chosen. The corners of the square SIW of the Rx/Tx element have a chamfer of 0.5 mm to increase the space between two diagonal SIWs. The SIW walls are coated by a copper layer with an assumed surface roughness of $R_q = 2.8\,\mu\text{m}$. The resulting cutoff frequencies and effective dielectric constants are listed in Tab. 5.1. The cutoff

Table 5.1: Waveguide modes of the square SIWs.

m	Mode	f_c (GHz)		$\epsilon_{r,eff}$		Symmetry	
		SIW 1	SIW 2	SIW 1	SIW 2	xz-Plane	yz-Plane
1[1]	TE_{01}	16.8	24.3	3.91	3.91	PEC	PMC
2[2]	TE_{10}	16.7	24.4	3.64	3.63	PMC	PEC
3	TM_{11}	22.8	-	3.85	-	PMC	PMC
4	TE_{11}	24.1	-	3.70	-	PMC	PMC

[1] Horizontal mode. [2] Vertical mode.

frequencies of the fundamental modes of the Rx/Tx SIW are reduced to about 16.7 GHz compared to Sec. 5.1.2. The cutoff frequencies of the fundamental modes of the Tx-only SIW are 24.3 GHz. To reduce the number of design parameters, some of them are fixed based on prior investigations. The main idea is to impress the shape of the square SIWs into the lens surface, whereby the surface above the SIWs should be relatively flat. To achieve this, the lens surface is defined by the widths $e_1 = 4.5\,\text{mm}$ and $e_2 = 3.1\,\text{mm}$, the factor $\alpha = 0.2$, and the weighting factors $w_1 = w_2 = 5$, $w_0 = 1$, and $w_0' = 0.2$. As a result, the transition between the surfaces of two elements is quite rapid but still smooth due to the NURBS. The remaining five parameters are the distances d_1, d_2, and d_0, as well as the lengths l_1 and l_2, defined in Fig. 5.12a. Their value is varied in the parameter study.

To investigate the performance of the lens, two simulation models are used, as depicted in Fig. 5.13a and Fig. 5.13b. The simulation time is kept as small as possible with 3×3 lens array antennas on an infinite ground plane. These setups approximate the array environment for the central element, i.e., the Rx/Tx or the Tx-only element, respectively. To determine the far-field patterns, the input reflections, and the coupling coefficients to neighboring elements, the central element is excited with the modes listed in Tab. 5.1. The model size is further reduced by considering the mode symmetries in the simulation setups, as listed in Tab. 5.1. The elements of the simulation models are numbered as shown in Fig. 5.13. The performance of the lens array is assessed through three different parameters, which are calculated in the typical frequency bands defined in Chapter 1. The

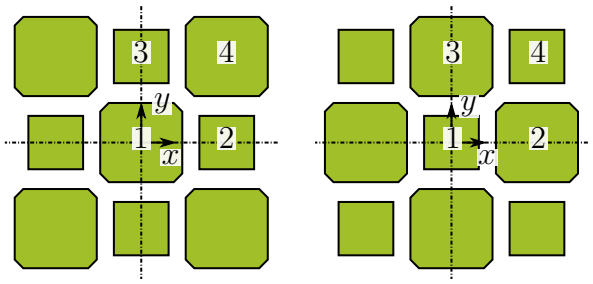

(a) (b)

Figure 5.13: Simulation models with (a) the Rx/Tx and (b) the Tx-only element at the center.

Table 5.2: Intervals of the parameter study.

Parameter	min.	max.
d_0 (mm)	0	1.5
d_1 (mm)	1.8	3
d_2 (mm)	1.5	2.1
l_1 (mm)	0	1.5
l_2 (mm)	0	1.5

Table 5.3: Performance of the selected lens geometries *ALEN1*, *ALEN2*, and *ALEN3*.

Element	Mode	Γ_{max} (dB)			L_{max} (dB)			D_{rel} (dB)		
		$\mathbf{1}^{1}$	$\mathbf{2}^{1}$	$\mathbf{3}^{1}$	$\mathbf{1}^{1}$	$\mathbf{2}^{1}$	$\mathbf{3}^{1}$	$\mathbf{1}^{1}$	$\mathbf{2}^{1}$	$\mathbf{3}^{1}$
Rx/Tx	1	−17.3	−17.5	−16.3	−13.2	−13.2	−13.3	1.2	1.1	1.2
Rx/Tx	2	−16.3	−16.5	−15.4	−12.7	−12.5	−13.2	1.5	1.5	1.5
Tx only	1	−18.0	−18.3	−19.2	−10.0	−10.0	−10.0	0.7	0.8	0.6
Tx only	2	−16.2	−16.5	−17.2	−9.8	−9.8	−9.9	0.8	0.9	0.7
all	all	−16.2	−16.5	−15.4	−9.8	−9.8	−9.9	1.8	2.0	1.6

[1] Index of lens geometry *ALEN*.

maximum input reflection Γ_{max} and the relative directivity variation D_{rel} are adapted from the design of a single element. In addition, the maximum coupling loss

$$L_{max} = \max_{f} \left(\sum_{\bar{n}[\bar{m}] \neq 1[m]} \left| S_{\bar{n}[\bar{m}],1[m]}(f) \right|^2 \right) \tag{5.2}$$

is evaluated. It is defined as the maximum of the sum of all parasitic couplings in the assessed frequency range. As it is a measure for the mutual coupling, small values are desired.

The five geometrical parameters of the lens antenna are varied in the intervals given in Tab. 5.2. For each parameter combination, the models are simulated and the performance parameters are calculated. From these results, the three most promising geometries, called *ALEN1*, *ALEN2*, and *ALEN3* in the following, are selected. The geometry parameters are listed in Tab. B.11. The assessed performance parameters are listed in Tab. 5.3. They differ for each element and mode combination. In the last row, they are combined to a single parameter. For Γ_{max} and L_{max}, the maximum values are chosen. In the case of D_{rel}, the variation is determined from the maximum and minimum element directivity of all element and mode combinations. For the selected geometries, Γ_{max} is lower for mode 1 of the waveguides and D_{rel} is lower for the Tx-only element. The optimization of the Rx/Tx element is in general more challenging because the two frequency bands are considered. *ALEN2* and *ALEN3* have the smallest Γ_{max} and D_{rel} values, respectively. The coupling losses of all selected geometries are nearly the same. *ALEN1* is a compromise between *ALEN2* and *ALEN3*.

Fig. 5.14 shows contour plots of the three performance parameters versus the different geometrical parameters. The selected lens geometries are marked by crosses. Fig. 5.14a shows Γ_{max} versus d_1 and d_2 for $l_1 = l_2 = 0$ and $d_0 = 0.3\,\text{mm}$. The geometry *ALEN2* exhibits the minimum value. Fig. 5.14g depicts D_{rel} for the same parameter variation. Here, *ALEN3* shows the minimum value and *ALEN1* is slightly better than *ALEN2*. For this parameter variation, L_{max} is almost constant, as depicted in Fig. 5.14d. The three performance parameters are plotted versus d_1 and d_0 for $l_1 = l_2 = 0$ and $d_2 = 1.8\,\text{mm}$ in Fig. 5.14b, Fig. 5.14e, and Fig. 5.14h. The geometry *ALEN1* has the best Γ_{max} value, but

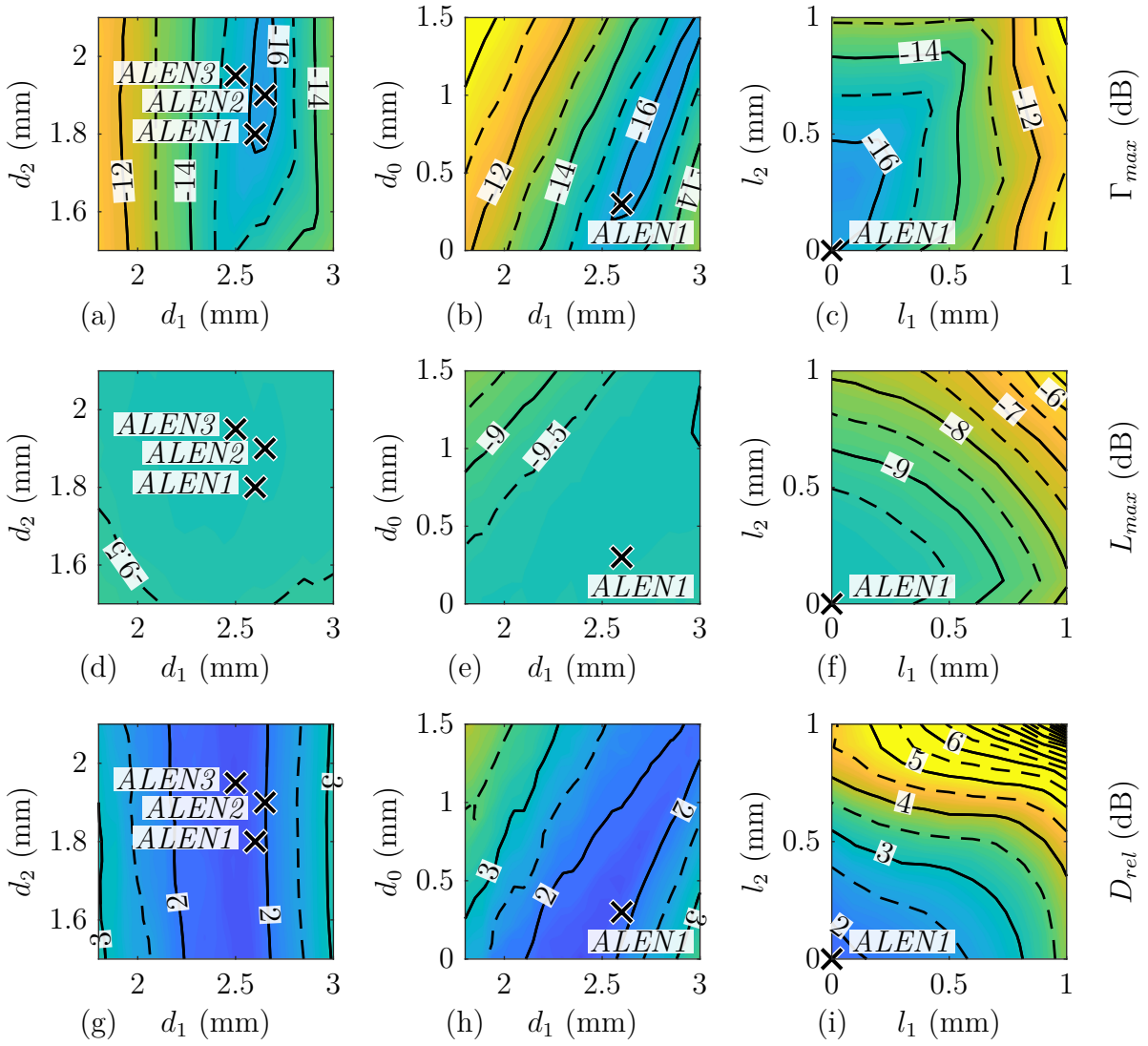

Figure 5.14: (a) Γ_{max}, (d) L_{max}, and (g) D_{rel} versus d_1 and d_2 ($d_0 = 0.3\,\text{mm}$, $l_1 = l_2 = 0$). (b) Γ_{max}, (e) L_{max}, and (h) D_{rel} versus d_1 and d_0 ($d_2 = 1.8\,\text{mm}$, $l_1 = l_2 = 0$). (c) Γ_{max}, (f) L_{max}, and (i) D_{rel} versus l_1 and l_2 ($d_0 = 0.3\,\text{mm}$, $d_1 = 2.6\,\text{mm}$, $d_2 = 1.8\,\text{mm}$).

D_{rel} could be improved by decreasing d_1. Finally, Fig. 5.14c, Fig. 5.14f, and Fig. 5.14i show the three parameters versus l_1 and l_2 for $d_0 = 0.3\,\text{mm}$, $d_2 = 2.6\,\text{mm}$, and $d_2 = 1.8\,\text{mm}$. Compared to *ALEN1*, Γ_{max} can be slightly improved by increasing l_2. However, D_{rel} deteriorates rapidly for larger l_1 or l_2. For $l_1 = l_2 = 0$, a good performance is achieved and the manufacturing is simplified because no cavity must be machined on the backside of the lens. In summary, the geometry *ALEN1* is selected, as it represents a good compromise. Its performance parameters are $\Gamma_{max} = -16.2\,\text{dB}$, $L_{max} = -9.8\,\text{dB}$, and $D_{rel} = 1.8\,\text{dB}$.

Fig. 5.15b and Fig. 5.15c shows the scattering parameters of the first simulation model. The input reflection and the coupling coefficients are very low in both frequency bands. The input reflection of the second mode at the upper edge of the Rx frequency band

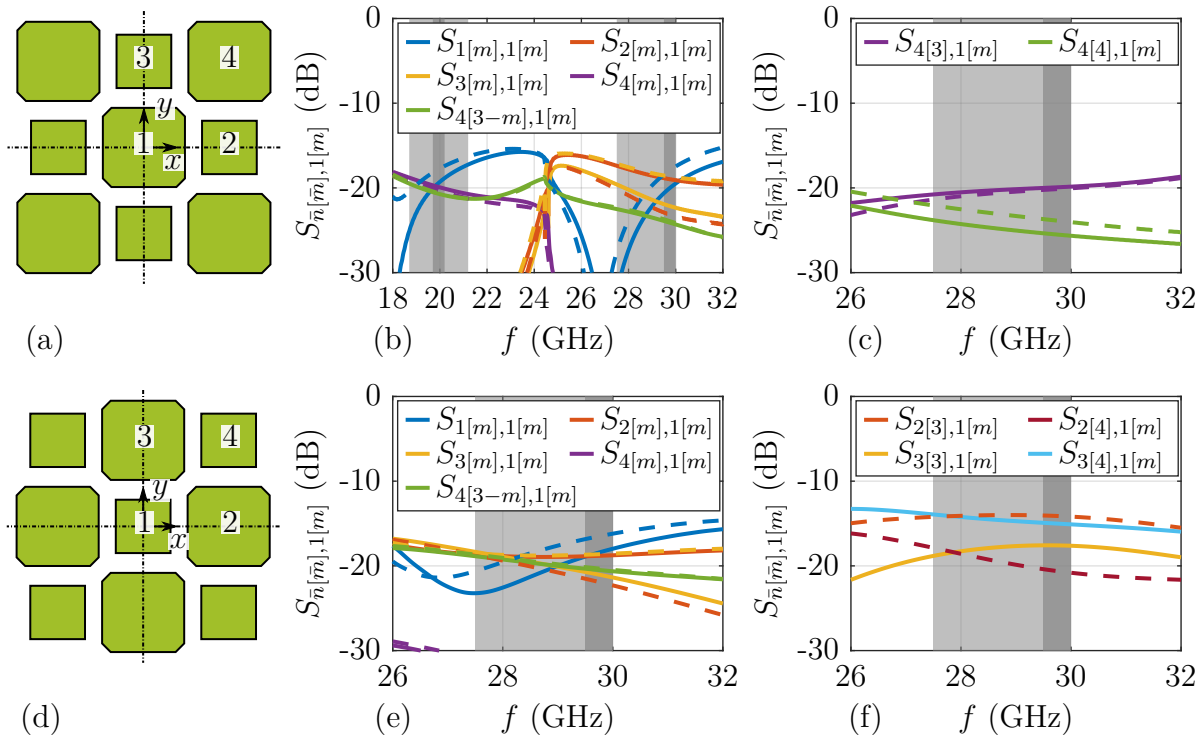

Figure 5.15: Simulation setup with the (a) Rx/Tx and (d) Tx-only element at the center. Scattering parameter of (b,e) the fundamental and (c,f) higher-order modes for both setups, respectively (— horizontal ($m = 1$), - - - vertical ($m = 2$), ■ typical / ■ reference bands).

is the largest scattering parameter. It defines Γ_{max}. For the Rx frequency band, the coupling coefficients of the fundamental modes between the elements 1 and 4 remains below −18.8 dB and are relatively similar for all mode combination. For the Tx frequency band, the fundamental modes of the elements 2 and 3 are above cutoff and, thus, these couplings must be considered. They are below −17.2 dB but higher than the diagonal coupling to element 4. The diagonal coupling to higher-order modes is less than −19.8 dB, as plotted in Fig. 5.15c. The simulated scattering parameters of the Tx-only element are plotted in Fig. 5.15e and Fig. 5.15f. The coupling coefficients of the fundamental modes

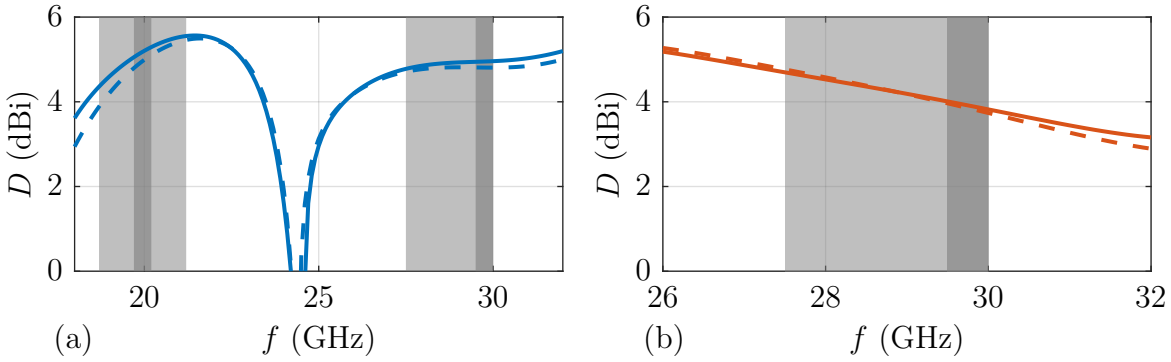

Figure 5.16: Directivity of *ALEN1* for (a) Rx/Tx and (b) Tx-only element (— horizontal ($m = 1$), - - - vertical ($m = 2$), ■ typical / ■ reference bands).

from element 1 to the other elements are below −18.3 dB. The coupling to higher-order modes of element 2 and 3 are below −14 dB. Fig. 5.16 shows the directivity of the Rx/Tx and Tx-only elements. It ranges between 3.9 dBi (3.7 dBi) and 5.6 dBi (4.8 dBi) for the Rx/Tx (Tx-only) element in the typical frequency bands. The directivity is relative flat and, thus, a similar performance is achieved over frequency.

5.2.2 Lens Array Antenna with Polarizers

The following reports an 8×8 element array antenna with polarizers. To mitigate edge effects, the outer elements are terminated. Thus, effectively, the performance of an undisturbed 4×4 array is investigated. The lens array antenna is combined with polarizers. For the Rx/Tx element, polarizer *POL2* from Sec. 4.2 is used. The Tx-only element utilizes polarizer *POL3* (see Tab. B.8). The feed SIWs of the central 4×4 array are depicted in Fig. 5.17a. Each antenna element n has two input ports (n,**1**) and (n,**2**) for LHCP and RHCP. The position of the polarizer septum alternates between the right and the left side. The polarization of the inputs changes accordingly.

Modeling the Lens Array Antenna with Polarizers

A full-wave simulation of the whole lens array antenna with the polarizers was not possible with the available computational resources. To overcome this, the lens array antenna is first simulated without the polarizers and, then, combined with them through an equivalent circuit. For this, the scattering parameters and the element far-field patterns of the fundamental modes are calculated by full-wave simulation. Additionally, the same characteristics are calculated for the higher-order modes of the Rx/Tx elements in the upper frequency band. Then, these results are combined with simulation results from the

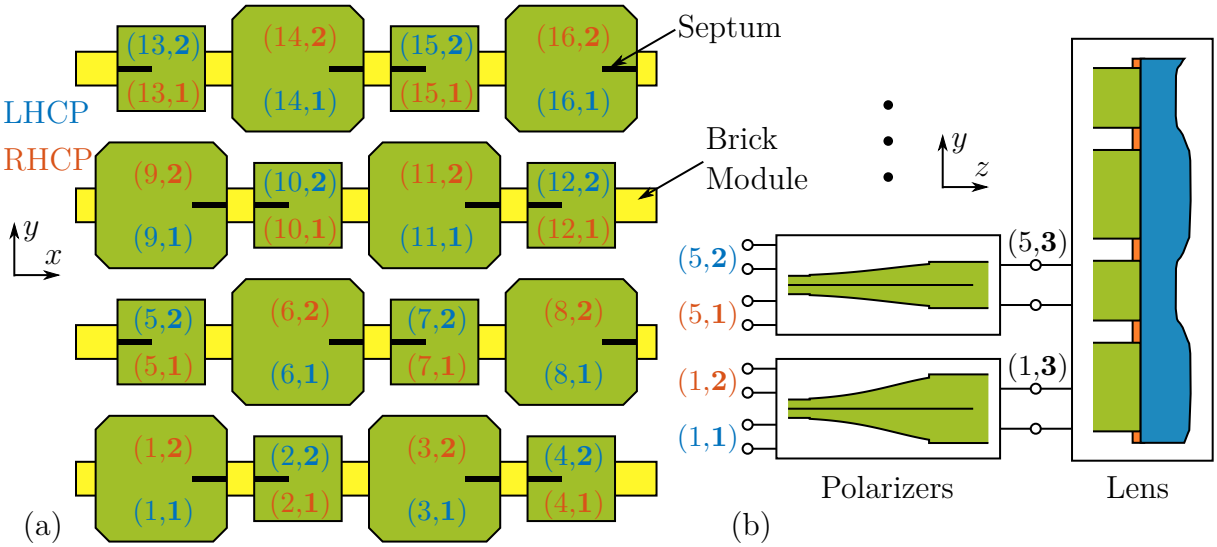

Figure 5.17: (a) Top-view and port numbering of the central SIW feeds and (b) equivalent circuit of lens array antenna.

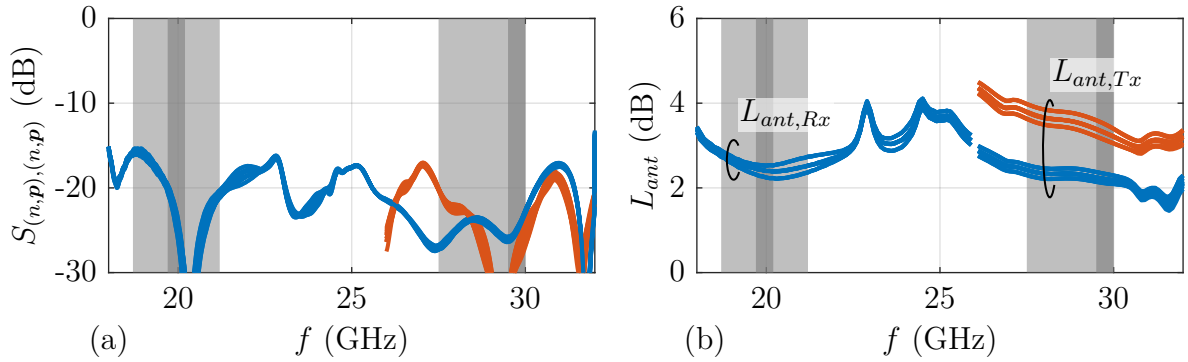

Figure 5.18: Simulated (a) input reflection and (b) antenna losses L_{Rx} and L_{Tx} of array elements (— Rx/Tx element, — Tx-only element, ■ typical / ■ reference bands).

polarizers at the ports (n,**3**), as depicted in the equivalent circuit of Fig. 5.17b. Here, the couplings through the square SIWs due to evanescent waveguide modes are neglected and, thus, the array characteristics are only approximated by the equivalent circuit model.

Fig. 5.18a shows the input reflections of the elements of the array antenna. The results show only little variation for the elements of the same type. The maximum reflection of the Rx/Tx elements is −15.3 dB and −22.6 dB in the typical Rx and Tx frequency bands, respectively. For the Tx-only element, the maximum input reflection is −20 dB. Fig. 5.18b depicts the element loss, which is an important figure for the array performance, as discussed in Sec. 2.5. For the Rx case, the element losses $L_{ant,Rx}$ range between 2.2 dB and 2.9 dB in the typical frequency band and about 2.4 dB are achieved in the reference frequency band. For the Tx case, the losses $L_{ant,Tx}$ range between 2.1 dB (3 dB) and 2.5 dB (4 dB) for the Rx/Tx (Tx-only) element with about 2.2 dB (3.3 dB) in the reference frequency band. Further properties of the lens array antenna, like mutual coupling and far-field characteristics, are discussed later in comparison with measurement results.

Realization and Manufacturing

The lens array antenna is based on brick modules, which are implemented in PCB technology. Fig. 5.19 shows the PCB with the two element types. To connect the polarizer inputs with the coaxial cables of the measurement equipment, transitions to very small SMPS connectors[2] are added on the left hand side of the polarizers. The connectors are soldered on top of CPWs. These have bends to shift the connector positions in opposite directions on the two sides of the PCB, a necessity in view of the limited available space. A combination of CPW-to-SIW transitions and SIW tapers is implemented to feed the medium height SIWs at the polarizer inputs. Tab. B.12 lists the relevant dimensions. The overall length of the PCB is 37 mm.

[2]Here, the SMPS (Sub-Miniature Push-on Sub-micro) connectors *3811-40003* from *SV Microwave* are used.

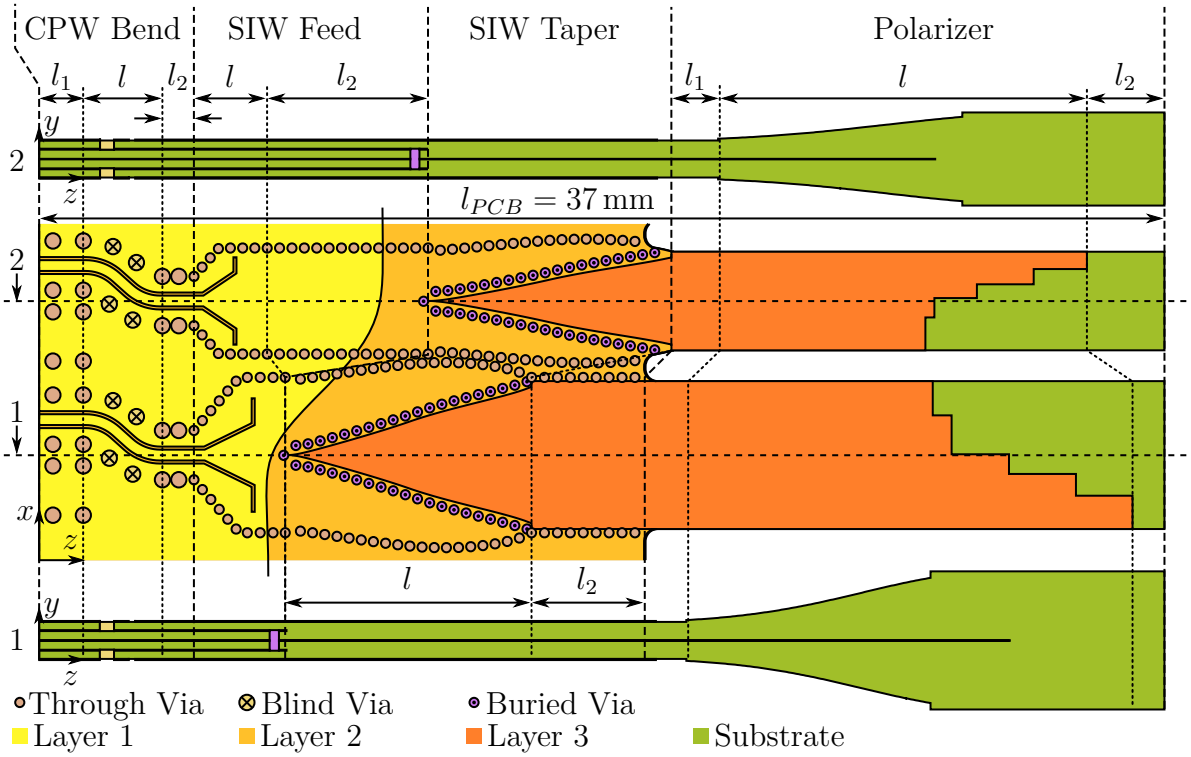

Figure 5.19: PCB of the brick modules with the Rx/Tx and Tx-only element. The dimensions are locally defined for each component.

The array is realized with laminates from the *Megtron 6* series and low-flow prepregs for bonding the superstrates. Fig. 5.20 depicts the layer stack. The following details the manufacturing steps:

1. Fig. 5.21a shows the inner multilayer with five metal layers. It is manufactured by standard PCB processes. For this, two bond cycles are necessary to realize buried, blind, and through vias. The structures are almost symmetric with respect to the middle metal layer, which contains the septa for the polarizers.
2. The superstrates are also made from *Megtron 6* laminates. They are bonded on both sides of the inner multilayer using shaped low-flow prepregs (*Arlon 49N*). These prepregs have only a thickness of 50 µm and very controlled flow properties. This is important at the edge of the superstrates to prevent prepreg from flowing over

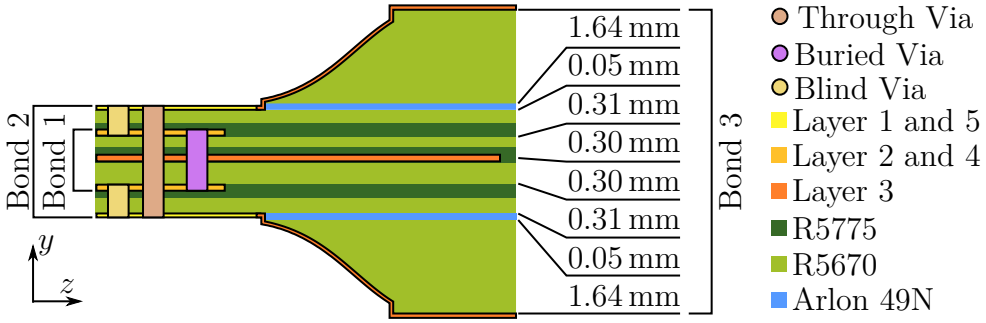

Figure 5.20: Multilayer stack of the lens array antenna.

the outer metal layers. These prepregs are often used to bond flex-rigid PCBs and are thus compatible with standard PCB technology. Fig. 5.21b depicts the resulting structure.

3. The taper of the polarizers and the sidewalls of the square SIWs are milled. Fig. 5.21c shows the resulting structure.
4. A Kapton film (*Nitto P-221*) is applied on the outer metal layers to protect them.
5. The PCB is metalized in several steps. A very thin copper layer is deposited by a chemical process. Then, the layer thickness is galvanically increased to 17 µm and the Kapton film is removed. Finally, the copper surface is protected by a conductor surface treatment. Here, an immersion silver and immersion gold process from *Hofstetter* is used. The silver layer has very good electrical properties, and the gold layer prevents oxidation.
6. Unplated holes are drilled and the brick modules are milled out. The final brick module is depicted in Fig. 5.21d.

The manufacturing of the brick modules is similar to that of the SIW feeds of a single lens antenna element, as discussed in Sec. 5.1.2. However, more standard processes are used and, thus, the manufacturing is simplified. Indeed, the brick modules are realized as a thick standard multilayer, the same laminates being used for the inner multilayer and the superstrates. The single element, on the other hand, is composed of different materials, which have to be glued together. Additionally, the low-flow prepreg has a better-controlled thickness and the process is more reliable. The relatively high dielectric losses of the low-flow prepreg are acceptable because of the very low thickness of 50 µm. As a further advantage, the materials used in the array can be metalized with standard processes.

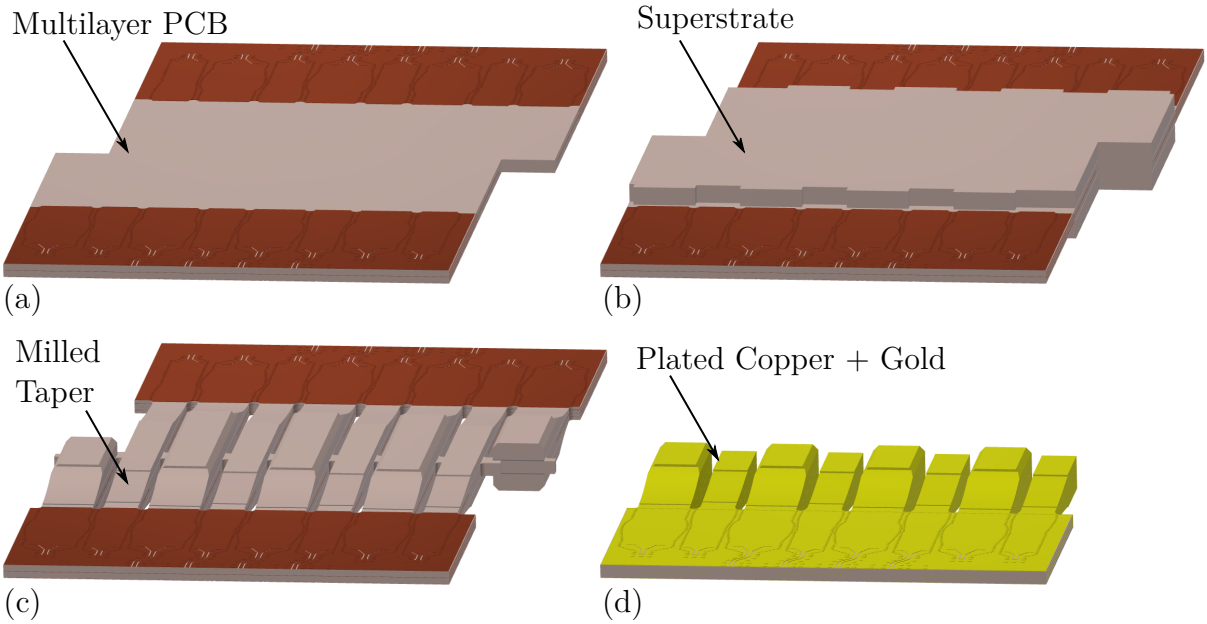

Figure 5.21: Manufacturing steps of a brick module.

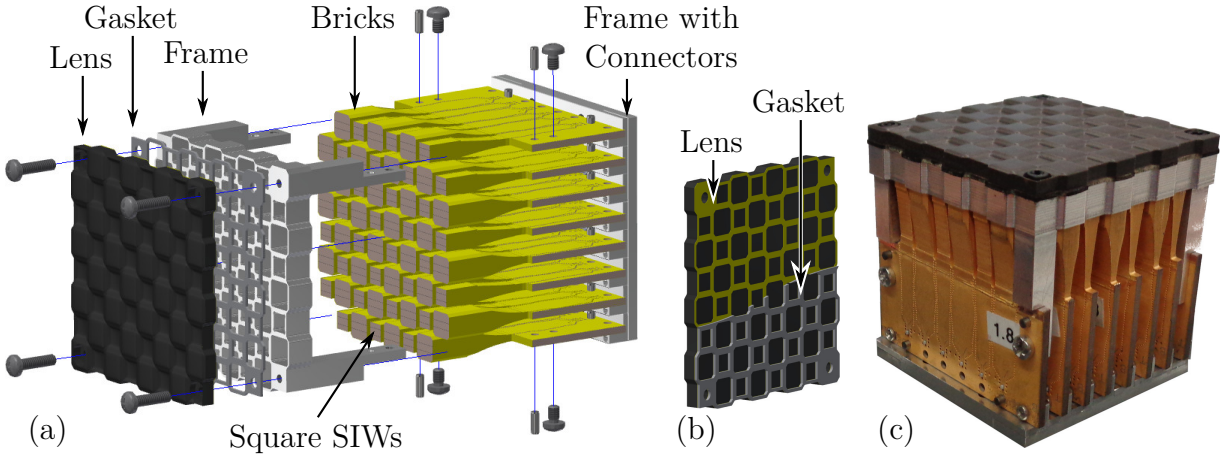

Figure 5.22: (a) Exploded view, (b) backside of the lens with gasket, and (b) photograph of the lens array antenna.

Eight of such brick modules are combined for the lens array antenna, as depicted in Fig. 5.22a. The inner 4×4 elements are fed via SMPS connectors and the others are terminated by SMD resistors (*CH02016-50RGFT* from *Vishay*). The lens is milled in a *Duroid 5880* substrate from *Rogers*. The bottom copper layer is selectively removed to fit the SIWs apertures, as illustrated in Fig. 5.22b. Because of its smooth surface, the lens could also be manufactured by injection molding. For high volumes, this would reduce manufacturing costs. An aluminum frame at the front side maintains the assembled brick modules and the lens. It features apertures to accommodate the SIW antennas and four screws at the edges fix the lens. A conductive gasket between the frame and the lens ensures the required galvanic contact with the SIWs. The gasket is fabricated from a 0.5 mm thick conductive silicon rubber sheet (*Compashield 8650* from *Nolato*) by means of a laser cutter. At the array inputs, a second frame assembles the brick modules and holds the SMPS connectors. A photograph of the realized lens array antenna is shown in Fig. 5.22c.

Measurements

The performance of the realized lens array antenna is verified by measurements in the following. The scattering parameters are analyzed first. The reference planes are placed at the CPWs by means of a TRL calibration. Manufacturing issues prevented shifting them to the polarizer inputs. Indeed, the coating applied during the final surface treatment partially covered some of the CPW gaps. As a result, their widths vary, thus preventing, accurate measurements of the input reflection at the polarizer ports. Nevertheless, the measured coupling coefficients can be roughly compared to simulation. Due to the losses between the reference planes, the measured coupling coefficients are about 2 dB to 4 dB lower than at the polarizer inputs.

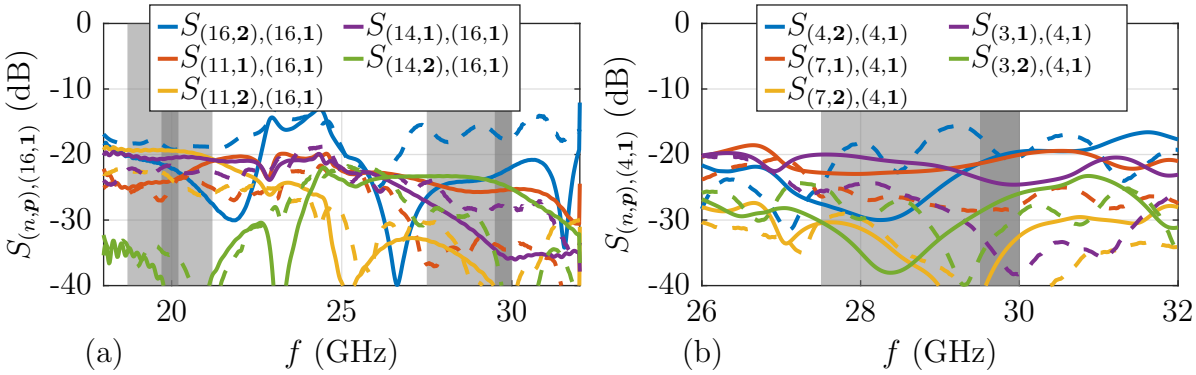

Figure 5.23: (a) Coupling coefficients $S_{(n,\boldsymbol{p}),(16,1)}$ from port $(16,\mathbf{1})$ to the elements 11 and 14 and (b) coupling coefficients $S_{(n,\boldsymbol{p}),(4,1)}$ from port $(4,\mathbf{1})$ to the elements 3 and 7 (— simulation, - - - measurements, ■ typical / ■ reference bands).

Fig. 5.23a shows the coupling coefficients from port (16,**1**) to neighboring ports. The measured transmission to the second polarizer input (16,**2**) remains below −15.7 dB in the typical frequency bands, which is higher than the simulated value of −18.7 dB. This difference could result from a slight misalignment of the septum due to manufacturing tolerances. The measured couplings to the ports of the elements 11 and 14 are below −21.7 dB, which matches quite well the simulated value of −19.3 dB. Fig. 5.23b depicts the coupling coefficients from port (4,**1**) to neighboring ports. Again, the measured transmission to the second polarizer input (4,**2**) in the typical frequency band is the largest. It reaches −15.6 dB and, thus, significantly exceeds the simulated value of −19.6 dB. The maximum coupling to elements 3 and 7 is −24.3 dB and −20 dB in measurement and simulation, respectively. In summary, these results demonstrate a relatively good agreement between measurements and simulation. The measured coupling of the polarizer inputs (e.g., $S_{(16,\mathbf{2}),(16,\mathbf{1})}$) is significantly larger than simulated, which hints at a malfunction of the polarizers.

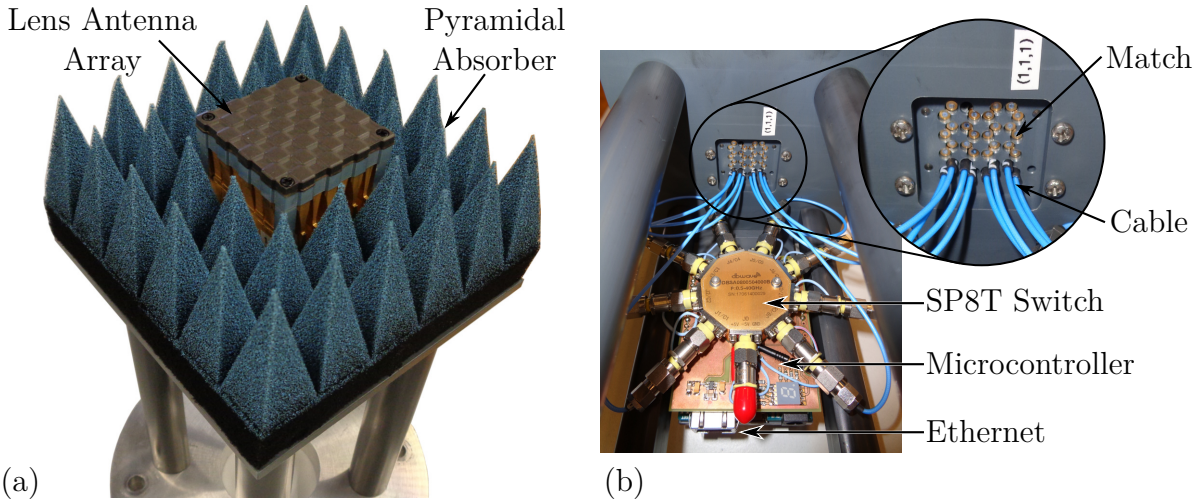

Figure 5.24: (a) Far-field measurement setup and (b) automated switch network.

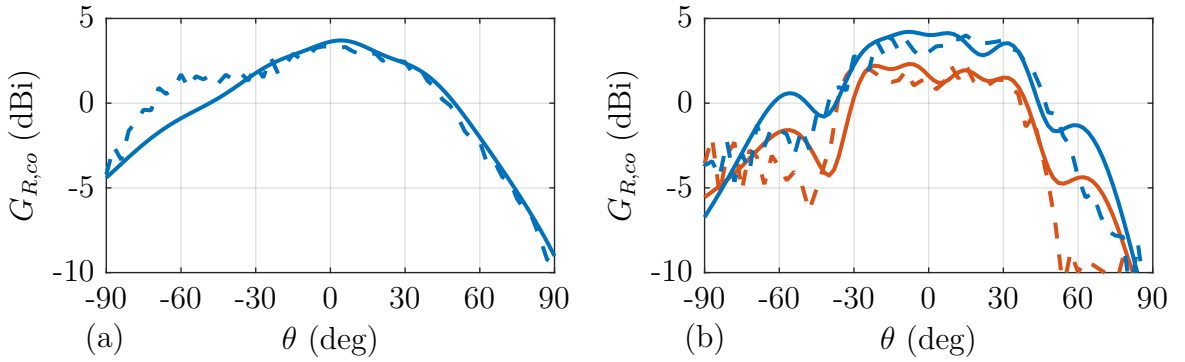

Figure 5.25: Realized co-polarized element gain $G_{R,co}$ in xz-plane versus θ for (a) 20 GHz and (b) 30 GHz (— simulation, - - · measurements, — port $(16, \mathbf{1})$, — port $(4, \mathbf{1})$).

The far-field characteristics of the lens array antenna are assessed in an anechoic chamber. Fig. 5.24a depicts the antenna mount. Pyramidal absorbers are placed around the array to reduce spurious reflections. The SMPS connectors are accessed as depicted in Fig. 5.24b. Eight of the ports at a time are connected through a computer controlled single-pole eight throw switch (*Qotana DBSA0800504000B*), the remaining ones being terminated by matched loads. This enables automated measurements of the far-field patterns of all array elements with a minimum connection effort. The measured radiation patterns are calibrated with the three-antenna method and the reference planes are shifted to the polarizer inputs. The measurement results are time gated with a window of 0.9 m to reduce the effect of multiple reflections in the measurement setup.

The realized co-polarized element gain in the xz-plane is plotted versus θ at 20 GHz and 30 GHz in Fig. 5.25. Exemplarily, the ports (16,**1**) and (4,**1**) from an Rx/Tx and a Tx-only element are shown, respectively. The measured and simulated results agree quite well. The realized gain in boresight direction is about 3.5 dBi at 20 GHz. At 30 GHz the gain is 4 dBi and 1.5 dBi for the Rx/Tx and the Tx-only element, respectively. The element pattern at 20 GHz is relatively flat. At 30 GHz, a minimum is visible at about $|\theta| = 45°$.

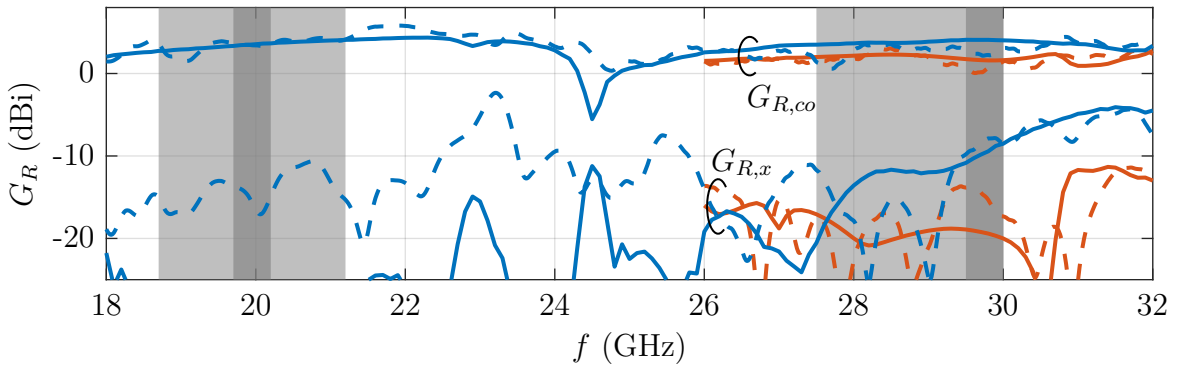

Figure 5.26: Realized co- and cross-polarized element gain G_R in boresight direction versus frequency (— simulation, - - · measurements, — port $(16, \mathbf{1})$, — port $(4, \mathbf{1})$, ■ typical / ■ reference bands).

The realized element gain in the boresight direction is plotted over frequency in Fig. 5.26 for the same ports as above. The simulated realized co-polarized gain ranges in the typical frequency bands between 2.7 dBi (1.6 dBi) and 4 dBi (2.3 dBi) for the Rx/Tx (Tx-only) element. The measured and the simulated gain are similar to each other but more ripples are visible. These can result from calibration issues due to multiple reflections between the SMPS connector and the CPW-to-SIW transition on the brick module. The measured cross-polarized gain is significantly higher in the Rx frequency band than simulated. This degradation could result from manufacturing issues, which is consistent with the observed increased coupling of the polarizer ports.

The simulated and measured element patterns are numerically superimposed to determine the LHCP and the RHCP array patterns, the respective polarizer ports are used. The ports have equal magnitude weights and the phase is adjusted for constructive interference in the pointing direction (θ_0, ϕ_0). Fig. 5.27 shows the LHCP array pattern in the xz-plane for the pointing directions $(-30°, 0°)$, $(0°, 0°)$, and $(30°, 0°)$ at 20 GHz and 30 GHz. The intended beam steering is clearly visible in the co-polarized patterns. The responses obtained from simulated and measured data are principally consistent. For boresight steering, the simulated realized gain is 12.3 dBi and 15.2 dBi at 20 GHz and 30 GHz, respectively. For the patterns eight and sixteen elements are used, which corresponds to a maximum array factor of 9 dB and 12 dB, respectively. Thus, the results are consistent with the element

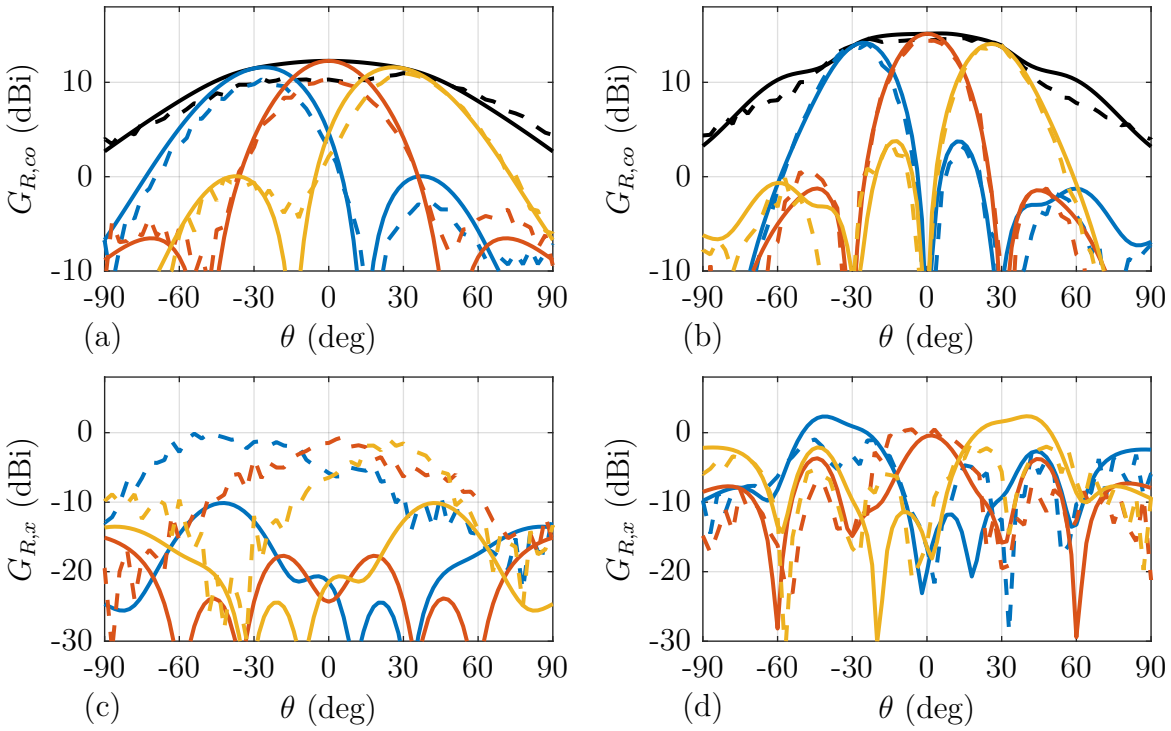

Figure 5.27: Realized (a,b) co- and (c,d) cross-polarized gain G_R of the LHCP array pattern in xz-plane versus θ for (a,c) 20 GHz and (b,d) 30 GHz (— simulation, - - - measurements, — $\theta_0 = -30°$, — $\theta_0 = 0°$, — $\theta_0 = 30°$, — envelope).

patterns. For the beams steered to $(\pm 30°, 0°)$, the gain drops by 0.8 dB and 1.4 dB for the respective patterns. The measured realized gain is about 2 dB and 0.8 dB lower than simulated at 20 GHz and 30 GHz, respectively. The significantly decreased performance at 20 GHz correlates with a reduced gain of the elements in the lower two brick modules of Fig. 5.17a. For these elements, the cross-polarization is drastically increased and the co-polarization is decreased. Consequently, an increased coupling of the polarizer ports is observed in the measurements. This indicates large manufacturing deviations for the polarizers of the lower two brick modules. Fig. 5.27 additionally reports the maximum gain versus the pointing direction. It has a $\cos(\theta_0)$ like dependence, as typical for an array, with a dip at around 45° in the 30 GHz pattern. This dip is already visible in the element patterns. It could be due to surface modes in the lens. For large arrays, this could lead to spot blindness at large scan angles [50, Sec. 6.3]. However, a detailed discussion is not in the scope of this work. The measured cross-polarized gain at 30 GHz agrees well with the simulated results but, at 20 GHz, the measured values are, as expected, higher than estimated by simulation. For steering angles up to $|\theta_0| = 30°$, the corresponding simulated (measured) axial ratios are below 1.1 dB (5 dB) and 4.3 dB (3.8 dB) in the pointing direction at 20 GHz and 30 GHz, respectively.

The relative high cross-polarization can be compensated as discussed in Sec. 4.2, when the LHCP and RHCP array patterns are used simultaneously. The excitation coefficients

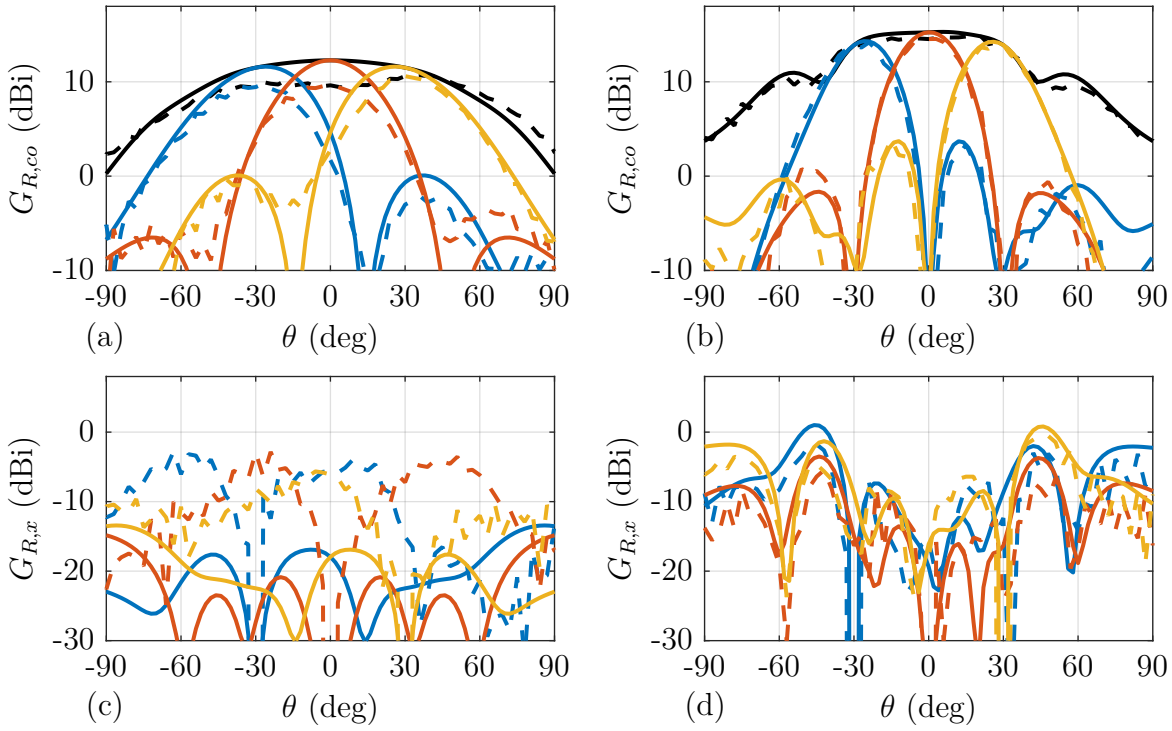

Figure 5.28: Realized (a,b) co- and (c,d) cross-polarized gain G_R of the LHCP array pattern in xz-plane versus θ for (a,c) 20 GHz and (b,d) 30 GHz with polarization compensation (— simulation, - - - measurements, — $\theta_0 = -30°$, — $\theta_0 = 0°$, — $\theta_0 = 30°$, — envelope).

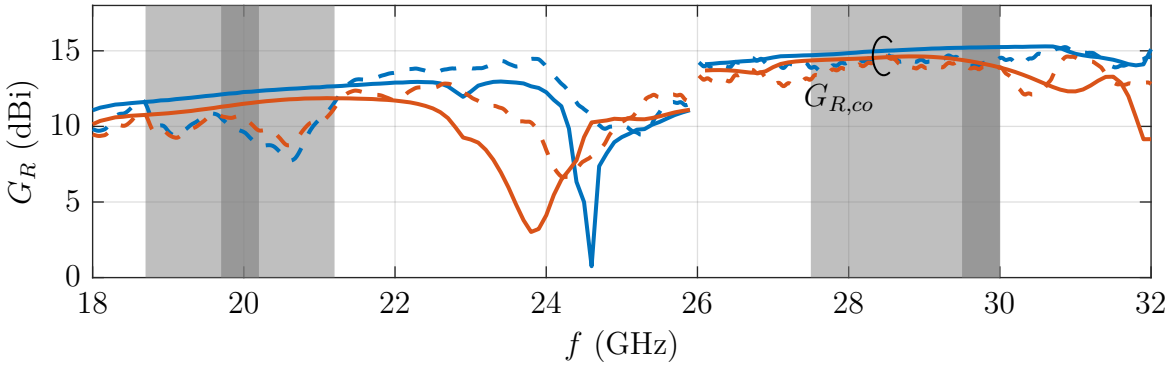

Figure 5.29: Realized co-polarized gain G_R of the LHCP array pattern in the pointing direction versus frequency with polarization compensation (— simulation, - - - measurements, — $\theta_0 = 0°$, — $\theta_0 = 30°$, ■ typical / ■ reference bands).

are calculated using (4.26) from the array patterns. Fig. 5.28 shows the realized array gain with this compensation. As intended, the cross-polarization vanishes in pointing direction. At 30 GHz, the level of cross-polarization generally decreases. Around $|\theta| = 45°$, this effect is not observed. This is consistent with the assumption that power couples to surface modes. At 20 GHz, a significant reduction of the cross-polarization level is only visible in the simulated results. Compared to the case without polarization compensation, the decrease of the co-polarized gain is less than 0.2 dB.

Fig. 5.29 shows the array gain with polarization compensation in the pointing directions $(0°, 0°)$ and $(30°, 0°)$ over frequency. In boresight direction, the gain ranges between 11.6 dB (14.7 dB) and 12.7 dB (15.3 dB) for the typical Rx (Tx) frequency band. The simulated gain of the steered beam is about 1 dB lower. For Tx, the measured results are consistent with the simulated ones, which is not the case for Rx. As discussed above, this is most likely due to manufacturing issues of some of the polarizers.

The measurement results validate the concept of the lens array antenna. The dual-polarization and dual-band functionality is shown. Furthermore, the feasibility of the polarization compensation is demonstrated with both simulated and measured results. A significant aperture size reduction is possible, when the Rx/Tx integrated lens array antenna is compared to separate Rx- and Tx-only arrays. As discussed in Sec. 2.5, the antenna losses have a major influence. The diplexer, which is needed for the Rx/Tx integration, adds to the loss, as discussed in Sec. 2.4. A diplexer such as in [42] increases the losses by 0.7 dB and 1.2 dB in the Rx and the Tx path, respectively. Together with the simulated element losses of Fig. 5.18, this yields a total loss of about 3.1 dB and 3.4 dB in the Rx and Tx reference bands, respectively. The Tx-only element features a loss of about 3.3 dB. Thus, the losses of the designed array are only slightly larger than the 3 dB assumed in Sec. 2.5. Hence, the separate Rx- and Tx-only arrays would be about 30 % larger than the integrated array antenna. If the EIRP is limited by the ETSI mask, the size would be even 50 % larger.

6 Conclusion and Outlook

In this work, an Rx/Tx integrated array antenna is developed and its performance is verified by means of a passive demonstrator. To start with, the satellite communication scenario is analyzed. A link budget analysis is carried out for a GEO satellite operating in the K/Ka-band. The possible data rate is calculated versus the EIRP and the G/T of a terminal antenna. Next, the terminal antenna parameters are determined as a function of the diameter of a circular aperture. For the arrangement of the array elements, an interleaved rectangular grid with Rx/Tx and Tx-only elements is chosen. Due to the specific frequency spread of Rx and Tx, this arrangement requires the lowest number of channels per area. The Tx power is limited by the spuriously radiated power. Considering this, the maximum EIRP of the array and the maximum output power per element are determined as a function of the antenna diameter. The Rx performance is limited by the received noise. A simple model is presented to determine the G/T of an antenna terminal. Based on this model, the performance of two exemplary terminals is evaluated. The size of an Rx/Tx integrated array antenna is compared to that of separate antennas for Rx and for Tx. Additional antenna losses degrade the terminal parameters and, thus, lower the possible size reduction. For Tx operation, the maximum EIRP can be limited by the available power of the frontends or by the allowed spurious radiation. In both cases, a significant size reduction is possible. However, a greater reduction is achieved in the latter case. For the implementation, a lens array antenna concept is proposed that is based on the brick architecture.

This concept is enabled by the SIW technology, which is analyzed in detail. This class of waveguide structures is extended to MSIWs, which utilize multiple metal layers and via rows. MSIW components are modeled by an equivalent circuit with multimode transmission lines and discontinuities. The parameters of the waveguide modes are determined from an equivalent cross-section. Here, the via rows are replaced by solid metal walls. For that, the scattering at a periodic via row is analyzed using a semi-analytical method. The modal characteristics of the lossless equivalent cross-section are determined by the TRM. The resulting modal fields are represented by a set of parallel-plate modes. For a lossy waveguide with rough conductors, the complex propagation coefficient is determined

using the perturbation method. Especially the skin effect in rough conductor surfaces is considered and empirical equations for the parameters of an equivalent conductor material are proposed. The conductor roughness increases the losses as well as the phase constant. For the equivalent circuit, the discontinuities of different MSIWs are determined using the mode matching method. The resulting model for MSIW components allows for very fast and accurate calculations.

Based on this model, transitions for the lens antenna concept are developed. An E-plane taper shows better performance than a stepped transition and is selected for the design. Further, a synthesis method for MSIW tapers is presented. The resulting ultra-broadband components can be implemented in multilayer PCBs. Septum polarizers are designed to generate two circular polarizations. A technique to compensate the cross-polarization in the pointing direction is presented. It uses the two polarizer inputs simultaneously.

The lens antenna concept is first demonstrated with a single antenna element. The square SIW is matched by a hemispherical lens and a bandwidth of over 58 % is achieved. In combination with the septum polarizer, a dual-band characteristic is obtained, which is suitable for the typical satellite communication bands. For the lens array antenna, two types of square SIW feeds are combined with a shaped dielectric lens. The lens surface is described by NURBS and optimized in terms of input match and far-field characteristics. A passive demonstrator of an 8×8 array is realized. To mitigate edge effects, the outer elements are terminated and effectively a 4×4 array is investigated. The antenna elements are grouped in brick modules. These modules are fabricated using standard multilayer PCB processes. The concept is verified by measurements. Discrepancies with respect to simulation results can be traced back to manufacturing issues. The Rx/Tx integrated array antenna features two polarizations and supports the typical satellite communication bands. With the compensation technique, the cross-polarization in the pointing direction can be significantly reduced. With this implementation, the aperture area of separate Rx- and Tx-only arrays would be 30 % larger than that of the integrated array antenna. The area is even 50 % larger if the EIRP is limited by the spuriously radiated power. Thus, a significant size reduction is achieved with the proposed concept.

An even greater size reduction is possible if the antenna losses could be further reduced. This can be achieved by using laminates with lower losses (e.g., *Megtron 7* from *Panasonic*) and copper foils with lower surface roughness. Furthermore, different component topologies with a shorter electrical length could reduce the antenna losses. An issue of the design is the coupling to surface waves in the Tx frequency band. For larger scan angles, this could lead to spot blindness. This effect could be considered during the design of the array elements by simulating an infinite array and optimizing for the scan reflection coefficient. For larger manufacturing quantities, the technological processes can be further simplified. The manual processing steps of the brick module fabrication, like covering the PCB structure

with *Kapton* tape, can be avoided by a suitable adaption of the process steps. For mass production, the smooth dielectric lens could be fabricated by injection molding.

As a next step, an active array antenna could be built based on this concept. For this, the Rx/Tx elements have to be combined with diplexers and the Rx signals have to be amplified by LNAs. Modern core-chip solutions can tune the phase and amplitude of the Rx and Tx signals and, thus, enable electrical beam steering. Nevertheless, a calibration of the channels is necessary and for this a method has to be developed. In combination with the polarization compensation technique, this is a challenging task. However, the Rx/Tx integrated lens antenna concept has great potential for very compact terminal antennas.

A Further Details for the Substrate Integrated Waveguide Theory

A.1 Circuit Elements of Waveguides with Rough Surfaces

In this section the equivalent circuit elements related to waveguides with rough and lossy conductors are determined. A waveguide of infinitesimal length dz is assumed. It is represented by the equivalent circuits of Fig. 3.7. The magnetic field inside the conductor stores magnetic energy, which is represented by the inner inductances $L_i' \, dz$ and L_i''/dz. Accordingly, the electric current inside the conductor dissipates power, which is represented by the resistances $R' \, dz$ and R''/dz. In each case, these values are determined by comparing the time-averaged stored magnetic energy W_m and the dissipated power P_d as calculated from the fields and the equivalent circuit, respectively [82, Tab. 1-6]. The fields are decomposed in longitudinal (index z) and transverse components (index t) and the comparisons can be written as

$$P_{d,z} = dz \iint_{\bar{S}} \frac{1}{\sigma} \, |J_z(x,y)|^2 \, d\bar{S} = dz \oint_C R_S \, |J_{s,z}(x,y)|^2 \, dC = R' \, dz \, I_z^2, \tag{A.1a}$$

$$P_{d,t} = dz \iint_{\bar{S}} \frac{1}{\sigma} \, \vec{J}_{xy}(x,y) \bullet \vec{J}_{xy}^{\,*}(x,y) \, d\bar{S} = dz \oint_C R_S \, |J_{s,t}(x,y)|^2 \, dC = \frac{R''}{dz} \, I_t^2, \tag{A.1b}$$

$$W_{m,z} = \frac{dz}{2} \iint_{\bar{S}} \mu_0 \, \vec{H}_{xy}(x,y) \bullet \vec{H}_{xy}^{\,*}(x,y) \, d\bar{S} = \frac{dz}{2} \oint_C L_S \, |J_{s,z}(x,y)|^2 \, dC = \frac{1}{2} \, L_i' \, dz \, I_z^2, \tag{A.1c}$$

and

$$W_{m,t} = \frac{dz}{2} \iint_{\bar{S}} \mu_0 \, |H_z(x,y)|^2 \, d\bar{S} = \frac{dz}{2} \oint_C L_S \, |J_{s,t}(x,y)|^2 \, dC = \frac{1}{2} \, \frac{L_i''}{dz} \, I_t^2. \tag{A.1d}$$

The surface integrals over the conductor $\bar{S}$ are simplified to contour integrals over the conductor boundary C with the surface current

$$\vec{J}_s(x,y) = \vec{u}_B \times \vec{H}(x,y) = J_{s,t} \, \vec{u}_t + J_{s,z} \, \vec{u}_z \tag{A.2}$$

and the surface impedance $Z_S = R_S + \mathrm{j} \, \omega \, L_S$, as introduced in Sec. 3.2.1. The surface current itself consist of a transverse component $J_{s,t}$ and a longitudinal component $J_{s,z}$, where the tangential unit vector $\vec{u}_t = \vec{u}_z \times \vec{u}_B$ is orthogonal to $\vec{u}_z$ and the normal boundary direction $\vec{u}_B$. The longitudinal current I_z and the transverse current I_t are determined by

comparing the time-averaged stored magnetic energy in the dielectric

$$W_{m,z} = \frac{dz}{2} \iint_S \mu_0 \, \vec{H}_{xy}(x,y) \bullet \vec{H}^*_{xy}(x,y) \, dS = \frac{1}{2} \, L'_o \, dz \, I_z^2 = \frac{\mu_0}{2} \, dz \, I_z^2, \tag{A.3a}$$

$$W_{m,t} = \frac{dz}{2} \iint_S \mu_0 \, |H_z(x,y)|^2 \, dS = \frac{1}{2} \, \frac{L''_o}{dz} \, I_t^2 = \frac{\mu_0}{2\,k_c^2} \, \frac{1}{dz} \, I_t^2. \tag{A.3b}$$

Here the outer inductances from Tab. 3.1 are used.

In the following, the transverse magnetic field

$$\vec{H}_{xy}(x,y) = I^+ \, \vec{h}_{xy}(x,y) \tag{A.4a}$$

of a mode propagating in the $+z$-direction is assumed (see (3.13)). Accordingly, the longitudinal magnetic field (3.17) is given for TE^z-modes by

$$H_z(x,y) = I^+ \, \frac{k_c^2}{\mathrm{j}\,\beta} \, \Psi_{xy}(x,y). \tag{A.4b}$$

With these fields and the normalization (3.20) the currents can be calculated from (A.3) to

$$I_z^2 = \iint_S \vec{H}_{xy}(x,y) \bullet \vec{H}^*_{xy}(x,y) \, dS = \left| I^+ \right|^2 \tag{A.5a}$$

and

$$I_t^2 = dz^2 \, k_c^2 \iint_S |H_z(x,y)|^2 \, dS = dz^2 \left| I^+ \, \frac{k_c^2}{\beta} \right|^2. \tag{A.5b}$$

Finally, the equivalent circuit parameters

$$R' = \frac{1}{I_z^2} \oint_C R_S \, |J_{s,z}(x,y)|^2 \, dC = R_S \, I' \tag{A.6a}$$

$$R'' = \frac{dz^2}{I_t^2} \oint_C R_S \, |J_{s,t}(x,y)|^2 \, dC = R_S \, I'' \tag{A.6b}$$

$$L'_i = \frac{1}{I_z^2} \oint_C L_S \, |J_{s,z}(x,y)|^2 \, dC = L_S \, I' \tag{A.6c}$$

and

$$L''_i = \frac{dz^2}{I_t^2} \oint_C L_S \, |J_{s,t}(x,y)|^2 \, dC = L_S \, I'' \tag{A.6d}$$

are determined from (A.1). Using (A.4), (A.2), and (A.5) the contour integrals can be simplified to

$$I' = \oint_C |h_t(x,y)|^2 \, dC \tag{A.6e}$$

and

$$I'' = \oint_C |\Psi_{xy}(x,y)|^2 \, dC. \tag{A.6f}$$

Here, a constant surface impedance for all boundaries is assumed. Note that the transverse elements R'' and L''_i are only necessary for TE^z-modes.

A.2 Scattering from a Periodic Via Array

Fig. A.1a shows a single via row. The vias have diameter d and pitch p. They are numbered by index ν. It is assumed that the incident Floquet modes $\vec{a}_{F,\mathbf{1}}$ propagate in the $-x$-direction towards the via row. These modes excite scattered $\vec{b}_{F,\mathbf{1}}$ and transmitted $\vec{b}_{F,\mathbf{2}}$ Floquet modes that propagate in the $-x$- and $+x$-direction, respectively. Here, the fundamental as well as higher-order modes are collected in vectors. In this section, the generalized scattering matrix (GSM) $[S_F]$ is determined. It relates the incident modes to the scattered and transmitted modes (see Fig. A.1c).

The scattering problem is solved in cylindrical coordinates and follows a procedure, which is used to calculate the scattering of plane waves at periodic circular cylinder arrangements [166, 167]. For each via, a local polar coordinate system (r_ν, ϕ_ν) is defined by the radius $r_\nu = \sqrt{x^2 + (z - \nu\, p)^2}$ and the angle $\cos(\phi_\nu) = (z - \nu\, p)/r_\nu$, as depicted in A.1b. For these coordinate systems, the two-dimensional Helmholtz equation (3.25) is solved by

$$\Psi_{C,\chi}(r_\nu, \phi_\nu) = \mathrm{J}_\chi\left(k_{xz} r_\nu\right) \mathrm{e}^{-\mathrm{j}\chi\phi_\nu} \tag{A.7a}$$

and

$$\Psi^{+}_{C,\chi}(r_\nu, \phi_\nu) = \mathrm{H}^{(2)}_\chi\left(k_{xz} r_\nu\right) \mathrm{e}^{-\mathrm{j}\chi\phi_\nu}. \tag{A.7b}$$

The standing wave potential $\Psi_{C,\chi}$ is associated with the Bessel function $\mathrm{J}_\chi(z)$ of the first kind and the traveling wave potential $\Psi^{+}_{C,\chi}$ is described by the Hankel function of the second kind $\mathrm{H}^{(2)}_\chi(z)$ [82, Sec. 3.4.2]. The wave propagates in $+r_\nu$-direction. This is marked by the sign in the superscript. The mode order χ is integer.

The incident potential

$$\Psi^{inc}(x, z) = \left(\vec{\Psi}^{-}_{xz}(x, z)\right)^T \vec{a}_{F,\mathbf{1}} = \left(\vec{\Psi}_C(r_0, \phi_0)\right)^T \vec{a}_C \tag{A.8a}$$

with

$$\vec{a}_C = \left[T^{-}_{CF}\right] \vec{a}_{F,\mathbf{1}},\ T^{\pm}_{CF,\chi\xi} = \mathrm{e}^{-\mathrm{j}\chi\theta^{\pm}_\xi},\ \text{and}\ \theta^{\pm}_\xi = \mathrm{atan2}\left(\pm k_{x,\xi}, k_{z,\xi}\right) \tag{A.8b}$$

can be represented by a superposition of Floquet modes $\vec{a}_{F,\mathbf{1}}$ or standing cylindrical waves $\vec{a}_C$ of the zeroth cell. The mode potentials are collected in the vector functions $\vec{\Psi}^{-}_{xz}(x, z)$

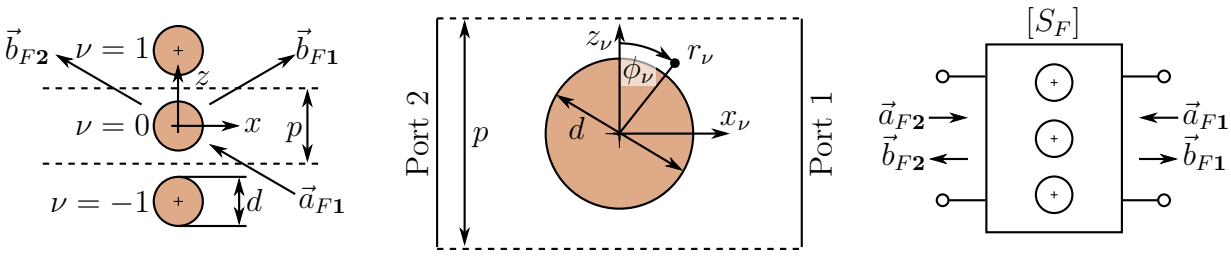

(a) (b) (c)

Figure A.1: Cross-section of (a) the via row and (b) the unit cell in the xz-plane. (c) Equivalent circuit of the via row.

and $\vec{\Psi}_C(r_0, \phi_0)$. The mode amplitudes are related by the transformation matrix $[T^-_{CF}]$ and the matrix elements $T^{\pm}_{CF,\chi\xi}$ are calculated from the propagation angle $\theta^{\pm}_{\xi}$. For the fundamental Floquet mode, $\theta^{\pm}_0$ is the propagation angle θ of the parallel-plate mode. For higher-order Floquet modes that are evanescent in the x-direction the four-quadrant inverse tangent $\operatorname{atan2}(x, y) = -\mathrm{j} \ln\left((x + \mathrm{j}y)/\sqrt{x^2 + y^2}\right)$ is defined by the principal value of the complex natural logarithm $\ln(z)$. In this case, the propagation angle is complex. To represent an arbitrary field distribution, an infinite number of modes is required. In practice, a finite number of modes is sufficient to approximate the field.

Using the phase shift Φ_z of the Floquet theorem, the scattered potential

$$\Psi^{sc}(x, z) = \sum_{\nu=-\infty}^{\infty} \left(\vec{\Psi}^{+}_{C}(r_\nu, \phi_\nu)\right)^T \mathrm{e}^{-\mathrm{j}\,\nu\,\Phi_z}\, \vec{b}_C \tag{A.9a}$$

can be written as a superposition of the scattered cylinder waves of an infinite number of vias. Here, $\vec{b}_C$ denotes a vector with the unknown scattered cylinder wave amplitudes of the zeroth cell. Using the addition theorems of Hankel functions [168] the potential of the cells $\nu \neq 0$ can be expanded with respect to the coordinate system of the zeroth cell with standing waves. The scattered potential is given by

$$\Psi^{sc}(x, z) = \left(\vec{\Psi}_C(r_0, \phi_0)\right)^T [L]\, \vec{b}_C + \left(\vec{\Psi}^{+}_{C}(r_0, \phi_0)\right)^T \vec{b}_C, \tag{A.10a}$$

for an observation point that is located in a cylinder with a radius $r_0 < p$. The square matrix $[L]$ connects the scattered potential of the cells $\nu \neq 0$ with the standing waves that are generated in the zeroth cell. The matrix elements $L_{\chi\bar{\chi}}$ result in

$$L_{\chi\bar{\chi}} = (-1)^{\chi-\bar{\chi}}\, S_{\chi-\bar{\chi}}(k_{xz}\, p, \Phi_z) \tag{A.11a}$$

with the infinite sum

$$S_\chi(\Phi_0, \Phi_z) = \sum_{\nu=1}^{\infty} \mathrm{H}^{(2)}_{\chi}(\nu\,\Phi_0)\, \mathrm{e}^{\mathrm{j}\,\nu\,\Phi_z} + (-1)^{\chi} \sum_{\nu=1}^{\infty} \mathrm{H}^{(2)}_{\chi}(\nu\,\Phi_0)\, \mathrm{e}^{-\mathrm{j}\,\nu\,\Phi_z}. \tag{A.11b}$$

$S_\chi(\Phi_0, \Phi_z)$ is called lattice sum [169] or Schlömilch series [170]. An efficient calculation method is described at the end of this section. The lattice sums are independent of the observation point and the polarization of the incident field, which is a major advantage of this formulation. The total potential can now be written as

$$\begin{aligned} \Psi^{tot}(x, z) &= \Psi^{inc}(x, z) + \Psi^{sc}(x, z) \\ &= \left(\vec{\Psi}_C(r_0, \phi_0)\right)^T \left(\vec{a}_C + [L]\, \vec{b}_C\right) + \left(\vec{\Psi}^{+}_{C}(r_0, \phi_0)\right)^T \vec{b}_C. \end{aligned} \tag{A.12}$$

To determine the unknown scattered wave amplitudes $\vec{b}_C$, the recursive T-matrix algorithm is used [171]. At first, the scattering of an isolated via is considered:

$$\vec{b}^{\,iso}_C = [S^{iso}_C]\, \vec{a}^{\,iso}_C \tag{A.13a}$$

with the matrix elements

$$S^{iso}_{C,\chi\bar{\chi}} = \begin{cases} -\frac{\mathrm{J}_\chi\left(k_{xz}\frac{d}{2}\right)}{\mathrm{H}^{(2)}_\chi\left(k_{xz}\frac{d}{2}\right)}\delta_{\chi-\bar{\chi}}, & \mathrm{TM}^\theta\text{-modes}, \\ -\frac{\mathrm{J}'_\chi\left(k_{xz}\frac{d}{2}\right)}{\mathrm{H}'^{(2)}_\chi\left(k_{xz}\frac{d}{2}\right)}\delta_{\chi-\bar{\chi}}, & \mathrm{TE}^\theta\text{-modes}. \end{cases} \tag{A.13b}$$

$[S^{iso}_C]$ is the GSM of a circular cylinder, which is also called T-matrix in literature. $\mathrm{J}'_\chi(z)$ and $\mathrm{H}'^{(2)}_\chi(z)$ denote the derivatives with respect to the argument. Combining (A.12) and (A.13a) gives the relation

$$\vec{b}_C = [S^{iso}_C]\left(\vec{a}_C + [L]\vec{b}_C\right). \tag{A.14}$$

This equation can be solved for the scattered amplitudes by

$$\vec{b}_C = [S_C]\vec{a}_C \qquad \text{with} \qquad [S_C] = \left([I] - [S^{iso}_C][L]\right)^{-1}[S^{iso}_C]. \tag{A.15}$$

Here, $[S_C]$ is the GSM that relates the incident and scattered cylinder wave amplitudes.

The incident and scattered wave amplitudes can be transformed to the reflected $\vec{b}_{F,\mathbf{1}}$ and transmitted $\vec{b}_{F,\mathbf{2}}$ Floquet modes by

$$\vec{b}_{F,\mathbf{1}} = [T^+_{FC}]\vec{b}_C \quad \text{and} \quad \vec{b}_{F,\mathbf{2}} = \vec{a}_{F,\mathbf{1}} + [T^-_{FC}]\vec{b}_C \quad \text{with} \quad T^\pm_{FC,\xi\chi} = \frac{2}{k_{x,\xi}\,p}\mathrm{e}^{\mathrm{j}\,\chi\,\theta^\pm_\xi} \tag{A.16}$$

using the transformation matrix $[T^\pm_{FC}]$. The sign in the superscript denotes the propagation in x-direction. Combining (A.8b), (A.15), and (A.16) leads to

$$\vec{b}_{F,\mathbf{1}} = [S_{F,\mathbf{11}}]\,\vec{a}_{F,\mathbf{1}} \quad \text{with} \quad [S_{F,\mathbf{11}}] = [S_{F,\mathbf{22}}] = [T^+_{FC}][S_C][T^-_{CF}] \tag{A.17a}$$

and

$$\vec{b}_{F,\mathbf{2}} = [S_{F,\mathbf{21}}]\,\vec{a}_{F,\mathbf{1}} \quad \text{with} \quad [S_{F,\mathbf{21}}] = [S_{F,\mathbf{12}}] = [I] + [T^-_{FC}][S_C][T^-_{CF}], \tag{A.17b}$$

which relate the Floquet modes. $[S_{F,\boldsymbol{\rho}\bar{\boldsymbol{\rho}}}]$ are block matrices of the GSM $[S_F]$. Due to the symmetric arrangement, an excitation from port **2** is equivalent to the given results.

Lattice Sums

The lattice sum defined in (A.11b) converges very slowly and therefore dominates the calculation time of the scattering matrix. To overcome this issue, the lattice sum can be transformed [169] by an integral representation of the Hankel functions to the semi-infinite contour integral

$$S_\chi(\Phi_0,\Phi_z) = (-1)^\chi\,\frac{1+\mathrm{j}}{\pi}\int_0^\infty \frac{\left(\tau - \mathrm{j}\sqrt{1-\tau^2}\right)^\chi + \left(-\tau - \mathrm{j}\sqrt{1-\tau^2}\right)^\chi}{\sqrt{1-\tau^2}} \left(\frac{\mathrm{e}^{-\mathrm{j}\left(\Phi_0\sqrt{1-\tau^2}-\Phi_z\right)}}{1-\mathrm{e}^{-\mathrm{j}\left(\Phi_0\sqrt{1-\tau^2}-\Phi_z\right)}} + (-1)^\chi\frac{\mathrm{e}^{-\mathrm{j}\left(\Phi_0\sqrt{1-\tau^2}+\Phi_z\right)}}{1-\mathrm{e}^{-\mathrm{j}\left(\Phi_0\sqrt{1-\tau^2}+\Phi_z\right)}}\right) dt, \tag{A.18}$$

where $\tau = (1+\mathrm{j})\,t$. By means of the substitution $\alpha = \sqrt{1-\tau^2} = \sqrt{1-2\,\mathrm{j}\,t^2}$, this integral can be further transformed into

$$S_\chi(\Phi_0,\Phi_z) = 2\,\mathrm{j}^\chi\,\frac{1+\mathrm{j}}{\pi}\int_0^\infty K(\alpha)\,dt \tag{A.19a}$$

with

$$K(\alpha) = \frac{\mathrm{T}_\chi(\alpha)}{\alpha}\left(\frac{1}{\mathrm{e}^{\mathrm{j}(\Phi_0\alpha-\Phi_z)}-1}+\frac{(-1)^\chi}{\mathrm{e}^{\mathrm{j}(\Phi_0\alpha+\Phi_z)}-1}\right). \tag{A.19b}$$

The integrand $K(\alpha)$ has a polynomial and an exponential part. The former is described by the Chebyshev polynomials

$$\mathrm{T}_\chi(\alpha) = \frac{1}{2}\left(\left(\alpha-\sqrt{\alpha^2-1}\right)^\chi+\left(\alpha+\sqrt{\alpha^2-1}\right)^\chi\right). \tag{A.20}$$

The integral in (A.19a) can be approximated by a trapezoidal numerical integration on a finite contour. A high accuracy is achieved, if the integrand is sufficiently small in the omitted part of the infinite contour. This means that the accuracy can be determined by the length of the contour and the discretization. The absolute value of the integrand has a maximum close to $t_b \approx (\chi - 1 + \delta_\chi)/|\Phi_0|$ and an asymptotic decay of $\mathrm{e}^{-|\Phi_0|\,t}$ for large values of $t \to \infty$. From this, an upper limit t_{max} for a required accuracy can be defined. For small values $t \to 0$ the integrand can show a singular behavior, if $\Phi_z \to \Phi_0$. In general, this could lead to a rapid change of the integrand at small values. To cope with this issue, the integration is performed over a logarithmic spacing $\Delta t = \Delta t_0\, t/t_{mid}$ for $t \leq t_{mid}$ and a linear spacing $\Delta t = \Delta t_0$ for $t \geq t_{mid}$. For the logarithmic spacing the value $|K(t)\,\Delta t|$ vanishes at very small values and shows a maximum close to $t_a \approx \sqrt{1-|\Phi_z/\Phi_0|}$. By incorporating the asymptotic behavior of the integrand, the empirical formulas for the boundaries of the integration spaces are given by

$$t_1 = [t_{min}, t_{mid}],\ \text{logarithmic space}, \tag{A.21a}$$

and

$$t_2 = [t_{mid}, t_{max}],\ \text{linear space}, \tag{A.21b}$$

with

$$t_{min} = \min\left(t_a\,\Delta\left|\frac{K(t_b)}{K(t_a)}\right|, t_{mid}\left(\Delta\left|\frac{K(t_b)}{K(t_{mid})}\right|\right)^{1/(\chi-2+\delta_{\chi-2})}\right), \tag{A.21c}$$

$$t_{mid} = \frac{1}{|\Phi_0|}, \tag{A.21d}$$

and

$$t_{max} = \frac{2.1\,(\chi-1)-\ln(\Delta)}{|\Phi_0|}, \tag{A.21e}$$

where Δ is a measure for the decay of the integrand. The relative error of the lattice sums for a particular discretization Δt_0 and decay Δ are determined by numerical tests. Tab. A.1 lists the discretization values for a required accuracy.

Table A.1: Discretization values for approximative relative errors of the lattice sums.

Rel. Error	Δ	$\lvert\Phi_0\rvert\ \Delta t_0$
$1\cdot10^{-7}$	$1\cdot10^{-10}$	$1\cdot10^{-3}$
$1\cdot10^{-6}$	$5\cdot10^{-9}$	$5\cdot10^{-3}$
$1\cdot10^{-5}$	$1\cdot10^{-7}$	$1\cdot10^{-2}$
$1\cdot10^{-4}$	$5\cdot10^{-6}$	$5\cdot10^{-2}$
$1\cdot10^{-3}$	$1\cdot10^{-4}$	$1\cdot10^{-1}$

A.3 Reflection and Transmission Matrices

In this section, the reflection and transmission matrices of an MSIW equivalent circuits are systematically determined. For illustration, again, the example shown in Fig. A.2a is used. The equivalent circuit is split into sub-circuits A and B. These generalized one-ports have the reflection matrices $[\Gamma_{\boldsymbol{A}}]$ and $[\Gamma_{\boldsymbol{B}}]$, respectively. Each port has an incident $\vec{a}_{(\nu,\boldsymbol{\rho})}$ and reflected $\vec{b}_{(\nu,\boldsymbol{\rho})}$ wave amplitude vector. They are related by the scattering matrices of the components and the connections between the components. These relations can be represented by a weighted graph, as depicted in Fig. A.2b. The nodes and edges of the graph represent ports and connections, respectively. With respect to the components, it is distinguished between internal and external edges in the following. The internal edges are weighted with the corresponding scattering matrices and the external edges are unweighted or rather weighted with unit matrices. The external edges are defined by a so-called netlist. For reciprocal components the scattering matrices are symmetric and, thus, the graph is undirected. The internal and external subgraphs are constructed from the internal and external edges, respectively. The internal subgraph is a disjoint union of component graphs, whereas the external subgraph is a combination of edges, each connecting two nodes. Detailed information on graph theory can be found in [172]. However, only basic knowledge is necessary for the following analysis.

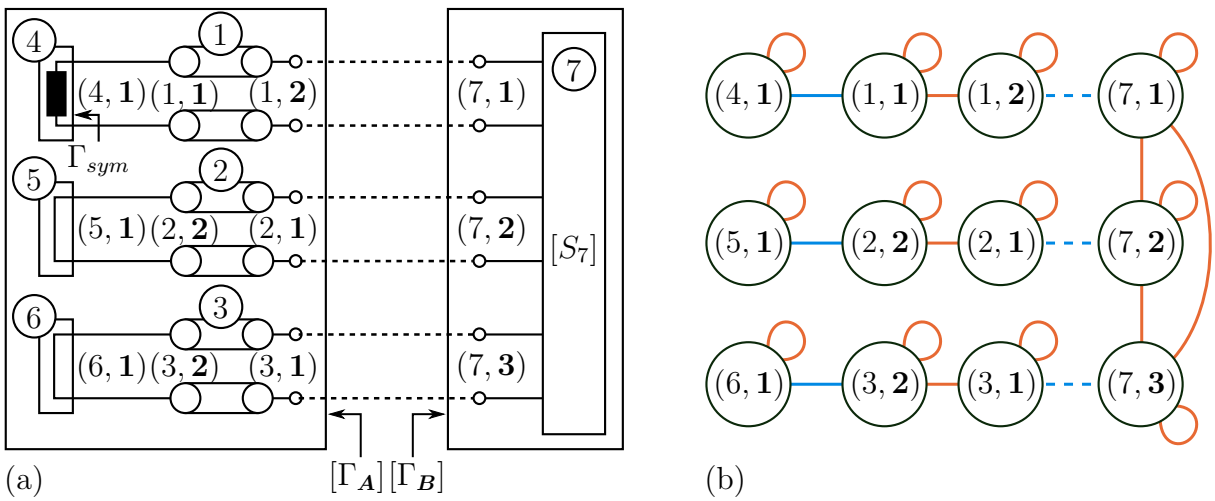

Figure A.2: (a) Equivalent circuit and (b) port node graph of multilayer waveguide (— internal and — external edges).

The adjacency matrices of the internal and the external subgraphs are given by

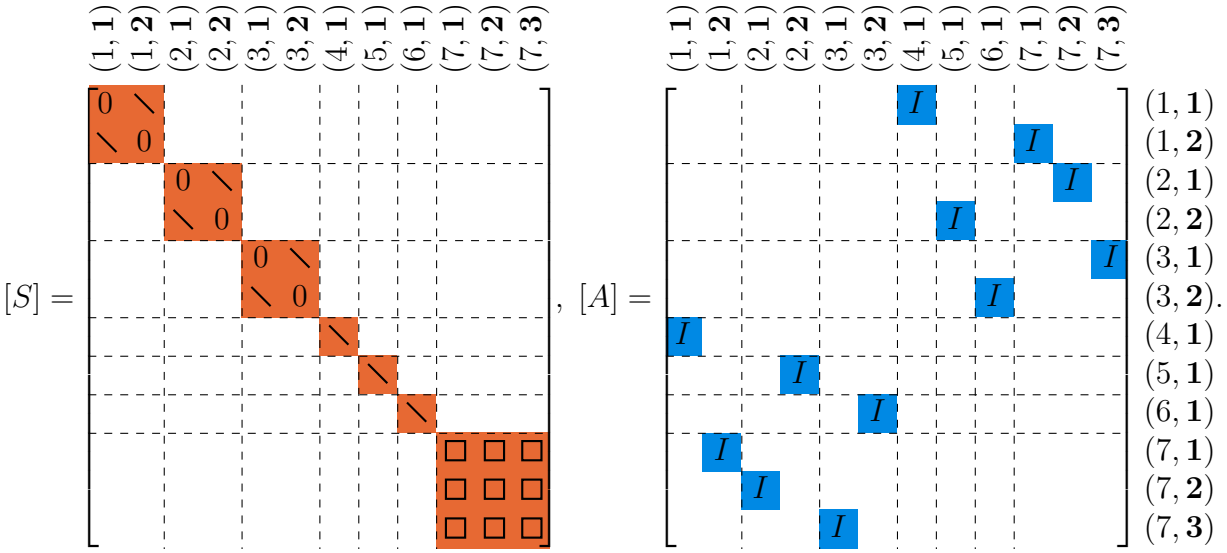

(A.22)

Matrix $[S]$ is of block diagonal form, where the blocks are the GSM of the components. The matrix of the example has a band structure. The first three blocks represent the transmission lines. They are in general matched at the ports (0) and the transmission is given by a diagonal block matrix (⟍). Blocks four to six represent the short and open circuits, they are unit matrices multiplied by a scalar. The last block represents the bifurcation and the blocks are dense matrices (□). Matrix $[A]$ is filled with unit matrices (I), which represent the connections between the components. Taking the different block types into account yields an efficient numerical implementation. However, implementation details are beyond the scope of this thesis.

The reflection and transmission matrices are now determined from the adjacency matrices. For this, the ports are assigned to different sets $s_{\boldsymbol{A}}$ and $s_{\boldsymbol{B}}$, which collect the input ports of the generalized one-port $\boldsymbol{A}$ and $\boldsymbol{B}$, respectively. The nodes of $s_{\boldsymbol{B}}$ are the neighbors of $s_{\boldsymbol{A}}$ and can be uniquely determined from the external subgraph. The remaining ports are assigned to $s_{\bar{\boldsymbol{A}}}$ and $s_{\bar{\boldsymbol{B}}}$. They are called hidden ports and can be determined from the graph of circuits A and B, respectively. For the example, these sets are given by

$$s_{\boldsymbol{A}} = \{(1,\mathbf{2}),(2,\mathbf{1}),(3,\mathbf{1})\}, \tag{A.23a}$$

$$s_{\boldsymbol{B}} = \{(7,\mathbf{1}),(7,\mathbf{2}),(7,\mathbf{3})\}, \tag{A.23b}$$

$$s_{\bar{\boldsymbol{A}}} = \{(1,\mathbf{1}),(4,\mathbf{1}),(2,\mathbf{2}),(5,\mathbf{1}),(3,\mathbf{2}),(6,\mathbf{1})\}, \tag{A.23c}$$

and

$$s_{\bar{\boldsymbol{B}}} = \{\}. \tag{A.23d}$$

Permuting the internal and external adjacency matrices yields

$$\begin{bmatrix}\vec{b}_{\boldsymbol{A}}\\ \vec{b}_{\boldsymbol{B}}\\ \vec{b}_{\bar{\boldsymbol{A}}}\\ \vec{b}_{\bar{\boldsymbol{B}}}\end{bmatrix} = \begin{bmatrix}[S_{\boldsymbol{AA}}] & 0 & [S_{\boldsymbol{A}\bar{\boldsymbol{A}}}] & 0\\ 0 & [S_{\boldsymbol{BB}}] & 0 & [S_{\boldsymbol{B}\bar{\boldsymbol{B}}}]\\ [S_{\bar{\boldsymbol{A}}\boldsymbol{A}}] & 0 & [S_{\bar{\boldsymbol{A}}\bar{\boldsymbol{A}}}] & 0\\ 0 & [S_{\bar{\boldsymbol{B}}\boldsymbol{B}}] & 0 & [S_{\bar{\boldsymbol{B}}\bar{\boldsymbol{B}}}]\end{bmatrix} \begin{bmatrix}\vec{a}_{\boldsymbol{A}}\\ \vec{a}_{\boldsymbol{B}}\\ \vec{a}_{\bar{\boldsymbol{A}}}\\ \vec{a}_{\bar{\boldsymbol{B}}}\end{bmatrix} \tag{A.24a}$$

and

$$\begin{bmatrix}\vec{a}_{\boldsymbol{A}}\\ \vec{a}_{\boldsymbol{B}}\\ \vec{a}_{\bar{\boldsymbol{A}}}\\ \vec{a}_{\bar{\boldsymbol{B}}}\end{bmatrix} = \begin{bmatrix}0 & [I] & 0 & 0\\ [I] & 0 & 0 & 0\\ 0 & 0 & [A_{\bar{\boldsymbol{A}}\bar{\boldsymbol{A}}}] & 0\\ 0 & 0 & 0 & [A_{\bar{\boldsymbol{B}}\bar{\boldsymbol{B}}}]\end{bmatrix} \begin{bmatrix}\vec{b}_{\boldsymbol{A}}\\ \vec{b}_{\boldsymbol{B}}\\ \vec{b}_{\bar{\boldsymbol{A}}}\\ \vec{b}_{\bar{\boldsymbol{B}}}\end{bmatrix}, \tag{A.24b}$$

with the ports ordered as $\{s_{\boldsymbol{A}}, s_{\boldsymbol{B}}, s_{\bar{\boldsymbol{A}}}, s_{\bar{\boldsymbol{B}}}\}$. The resulting block matrices connect the input and hidden ports of both sub-circuits. It is assumed that sub-circuits A and B are only connected at the input ports. From these equations the reflected wave amplitudes of the hidden ports are related by

$$\vec{a}_{\bar{\boldsymbol{A}}} = [A_{\bar{\boldsymbol{A}}\bar{\boldsymbol{A}}}]\,\vec{b}_{\bar{\boldsymbol{A}}} = [A_{\bar{\boldsymbol{A}}\bar{\boldsymbol{A}}}]\,[S_{\bar{\boldsymbol{A}}\boldsymbol{A}}]\,\vec{a}_{\boldsymbol{A}} + [A_{\bar{\boldsymbol{A}}\bar{\boldsymbol{A}}}]\,[S_{\bar{\boldsymbol{A}}\bar{\boldsymbol{A}}}]\,\vec{a}_{\bar{\boldsymbol{A}}} \tag{A.25a}$$

and

$$\vec{a}_{\bar{\boldsymbol{B}}} = [A_{\bar{\boldsymbol{B}}\bar{\boldsymbol{B}}}]\,\vec{b}_{\bar{\boldsymbol{B}}} = [A_{\bar{\boldsymbol{B}}\bar{\boldsymbol{B}}}]\,[S_{\bar{\boldsymbol{B}}\boldsymbol{B}}]\,\vec{a}_{\boldsymbol{B}} + [A_{\bar{\boldsymbol{B}}\bar{\boldsymbol{B}}}]\,[S_{\bar{\boldsymbol{B}}\bar{\boldsymbol{B}}}]\,\vec{a}_{\bar{\boldsymbol{B}}}, \tag{A.25b}$$

which yields the equations

$$\vec{a}_{\bar{\boldsymbol{A}}} = [T_{\bar{\boldsymbol{A}}\boldsymbol{A}}]\,\vec{a}_{\boldsymbol{A}} \quad \text{with} \quad [T_{\bar{\boldsymbol{A}}\boldsymbol{A}}] = ([I] - [A_{\bar{\boldsymbol{A}}\bar{\boldsymbol{A}}}]\,[S_{\bar{\boldsymbol{A}}\bar{\boldsymbol{A}}}])^{-1}\,[A_{\bar{\boldsymbol{A}}\bar{\boldsymbol{A}}}]\,[S_{\bar{\boldsymbol{A}}\boldsymbol{A}}] \tag{A.26a}$$

and

$$\vec{a}_{\bar{\boldsymbol{B}}} = [T_{\bar{\boldsymbol{B}}\boldsymbol{B}}]\,\vec{a}_{\boldsymbol{B}} \quad \text{with} \quad [T_{\bar{\boldsymbol{B}}\boldsymbol{B}}] = ([I] - [A_{\bar{\boldsymbol{B}}\bar{\boldsymbol{B}}}]\,[S_{\bar{\boldsymbol{B}}\bar{\boldsymbol{B}}}])^{-1}\,[A_{\bar{\boldsymbol{B}}\bar{\boldsymbol{B}}}]\,[S_{\bar{\boldsymbol{B}}\boldsymbol{B}}]. \tag{A.26b}$$

With the transmission matrices $[T_{\bar{\boldsymbol{A}}\boldsymbol{A}}]$ and $[T_{\bar{\boldsymbol{B}}\boldsymbol{B}}]$ the incident wave amplitudes at the hidden ports can be calculated from the incident wave amplitudes at input ports. The reflection matrices of the input ports are given by

$$\vec{b}_{\boldsymbol{A}} = [\Gamma_{\boldsymbol{A}}]\,\vec{a}_{\boldsymbol{A}} \quad \text{with} \quad [\Gamma_{\boldsymbol{A}}] = [S_{\boldsymbol{AA}}] + [S_{\boldsymbol{A}\bar{\boldsymbol{A}}}]\,[T_{\bar{\boldsymbol{A}}\boldsymbol{A}}] \tag{A.27a}$$

and

$$\vec{b}_{\boldsymbol{B}} = [\Gamma_{\boldsymbol{B}}]\,\vec{a}_{\boldsymbol{B}} \quad \text{with} \quad [\Gamma_{\boldsymbol{B}}] = [S_{\boldsymbol{BB}}] + [S_{\boldsymbol{B}\bar{\boldsymbol{B}}}]\,[T_{\bar{\boldsymbol{B}}\boldsymbol{B}}]. \tag{A.27b}$$

They relate the incident and reflected wave amplitudes. The wave amplitudes at the input ports are simply connected by

$$\vec{a}_{\boldsymbol{A}} = \vec{b}_{\boldsymbol{B}} \quad \text{and} \quad \vec{a}_{\boldsymbol{B}} = \vec{b}_{\boldsymbol{A}}. \tag{A.28}$$

For the hidden ports, they are related by

$$\vec{b}_{\bar{\boldsymbol{A}}} = [A_{\bar{\boldsymbol{A}}\bar{\boldsymbol{A}}}]\,\vec{a}_{\bar{\boldsymbol{A}}} \quad \text{and} \quad \vec{b}_{\bar{\boldsymbol{B}}} = [A_{\bar{\boldsymbol{B}}\bar{\boldsymbol{B}}}]\,\vec{a}_{\bar{\boldsymbol{B}}}. \tag{A.29}$$

All wave amplitudes can be calculated with the given equations from a valid set of input wave amplitudes (e.g., $\vec{b}_{\boldsymbol{A}}$).

A.4 Coupling Matrices

A.4.1 Parallel-Plate N-Furcation

The coupling coefficients of the sine and cosine potentials are given by

$$C^{s}_{\boldsymbol{\rho}[\mu],\bar{\boldsymbol{\rho}}[\bar{\mu}]} = \int_{y_{\mathbf{1}}}^{y_{\mathbf{2}}} \Psi_{s,\boldsymbol{\rho}[\mu]}(y)\, \Psi_{s,\bar{\boldsymbol{\rho}}[\bar{\mu}]}(y)\, dy = \sqrt{\frac{\varepsilon_{\mu}\varepsilon_{\bar{\mu}}}{h_{\boldsymbol{\rho}}\, h_{\bar{\boldsymbol{\rho}}}}}\, \frac{y_{\mathbf{2}} - y_{\mathbf{1}}}{2}\, (I'_{\boldsymbol{\rho}[\mu],\bar{\boldsymbol{\rho}}[\bar{\mu}]} - I''_{\boldsymbol{\rho}[\mu],\bar{\boldsymbol{\rho}}[\bar{\mu}]}) \tag{A.30a}$$

and

$$C^{c}_{\boldsymbol{\rho}[\mu],\bar{\boldsymbol{\rho}}[\bar{\mu}]} = \int_{y_{\mathbf{1}}}^{y_{\mathbf{2}}} \Psi_{c,\boldsymbol{\rho}[\mu]}(y)\, \Psi_{c,\bar{\boldsymbol{\rho}}[\bar{\mu}]}(y)\, dy = \sqrt{\frac{\varepsilon_{\mu}\varepsilon_{\bar{\mu}}}{h_{\boldsymbol{\rho}}\, h_{\bar{\boldsymbol{\rho}}}}}\, \frac{y_{\mathbf{2}} - y_{\mathbf{1}}}{2}\, (I'_{\boldsymbol{\rho}[\mu],\bar{\boldsymbol{\rho}}[\bar{\mu}]} + I''_{\boldsymbol{\rho}[\mu],\bar{\boldsymbol{\rho}}[\bar{\mu}]}) \tag{A.30b}$$

with

$$I'_{\boldsymbol{\rho}[\mu],\bar{\boldsymbol{\rho}}[\bar{\mu}]} = \cos\left(k_{y,\mu}\, \frac{2\, y_{0,\boldsymbol{\rho}} - y_{\mathbf{1}} - y_{\mathbf{2}}}{2} - k_{y,\bar{\mu}}\, \frac{2\, y_{0,\bar{\boldsymbol{\rho}}} - y_{\mathbf{1}} - y_{\mathbf{2}}}{2}\right) \mathrm{si}\left((k_{y,\mu} - k_{y,\bar{\mu}})\, \frac{y_{\mathbf{2}} - y_{\mathbf{1}}}{2}\right) \tag{A.30c}$$

and

$$I''_{\boldsymbol{\rho}[\mu],\bar{\boldsymbol{\rho}}[\bar{\mu}]} = \cos\left(k_{y,\mu}\, \frac{2\, y_{0,\boldsymbol{\rho}} - y_{\mathbf{1}} - y_{\mathbf{2}}}{2} + k_{y,\bar{\mu}}\, \frac{2\, y_{0,\bar{\boldsymbol{\rho}}} - y_{\mathbf{1}} - y_{\mathbf{2}}}{2}\right) \mathrm{si}\left((k_{y,\mu} + k_{y,\bar{\mu}})\, \frac{y_{\mathbf{2}} - y_{\mathbf{1}}}{2}\right), \tag{A.30d}$$

where the integration limits are

$$y_{\mathbf{1}} = \begin{cases} y_{0,\bar{\boldsymbol{\rho}}}, & \text{parallel plate,} \\ y_{0,\bar{\boldsymbol{\rho}}} + h_{\bar{\boldsymbol{\rho}}}, & \text{septum,} \end{cases} \tag{A.31a}$$

and

$$y_{\mathbf{2}} = \begin{cases} y_{0,\bar{\boldsymbol{\rho}}} + h_{\bar{\boldsymbol{\rho}}}, & \text{parallel plate,} \\ y_{0,\bar{\boldsymbol{\rho}}+1}, & \text{septum.} \end{cases} \tag{A.31b}$$

Removable singularities are avoided by using the function $\mathrm{si}\,(z) = \sin(z)/z$.

A.4.2 Parallel-Plate Integral

The calculation of the coupling coefficients requires an integration of exponential functions in x-direction. The resulting coupling matrix is given by

$$\begin{aligned} [C_{x,\nu[\mu],\bar{\nu}[\bar{\mu}]}] = &\int_{x_{\mathbf{1}}}^{x_{\mathbf{2}}} \begin{bmatrix} \mathrm{e}^{-\mathrm{j}\, k_{x,\nu[\mu]}\, (x - x_{(\nu,\mathbf{1})})} \\ \mathrm{e}^{\mathrm{j}\, k_{x,\nu[\mu]}\, (x - x_{(\nu,\mathbf{2})})} \end{bmatrix} \begin{bmatrix} \mathrm{e}^{-\mathrm{j}\, k_{x,\bar{\nu}[\bar{\mu}]}\, (x - x_{(\bar{\nu},\mathbf{1})})} \\ \mathrm{e}^{\mathrm{j}\, k_{x,\bar{\nu}[\bar{\mu}]}\, (x - x_{(\bar{\nu},\mathbf{2})})} \end{bmatrix}^{T} dx \\ = &\mathrm{j}\, w\, \mathrm{e}^{-\mathrm{j}\, (k_{x,\nu[\mu]} + k_{x,\bar{\nu}[\bar{\mu}]})\, \frac{w}{2}} \\ &\begin{bmatrix} \mathrm{si}\left(\mathrm{j}\, (k_{x,\nu[\mu]} + k_{x,\bar{\nu}[\bar{\mu}]})\, \frac{w}{2}\right) & \mathrm{si}\left(\mathrm{j}\, (k_{x,\nu[\mu]} - k_{x,\bar{\nu}[\bar{\mu}]})\, \frac{w}{2}\right) \\ \mathrm{si}\left(\mathrm{j}\, (k_{x,\bar{\nu}[\bar{\mu}]} - k_{x,\nu[\mu]})\, \frac{w}{2}\right) & \mathrm{si}\left(\mathrm{j}\, (k_{x,\nu[\mu]} + k_{x,\bar{\nu}[\bar{\mu}]})\, \frac{w}{2}\right) \end{bmatrix} \\ &\circ \left(\begin{bmatrix} \mathrm{e}^{-\mathrm{j}\, k_{x,\nu[\mu]}\, (x_{\mathbf{1}} - x_{(\nu,\mathbf{1})})} \\ \mathrm{e}^{\mathrm{j}\, k_{x,\nu[\mu]}\, (x_{\mathbf{2}} - x_{(\nu,\mathbf{2})})} \end{bmatrix} \begin{bmatrix} \mathrm{e}^{-\mathrm{j}\, k_{x,\bar{\nu}[\bar{\mu}]}\, (x_{\mathbf{1}} - x_{(\bar{\nu},\mathbf{1})})} \\ \mathrm{e}^{\mathrm{j}\, k_{x,\bar{\nu}[\bar{\mu}]}\, (x_{\mathbf{2}} - x_{(\bar{\nu},\mathbf{2})})} \end{bmatrix}^{T} \right), \end{aligned} \tag{A.32}$$

where the integration limits and the width are

$$x_{\mathbf{1}} = \begin{cases} \max\left(x_{(\nu,\mathbf{1})}, x_{(\bar{\nu},\mathbf{1})}\right), & \text{parallel-plate region,} \\ \min\left(x_{(\nu,\mathbf{1})}, x_{(\bar{\nu},\mathbf{1})}\right), & \text{furcation region,} \end{cases} \tag{A.33a}$$

$$x_{\mathbf{2}} = \begin{cases} \min\left(x_{(\nu,\mathbf{2})}, x_{(\bar{\nu},\mathbf{2})}\right), & \text{parallel-plate region,} \\ \max\left(x_{(\nu,\mathbf{2})}, x_{(\bar{\nu},\mathbf{2})}\right), & \text{furcation region,} \end{cases} \tag{A.33b}$$

and

$$w = x_{\mathbf{2}} - x_{\mathbf{1}}. \tag{A.33c}$$

Here, it is differentiated between parallel-plate and furcation regions. It is assumed that the parallel-plate limits are in ascending order $x_{(\nu,\mathbf{1})} \leq x_{(\nu,\mathbf{2})}$.

A.4.3 Current Distribution Integrals

The contour integrals of the longitudinal

$$I' = \oint_C h_t^2(x,y)\,dC = \sum_{s_1}\left(I'_{x,\nu}(y_{0,\nu}) + I'_{x,\nu}(y_{0,\nu}+h_\nu)\right) + \sum_{s_2} I'_{y,\nu}(x_{0,\nu}) \tag{A.34a}$$

and the transverse current distribution

$$I'' = \oint_C \Psi_{xy}^2(x,y)\,dC = \sum_{s_1}\left(I''_{x,\nu}(y_{0,\nu}) + I''_{x,\nu}(y_{0,\nu}+h_\nu)\right) + \sum_{s_2} I''_{y,\nu}(x_{0,\nu}) \tag{A.34b}$$

are split into integrals associated with the parallel-plate components. The first summation over the set s_1 considers the top and the bottom wall of the parallel plates. Short circuits and the septa of the furcations are taken into account by the second summation over the set s_2. The individual integrals are defined by

$$I'_{x,\nu}(y_0) = \int_{x_1}^{x_2} h_{x,\nu}^2(y_0)\,dx, \qquad I'_{y,\nu}(x_0) = \int_{y_1}^{y_2} h_{y,\nu}^2(x_0)\,dy, \tag{A.35a}$$

$$I''_{x,\nu}(y_0) = \int_{x_1}^{x_2} \Psi_{xy}^2(y_0)\,dx, \quad \text{and} \quad I''_{y,\nu}(x_0) = \int_{y_1}^{y_2} \Psi_{xy}^2(x_0)\,dy. \tag{A.35b}$$

These integrals can be calculated analytically with the modal fields given in Sec. 3.5.1. The longitudinal integrals yield

$$I'_{x,\nu}(y_0) = \sum_{\mu,\bar{\mu}} \Psi_{c,\mu}(y_0)\Psi_{c,\bar{\mu}}(y_0) \begin{bmatrix}1\\1\end{bmatrix}^T \left([C_{x,\mu,\bar{\mu}}] \circ \begin{bmatrix} A_{\mathbf{2}[\mu],\mathbf{1}[\mu]} \\ A_{\mathbf{2}[\mu],\mathbf{2}[\mu]} \end{bmatrix} \begin{bmatrix} A_{\mathbf{2}[\bar{\mu}],\mathbf{1}[\bar{\mu}]} \\ A_{\mathbf{2}[\bar{\mu}],\mathbf{2}[\bar{\mu}]} \end{bmatrix}^T \right) \begin{bmatrix}1\\1\end{bmatrix}, \tag{A.36a}$$

$$I'_{y,\nu}(x_0) = \sum_{\mu,\bar{\mu}} C^s_{\mu,\bar{\mu}} \begin{bmatrix} \mathrm{e}^{-\mathrm{j}\,k_{x,\mu}(x_0-x_{\mathbf{1}})} \\ \mathrm{e}^{\mathrm{j}\,k_{x,\mu}(x_0-x_{\mathbf{2}})} \end{bmatrix}^T \begin{bmatrix} A_{\mathbf{1}[\mu],\mathbf{1}[\mu]} \\ A_{\mathbf{1}[\mu],\mathbf{2}[\mu]} \end{bmatrix} \begin{bmatrix} A_{\mathbf{1}[\bar{\mu}],\mathbf{1}[\bar{\mu}]} \\ A_{\mathbf{1}[\bar{\mu}],\mathbf{2}[\bar{\mu}]} \end{bmatrix}^T \begin{bmatrix} \mathrm{e}^{-\mathrm{j}\,k_{x,\bar{\mu}}(x_0-x_{\mathbf{1}})} \\ \mathrm{e}^{\mathrm{j}\,k_{x,\bar{\mu}}(x_0-x_{\mathbf{2}})} \end{bmatrix}, \tag{A.36b}$$

and

$$I'_{y,\nu}(x_0) = \sum_{\mu} C^s_{\mu,\mu} \left(\begin{bmatrix} A_{\mathbf{1}[\mu],\mathbf{1}[\mu]} \\ A_{\mathbf{1}[\mu],\mathbf{2}[\mu]} \end{bmatrix}^T \begin{bmatrix} \mathrm{e}^{-\mathrm{j}\,k_{x,\mu}(x_0-x_{\mathbf{1}})} \\ \mathrm{e}^{\mathrm{j}\,k_{x,\mu}(x_0-x_{\mathbf{2}})} \end{bmatrix} \right)^2 \tag{A.36c}$$

for the parallel plates, the furcations, and the short circuits, respectively. Open and short circuits, which model symmetry planes, do not contribute. The transverse integrals of

TE^z-modes are given by

$$I''_{x,\nu}(y_0) = \sum_{\mu,\bar{\mu}} \Psi_{c,\mu}(y_0)\, \Psi_{c,\bar{\mu}}(y_0) \begin{bmatrix} 1 \\ 1 \end{bmatrix}^T \left([C_{x,\mu,\bar{\mu}}] \circ \begin{bmatrix} \frac{\mathrm{j}\, a_{\mathbf{1}[\mu]}}{\sqrt{k_c\, k_{x,\mu}}} \\ \frac{-\mathrm{j}\, a_{\mathbf{2}[\mu]}}{\sqrt{k_c\, k_{x,\mu}}} \end{bmatrix} \begin{bmatrix} \frac{\mathrm{j}\, a_{\mathbf{1}[\bar{\mu}]}}{\sqrt{k_c\, k_{x,\bar{\mu}}}} \\ \frac{-\mathrm{j}\, a_{\mathbf{2}[\bar{\mu}]}}{\sqrt{k_c\, k_{x,\bar{\mu}}}} \end{bmatrix}^T \right) \begin{bmatrix} 1 \\ 1 \end{bmatrix}, \quad \text{(A.37a)}$$

$$I''_{y,\nu}(x_0) = \sum_{\mu,\bar{\mu}} C^c_{\mu,\bar{\mu}} \begin{bmatrix} \mathrm{e}^{-\mathrm{j}\, k_{x,\mu}(x_0 - x_{\mathbf{1}})} \\ \mathrm{e}^{\mathrm{j}\, k_{x,\mu}(x_0 - x_{\mathbf{2}})} \end{bmatrix}^T \begin{bmatrix} \frac{\mathrm{j}\, a_{\mathbf{1}[\mu]}}{\sqrt{k_c\, k_{x,\mu}}} \\ \frac{-\mathrm{j}\, a_{\mathbf{2}[\mu]}}{\sqrt{k_c\, k_{x,\mu}}} \end{bmatrix} \begin{bmatrix} \frac{\mathrm{j}\, a_{\mathbf{1}[\bar{\mu}]}}{\sqrt{k_c\, k_{x,\bar{\mu}}}} \\ \frac{-\mathrm{j}\, a_{\mathbf{2}[\bar{\mu}]}}{\sqrt{k_c\, k_{x,\bar{\mu}}}} \end{bmatrix}^T \begin{bmatrix} \mathrm{e}^{-\mathrm{j}\, k_{x,\bar{\mu}}(x_0 - x_{\mathbf{1}})} \\ \mathrm{e}^{\mathrm{j}\, k_{x,\bar{\mu}}(x_0 - x_{\mathbf{2}})} \end{bmatrix}, \quad \text{(A.37b)}$$

and

$$I''_{y,\nu}(x_0) = \sum_{\mu} C^c_{\mu,\mu} \left(\begin{bmatrix} \frac{\mathrm{j}\, a_{\mathbf{1}[\bar{\mu}]}}{\sqrt{k_c\, k_{x,\bar{\mu}}}} \\ \frac{-\mathrm{j}\, a_{\mathbf{2}[\bar{\mu}]}}{\sqrt{k_c\, k_{x,\bar{\mu}}}} \end{bmatrix}^T \begin{bmatrix} \mathrm{e}^{-\mathrm{j}\, k_{x,\bar{\mu}}(x_0 - x_{\mathbf{1}})} \\ \mathrm{e}^{\mathrm{j}\, k_{x,\bar{\mu}}(x_0 - x_{\mathbf{2}})} \end{bmatrix} \right)^2 \quad \text{(A.37c)}$$

for the parallel plates, the furcations, and the short circuits, respectively. For TM^z-modes they are zero because of the missing longitudinal magnetic field components. Due to the orthogonality of the parallel-plate modes, a single summation is sufficient for the short circuits, while a double summation is necessary for the septa of the furcations.

B Dimensions and Parameters of the Components

B.1 Pitch of Via Rows

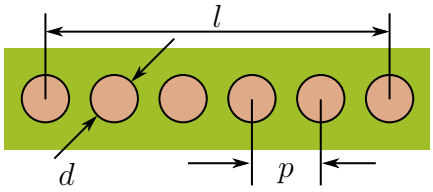

Figure B.1: Dimensions of a via row.

A via row of length l, as depicted in Fig. B.1, consists of vias with diameter d. They are placed with a pitch

$$p = \frac{l}{N-1}, \tag{B.1a}$$

where N is the number of vias. This number is given by

$$N = \min\left(N_0, N_{max}\right) \tag{B.1b}$$

with the maximum

$$N_{max} = \left\lfloor \frac{l}{p_{min}} \right\rfloor + 1 \tag{B.1c}$$

and the nominal

$$N_0 = \left\lfloor \frac{l}{p_0} + \frac{1}{2} \right\rfloor + 1 \tag{B.1d}$$

via numbers. For very short length only one via is placed at the start of the row. Otherwise, the pitch is close to the nominal pitch p_0 but not below the minimum pitch p_{min}.

B.2 Material and Stack Parameters

The dielectric properties of the used substrate materials are listed in Tab. B.1. For composite materials, the permittivity ϵ_r and the loss tangent $\tan\left(\delta_d\right)$ are modeled by anisotropic parameters. The orthogonal and parallel directions of the substrate are marked by $\perp$ and $\parallel$, respectively.

Based on these materials, stacks for single and multilayer PCBs are listed in Tab. B.2. The substrate thickness h_i and metalization height m_i are defined for each layer i.

Table B.1: Material parameters.

Name	$\epsilon_{r,\perp}$	$\epsilon_{r,\parallel}$	$\tan(\delta_{d,\perp})$	$\tan(\delta_{d,\parallel})$
Rogers RO4003C	3.38[1]	3.65[6]	0.0027[1]	0.0035[6]
Rogers RO4450F	3.52[1]	3.80[6]	0.0040[1]	0.0040[6]
Rogers Duroid 5880	2.20[1]	2.20[1]	0.0009[1]	0.0009[1]
Megtron 6	3.62[2]	3.90[6]	0.0050[2]	0.0060[6]
Preperm L335	3.35[3]	3.35[3]	0.0005[3]	0.0005[3]
Arlon 49N	4.80[4]	-	0.0250[4]	-
PTFE	2.10[5]	2.10[5]	0.0002[5]	0.0002[5]

[1] From material data sheet at 10 GHz. [2] From material data sheet at 23 GHz.
[3] From material data sheet at 1 GHz. [4] From material data sheet at 1 MHz.
[5] From material library of *CST Microwave Studio* at 10 GHz.
[6] Measured by resonator at 20 GHz [157].

Table B.2: Stack parameters.

Name	Material	m_1 (µm)	h_1 (mm)	m_2 (µm)	h_2 (mm)	m_3 (µm)
Stack1	Megtron 6	35	0.27	35	0.30	18
Stack2	RO4003C	25	0.20	20	0.30	35
Stack3	RO4003C	35	0.61			
Stack4	RO4003C	25	0.51			
Stack5	RO4003C	27	0.48			

B.3 Transmission Line Parameters

The geometry of different CPWs and SIWs as depicted in Fig. B.2a and Fig. B.2b is defined by the listed parameters. The transmission lines are implemented on stacks defined in Tab. B.2 and the used metal layers are marked by $i-j$. The attenuation coefficient α is calculated and listed for 20 GHz and 30 GHz. Tab. B.3 lists the parameters of the CPWs. The strip width s_{CPW} and the gap width g_{CPW} define the geometry of the top metalization. The via rows are separated by w_{CPW} and connect the layers $1-2$ of the stack. The vias

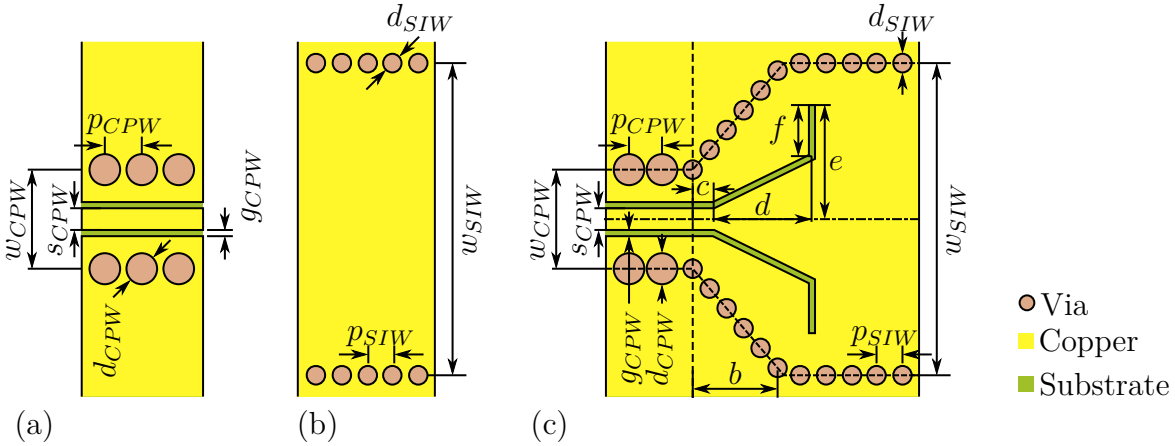

Figure B.2: Dimensions of (a) CPW, (b) SIW, and (c) CPW-to-SIW transition.

have diameter d_{CPW} and the pitch of the rows is defined by a nominal $p_{0,CPW}$ and minimum pitch $p_{min,CPW}$, as discussed in Sec. B.1. Tab. B.4 lists the parameters of the SIWs. The via rows are defined analogously to the ground vias of the CPW by the parameters w_{SIW}, d_{SIW}, $p_{0,SIW}$, and $p_{min,SIW}$. a is the width of the equivalent waveguide, as discussed in Sec. 3.3.1.

Table B.3: CPW parameters.

Name	Stack	s_{CPW} (mm)	g_{CPW} (mm)	w_{CPW} (mm)	d_{CPW} (mm)	$p_{0,CPW}$ (mm)	$p_{min,CPW}$ (mm)	α(20 GHz) (dB/mm)	α(30 GHz) (dB/mm)
CPW1	Stack1	0.35	0.1	1.60	0.5	1	0.50	0.043	0.056
CPW2	Stack2	0.31	0.1	2	0.5	0.75	0.60	0.034	0.043
CPW3	Stack3	0.53	0.1	2	0.5	0.75	0.60	0.032	0.040
CPW4	Stack4	0.56	0.1	2	0.3	0.60	0.36	0.030	0.038
CPW5	Stack5	0.83	0.2	2.23	0.5	0.70	0.70	0.028	0.033

Table B.4: SIW parameters.

Name	Stack	Layers	w_{SIW} (mm)	d_{SIW} (mm)	$p_{0,SIW}$ (mm)	$p_{min,SIW}$ (mm)	a_{SIW} (mm)	α(20 GHz) (dB/mm)	α(30 GHz) (dB/mm)
SIW1	Stack1	1-2	5.04	0.3	0.40	0.40	4.80	0.058	0.058
SIW2	Stack1	1-2	3.44	0.3	0.40	0.40	3.20	4.835[1]	0.086
SIW3	Stack2	1-2	5.06	0.5	0.80	0.80	4.69	0.065	0.058
SIW4	Stack3	1-2	5.06	0.5	0.75	0.60	4.67	0.057	0.049
SIW5	Stack4	1-2	5.25	0.3	0.45	0.36	5.02	0.053	0.053
SIW6	Stack4	1-2	3.72	0.3	0.45	0.36	3.49	3.777[1]	0.074
SIW7	Stack5	1-2	4.85	0.5	0.70	0.70	4.46	0.077	0.059
SIW8	Stack1	1-3	5.04	0.3	0.40	0.40	4.80	0.044	0.044
SIW9	Stack1	1-3	3.44	0.3	0.40	0.40	3.20	4.901[1]	0.066
SIW10	Stack2	1-3	5.06	0.5	0.80	0.80	4.69	0.039	0.034

[1] Frequency is below cutoff.

B.4 Parameters of Components

This section summarizes the parameters of the designed components. Tab. B.5 lists the parameters of several optimized CPW-to-SIW transitions. The columns CPW and SIW refer to the transmission lines defined in Sec. B.3. The via rows and the central strip of the transition are linearly tapered and the CPW gaps are short circuited by stubs. The dimension b, c, d, e, and f are depicted in Fig. B.2c. The presented structure is slightly extended and has more degrees of freedom than the one proposed in [17]. Tab. B.6, Tab. B.7, and Tab. B.8 list the parameters of the E-plane tapers, multilayer tapers, and polarizers, as discussed in Chapter 4.

Table B.5: Parameters of the CPW-to-SIW transitions.

Name	CPW	SIW	b (mm)	c (mm)	d (mm)	e (mm)	f (mm)
CPW-SIW1	CPW1	SIW1	1.49	0.34	1.61	1.84	0.84
CPW-SIW2	CPW1	SIW2	0.82	0.30	1.05	1.42	0.50
CPW-SIW3	CPW2	SIW3	1.30	0.38	1.68	1.60	0.80
CPW-SIW4	CPW3	SIW4	0.50	0.56	1.89	2.22	0
CPW-SIW5	CPW4	SIW5	1.80	0.36	1.87	2.16	0.74
CPW-SIW6	CPW4	SIW6	0.21	0.37	1.30	1.56	0.27
CPW-SIW7[1]	CPW5	SIW7	0	0.10	1.11	2.02	0.59

[1] Last CPW via omitted.

Table B.6: Parameters of the E-plane tapers (see Sec. 4.1.2).

Name	Material	a (mm)	$\epsilon_{r,eff}$	b_1 (mm)	b_2 (mm)	L (mm)	Profile	Γ_M (dB)
TAP1	RO4003C/L335	4.70	3.55	0.61	2.34	8	Cheb.	-20
TAP2[1]	RO4003C/L335	4.70	3.55	0.61	2.34	8	Cheb.	-20
TAP3[2]	Megtron 6	4.80	3.75	0.61	2.29	8	Cheb.	-20
TAP4	Megtron 6	3.20	3.75	0.61	1.54	8	Cheb.	-20

[1] Rounded upper edges with a radius of 0.5 mm.
[2] Upper edges with a chamfer of 0.5 mm.

Table B.7: Parameters of the SIW tapers (see Sec. 4.1.3).

Name	Material	Input	Output	L (mm)	Profile
SIWTAP1	RO4003C	SIW3	SIW10	8	Triang.
SIWTAP2	Megtron 6	SIW1	SIW8	8	Triang.
SIWTAP3	Megtron 6	SIW2	SIW9	8	Triang.

Table B.8: Parameters of the polarizers (see Sec. 4.2).

Name	Material	Taper	l (mm)	s_0 (mm)	s_1 (mm)	s_2 (mm)	s_3 (mm)	s_4 (mm)
POL1	RO4003C/L335	TAP2	12.39	6.05	0.81	1.77	2.07	1.69
POL2	Megtron 6	TAP3	14.66	8.09	0.62	1.89	2.20	1.86
POL3	Megtron 6	TAP4	12.12	6.81	0.30	1.40	1.87	1.75

Name	w_1 (mm)	w_2 (mm)	w_3 (mm)	w_4 (mm)
POL1	3.59	2.41	1.71	0.90
POL2	3.69	2.43	1.79	1.08
POL3	2.13	1.50	1.06	0.56

B.5 Parameters of Lens Antennas

The single lens antenna feeds a hemispherical lens, the parameters of which are listed in Tab. B.9. The dimensions of the used test-fixture are given in Tab. B.10. For the array antenna, the lens surface is describes by NURBS. For each element, sixteen control points with the coordinates

$$[B_{x,n}] = \frac{1}{2}\begin{bmatrix} -f'_n & -f_n & -f_n & -f'_n \\ -e'_n & -e_n & -e_n & -e'_n \\ e'_n & e_n & e_n & e'_n \\ f'_n & f_n & f_n & f'_n \end{bmatrix}, \tag{B.2a}$$

$$[B_{y,n}] = \frac{1}{2}\begin{bmatrix} -f'_n & -e'_n & e'_n & f'_n \\ -f_n & -e_n & e_n & f_n \\ -f_n & -e_n & e_n & f_n \\ -f'_n & -e'_n & e'_n & f'_n \end{bmatrix}, \tag{B.2b}$$

and

$$[B_{z,n}] = \begin{bmatrix} h_0 & h_0 & h_0 & h_0 \\ h_0 & h_n & h_n & h_0 \\ h_0 & h_n & h_n & h_0 \\ h_0 & h_0 & h_0 & h_0 \end{bmatrix} \tag{B.2c}$$

and the weightings

$$[W_n] = \begin{bmatrix} w'_0 & w_0 & w_0 & w'_0 \\ w_0 & w_n & w_n & w_0 \\ w_0 & w_n & w_n & w_0 \\ w'_0 & w_0 & w_0 & w'_0 \end{bmatrix} \tag{B.2d}$$

are defined. Hereby, the geometrical parameters are given in (5.1). The values for the selected lens geometries are listed in Tab. B.11. The various components of the realized array and the distances between them are listed in Tab. B.12.

Table B.9: Parameters of the hemispherical lenses (see Sec. 5.1).

Name	**SIW Material**	**Lens Mat.**	a **(mm)**	b **(mm)**	r_D **(mm)**	z_0 **(mm)**	r **(mm)**	l_0 **(mm)**	l_1 **(mm)**
LEN1	RO4003C	PTFE	4.47	4.47	0.4[1]	3.5	3.5	4	0.3
LEN2	RO4003C/L335	PTFE	4.7	4.7	0.5[2]	3.75	3.5	4.25	0.4

[1] See Fig. 5.1. [2] See Fig. 5.7.

Table B.10: Parameters of the test fixture (see Sec. 5.1.1).

i	0	1	2	3	4	5	6	7	8	9
s_i (mm)	0	0.39	0.93	1.47	2	2.27	2.59	3.17	3.61	4.5
w_i (mm)	10.66	9.55	7.65	6.97	6.72	6.07	5.35	4.82	4.61	4.5
l_i (mm)	-	3.15	3.4	2.82	2.27	4.36	4.6	4.07	4.33	-

Table B.11: Parameters of the array elements with different lenses (see Sec. 5.2.1).

Name	d_0 (mm)	d_1 (mm)	d_2 (mm)	l_1 (mm)	l_2 (mm)
ALEN1	0.3	2.6	1.8	0.0	0.0
ALEN2	0.3	2.6	1.9	0.0	0.0
ALEN3	0.3	2.5	2.0	0.0	0.0

Name	e_1 (mm)	e_2 (mm)	α	w_1	w_2	w_0	w_0'
ALEN*	4.5	3.1	0.2	5	5	1	0.2

Table B.12: PCB components of the lens array antenna with their length and the distances between them (see Fig. 5.19).

Component	Element 1 (Rx/Tx)				Element 2 (Tx-only)			
	ID	l_1 (mm)	l (mm)	l_2 (mm)	ID	l_1 (mm)	l (mm)	l_2 (mm)
CPW Bend	-	1.50	2.60	1.04	-	1.50	2.60	1.04
SIW Feed	CPW-SIW1	0	3	0.10	CPW-SIW2	0	2	5.70
SIW Taper	SIWTAP2	0	8	3.70	SIWTAP3	0	8	0
Polarizer	POL2	1.40	14.66	1	POL3	1.54	12.12	2.50

Bibliography

[1] ITU, *Measuring the Information Society Report*. Geneva, 2018.

[2] H. Fenech, S. Amos, A. Tomatis, and V. Soumpholphakdy, "High Throughput Satellite Systems: An Analytical Approach", *IEEE Trans. Aerosp. Electron. Syst.*, vol. 51, no. 1, pp. 192–202, 2015.

[3] Caleb Henry, "LEO and MEO Broadband Constellations Mega Source of Consternation", *SpaceNews Magazine*, 2018.

[4] ECC, *The European Table of Frequency Allocations and Applications in the Frequency Range 8.3 kHz to 3000 GHz*, ERC Report 25, 2019.

[5] FCC, *Rule Part 5.516B*, 2019.

[6] FCC, *ViaSat 2, Attachment A: Technical Information to Supplement Schedule S*, SAT-MOD-20141105-00121, 2014.

[7] B.-W. Min and G. M. Rebeiz, "Single-Ended and Differential Ka-Band BiCMOS Phased Array Front-Ends", *IEEE J. Solid-State Circuits*, vol. 43, no. 10, pp. 2239–2250, 2008.

[8] C. Liu, Q. Li, Y. Li, X.-D. Deng, H. Tang, R. Wang, H. Liu, and Y.-Z. Xiong, "A Ka-Band Single-Chip SiGe BiCMOS Phased-Array Transmit/Receive Front-End", *IEEE Trans. Microwave Theory Techn.*, vol. 64, no. 11, pp. 3667–3677, 2016.

[9] F. Tabarani, L. Boccia, T. Purtova, A. Shamsafar, H. Schumacher, and G. Amendola, "0.25-um BiCMOS System-on-Chip for K-/Ka-Band Satellite Communication Transmit–Receive Active Phased Arrays", *IEEE Trans. Microwave Theory Techn.*, vol. 66, no. 5, pp. 2325–2339, 2018.

[10] W. Theunissen, V. Jain, and G. Menon, "Development of a Receive Phased Array Antenna for High Altitude Platform Stations using Integrated Beamformer Modules", in *IEEE MTT-S International Microwave Symposium Digest (IMS)*, 2018, pp. 779–782.

[11] W. M. Abdel-Wahab, H. Al-Saedi, E. H. Mirza Alian, M. Raeis-Zadeh, A. Ehsandar, A. Palizban, N. Ghafarian, G. Chen, H. Gharaee, M. R. Nezhad-Ahmadi, and S. Safavi Naeini, "A Modular Architecture for Wide Scan Angle Phased Array Antenna for K/Ka Mobile SatCom", in *IEEE MTT-S International Microwave Symposium Digest (IMS)*, 2019, pp. 1076–1079.

[12] K. K. Wei Low, A. Nafe, S. Zihir, T. Kanar, and G. M. Rebeiz, "A Scalable Circularly-Polarized 256-Element Ka-Band Phased-Array SatCom Transmitter with ±60° Beam Scanning and 34.5 dBW EIRP", in *IEEE MTT-S International Microwave Symposium Digest (IMS)*, 2019, pp. 1064–1067.

[13] Q. Luo, S. Gao, T. Chaloun, W. Menzel, L. Boccia, E. Arnieri, G. Amendola, and V. Ziegler, "Antenna Array Elements for Ka-Band Satellite Communication on the Move", in *Loughborough Antennas & Propagation Conference (LAPC)*, 2013, pp. 135–139.

[14] T. Chaloun, C. Hillebrand, C. Waldschmidt, and W. Menzel, "Active Transmitarray Submodule for K/Ka Band SatCom Applications", in *Proc. German Microwave Conference (GeMiC)*, 2015, pp. 198–201.

[15] M. Geissler, M. Arias Campo, M. Böttcher, P. Buchner, S. Bruni, R. Gieron, J. Letschnik, A. F. Jacob, T. Jaschke, N. Pham, B. Rohrdantz, and C. Hunscher, *Hochintegrierte Santana-Antenne für mobile Applikationen : SAMOA : Schlussbericht zum Verbundprojekt : Förderzeitraum: 01.01.2013-30.06.2017*, 2017.

[16] F. Shigeki, "Waveguide Line", Jap. Pat. 06-53 711, 1994.

[17] X.-P. Chen and K. Wu, "Low-Loss Ultra-Wideband Transition Between Conductor-Backed Coplanar Waveguide and Substrate Integrated Waveguide", in *IEEE MTT-S International Microwave Symposium Digest (IMS)*, 2009, pp. 349–352.

[18] F. Taringou, D. Dousset, J. Bornemann, and K. Wu, "Substrate-Integrated Waveguide Transitions to Planar Transmission-Line Technologies", in *IEEE MTT-S International Microwave Symposium Digest (IMS)*, 2012, pp. 1–3.

[19] Z. Kordiboroujeni and J. Bornemann, "New Wideband Transition From Microstrip Line to Substrate Integrated Waveguide", *IEEE Trans. Microwave Theory Techn.*, vol. 62, no. 12, pp. 2983–2989, 2014.

[20] X.-P. Chen, K. Wu, and D. Drolet, "Substrate Integrated Waveguide Filter With Improved Stopband Performance for Satellite Ground Terminal", *IEEE Trans. Microwave Theory Techn.*, vol. 57, no. 3, pp. 674–683, 2009.

[21] Z. Kordiboroujeni, J. Bornemann, and T. Sieverding, "K-Band Substrate Integrated Waveguide T-Junction Diplexer Design by Mode-Matching Techniques", in *Proc. Asia-Pacific Microwave Conference (APMC)*, 2014, pp. 1297–1299.

[22] S. Sirci, J. D. Martinez, J. Vague, and V. E. Boria, "Substrate Integrated Waveguide Diplexer Based on Circular Triplet Combline Filters", *IEEE Microw. Wireless Compon. Lett.*, vol. 25, no. 7, pp. 430–432, 2015.

[23] L. Yan, W. Hong, G. Hua, J. Chen, K. Wu, and T. J. Cui, "Simulation and Experiment on SIW Slot Array Antennas", *IEEE Microw. Wireless Compon. Lett.*, vol. 14, no. 9, pp. 446–448, 2004.

[24] K. Kuhlmann, K. Rezer, and A. F. Jacob, "Circularly Polarized Substrate-Integrated Waveguide Antenna Array at Ka-Band", in *Proc. German Microwave Conference (GeMiC)*, 2008, pp. 471–174.

[25] A. J. Martinez-Ros, J. L. Gomez-Tornero, F. Quesada-Pereira, and A. Alvarez-Melcon, "Transverse Resonance Analysis of a Planar Leaky Wave Antenna with Flexible Control of the Complex Propagation Constant", in *IEEE Antennas and Propagation Society International Symposium Digest (APSURSI)*, 2011, pp. 1289–1292.

[26] K. Kuhlmann and A. F. Jacob, "Active 30 GHz Antenna Array for Digital Beamforming and Polarization Multiplexing", in *IEEE MTT-S International Microwave Symposium Digest (IMS)*, 2010, pp. 1276–1279.

[27] ITU, *Attenuation by Atmospheric Gases*, ITU-R Rec. P.676-11, 2016.

[28] ITU, *Reference Standard Atmospheres*, ITU-R Rec. P.835-6, 2017.

[29] ITU, *Attenuation Due to Clouds and Fog*, ITU-R Rec. P.840-7, 2017.

[30] ITU, *Propagation Data and Prediction Methods Required for the Design of Earth-Space Telecommunication Systems*, ITU-R Rec. P.618-13, 2017.

[31] ETSI, *Digital Video Broadcasting (DVB); Second Generation Framing Structure, Channel Coding and Modulation Systems for Broadcasting, Interactive Services, News Gathering and Other Broadband Satellite Applications; Part 1: DVB-S2*, ETSI EN 302 307-1 V1.4.1, 2014.

[32] ETSI, *Digital Video Broadcasting (DVB); Second Generation Framing Structure, Channel Coding and Modulation Systems for Broadcasting, Interactive Services, News Gathering and Other Broadband Satellite Applications; Part 2: DVB-S2 Extensions (DVB-S2X)*, ETSI EN 302 307-2 V1.1.1, 2014.

[33] ETSI, *DVB Fact Sheet, Extending DVB-S2*, 2018.

[34] T. Jaschke, B. Rohrdantz, H. K. Mitto, and A. F. Jacob, "Rx/Tx Integration Concepts for Ground Segment SatCom Antenna Arrays", in *Proc. German Microwave Conference (GeMiC)*, 2016, pp. 27–30.

[35] E. Arnieri, L. Boccia, and G. Amendola, "A Ka-Band Dual-Frequency Radiator for Array Applications", *IEEE Antennas and Wirel. Propag. Lett.*, vol. 8, pp. 894–897, 2009.

[36] J. E. Hansen, Ed., *Spherical Near-Field Antenna Measurements*, ser. IEE Electromagnetic Wave Ser. Peregrinus, London, 1987, vol. 26.

[37] R. J. Mailloux, *Phased Array Antenna Handbook*, 2nd Ed., ser. Ant. and Propag. Library. Artech House, Boston, 2005.

[38] T. Taylor, "Design of Circular Apertures for Narrow Beamwidth and Low Sidelobes", *IRE Trans. Antennas Propag.*, vol. 8, no. 1, pp. 17–22, 1960.

[39] ETSI, *Satellite Earth Stations and Systems (SES); Harmonised Standard for Earth Stations on Mobile Platforms (ESOMP)*, ETSI EN 302 978 V2.1.2, 2016.

[40] T. Jaschke, B. Rohrdantz, J.-P. Mohncke, and A. F. Jacob, "A Ka-Band Substrate-Integrated Waveguide Diplexer with Wide Frequency Spread", in *Proc. European Microwave Conference (EuMC)*, 2016, pp. 779–782.

[41] A. Sieganschin, T. Jaschke, D. Safi, and A. F. Jacob, "On the Design of Active Rx/Tx-Diplexers with Wide Frequency Spread", in *Proc. German Microwave Conference (GeMiC)*, 2018, pp. 1–4.

[42] A. Sieganschin, T. Jaschke, H. K. Mitto, N. J. Lamann, J. Waldhelm, and A. F. Jacob, "A Compact Low-Loss Multilayer SIW Diplexer at K/Ka-Band", in *Proc. German Microwave Conference (GeMiC)*, 2019, pp. 51–54.

[43] A. Sieganschin, T. Jaschke, and A. F. Jacob, "A Compact Diplexer for Circularly Polarized 20/30 GHz SIW-Antennas", in *IEEE MTT-S International Microwave Symposium Digest (IMS)*, to be published, 2020.

[44] A. Sieganschin, T. Jaschke, and A. F. Jacob, "A Compact Low-Noise Frontend for Rx/Tx-Integrated SatCom Arrays", in *Proc. European Microwave Conference (EuMC)*, 2020, pp. 1–4.

[45] B. Rohrdantz, K. Kuhlmann, A. Stark, A. Geise, and A. F. Jacob, "Digital Beamforming Antenna Array with Polarisation Multiplexing for Mobile High-Speed Satellite Terminals at Ka-Band", *The J. of Engineering*, vol. 6, no. 6, pp. 180–188, 2016.

[46] M. N. Pham, "An External Calibration System for DBF Receiver Arrays at Ka-Band", Ph.D. Thesis, Techn. Univ. Hamburg, 2019.

[47] M. L. Livingston, "The Effect of Antenna Characteristics on Antenna Noise Temperature and System SNR", *IRE Trans. Space Electron. Telem.*, vol. 7, no. 3, pp. 71–79, 1961.

[48] ITU, *Determination of the G/T Ratio for Earth Stations Operating in the Fixed-Satellite Service*, ITU-R Rec. S.733-2, 2001.

[49] J. A. Kinzel, B. J. Edward, and D. Rees, "V-Band, Space-Based Phased Arrays", *Microwave J.*, vol. 30, no. 1, pp. 89–102, 1987.

[50] R. J. Mailloux, "Antenna Array Architecture", *Proc. IEEE*, vol. 80, no. 1, pp. 163–172, 1992.

[51] T. Chaloun, V. Ziegler, and W. Menzel, "Design of a Dual-Polarized Stacked Patch Antenna for Wide-Angle Scanning Reflectarrays", *IEEE Trans. Antennas Propagat.*, vol. 64, no. 8, pp. 3380–3390, 2016.

[52] E. J. Wilkinson, "An N-Way Hybrid Power Divider", *IEEE Trans. Microwave Theory Techn.*, vol. 8, no. 1, pp. 116–118, 1960.

[53] B. Rohrdantz, T. Jaschke, T. Reuschel, S. Radzijewski, A. Sieganschin, and A. F. Jacob, "An Electronically Scannable Reflector Antenna Using a Planar Active Array Feed at Ka-Band", *IEEE Trans. Microwave Theory Techn.*, vol. 65, no. 5, pp. 1650–1661, 2017.

[54] A. F. Jacob, T. Jaschke, and B. Rohrdantz, "Advanced Terminal Antenna Concepts for Mobile Satellite Communications", in *Proc. Asia-Pacific Microwave Conference (APMC)*, 2018, pp. 1–3.

[55] J. Howell, "Microstrip Antennas", *IEEE Trans. Antennas Propagat.*, vol. 23, no. 1, pp. 90–93, 1975.

[56] T. Chaloun, C. Waldschmidt, and W. Menzel, "Wide-Angle Scanning Cavity Antenna Element for Mobile SatCom Applications at Ka Band", in *Proc. European Conference on Antennas and Propagation (EuCAP)*, IEEE, 2016, pp. 1–5.

[57] B. Rohrdantz, T. Jaschke, F. K. Gellersen, and A. F. Jacob, "A Dual-Frequency and Dual-Polarized Patch Antenna at Ka-Band", in *Proc. European Microwave Conference (EuMC)*, 2015, pp. 1495–1498.

[58] B. Rohrdantz, T. Jaschke, F. Gellersen, A. Sieganschin, and A. F. Jacob, "Ka-Band Antenna Arrays with Dual-Frequency and Dual-Polarized Patch Elements", *Int. J. Microwave and Wireless Tech.*, vol. 8, no. 6, pp. 963–972, 2016.

[59] S. S. Holland, D. H. Schaubert, and M. N. Vouvakis, "A 7–21 GHz Dual-Polarized Planar Ultrawideband Modular Antenna (PUMA) Array", *IEEE Trans. Antennas Propagat.*, vol. 60, no. 10, pp. 4589–4600, 2012.

[60] J. T. Logan and M. N. Vouvakis, "Planar Ultrawideband Modular Antenna (PUMA) Arrays Scalable to mm-Waves", in *IEEE Antennas and Propagation Society International Symposium Digest (APSURSI)*, 2013, pp. 624–625.

[61] C. Rave, T. Jaschke, B. Rohrdantz, and A. F. Jacob, "A Curved-Edge Dipole Antenna for UWB Applications", in *Proc. European Microwave Conference (EuMC)*, 2013, pp. 648–651.

[62] P. J. Gibson, "The Vivaldi Aerial", in *Proc. European Microwave Conference (EuMC)*, 1979, pp. 101–105.

[63] K. Trott, B. Cummings, R. Cavener, M. Deluca, and J. Biondi, "7-21 GHz Wideband Phased Array Radiator", in *IEEE Antennas and Propagation Society International Symposium Digest (APSURSI)*, vol. 3, 2004, pp. 2265–2268.

[64] K. F. Braun, "Electrical Oscillations and Wireless Telegraphy", *Nobel Lecture*, pp. 226–245, 1909.

[65] F. Greco, G. Amendola, E. Arnieri, L. Boccia, and A. I. Sandhu, "A Dual-Band, Dual-Polarized Array Element for Ka Band SatCom on the Move Terminals", in *Proc. European Conference on Antennas and Propagation (EuCAP)*, 2014, pp. 2432–2435.

[66] R. J. Bolt, D. Cavallo, G. Gerini, D. Deurloo, R. Grooters, A. Neto, and G. Toso, "Characterization of a Dual-Polarized Connected-Dipole Array for Ku-Band Mobile Terminals", *IEEE Trans. Antennas Propagat.*, vol. 64, no. 2, pp. 591–598, 2016.

[67] S. Lee, "Aperture Matching for an Infinite Circular Polarized Array of Rectangular Waveguides", *IEEE Trans. Antennas Propagat.*, vol. 19, no. 3, pp. 332–342, 1971.

[68] C.-C. Chen, "Wideband Wide-Angle Impedance Matching and Polarization Characteristics of Circular Waveguide Phased Arrays", *IEEE Trans. Antennas Propagat.*, vol. 22, no. 3, pp. 414–418, 1974.

[69] G. Tsandoulas and G. Knittel, "The Analysis and Design of Dual-Polarization Square-Waveguide Phased Arrays", *IEEE Trans. Antennas Propagat.*, vol. 21, no. 6, pp. 796–808, 1973.

[70] T. Jaschke, H. K. Mitto, and A. F. Jacob, "An SIW Fed Dual-Band and Dual-Polarized Lens Antenna at K/Ka-Band", in *Proc. European Microwave Conference (EuMC)*, 2017, pp. 62–65.

[71] T. Jaschke, B. Rohrdantz, H. K. Mitto, and A. F. Jacob, "Ultrawideband SIW-Fed Lens Antenna", *IEEE Antennas and Wirel. Propag. Lett.*, vol. 16, pp. 2010–2013, 2017.

[72] T. Jaschke, H. K. Mitto, and A. F. Jacob, "K/Ka-Band Dual-Polarized SIW-Fed Lens Antennas for Rx/Tx Integration", *Int. J. Microwave and Wireless Tech.*, vol. 10, no. 5-6, pp. 627–634, 2018.

[73] D. F. Filipovic, S. S. Gearhart, and G. M. Rebeiz, "Double-Slot Antennas on Extended Hemispherical and Elliptical Silicon Dielectric Lenses", *IEEE Trans. Microwave Theory Techn.*, vol. 41, no. 10, pp. 1738–1749, 1993.

[74] B. Chantraine-Bares and R. Sauleau, "Electrically-Small Shaped Integrated Lens Antennas: A Study of Feasibility in Q-Band", *IEEE Trans. Antennas Propagat.*, vol. 55, no. 4, pp. 1038–1044, 2007.

[75] T. Jaschke, B. Rohrdantz, and A. F. Jacob, "A Flexible Surface Description for Arbitrarily Shaped Dielectric Lens Antennas", in *Proc. German Microwave Conference (GeMiC)*, 2014, pp. 1–4.

[76] T. Jaschke, B. Rohrdantz, and A. F. Jacob, "A Flexible Surface Description for Arbitrarily Shaped Dielectric Lens Antennas", *Frequenz*, vol. 69, no. 1-2, pp. 29–37, 2015.

[77] W. Che, B. Fu, P. Yao, and Y. L. Chow, "Substrate Integrated Waveguide Horn Antenna with Dielectric Lens", *Microw. Opt. Technol. Lett.*, vol. 49, no. 1, pp. 168–170, 2007.

[78] M. Chen and G. Tsandoulas, "A Wide-Band Square-Waveguide Array Polarizer", *IEEE Trans. Antennas Propagat.*, vol. 21, no. 3, pp. 389–391, 1973.

[79] J. Esteban and J. M. Rebollar, "Field Theory CAD of Septum OMT-Polarizers", in *IEEE Antennas and Propagation Society International Symposium Digest (APSURSI)*, vol. 4, 1992, pp. 2146–2149.

[80] R. Ihmels, U. Papziner, and F. Arndt, "Field Theory Design of a Corrugated Septum OMT", in *IEEE MTT-S International Microwave Symposium Digest (IMS)*, 1993, pp. 909–912.

[81] R. F. Harrington, *Time-Harmonic Electromagnetic Fields*, ser. Electrical and Electronic Engineering Series. McGraw-Hill, New York, 1961.

[82] C. A. Balanis, *Advanced Engineering Electromagnetics*. Wiley, New York, 1989.

[83] N. Marcuvitz, *Waveguide Handbook*, 1st Ed., ser. IEE Electromagnetic Wave Ser. McGraw-Hill, New York, 1951, vol. 21.

[84] F. Sporleder and H.-G. Unger, *Waveguide Tapers Transitions and Couplers*, ser. IEE Electromagnetic Wave Ser. Peregrinus, Stevenage, 1979, vol. 6.

[85] R. E. Collin, *Foundations for Microwave Engineering*, 2nd Ed., ser. IEEE Press Ser. on Electromagnetic Wave Theory. New York, 2001.

[86] E. Hammerstad and O. Jensen, "Accurate Models for Microstrip Computer-Aided Design", in *IEEE MTT-S International Microwave Symposium Digest (IMS)*, 1980, pp. 407–409.

[87] A. F. Horn, J. W. Reynolds, and J. C. Rautio, "Conductor Profile Effects on the Propagation Constant of Microstrip Transmission Lines", in *IEEE MTT-S International Microwave Symposium Digest (IMS)*, 2010, pp. 868–871.

[88] X. Chen, "EM Modeling of Microstrip Conductor Losses Including Surface Roughness Effect", *IEEE Microw. Wireless Compon. Lett.*, vol. 17, no. 2, pp. 94–96, 2007.

[89] M. V. Lukic and D. S. Filipovic, "Modeling of 3-D Surface Roughness Effects With Application to µ-Coaxial Lines", *IEEE Trans. Microwave Theory Techn.*, vol. 55, no. 3, pp. 518–525, 2007.

[90] P. G. Huray, O. Oluwafemi, J. Loyer, E. Bogatin, and X. Ye, "Impact of Copper Surface Texture on Loss: A Model that Works", *DesignCon*, vol. 1, pp. 462–483, 2010.

[91] G. Gold and K. Helmreich, "A Physical Model for Skin Effect in Rough Surfaces", in *Proc. European Microwave Integrated Circuits Conference (EuMIC)*, 2012.

[92] G. Gold and K. Helmreich, "Surface Impedance Concept for Modeling Conductor Roughness", in *IEEE MTT-S International Microwave Symposium Digest (IMS)*, 2015, pp. 1–4.

[93] G. Gold and K. Helmreich, "A Physical Surface Roughness Model and Its Applications", *IEEE Trans. Microwave Theory Techn.*, vol. 65, no. 10, pp. 3720–3732, 2017.

[94] DIN, *Geometrical Product Specifications (GPS) - Surface texture: Profile method - Terms, definitions and surface texture parameters*, DIN EN ISO 4287, 2010.

[95] J. Kierzenka and L. F. Shampine, "A BVP Solver Based on Residual Control and the Maltab PSE", *ACM Trans. Math. Softw.*, vol. 27, no. 3, pp. 299–316, 2001.

[96] K. Lomakin, G. Gold, and K. Helmreich, "Analytical Waveguide Model Precisely Predicting Loss and Delay Including Surface Roughness", *IEEE Trans. Microwave Theory Techn.*, pp. 1–14, 2018.

[97] J. A. Stratton, *Electromagnetic Theory*, ser. Int. Ser. in Pure and Applied Phys. McGraw-Hill, New York, 1941.

[98] M. Schmidt and H. Lipson, "Distilling Free-Form Natural Laws from Experimental Data", *Science*, vol. 324, no. 5923, pp. 81–85, 2009.

[99] D. M. Pozar, *Microwave Engineering*, 4th Ed. Wiley, Hoboken, 2012.

[100] H.-G. Unger and J. H. Hinken, *Elektromagnetische Theorie für die Hochfrequenztechnik, Teil II*, 2nd Ed., ser. ELTEX - Studientexte Elektrotechnik. Hüthig, Heidelberg, 1989.

[101] K. Lomakin, G. Gold, and K. Helmreich, "Transmission Line Model for Rectangular Waveguides Accurately Incorporating Loss Effects", in *IEEE Workshop on Signal and Power Integrity (SPI)*, 2017, pp. 1–4.

[102] A. F. Horn, P. A. LaFrance, J. W. Reynolds, and J. Coonrod, "The Influence of Test Method, Conductor Profile and Substrate Anisotropy on the Permittivity Values Required for Accurate Modeling of High Frequency Planar Circuits", *Circuit World*, vol. 38, no. 4, pp. 219–231, 2012.

[103] R. Garg, I. Bahl, and M. Bozzi, *Microstrip Lines and Slotlines*, 3rd Ed. Artech House, Norwood, 2013.

[104] F. Xu, Y. Zhang, W. Hong, K. Wu, and T. J. Cui, "Finite-Difference Frequency-Domain Algorithm for Modeling Guided-Wave Properties of Substrate Integrated Waveguide", *IEEE Trans. Microwave Theory Techn.*, vol. 51, no. 11, pp. 2221–2227, 2003.

[105] F. Xu and K. Wu, "Numerical Multimode Calibration Technique for Extraction of Complex Propagation Constants of Substrate Integrated Waveguide", in *IEEE MTT-S International Microwave Symposium Digest (IMS)*, 2004, pp. 1227–1230.

[106] F. Xu and K. Wu, "Guided-Wave and Leakage Characteristics of Substrate Integrated Waveguide", *IEEE Trans. Microwave Theory Techn.*, vol. 53, no. 1, pp. 66–73, 2005.

[107] J. Hirokawa and M. Ando, "Single-Layer Feed Waveguide Consisting of Posts for Plane TEM Wave Excitation in Parallel Plates", *IEEE Trans. Antennas Propagat.*, vol. 46, no. 5, pp. 625–630, 1998.

[108] D. Deslandes and K. Wu, "Accurate Modeling, Wave Mechanisms, and Design Considerations of a Substrate Integrated Waveguide", *IEEE Trans. Microwave Theory Techn.*, vol. 54, no. 6, pp. 2516–2526, 2006.

[109] Y. Cassivi, L. Perregrini, P. Arcioni, M. Bressan, K. Wu, and G. Conciauro, "Dispersion Characteristics of Substrate Integrated Rectangular Waveguide", *IEEE Microw. Wireless Compon. Lett.*, vol. 12, no. 9, pp. 333–335, 2002.

[110] L. Yan, W. Hong, K. Wu, and T. J. Cui, "Investigations on the Propagation Characteristics of the Substrate Integrated Waveguide Based on the Method of Lines", *IEE Proc. Microw. Antennas Propag.*, vol. 152, no. 1, pp. 35–42, 2005.

[111] R. Sorrentino and M. Mongiardo, "Transverse Resonance Techniques", in *Encyclopedia of RF and Microwave Engineering*, K. Chang, Ed., vol. 32, Wiley-Interscience, Hoboken, NJ, 2005, pp. 5357–5363.

[112] T. Itoh, *Numerical Techniques for Microwave and Millimeter-Wave Passive Structures*, ser. A Wiley-Interscience Publication. Wiley, New York, 1989.

[113] J. E. Varela and J. Esteban, "Analysis of Laterally Open Periodic Waveguides by Means of a Generalized Transverse Resonance Approach", *IEEE Trans. Microwave Theory Techn.*, vol. 59, no. 4, pp. 816–826, 2011.

[114] Rogers Corporation, *Copper Foils for High Frequency Materials*, 2018. [Online]. Available: `www.rogerscorp.com`.

[115] J. A. Marshall, "Measuring Copper Surface Roughness for High Speed Applications", *Proc. IPC*, pp. 1–6, 2015.

[116] W. C. Hahn, "A New Method for the Calculation of Cavity Resonators", *J. of Applied Phys.*, vol. 12, no. 1, pp. 62–68, 1941.

[117] J. R. Whinnery and H. W. Jamieson, "Equivalent Circuits for Discontinuities in Transmission Lines", *Proc. IRE*, vol. 32, no. 2, pp. 98–114, 1944.

[118] F. Arndt, "Mode-Matching Methods", in *Encyclopedia of RF and Microwave Engineering*, K. Chang, Ed., vol. 32, Wiley-Interscience, Hoboken, NJ, 2005, pp. 3162–3176.

[119] G. V. Eleftheriades, A. S. Omar, L. Katehi, and G. M. Rebeiz, "Some Important Properties of Waveguide Junction Generalized Scattering Matrices in the Context of the Mode Matching Technique", *IEEE Trans. Microwave Theory Techn.*, vol. 42, no. 10, pp. 1896–1903, 1994.

[120] A. Morini and T. Rozzi, "On the Definition of the Generalized Scattering Matrix of a Lossless Multiport", *IEEE Trans. Microwave Theory Techn.*, vol. 49, no. 1, pp. 160–165, 2001.

[121] H. D. Knetsch, "Beitrag zur Theorie sprunghafter Querschnittsveränderungen von Hohlleitern", *AEÜ*, vol. 22, no. 12, pp. 591–600, 1968.

[122] G. Conciauro, M. Guglielmi, and R. Sorrentino, *Advanced Modal Analysis: CAD Techniques for Waveguide Components and Filters*. Wiley, Chichester, 2000.

[123] T. E. Rozzi and W. F. G. Mecklenbräuker, "Wide-Band Network Modeling of Interacting Inductive Irises and Steps", *IEEE Trans. Microwave Theory Techn.*, vol. 23, no. 2, pp. 235–245, 1975.

[124] R. R. Mansour and R. H. Macphie, "Scattering at an N-Furcated Parallel-Plate Waveguide Junction (Short Paper)", *IEEE Trans. Microwave Theory Techn.*, vol. 33, no. 9, pp. 830–835, 1985.

[125] W. Che, C. Li, P. Russer, and Y. L. Chow, "Propagation and Band Broadening Effect of Planar Integrated Ridged Waveguide in Multilayer Dielectric Substrates", in *IEEE MTT-S International Microwave Symposium Digest (IMS)*, 2008, pp. 217–220.

[126] M. Bozzi, S. A. Winkler, and K. Wu, "Broadband and Compact Ridge Substrate-Integrated Waveguides", *IET Microw., Antennas & Propag.*, vol. 4, no. 11, pp. 1965–1973, 2010.

[127] J. M. E. Ainsworth, "A Numerical Model of the Propagation Characteristics of Multi-Layer Ridged Substrate Integrated Waveguide", Ph.D. Thesis, Univ. of Manchester, United Kingdom, 2012.

[128] N. Grigoropoulos, B. Sanz-Izquierdo, and P. R. Young, "Substrate Integrated Folded Waveguides (SIFW) and Filters", *IEEE Microw. Wireless Compon. Lett.*, vol. 15, no. 12, pp. 829–831, 2005.

[129] G. H. Zhai, W. Hong, K. Wu, J. X. Chen, P. Chen, J. Wei, and H. J. Tang, "Folded Half Mode Substrate Integrated Waveguide 3 dB Coupler", *IEEE Microw. Wireless Compon. Lett.*, vol. 18, no. 8, pp. 512–514, 2008.

[130] T. Jaschke and A. F. Jacob, "Novel Multilayer SIW Tapers Synthesized Using an Extended Transverse Resonance Method", in *IEEE MTT-S International Microwave Symposium Digest (IMS)*, 2017, pp. 715–718.

[131] R. Beyer and F. Arndt, "Efficient Modal Analysis of Waveguide Filters Including the Orthogonal Mode Coupling Elements by an MM/FE Method", *IEEE Microw. Guid. Wave Lett.*, vol. 5, no. 1, pp. 9–11, 1995.

[132] J. P. Montgomery, "On the Complete Eigenvalue Solution of Ridged Waveguide", *IEEE Trans. Microwave Theory Techn.*, vol. 19, no. 6, pp. 547–555, 1971.

[133] F.-L. C. Lin, "Modal Characteristics of Crossed Rectangular Waveguides", *IEEE Trans. Microwave Theory Techn.*, vol. 25, no. 9, pp. 756–763, 1977.

[134] S. Güttel and F. Tisseur, "The Nonlinear Eigenvalue Problem", *Acta Numerica*, vol. 26, pp. 1–94, 2017.

[135] H. Voss, "Nonlinear Eigenvalue Problems", in *Handbook of Linear Algebra*, ser. Discrete Mathematics and its Applications, L. Hogben, Ed., CRC Press/Taylor & Francis Group, Boca Raton, Florida, 2016, pp. 60-1–60-24.

[136] M. J. D. Powell, “A Fortran Subroutine for Solving Systems of Nonlinear Algebraic Equations”, in *Numerical Methods for Nonlinear Algebraic Equations*, London, GB, 1970, Cha. 7.

[137] V. Mehrmann and H. Voss, “Nonlinear Eigenvalue Problems: A Challenge for Modern Eigenvalue Methods”, *GAMM-Mitteilungen*, vol. 27, no. 2, pp. 121–152, 2004.

[138] D. Kressner, “A Block Newton Method for Nonlinear Eigenvalue Problems”, *Numer. Math.*, vol. 114, no. 2, pp. 355–372, 2009.

[139] D. Deslandes and K. Wu, “Integrated Microstrip and Rectangular Waveguide in Planar Form”, *IEEE Microw. Wireless Compon. Lett.*, vol. 11, no. 2, pp. 68–70, 2001.

[140] A. Patrovsky, M. Daigle, and K. Wu, “Millimeter-Wave Wideband Transition from CPW to Substrate Integrated Waveguide on Electrically Thick High-Permittivity Substrates”, in *Proc. European Microwave Conference (EuMC)*, 2007, pp. 138–141.

[141] E. Diaz Caballero, A. Belenguer Martinez, H. E. Gonzalez, O. M. Belda, and V. B. Esbert, “A Novel Transition from Microstrip to a Substrate Integrated Waveguide with Higher Characteristic Impedance”, in *IEEE MTT-S International Microwave Symposium Digest (IMS)*, 2013, pp. 1–4.

[142] T. Jaschke, B. Rohrdantz, and A. F. Jacob, “Dual-Band Stepped-Impedance Transformer to Full-Height Substrate-Integrated Waveguide”, in *Proc. European Microwave Conference (EuMC)*, 2015, pp. 367–370.

[143] T. Jaschke, B. Rohrdantz, W. M. Gitzel, and A. F. Jacob, “Modeling and Design of Stepped Transitions for Substrate-Integrated Waveguides”, in *Proc. German Microwave Conference (GeMiC)*, 2016, pp. 124–127.

[144] P. A. Rizzi, *Microwave Engineering: Passive Circuits*. Prentice Hall, Englewood Cliffs, N.J., 1988.

[145] H.-J. Eul and B. Schiek, “A Generalized Theory and New Calibration Procedures for Network Analyzer Self-Calibration”, *IEEE Trans. Microwave Theory Techn.*, vol. 39, no. 4, pp. 724–731, 1991.

[146] H. Heuermann and B. Schiek, “Robust Algorithms for Txx Network Analyzer Self-Calibration Procedures”, *IEEE Trans. Instrum. Meas.*, vol. 43, no. 1, pp. 18–23, 1994.

[147] L. Solymar, “Spurious Mode Generation in Nonuniform Waveguide”, *IEEE Trans. Microwave Theory Techn.*, vol. 7, no. 3, pp. 379–383, 1959.

[148] C. Rave and A. F. Jacob, "A Design Approach for Tapered Waveguide to Substrate-Integrated Waveguide Transitions", *IEEE Trans. Microwave Theory Techn.*, vol. 64, no. 8, pp. 2502–2510, 2016.

[149] K.-D. Kammeyer and K. Kroschel, *Digitale Signalverarbeitung: Filterung und Spektralanalyse mit MATLAB-Übungen*, 9th Ed., ser. Lehrbuch. Springer Vieweg, Wiesbaden, 2018.

[150] R. Klopfenstein, "A Transmission Line Taper of Improved Design", *Proc. IRE*, vol. 44, no. 1, pp. 31–35, 1956.

[151] R. Collin, "The Optimum Tapered Transmission Line Matching Section", *Proc. IRE*, vol. 44, no. 4, pp. 539–548, 1956.

[152] K. Matsumaru, "Reflection Coefficient of E-Plane Tapered Waveguides", *IEEE Trans. Microwave Theory Techn.*, vol. 6, no. 2, pp. 143–149, 1958.

[153] P. H. Siegel, D. W. Peterson, and A. R. Kerr, "Design and Analysis of the Channel Waveguide Transformer", *IEEE Trans. Microwave Theory Techn.*, vol. 31, no. 6, pp. 473–484, 1983.

[154] P. H. Siegel, D. W. Peterson, and A. R. Kerr, "The Channel Waveguide Transformer: An Easily Fabricated H-Plane Transition for the Rectangular TE-10 Mode", in *IEEE MTT-S International Microwave Symposium Digest (IMS)*, 1983, pp. 172–174.

[155] C. Ernst, V. Postoyalko, and N. G. Khan, "Relationship Between Group Delay and Stored Energy in Microwave Filters", *IEEE Trans. Microwave Theory Techn.*, vol. 49, no. 1, pp. 192–196, 2001.

[156] L. Hogben, Ed., *Handbook of Linear Algebra*, 2nd Ed., ser. Discrete Mathematics and its Applications. CRC Press/Taylor & Francis Group, Boca Raton, Florida, 2016.

[157] M. D. Janezic, "Nondestructive Relative Permittivity and Loss Tangent Measurements Using a Split-Cylinder Resonator", Ph.D. Thesis, Univ. of Colorado, 2003.

[158] J. Thornton and K.-C. Huang, *Modern Lens Antennas for Communications Engineering*. Wiley IEEE Press, Hoboken, New Jersey, 2013.

[159] E. L. Holzman, "A Highly Compact 60-GHz Lens-Corrected Conical Horn Antenna", *IEEE Antennas and Wirel. Propag. Lett.*, vol. 3, pp. 280–282, 2004.

[160] M. K. T. Al-Nuaimi, W. Hong, and Y. Zhang, "Design of High-Directivity Compact-Size Conical Horn Lens Antenna", *IEEE Antennas and Wirel. Propag. Lett.*, vol. 13, pp. 467–470, 2014.

[161] K. Uehara, K. Miyashita, K.-I. Natsume, K. Hatakeyama, and K. Mizuno, "Lens-Coupled Imaging Arrays for the Millimeter- and Submillimeter-Wave Regions", *IEEE Trans. Microwave Theory Techn.*, vol. 40, no. 5, pp. 806–811, 1992.

[162] D. Lemaire, C. Fernandes, P. Sobieski, and A. Barbosa, "A Method to Overcome the Limitations of G.O. in Axis-Symmetric Dielectric Lens Shaping", *Int. J. Infrared Milli. Waves*, vol. 17, no. 8, pp. 1377–1390, 1996.

[163] B. Chantraine-Bares, R. Sauleau, L. Le Coq, and K. Mahdjoubi, "A New Accurate Design Method for Millimeter-Wave Homogeneous Dielectric Substrate Lens Antennas of Arbitrary Shape", *IEEE Trans. Antennas Propagat.*, vol. 53, no. 3, pp. 1069–1082, 2005.

[164] IEEE, *Standard Test Procedures for Antennas*, IEEE 149, Piscataway, NJ, USA, 1979.

[165] D. F. Rogers, *An Introduction to NURBS: With Historical Perspective*. Morgan Kaufmann Publishers, San Francisco, 2001.

[166] T. Kushta and K. Yasumoto, "Electromagnetic Scattering From Periodic Arrays of Two Circular Cylinders Per Unit Cell", *J. of Electromagnetic Waves and Applications*, vol. 14, no. 6, pp. 853–854, 2000.

[167] J. Yang, L.-W. Li, K. Yasumoto, and C.-H. Liang, "Two-Dimensional Scattering of a Gaussian Beam by a Periodic Array of Circular Cylinders", *IEEE Trans. Geosci. Remote Sensing*, vol. 43, no. 2, pp. 280–285, 2005.

[168] F. W. J. Olver, D. W. Lozier, R. F. Boisvert, and C. W. Clark, Eds., *NIST Handbook of Mathematical Functions*. Cambridge University Press, Cambridge, New York, and Melbourne, 2010.

[169] K. Yasumoto and K. Yoshitomi, "Efficient Calculation of Lattice Sums for Free-Space Periodic Green's Function", *IEEE Trans. Antennas Propagat.*, vol. 47, no. 6, pp. 1050–1055, 1999.

[170] C. M. Linton, "Schlömilch Series that Arise in Diffraction Theory and Their Efficient Computation", *J. of Phys. A: Math. Gen.*, vol. 39, no. 13, pp. 3325–3339, 2006.

[171] W. C. Chew, *Waves and Fields in Inhomogenous Media*. IEEE, 1999.

[172] J. L. Gross and J. Yellen, *Graph Theory and Its Applications*, 2nd Ed., ser. Discrete Mathematics and its Applications. Chapman & Hall/CRC, Boca Raton, 2006.